

Roice Nelson

# TECHNICAL ABSTRACTS



**SEG Research Workshop  
on Lithology:  
Relating Elastic  
Properties to Lithology  
at all Scales**

July 28-August 1, 1991  
St. Louis, Missouri

Society of Exploration Geophysicists

**LITHOLOGY: RELATING ELASTIC PROPERTIES  
TO LITHOLOGY AT ALL SCALES**

SEG Research Workshop  
July 28-August 1, 1991  
St. Louis, Missouri

A Presentation of the  
Society of Exploration Geophysicists  
Research Committee

**ABSTRACTS OF PAPERS PRESENTED**

## TABLE OF CONTENTS

TITLE	PAGE
<u>Session 1</u> Laboratory/Theoretical	
Advances in Relation Between Seismic and Reservoir Rock Properties	1
P- and S-Wave Velocity Relation in Sedimentary Rocks	2
Effect of Cementation on the Elastic Properties of Rock	13
Estimation of Lithology from Elastic Properties?	15
Effect of Clay Content on Compressional and Shear Wave Velocities and Attenuation in Tight Gas Sand Formations	16
The Effects of Non-Welded Interfaces on Seismic Wave Propagation and Attenuation	18
The Effects of Grain Contacts on Elastic Waves in Granular Rock	23
Scale-Dependent Effects of Anisotropic Mechanisms	31
The Effect of Pore Fluids and Pressures on the Seismic Velocities in Cracked and/or Porous Rocks	35
Anisotropic Acoustic Properties of Coal	39
Elastic Property Scaling Relationships: Core Measurements Results and Acoustic Logging Experiments	43
Modeling Borehole Stoneley Wave Propagation Across Permeable In-situ Fractures	51
Scale of Anisotropy: A Theoretical Study of Velocity Anisotropy for Micro and Macro Fractures	55
Propagation of Seismic Waves Through 2-D Random Media: Implications for Travel Times	59

<b>TITLE</b>	<b>PAGE</b>
Acoustic Anisotropy of Synthetics with Controlled Crack Geometries	68
The Role of Surface Roughness in Porous Media Acoustics	69

**Session 2**  
**Development and Production**

Talking to Seismologists	N/A
Relating Rock Physics from the Laboratory to an In-situ Velocity Tomogram	80
The Effect of Permeability Heterogeneity on Oil-Water Displacement in Porous Media	82
A Case Study of Reservoir Heterogeneity in a Fluvial Sandstone: The Gypsy Sandstone of Oklahoma	88
Integration of Geology and Geophysics in Stochastic Models	89
Closing the Loop: How Reservoir Testing, Production, and Simulation Results Feed Back to Seismic Reprocessing and Interpretation	92
Multicomponent Vertical Seismic Profiles for Reservoir Characterization, South Casper Creek Field, Natrona County, Wyoming	102
Shear-Wave Polarization Analysis as a Tool for Deducing Subsurface Rock Properties	106
Transverse Isotropy: An Indicator of Horizontal Microfractures	115
Characterizing Hydraulically Fractured Reservoirs using Induced Microearthquakes	117

**TITLE** **PAGE**

**Session 3**  
**Mature Exploration**

Implications of Thin Layers in Extracting Lithology using Amplitude versus Offset	124
Lithology Prediction in Clastic Sedimentary Rocks Using Seismic Velocity	136
Optimal Resolution of Anisotropy using Zero-offset VSP Data	139
Predicting Lithology from Elastic Properties using Discriminant Analysis	144
Relating Rock Physics to Seismic Lithology in a North Sea Reservoir	145
Reconciliation of Dip Data and VSP Data, and the Illumination of West Texas Reefs	154
Use of Three-Component Downhole Geophones Results in Improved Salt Proximity Surveys	N/A
Synthetic Shear Wave Sonic Logs for Seismic Models	N/A

**Session 4**  
**Frontier/Submature Exploration**

The Effect of Small Quantities of Sand on Average Interval Velocity in Overpressured Clastic Sections	159
Brent Calcite and Porosity Prediction using Seismic Elastic Perturbation Modeling	161
Chaotic Sedimentary Sequences Inferred from Seismic Reflectivity Well Logs	174
Prediction of Pore Fluids using Poisson's Ratios from Seismic Data	194
Reconnaissance AVO on Surface Seismic Data	201

<b>TITLE</b>	<b>PAGE</b>
<b>GEM: A New Concept in Quantitative Core Characterization</b>	210
<b>Geostatistical Applications for Exploration and Development: Porosity Estimations from 3-D Seismic Data Conditioned to Well Data</b>	213
<b>Systems Tracts of the Zambezi Delta, Mozambique</b>	N/A
<b>Lithology Prediction in a Carbonate Regime</b>	N/A
<b>Predicting Lithofacies from Seismic Data using Sequence Stratigraphy Principles</b>	217

Society of Exploration Geophysicists

Summer Research Workshop on Lithology:  
Relating Elastic Properties to Lithology at all Scales  
July 28-August 1, 1991 . St. Louis, Missouri

Registration of Attendees

Hassan Ahmed  
Simon-Geolithic  
Swanley, England

Hasan Al Kaf  
Saudi Aramco  
Geophysical Department, Room X-4030  
Dhahran 31311, Saudi Arabia  
(966) 3-876-8512

R.H. (Dick) Angerer  
Assoc. Geophysical Analysts  
Box 280888  
Lakewood, CO 80228  
(303) 933-0211

Stewart Archer  
HGS LTD.  
Riverside House, 6 Horne Lane  
Bedford MK40 1PY, U.K.  
0234 273388

Tutuncu Azra  
The University of Texas  
at Austin  
CPE 5116, Dept. of  
Petroleum Engineering  
Austin, TX 78712  
(512) 471-0277

Dan Babaluk  
Petro-Canada  
PO Box 2844  
Calgary, Alberta,  
Canada T2P 3E3  
(403) 296-8224

Laurel Babcock  
Amoco Production Co.  
Box 3385  
Tulsa, OK 74102  
(918) 660-3471

Michael Batzle  
Arco  
2300 W. Plano Parkway  
Plano, TX 75075  
(214) 754-6975

Gerard Beaudoin  
Amoco Production Co.  
PO Box 3092  
Houston, TX 77253  
(713) 556-3586

Wallace Beckham  
Texaco Inc.  
3901 Briarpark  
Houston, TX 77042  
(713) 954-6354

William Benzing  
Conoco  
600 N. Dairy Ashford  
Houston, TX 77450  
(713) 293-3051

Jéan-Pierre Blangy  
Stanford University  
Geophysics Dept., Mitchell Bldg.  
Stanford, CA 94305-2215  
(415) 725-1345

Eric J. Bocage  
Shell  
2613 Highland Dr. West  
Gretna, LA 70056  
(504) 588-0625

Brian Bonner  
L.L.N.L.  
L.201 Box 808  
Livermore, CA 94550  
(415) 422-7080

Steve Burdine  
Oklahoma Seismic  
6101 W. Reno, Ste 600  
Oklahoma City, Okla. 73127

Daniel Burns  
NER  
1100 Crown Colony Dr.  
Quincy, MA 02169  
(617) 774-0301

Jack Caldwell  
Schlumberger  
4100 Spring Valley Rd., Ste. 600  
Dallas, TX 75244  
(214) 385-4040

Jack Cameron  
Unocal  
PO Box 76  
Brea, CA 92621  
(714) 577-1206

Melvan D. Carter  
EAI/LGC  
2777 Stemmons Fwy.,  
Ste. 655  
Dallas, TX 75207  
(214) 638-1065

Richard Chambers  
Amoco Production Co.  
4502 E. 41st Street  
Tulsa, OK 74102  
(918) 660-3928

Sen Chen  
Exxon Production  
Reserch Co.  
PO Box 2189  
Houston, TX 77252-2189  
(713) 965-4615

Arthur C.H. Cheng  
M.I.T.  
E34-454-M.I.T.  
Cambridge, MA 02139  
(617) 253-7206

Edward Chilburis  
Saudi Aramco  
Geophysical Department RM X-3480  
Dhahran 31311, Saudi Arabia  
(966) 3-876-8320

Terje Dahl  
Statoil  
Statoil, Postvttak  
Trondheim, Norway N-7004  
47-7-584011

David Dalley  
Chevron Canadian Resources  
500 5th Ave.S.W.  
Calgary, Alberta, Canada T1Y 3M6  
(403) 234-5832

Harry Debeye  
Jason Geosystems  
PO Box 596  
Delft, Netherlands  
2600AH  
(31) 15-147241

David C. DeMartini  
Shell Development  
Company  
PO Box 481  
Houston, TX 77001  
(713) 245-7689

James Doyle  
BP Exploration  
5151 San Felipe  
Houston, TX 77056  
(713) 552-8782

Chris Drexler  
Exxon  
Houston, TX 77388  
(713) 965-7603

Guy Drjkoningen  
Technical Univ.  
Mijnboynstraat 120  
Delft, Holland 2628RX  
(31) 15-786105

Jack Dvorkin  
Standford University  
Geophysics Department  
Stanford, CA 96305-3315  
(415) 723-9508

Charles E. Edwards  
Landmark  
1502 So. Bessner  
Houston, TX 77063  
(713) 785-7115

Michael Fehler  
Los Alamos National Lab  
MS D443  
Los Alamos, NM 87545  
(505) 667-1925

Daniel Ebrom  
University of Houston  
AGL Bldg. Univ. of Houston  
Houston, TX 77204-4231  
(712) 749-7336

James Forgotson Jr.  
Univeristy of Oklahoma  
School of Geology, 100 E. Boyd  
Norman, OK 73019  
(405) 325-4424

John Friess  
Conoco Inc.  
PO Box 1267  
Ponca City, OK 74603  
(405) 767-4339

Al Frisillo  
Amoco Production Company  
4502 E. 41st  
Tulsa, OK 74102  
(918) 3650

Alain Galli  
ENSMP  
35 Rue Saint Honore  
Fontainebleau, France 77305  
(33) 1 64694773

Anthony F. Gangi  
Texas A&M Univeristy  
Department of Geophysics,MS3114  
College Station, TX  
77843-3114  
(409) 845-1381

Michael Garner  
J.M. Huber  
3310 Lakehaven Dr.  
Kingwood, TX 77339  
(713) 358-9344

Gary Gassaway  
Terra Linda  
237 Crescent Rd.  
San Ansermo, California 94960  
(415) 459-1943

De-Hua Ham  
UNOCAL  
376 S. Valencia Ave.  
Brea, CA 92621  
(714) 577-1327

Joel Hendrickson  
Shell Offshore Inc.  
318 Lake Marina Dr. #322  
New Orleans, CA 70124  
(504) 588-6892

Ron Hietala  
Canadian Hunter Exploration  
435-4th Ave. S.W.  
Calgary, Alberta, Canada T2P 3A8  
(403) 260-1955

Dr. Alan R. Huffman  
Exxon  
PO Box 4279  
Houston, TX 77210-4279  
(713) 591-5427

Stephen Johnson  
Amoco Production Co.  
PO Box 3385  
Tulsa, OK 74102  
(918) 660-3570

Lue Ikelle  
Schlumberger  
Hich Cross, Madingley Rd.  
Cambridge, United Kingdom CB30EL  
(44) 223-325-444

Diane Jizba  
E H Aquitaine  
CSTCS, Batm Burequ09  
Pav, France 64000  
(33) 59-30-64-70

Costas J. Karavas  
McGill Univeristy  
3450 Univeristy ST.  
Montreal, Quebec Canada H3A-2A7  
(514) 398-6767

Timothy H. Ketto  
ARCO  
2300 W. Plano Parkway  
Plano, TX 75075  
(214) 754-3459

Darrell Kramer  
Unocal  
PO Box 68076, Rm. 2024  
West Anaheim, CA 92807  
(214) 693-

Mark Kramer  
Chevron  
PO Box 42832  
Houston, TX 77242-2832  
(713) 596-2015

Thomas Latham  
ARCO  
2300 W. Plano Pkwy.  
Plano, TX 75075  
(214) 754-4606

Martin Layzell  
Westcoast Petroleum  
421 7th Avenue S.W.  
Calgary, Alta., Canada  
(403) 260-9573

Doo Sung Lee  
Unocal  
376 S. Valencia  
Brea, CA 92621  
(714) 577-2446

Richard Lindsay  
Amoco  
7428 S. 68 E. Avenue  
Tulsa, OK 74133  
(918) 492-1139

Edward C. Loomis  
Amoco Egypt  
501 Westlake Park Blvd.  
Houston, TX 77253  
(713) 556-3079

Elizabeth Lorenzetti  
Texico Inc.  
PO Box 770070  
Houston, TX 77215-0070  
(713) 954-6140

Albert Louie  
J.M. Huber Corporation  
500, 700 - 9 Ave. S.W.  
Calgary, Alberta, Canada T2P 3V4  
(403) 266-5631

Heloise Lynn  
Lynn Inc.  
1642 Fall Valley Dr.  
Houston, TX 77077  
(713) 496-5358

Colin Macbeth  
British Geological Survey  
West Mains Road  
Edinburgh, U.K. EH93LA  
(013) 662-1000, x 208

Batakrishna Mandal  
M.I.T.  
42 Carleton ST., E34-404  
Cambridge, MA 02142  
(617) 253-7858

Gary Mavko  
Stanford Univeristy  
Dept. of Geophysics  
Stanford, CA 94305-2215  
(414) 723-9439

Randy S. McKnight  
Marathon Oil Company  
PO Box 269  
Littleton, CO 80160  
(303) 794-2601

Deborah Miles  
Terra Linda  
600 510 5th St. S.W.  
Calgary, Alberta, Canada T2P 3S2  
(403) 262-2170

Larry Myer  
Lawrence Berkely Lab  
Bldg. 50A, Room 1145  
Berkely, CA 94720  
(415) 486-6456

H. Roice Nelson, Jr.  
Landmark  
333 Cypress Run  
Houston, TX 77094  
(713) 579-4794

Tai Ng  
Canadian Hunter  
435-4 Ave. S.W.  
Calgary, Alberta, Canada T2P 3A8  
(403) 260-1074

Kurt Nihei  
Univeristy of California  
Hearst Mining Bldg.  
Berleley. CA 94720  
(415) 642-3809

Eugene Nosal  
Marathon  
PO Box 3128  
Houston, TX 77253  
(713) 629-6600

Azik Perelberg  
E.P.R. Co.  
PO Box 2189  
Houston, TX 77001  
(713) 965-4072

Steven Poe  
UPRC  
801 Cherry ST., M.S. 3502  
Ft. Worth, TX 76102  
(817) 877-6810

Manika Prasad  
3562 Juergens Dr.  
San Jose, California

Bradford Prather  
Shell Development Company  
One Shell Square, RM. 3078  
New Orleans, LA 70122  
(504) 588-7257

Steve Pride  
Erl/mit  
65 Phillips St. #2  
Boston, MA 02114  
(617) 742-8363

Sue Raikes  
BP  
BP Research Centre, Chertsey Rd.  
Sunbury-on-Thames, English Twi6t1m  
(932) 762726

Charles Rego  
BP Exploration  
5151 San Felipe  
Houston, TX 77210  
(713) 552-3718

David Risch  
Geco-Prakla  
1325 S. Dairy Ashford  
Houston, TX 77077  
(713) 596-1452

Don Robinson  
Oklahoma Seismic  
6101 W. Reno, Ste. 600  
Oklahoma City, OK 73127  
(405) 787-6200

James Robinson  
Shell Development Company  
PO Box 481  
Houston, TX 77001  
(713) 245-7898

Rick Saenfer  
J.M. Huber Corp.  
7120 I-40 W., Ste. 200  
Amarillo, TX 79106  
(806) 353-9837

Thomas Schultz  
BPX  
5151 San Felipe  
Houston, TX 77210  
(713) 552-3070

Yuzo Sengoku  
JNOC  
2-2 Hamad 1-Chome  
Chiba, Japan 260  
(0472) 76-9256

Mrinal K. Sengupta  
Exxon  
PO Box 2159  
Houston, TX 77252-2159  
(713) 531-5346

Mukul Sharma  
The University of Texas at Austin  
Dept. of Petroleum Engineering  
Austin, TX 78712  
(512) 471-3757

Nobuyuki Shimizu  
JNOC  
2-2Hamada 1-chome  
Chiba, Japan 260  
(0472) 76-9258

Rajendra Shrestha  
University of Oklahoma  
100 E. Boyd, #810  
Norman, OK 73019-0628  
(405) 325-3253

Yoram Shoham  
Shell Development Co.  
PO Box 481  
Houston, TX 77001  
(713) 245-7282

Carl H. Sondergeld  
Amoco Production Co.  
PO Box 3385  
Tulsa, Ok 74102  
(918) 660-3917

Tracy J. Stark  
Exxon  
PO Box 2189  
Houston, TX 77252-2189  
(713) 966-3011

Lisa Stewart  
Schlumberger  
Old Quarry Rd.  
Ridgefield, CT 06877  
(203) 431-5532

Robert Stewart  
University of Calgary  
Department of Geophysics  
Calgary, Alberta, Canada T2N 1N4  
(403) 220-3265

Sverre Strandenæs  
Norsk Hydro  
Stanford University  
Geophysics Dept.  
Stanford, CA 94305-2215  
(415) 725-1345

Roberto Suarez-Rivera  
University of California  
Hearst Mining Bldg.  
Berkeley, CA 94720  
(415) 642-9278

M. Turhan Taner  
Seismic Research  
2401 Ports Mouth Ste. 250  
Houston, TX 77098  
(713) 520-8606

Robert H. Tatham  
Texaco  
PO BOX 770070  
Houston, TX 77215-0070  
(713)

Leon Thomsen  
Amoco  
PO Box 3385  
Tulsa, OK 74102  
(918) 660-3920

Cornelis Van Der Kolk  
Shell Development Co.  
Volmerlaan 6  
Rijswijk, Netherlands 2288 GD  
(070) 3118944

Lev Vernik  
Stanford University  
Dept. of Geophysics  
Stanford, CA 94305  
(415) 723-5798

John Ward  
Simon-Geolithic  
7802 Beaver Lake Ct.  
Humble, TX 77346  
(713) 820-2116

Ronald W. Ward  
LL&E  
PO Box 60350  
New Orleans, LA 70160  
(504) 566-6789

Terry L. Watt  
Amerada Hess Corp.  
PO Box 2040  
Tulsa, Ok 74102  
(918) 599-4408

Don Winterstein  
Chevron  
PO Box 446  
LaHabra, CA 90633-0446  
(213) 694-7366

E.J. Witterholt  
BP Exploration  
5151 San Felipe PO Box 4489  
Houston, TX 77210  
(713) 552-4439

Keith Wrolstad  
UNOCAL  
376 S. Valencia  
Brea, CA 92621  
(714) 528-7201

Mai Yang  
UNOCAL  
PO Box 4551  
Houston, TX 77210  
(713) 287-7238

John S. Yantosca  
J.M. Huber  
1900 W. Loop South, Ste. 1600  
Houston, TX 77027  
(713) 871-4595

Roger Young  
University of Oklahoma  
201 S. Creekdale Dr. #809  
Norman, OK 73072

Xianhuai Zhu  
UPRC  
PO Box 7  
Ft. Worth, TX 76101-0007  
(817) 877-6946

Ziqiong Zheng  
Terra Tek. Inc.  
420 Wakaraway  
Salt Lake City, Utah 84108  
(801) 584-2484

David Zimmerman  
Conoco  
1001 W. Grand  
Ponca City, OK 74601  
(405) 767-3366

Carol J. Zimmerman  
Exxon  
440 Benmar PO Box 4279  
Houston, TX 77210-4279  
(713) 591-5140

27 July 1991

Geophysical Vice-President  
Geophysical Manager  
Division Geophysicist  
Research Geophysicist  
Exploration Geophysicist

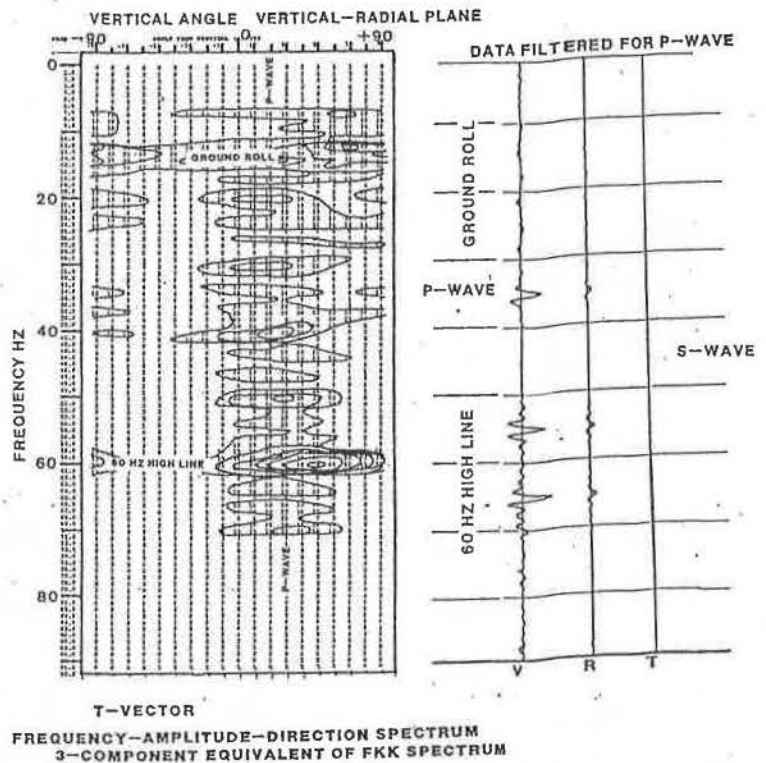
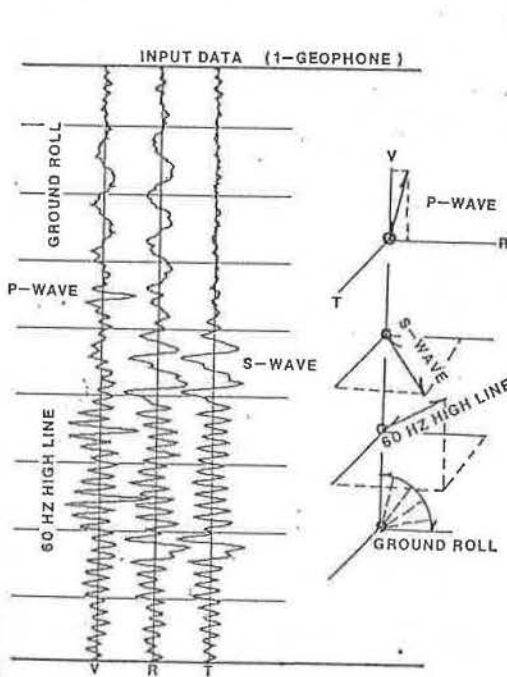
Sirs:

The newly developed FDD transform (Frequency-vibration Direction-vibration Direction) for seismic processing is more powerful than the FK and FKK transforms that currently exist.

INPUT  
(3-component  
geophone)

FDD transform

Filtered Output  
(3-component  
geophone)



**Terra Linda Group**

office: 237 Crescent Rd, San Anselmo, CA 94960

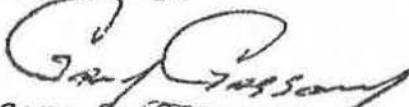
mail: P.O. Box 2723, San Anselmo, CA 94979

phone: (415) 459-1943 (San Anselmo) or (713) 723-3171 (Houston)

A few months ago Terra Linda Group Inc. started the T-Vector software development project. Although we believed that true vector processing would prove to be very powerful, it has exceeded our wildest dreams. As you can see from the enclosed tests, the FDD transform is extremely powerful.

If your business needs better seismic data processing, then this software is for you. For more information please contact your local Terra Linda Group representative or call me at (415) 459-1943.

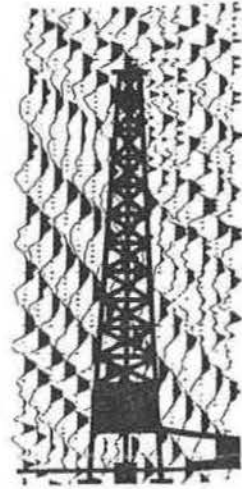
Sincerely,



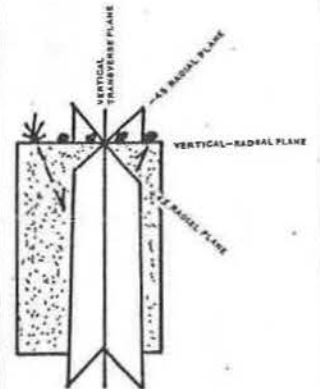
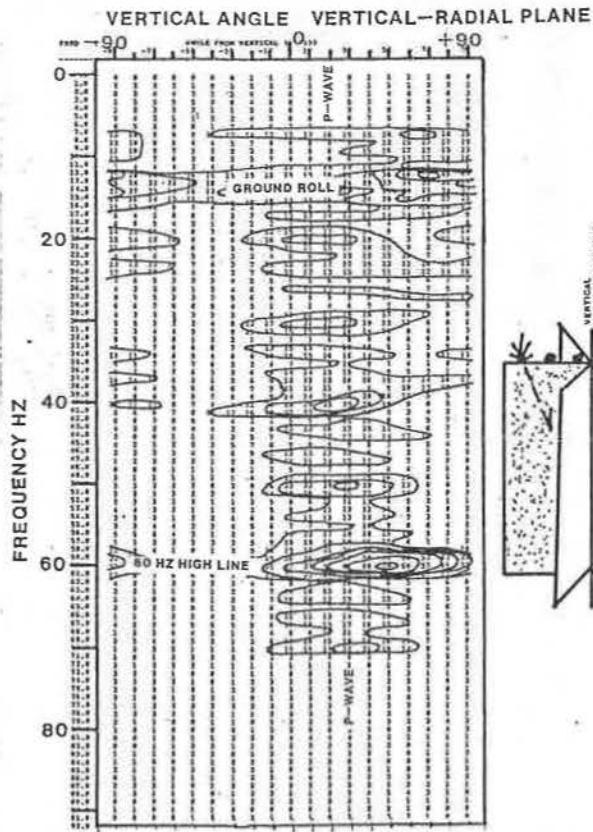
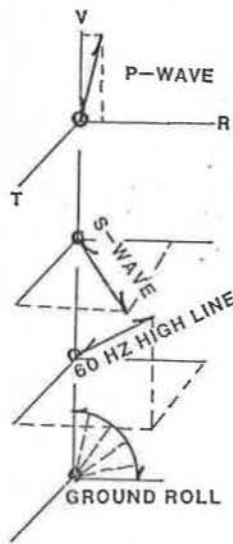
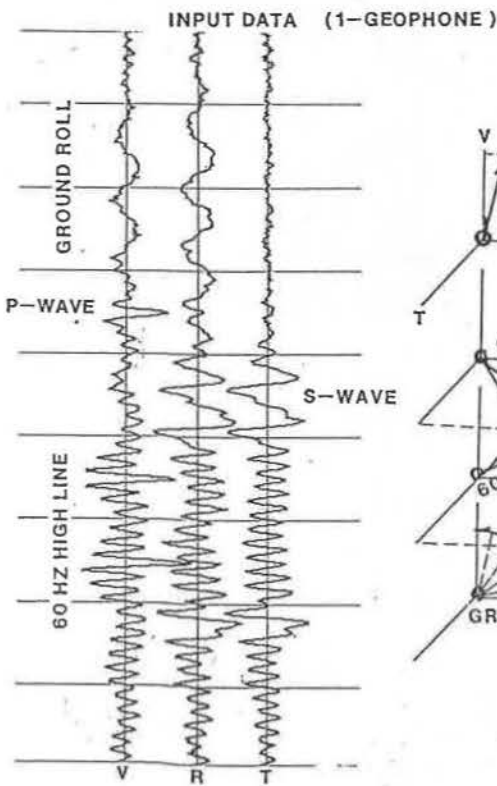
Gary S. Gassaway  
President, Terra Linda Group Inc.

GSG:jg

## FDD TRANSFORM SPECTRUM FILTERS



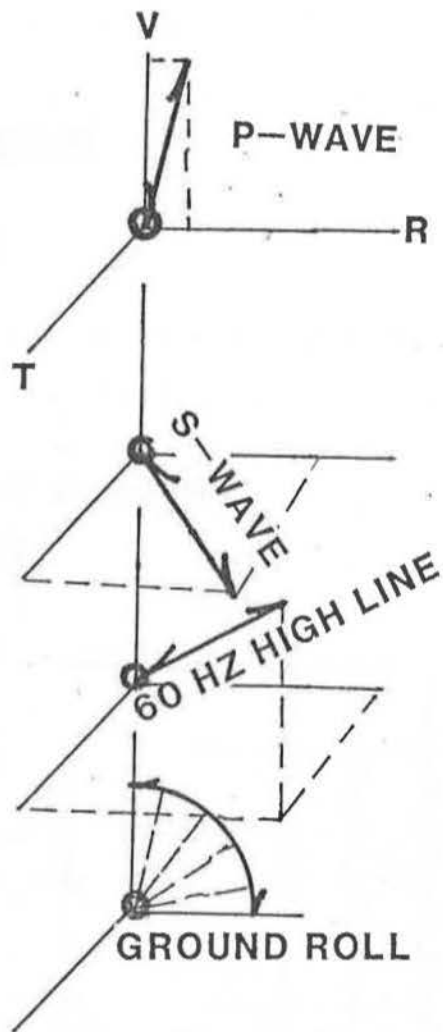
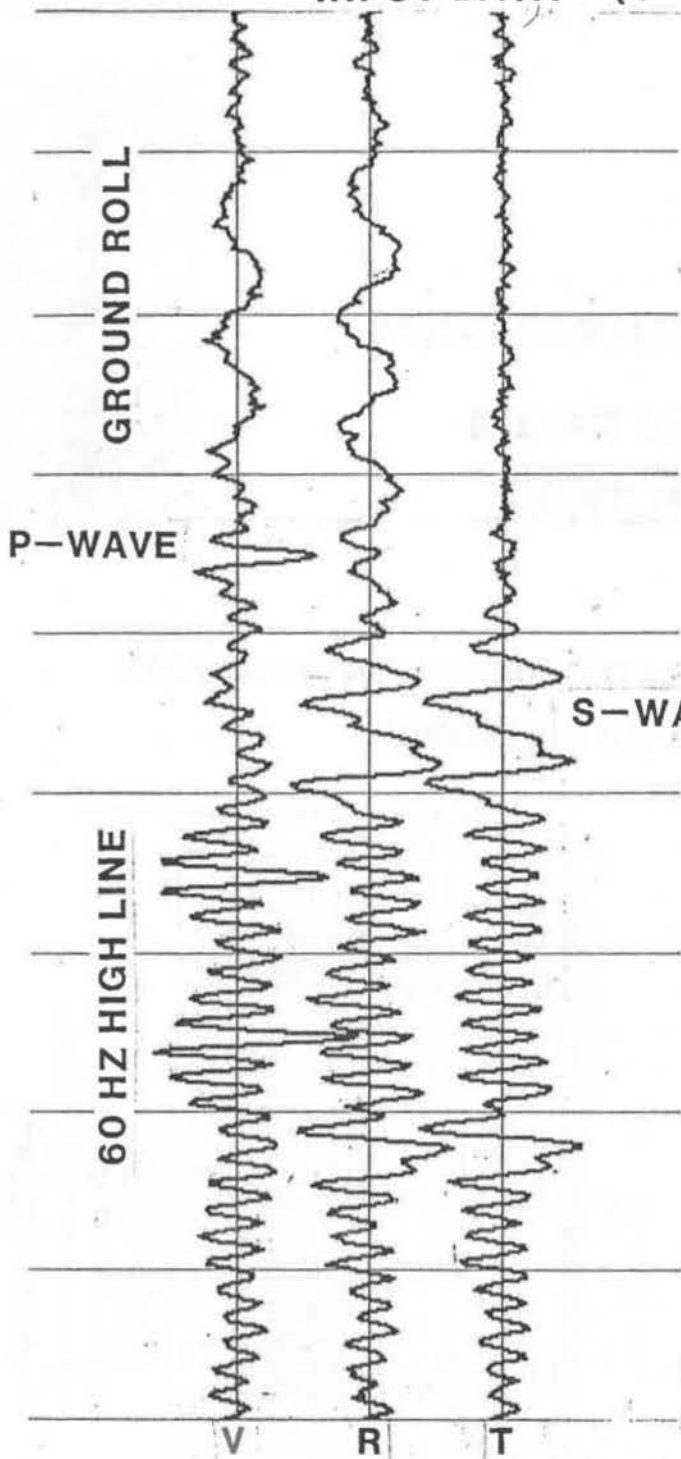
### FREQUENCY-VIBRATION DIRECTION TRANSFORM (SPECTRUM FILTERING)



T-VECTOR  
 FREQUENCY-AMPLITUDE-DIRECTION SPECTRUM

**3-COMPONENT EQUIVALENT OF FKK TRANSFORM  
 AT A SINGLE GEOPHONE**

INPUT DATA (1-GEOPHONE)

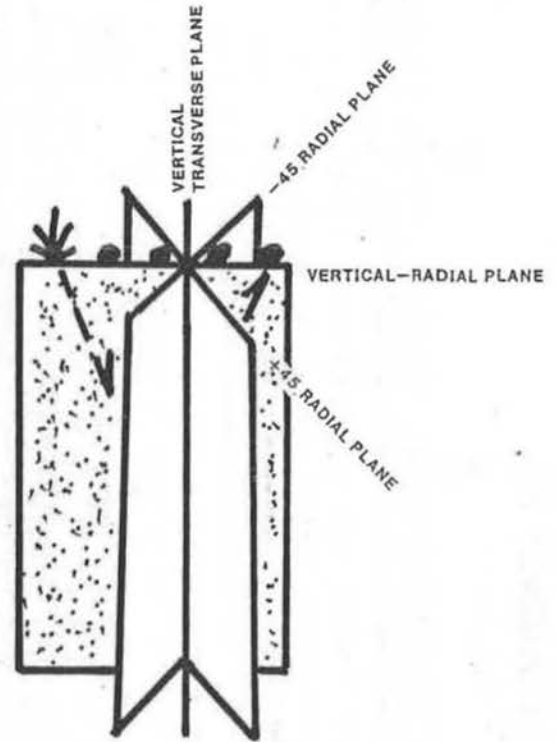
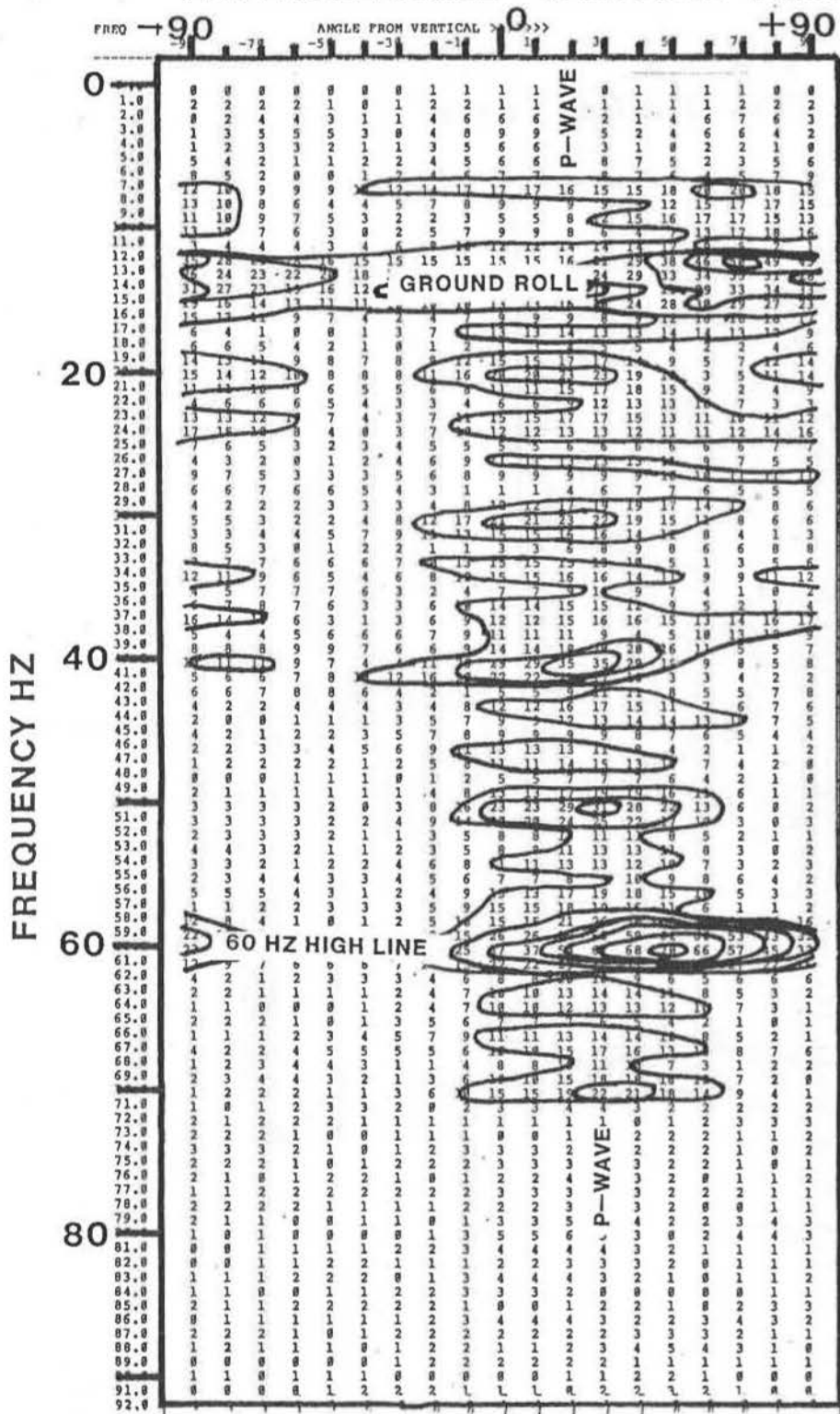


T-VECTOR

FREQUENCY-AMPLITUDE-DIRECTION SPECTRUM  
3-COMPONENT EQUIVALENT OF FKK SPECTRUM

TERRA LINDA GROUP INC

# VERTICAL ANGLE VERTICAL-RADIAL PLANE



**T-VECTOR**

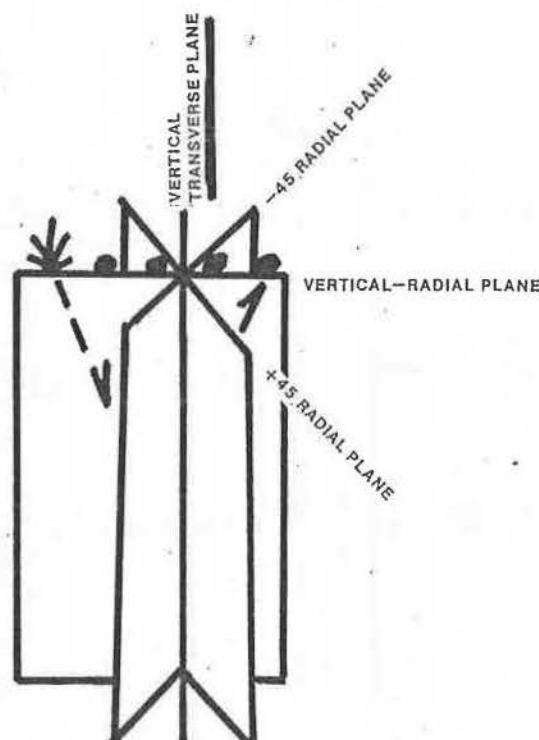
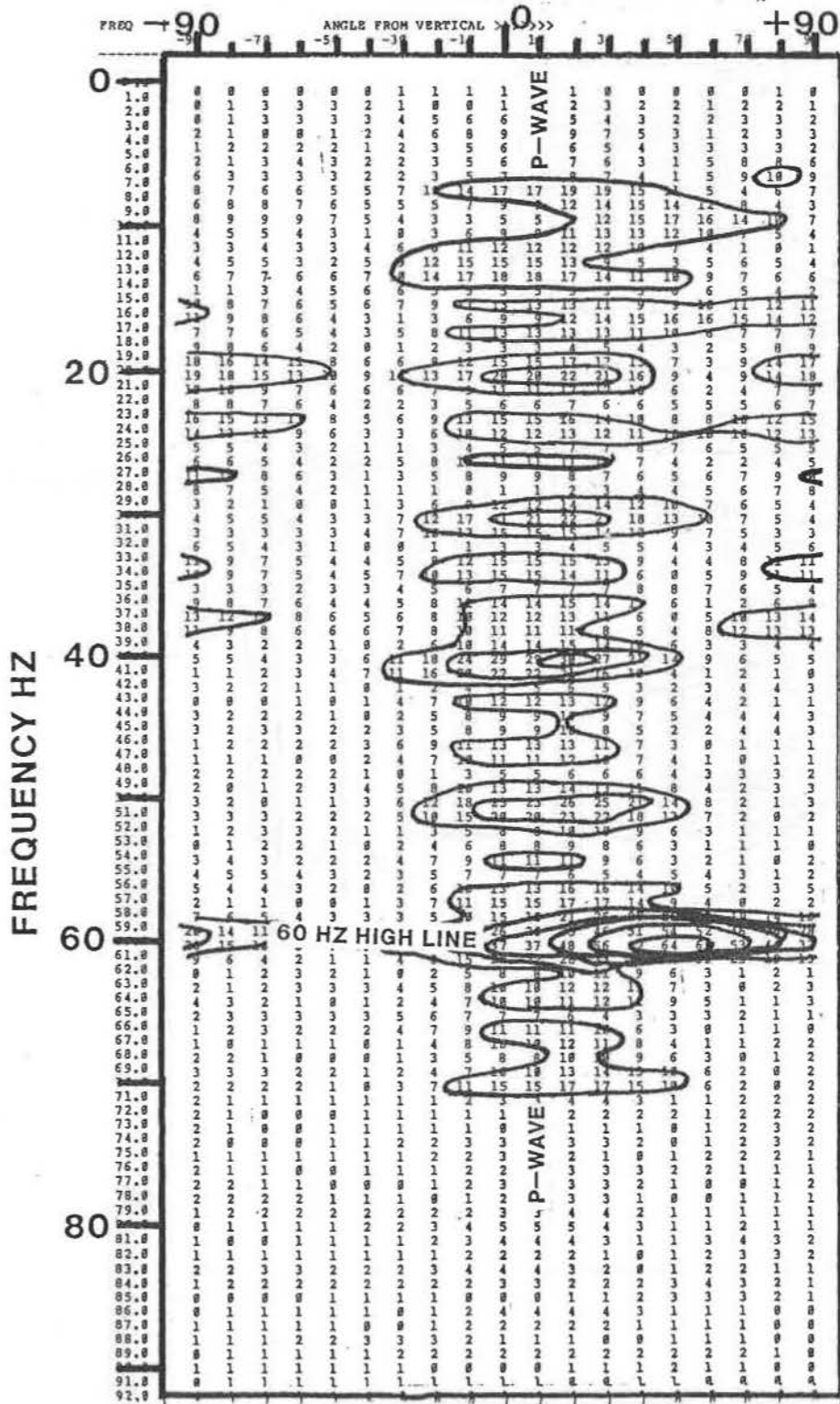
**FREQUENCY-AMPLITUDE-DIRECTION SPECTRUM  
3-COMPONENT EQUIVALENT OF FKK SPECTRUM**

TERRA LINDA GROUP INC

VERTICAL

VERTICAL ANGLE

TRANSVERSE PLANE

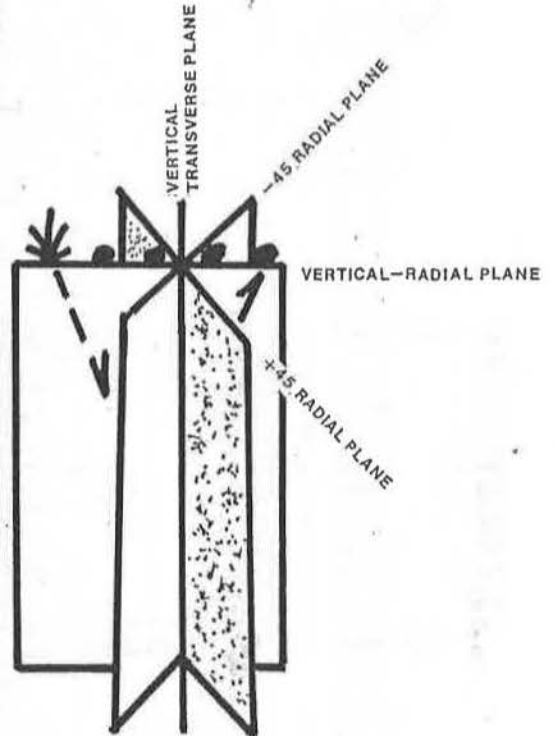
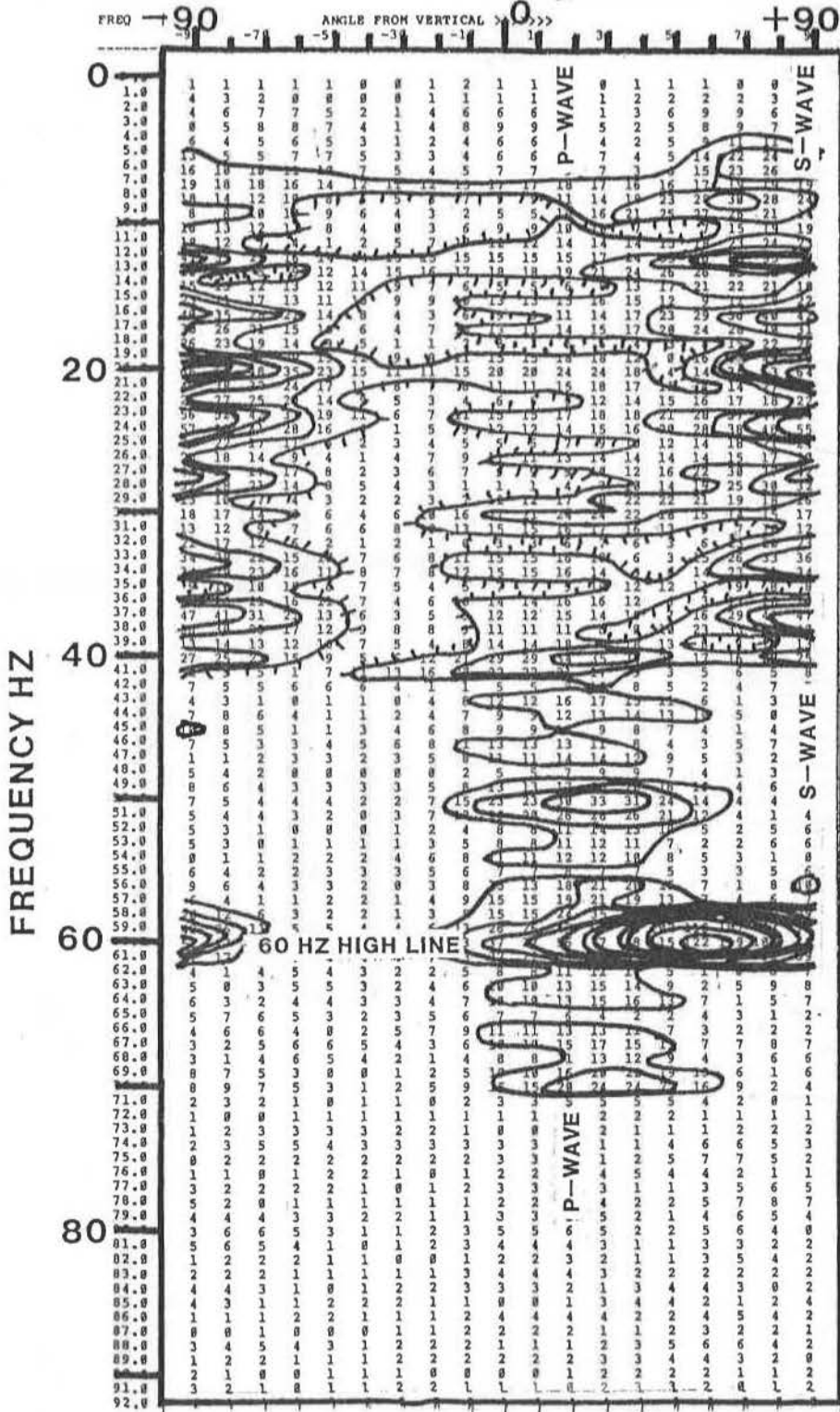


T-VECTOR

FREQUENCY-AMPLITUDE-DIRECTION SPECTRUM 3-COMPONENT EQUIVALENT OF FKK SPECTRUM

FREQUENCY-AMPLITUDE-DIRECTION SPECTRUM

# VERTICAL ANGLE +45 RADIAL PLANE

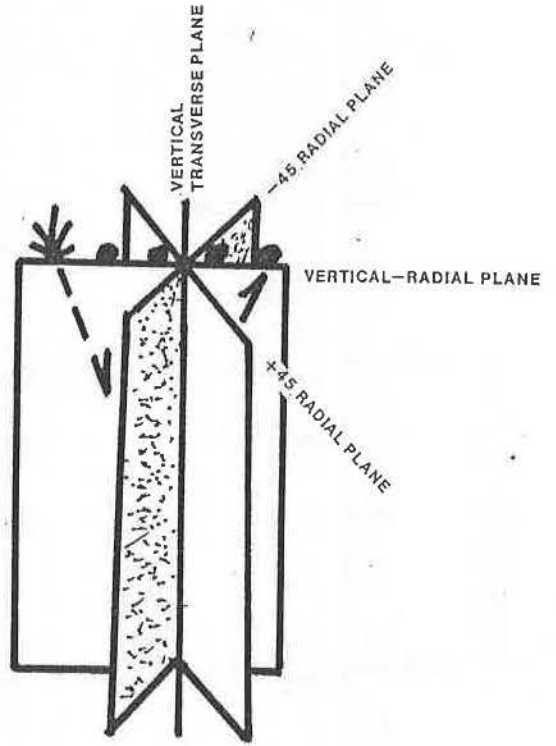
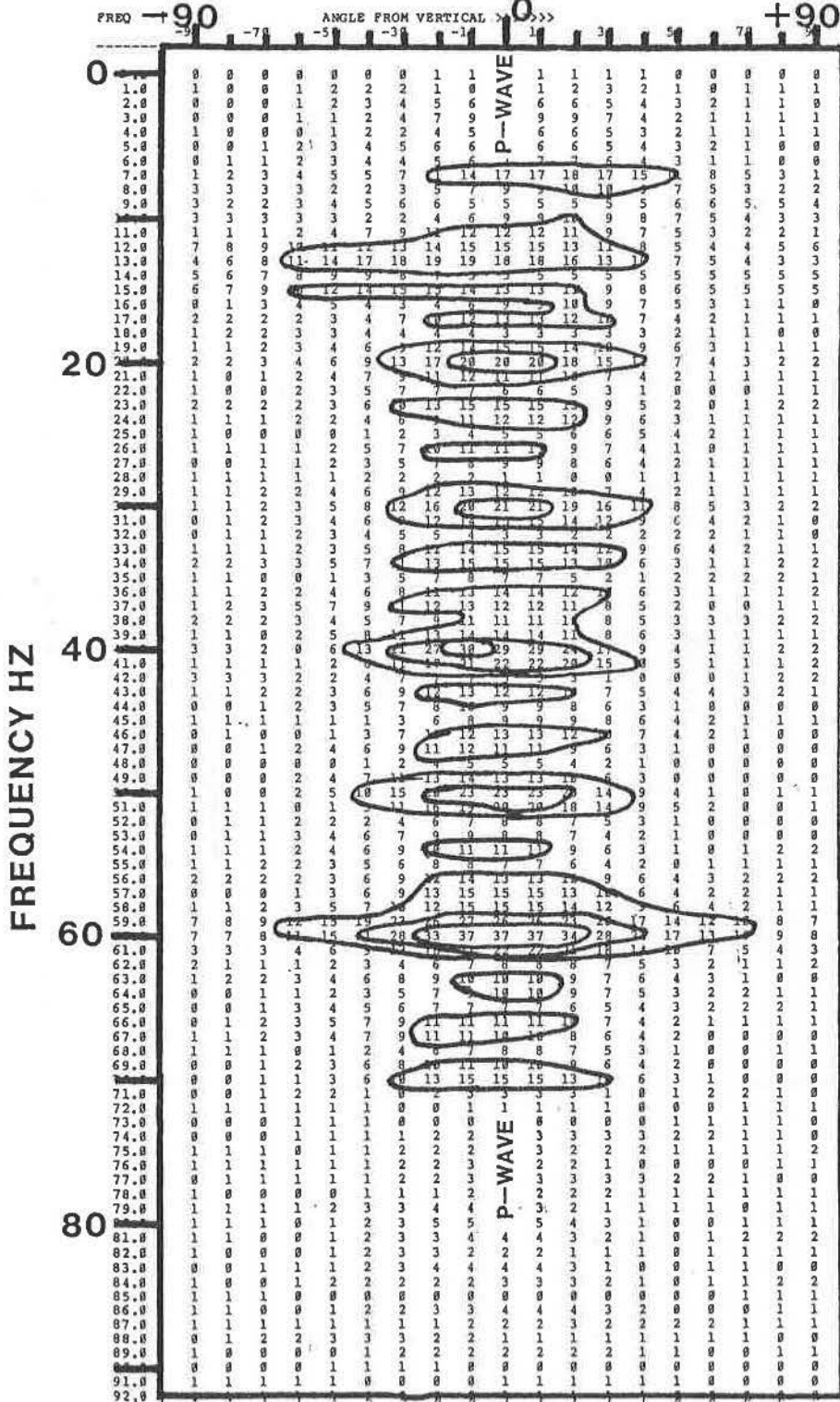


T-VECTOR

FREQUENCY-AMPLITUDE-DIRECTION SPECTRUM  
3-COMPONENT EQUIVALENT OF FKK SPECTRUM

TERRA LINDA GROUP INC

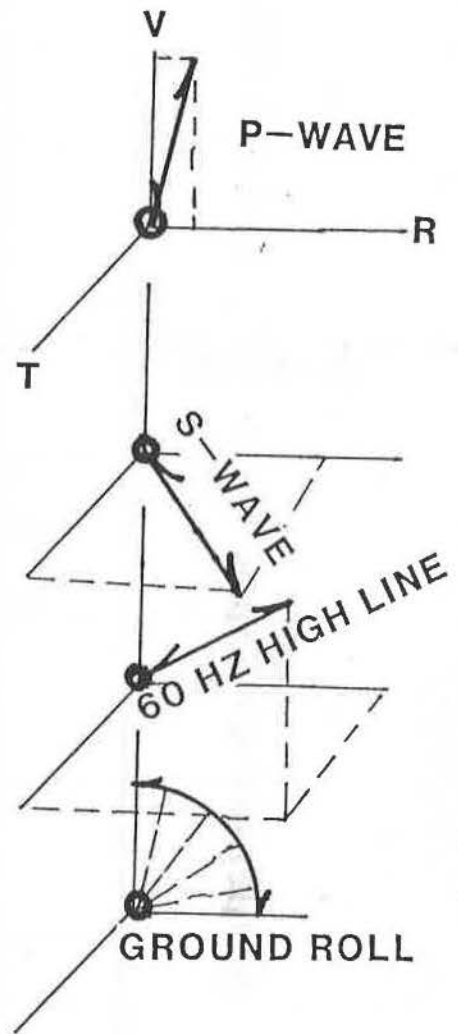
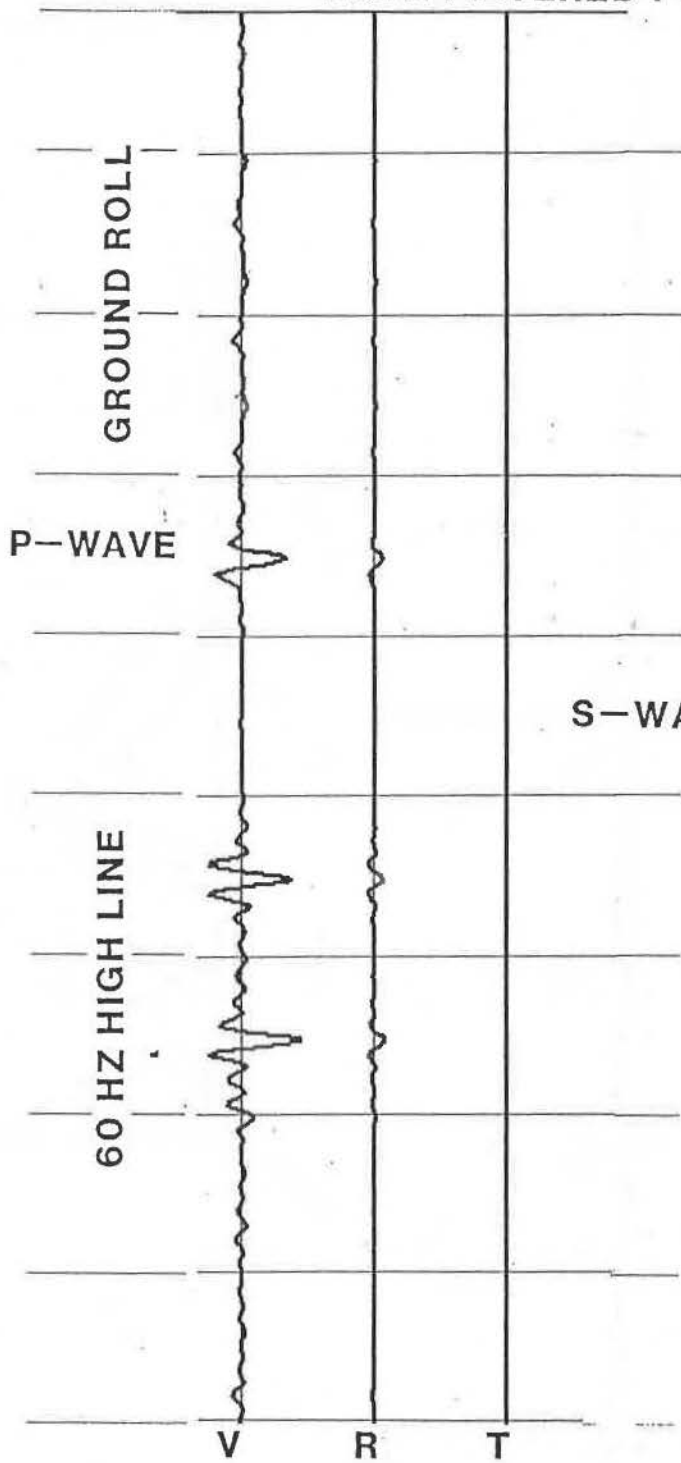
( T ) VERTICAL ANGLE -45 RADIAL PLANE



T-VECTOR

FREQUENCY-AMPLITUDE-DIRECTION SPECTRUM  
3-COMPONENT EQUIVALENT OF FKK SPECTRUM

DATA FILTERED FOR P-WAVE

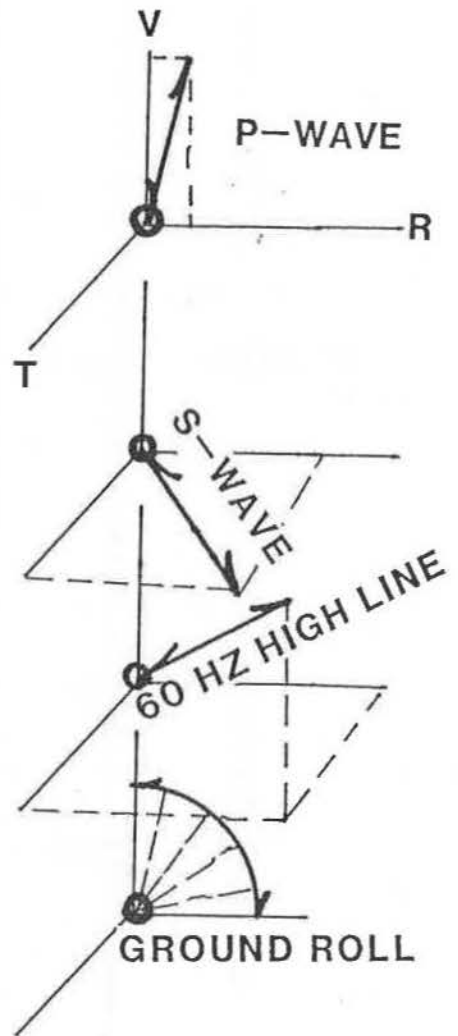
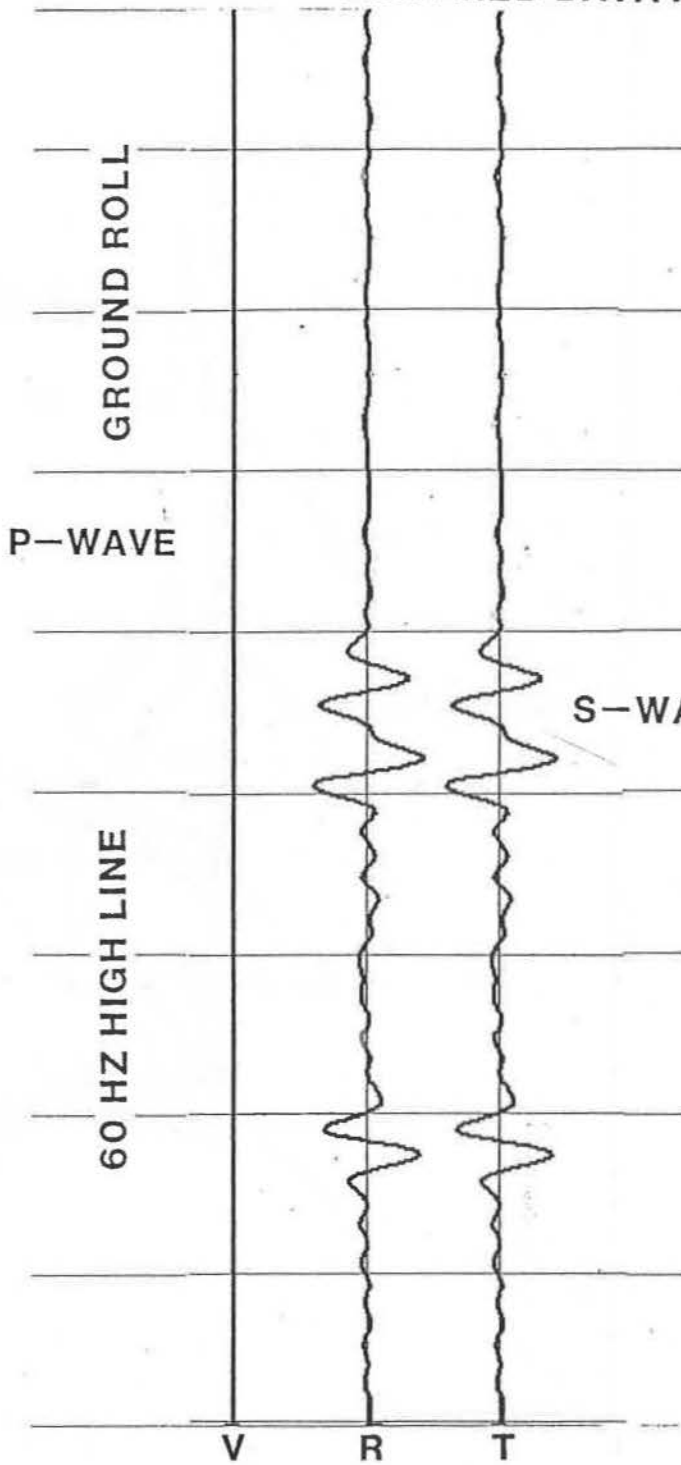


T-VECTOR

FREQUENCY-AMPLITUDE-DIRECTION SPECTRUM  
3-COMPONENT EQUIVALENT OF FKK SPECTRUM

TERRA LINDA GROUP INC

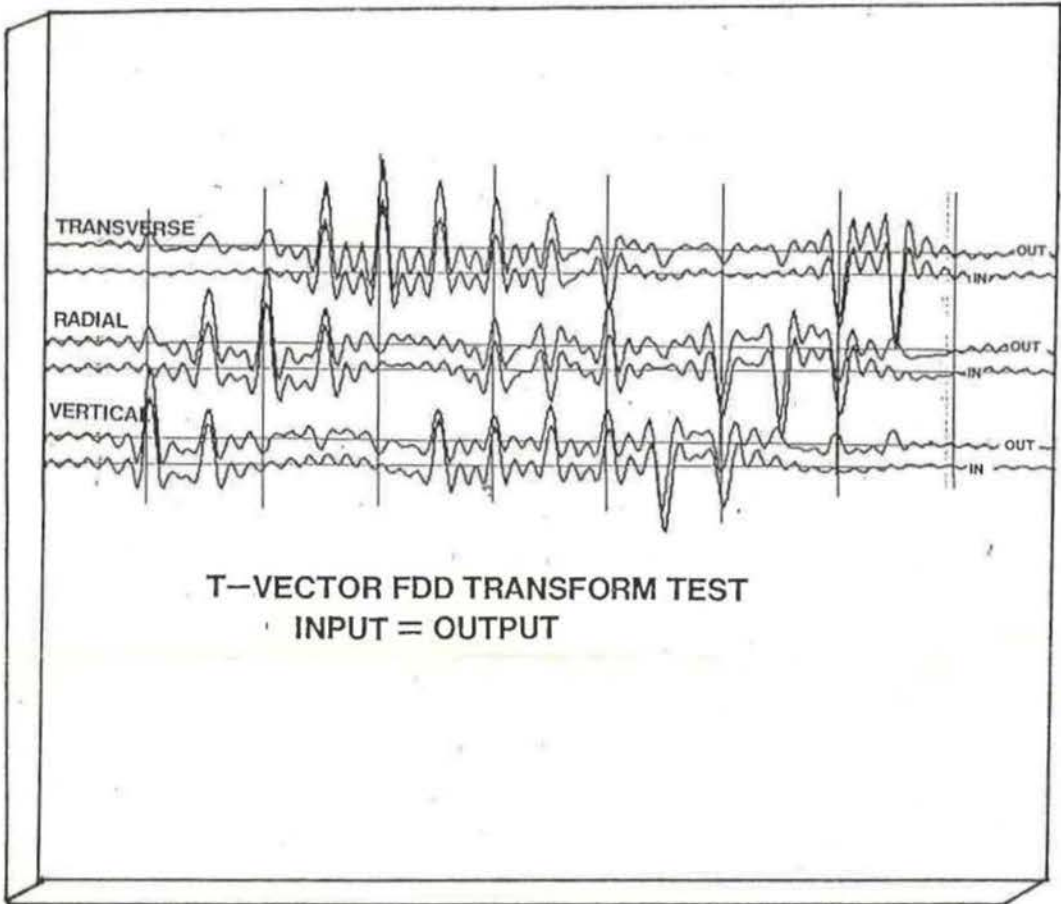
**FILTERED DATA FOR S-WAVE**



**T-VECTOR**

**FREQUENCY-AMPLITUDE-DIRECTION SPECTRUM  
3-COMPONENT EQUIVALENT OF FKK SPECTRUM**

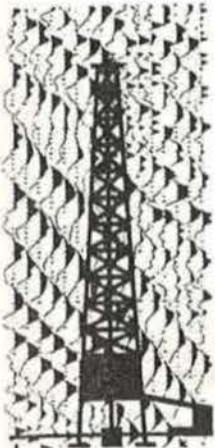
**TERRA LINDA GROUP INC**



**SINGLE SITE LICENSE: \$30,000**

**MULTI-SITE AND CORPORATE LICENSES AVAILABLE**

**Terra Linda Group**  
Interpreting the  
Total Wave Field  
237 Crescent Road  
San Anselmo, CA 94960  
Telephone 415 459-1943



Mr. Roise Nelson  
Landmark Graphics  
333 Cypress Run, Ste. 100  
Houston, TX, 77094

**SESSION 1**

**LABORATORY/THEORETICAL**

Monday Morning  
Session Chairman: L. Thomsen

# ADVANCES IN RELATION BETWEEN SEISMIC AND RESERVOIR ROCK PROPERTIES

by

Amos Nur and Gary Mavko  
Rockphysics Laboratory  
Department of Geophysics  
Stanford University

## *Abstract*

The purpose of seismic imaging of reservoirs is to infer the spatial distribution of rockmass properties, especially fluid flow related properties in heterogeneous rock systems. Of interest are also the time change of these properties i.e., during steam and water flooding, or gas injection. To use seismically imaged data, it is necessary to transform seismic characteristics (velocities and attenuation) into rock properties of interest:

- |                |                    |                   |
|----------------|--------------------|-------------------|
| ■ Porosity     | ■ Hydrocarbon type | ■ Strength        |
| ■ Permeability | ■ Pore pressure    | ■ Compressibility |
| ■ Saturation   | ■ Insitu stress    | ■ Clay content    |

Experimental and theoretical results, obtained by us over the past decade, have revealed several new relations between these properties and seismic properties. Specifically, we have uncovered (1) the precise relation between velocity and porosity in sandstones and sand, as a function of overburden pressure; (2) a relation between permeability and velocity in clay bearing sandstone; (3) relation between velocities, attenuation, and partial saturation (i.e., gas content); (4) the effects of hydrocarbons in porous rocks, and the effects of temperature; (5) the relations between rock strength and velocities; and (6) the seismic effects, especially anisotropy, of kerogene in petroleum source rock.

These results together provide a major advance in our ability to transform seismic images, such as 3-D seismic data cubes, or crosswell seismic data sets, into reservoir property cubes or maps. Future planned work includes, besides further study of the effects listed above, modeling and integration of wave propagation, reservoir description and core and log data bases. Much of this will involve the development of a fundamental model for porous rock with fluids, based on the extensive data we now have on the one hand, and theoretical mechanics on the other.

# P- AND S-WAVE VELOCITY RELATION IN SEDIMENTARY ROCKS

De-Hua Han  
Unocal

## SUMMARY

Measured velocity data suggest that shear velocity correlates with compressional velocity linearly for consolidated sandstones. This study revealed that the  $V_s$ - $V_p$  relation of dry sandstones is controlled mainly by mineral composition, and by porosity, and slightly by clay content, pore structure, cementation and effective pressure. Water saturation can significantly increase the slope of the  $V_s$ - $V_p$  relation of shaly sandstones. The  $V_s$ - $V_p$  relationship of carbonate rocks is also discussed. These results provide a guide to estimate lithology using  $V_s$ - $V_p$  relation, or shear velocity from measured compressional velocity for sedimentary rocks.

## INTRODUCTION

In addition to P-wave surveys, S-wave data from wireline logs and the surface seismic acquisition are often necessary for today's hydrocarbon exploration. The  $V_p/V_s$  ratio has been used as a lithology and fluid saturation indicator for many years (Pickett, 1963; Gregory, 1977; Castagna et al., 1985 and elsewhere). In the AVO technique, both  $V_p$  and  $V_s$  are major inputs for evaluating fluid saturation of a target reservoir. In many cases, however, there is no S-wave data available. Seismologists have to make rough estimate of  $V_s$  and Poisson's ratio for rock formations based on measured compressional velocity and field conditions. Unfortunately, no correlations among  $V_p$ ,  $V_s$ , lithology, and other rock parameter have yet been carefully established. Variation of  $V_p/V_s$  ratio with rock parameters and physical conditions has not been fully investigated under controlled laboratory conditions. Therefore, estimating  $V_s$  based on measured P-wave velocity, or using the  $V_p/V_s$  ratio as a lithology and fluid saturation indicators are still questionable. In this study, I investigate how the  $V_s$ - $V_p$  relations (not  $V_p/V_s$  ratio) of sandstones are affected by mineral compositions, porosity, pore structure, clay content, cementation and other rock parameters, and by fluid saturation and pressure conditions.

## $V_s$ - $V_p$ RELATION FOR CLEAN SANDSTONES

Ten clean sandstone samples with porosities ranging from 5 to 20 percent were measured under different pressure and fluid saturation conditions (Han, 1987). These rocks are pure quartz aggregates. The quartz grains with spherical shapes form a simple pore structure.

From the measured  $V_s$  and  $V_p$  at a differential pressure of 40 MPa, we found that for dry clean sandstones, the  $V_s$  is linearly correlated to the  $V_p$  as

$$V_s = 0.736 * V_p - 0.368 \quad (1)$$

with a correlation coefficient 0.99 as shown in Figure 1. Equation (1) tells us that the  $V_p/V_s$  ratio is not a constant, which increases with a decrease of  $V_p$ . Better correlation between  $V_s$  and  $V_p$  than that between velocity and porosity (Han, 1987) is not surprising because we are not only take porosity into account, we also take pore structure and cementation effects on velocities into account.

Our measured data suggest that the  $V_p/V_s$  ratio decreases with decreasing differential pressure. For dry clean sandstones at a differential pressure of 10 MPa,  $V_s$  can linearly correlated with  $V_p$  as

$$V_s = 0.703 * V_p - 0.190 \quad (2)$$

with correlation coefficient 0.98. We can see (Figure 1) that the differential pressure has a minor effects on the  $V_s$ - $V_p$  relation. The slope of the  $V_s$ - $V_p$  relation decreases with decreasing the differential pressure.

We found fluid saturation can change  $V_s$ - $V_p$  relation significantly. In contrast to the dry case,  $V_p$  for water saturated clean sandstones increases while  $V_s$  decreases. Thus, the  $V_p/V_s$  ratio increases. For water saturated clean sandstones at a different pressure of 40 MPa, the  $V_s$  can correlate with the  $V_p$  linearly as

$$V_s = 0.776 * V_p - 0.663. \quad (3)$$

When the differential pressure decreases, in contrast to the dry case, the slope of the  $V_s$ - $V_p$  relation for water saturated clean sandstones increases slightly.

#### $V_s$ - $V_p$ RELATION FOR SHALY SANDSTONES

As is the case for clean sandstones,  $V_s$  for shaly sandstones also linearly correlates with  $V_p$ . Velocity measurements were made on 59 shaly sandstones by Han (1987). Porosity of the samples ranges from 5 to 30 percent and clay content (volume fraction) ranges from 1 to 50 percent. The dry  $V_p$  and  $V_s$  measured on these samples at a confining pressure of 40 MPa are shown in Figures 2a and 2b. Notice that for clean sandstones, the  $V_p$  and the  $V_s$  show nice correlations with porosity while for shaly sandstones, the data have considerable scatter. This scatter is mainly caused by different clay contents, and is slightly affected by differences in pore structure, cementation and mineral composition (Han et al., 1986). However, the least-squares regression of the  $V_s$ - $V_p$  relation for dry shaly (59) and clean (10) sandstones at a differential pressure of 40 MPa is extremely well defined as

$$V_s = 0.703 * V_p - 0.219 \quad (4)$$

with a correlation coefficient of 0.99 as shown in Figure 3. The data suggest that although the samples contain clay from 0 (for clean sandstones) to 50 percent (very shaly sandstones), and although the effects of the clay fraction on the  $V_p$  and  $V_s$  are significant, no clay effects on  $V_s$ - $V_p$  relation were shown in Figure 3. The  $V_s$ - $V_p$  relation is similar to that for dry clean sandstones. Therefore, for dry shaly

sandstones, the effects of clay fraction on the Vs-Vp relation is small and can be neglected.

For the dry shaly sandstones, Vp and Vs are linearly correlated with porosity and clay content as follows (Han, 1987)

$$V_p = 5.41 - 6.35 * \phi - 2.87 * C \quad (5)$$

and

$$V_s = 3.57 - 4.57 * \phi - 1.83 * C$$

Setting porosity equal to zero, and the clay content equal to 100 percent the 'dry clay point' velocities can be calculated.

$$V_{pc} = 2.54 \text{ km/s}; V_{sc} = 1.74 \text{ km/s} \quad (6)$$

The 'dry clay point' velocity ratio,  $V_{pc}/V_{sc}$ , is equal to 1.46. This value is slightly lower than the velocity ratio of 1.5 for quartz aggregates. A dry sandstone with a high clay content may have a lower  $V_p/V_s$  ratio than the predicted by equation (4). We also found that other mineral fraction than quartz and clays will cause a high  $V_p/V_s$  ratio than the predicted.

We found that pressure effect on the Vs-Vp relation is very small. The least squares regression of the Vs-Vp relation for 69 sandstones at a differential pressure of 10 MPa is

$$V_s = 0.683 * V_p - 0.090. \quad (7)$$

For dry sandstones, the  $V_p/V_s$  ratio increases with increasing the pressure. The slope of the Vs-Vp relation at 10 MPa is slightly less than that at 40 MPa. Therefore, the pressure effects on the dry Vs-Vp relation can be predicted or even be ignored.

For water saturated sandstones, the measured data (Han, 1987) suggest that Vs correlates with Vp linearly as

$$V_s = 0.795 * V_p - 0.834 \quad (8)$$

as shown in Figure 4. The correlation coefficient is 0.97. We found that the increase of Vp and decrease of Vs of water saturated shaly sandstones are enhanced by an interaction between water and clay fraction. Thus, the slope of the Vs-Vp relation for shaly sandstones is significantly higher than that for clean sandstones.

From velocities measured on water saturated shaly sandstones, the 'wet clay point' were found by Castagna et al. (1985) and Han (1987)

$$V_{pcw} = 3.40 \text{ km/s}; V_{scw} = 1.63 \text{ km/s} \quad (9)$$

The 'wet clay point', as shown in Figure 4, is consistent with the clay effects on water saturated shaly sandstones. The mudstone line presented by Castagna et al. (1985) is also shown in Figure 4.

#### Vs-Vp RELATION FOR CARBONATE ROCKS

We have velocity data collected from a group limestone samples. with intergranular porosities. The data were measured on dry samples at a confining pressure of 40 MPa. Although the data show more scattering than those for sandstones, the  $V_s$  correlates with the  $V_p$  linearly as

$$V_s = 0.50 * V_p + 0.255 \quad (10)$$

shown in Figure 5. The correlation coefficient is 0.97. The  $V_p/V_s$  ratio for limestone is not a constant. In contrast to sandstones, the  $V_p/V_s$  ratio for limestones decreases with decreasing  $V_p$ .

For limestone samples with a significant amount of clays, the  $V_p/V_s$  ratio is lower than the value predicted using the regression line. This may be a result from the low  $V_p/V_s$  ratio of dry clays (the dry clay point,  $V_p/V_s = 1.46$ ).

We measured velocity on vuggy limestone samples. Their velocities decrease slightly with increasing porosities. However, the  $V_s$ - $V_p$  relation of vuggy limestones is similar to the limestone line

$$V_s = 0.515 * V_p + 0.06 \quad (11)$$

as shown in Figure 5. This result suggest again that pore geometry has a minor effect on the  $V_s$ - $V_p$  relation. Mineral composition is the most important factor to determine the  $V_s$ - $V_p$  relation.

For dolomite, the data from 8 samples were measured by pickett (1963). The  $V_s$  correlate linearly with the  $V_p$  as

$$V_s = 0.505 * V_p + 0.235. \quad (12)$$

Usually dolomite have complicated mineral compositions and structures. The data used here may not be typical. The data suggest that the  $V_s$ - $V_p$  relation for dolomite is similar to that for limestones.

### CONCLUSIONS

Although the above data were measured on typical rock samples, the results are generally significant. The empirical  $V_s$ - $V_p$  relations may not be quantitatively universal, especially for carbonate rocks, but they are still valuable references. More important is the physical relations among rock parameters and conditions found in this study.

for sandstones:

1.  $V_s$ - $V_p$  relation is mainly controlled by elastic properties of quartz grains and common pore structure of sandstones.
2. Pore geometer, cementation, clay content and other rock parameters have minor effects on the dry  $V_s$ - $V_p$  relationship.

3. Mineral fractions other than quartz and clays cause a high  $V_p/V_s$  ratio. Quartz and clays have exclusive low  $V_p/V_s$  ratio in comparison with other minerals.

4. Differential pressure has a minor effects on  $V_s-V_p$  relation. When the differential pressure decreases the slope of the  $V_s-V_p$  relation increases for saturated rocks while decreases for dry rocks.

5.  $V_p/V_s$  ratio is not a constant. When porosity increases, the  $V_p/V_s$  ratio for sandstones increases.

6. The slope of the  $V_s-V_p$  relation increases significantly with water saturation. This effect is enhanced by the interaction between water and clay fraction in sandstones.

For carbonates:

1. When  $V_p$  is higher than 3.5 km/s, the  $V_p/V_s$  ratio for carbonate rocks is higher than that for sandstones.

2. The velocity ratio for dry carbonate rocks decreases with increase rock porosities.

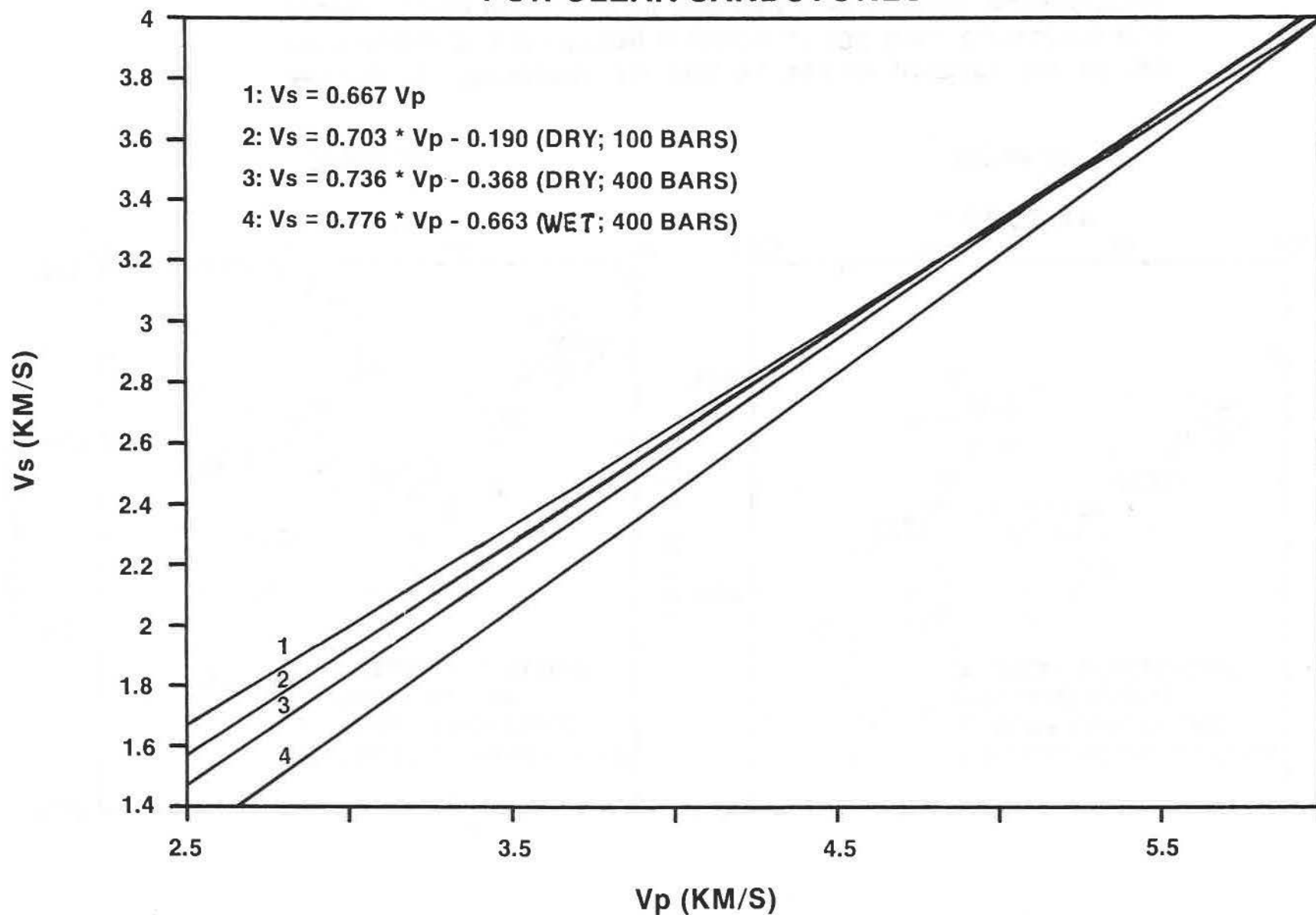
3. Fluid saturation effects on the  $V_s-V_p$  relation can be calculated using the Biot-Gassmann relation. The slope of the  $V_s-V_p$  line increases as shown in Figure 6.

Figure 6 summarized  $V_s-V_p$  relations for sandstones and carbonates. We can conclude that  $V_s-V_p$  relation can be used to distinguish sandstones from carbonates if  $V_p$  of rocks are greater than 3.5 km/s. The saturation state can also be estimated if  $V_p$  of rocks are low enough such as 4.5 km/s.

#### REFERENCES

- Castagna, J. P., Batzle, M. L., and Eastwood, R. L., 1985, Relationship Between compressional wave and shear wave velocities in clastic silicate rocks: *Geophysics*, 50, 551-570.
- Gregory, A. R., 1977, Aspects of rock physics from laboratory and log data that are important to seismic interpretation: *Am. Assoc. Pet. Geol. Memoir* 26, 15-46.
- Han, De-hua, 1987, Effects of porosity and clay content on acoustic properties of sandstones and unconsolidated sediments: Ph.D dissertation, Stanford University.
- Han, D., Nur. A and Morgan, F. D. 1986, Effect of porosity and clay content on wave velocities of sandstones: *Geophysics*, 51, 2093-2107.
- Pickett, G. R., 1963, Acoustic character logs and their application in formation evaluation: *J. Petr. Tech.*, 15, 659-667.

# Vs-Vp RELATION FOR CLEAN SANDSTONES



**FIGURE 1:** Vs-Vp relationships for clean sandstones with dry and water saturated states at effective pressures of 100 and 400 Bars.

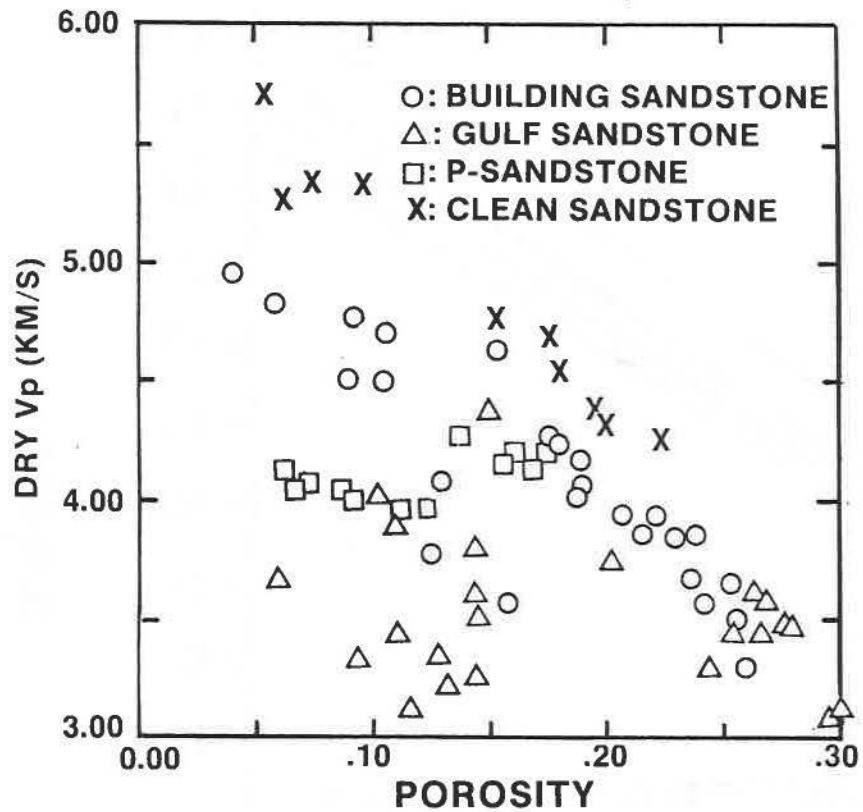


Figure 2a

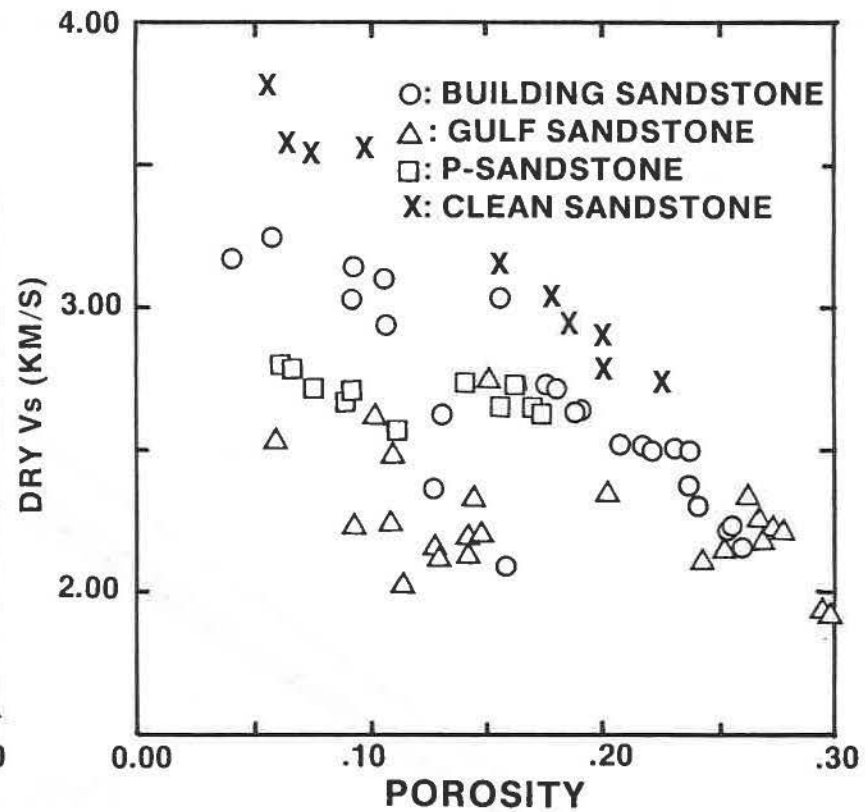
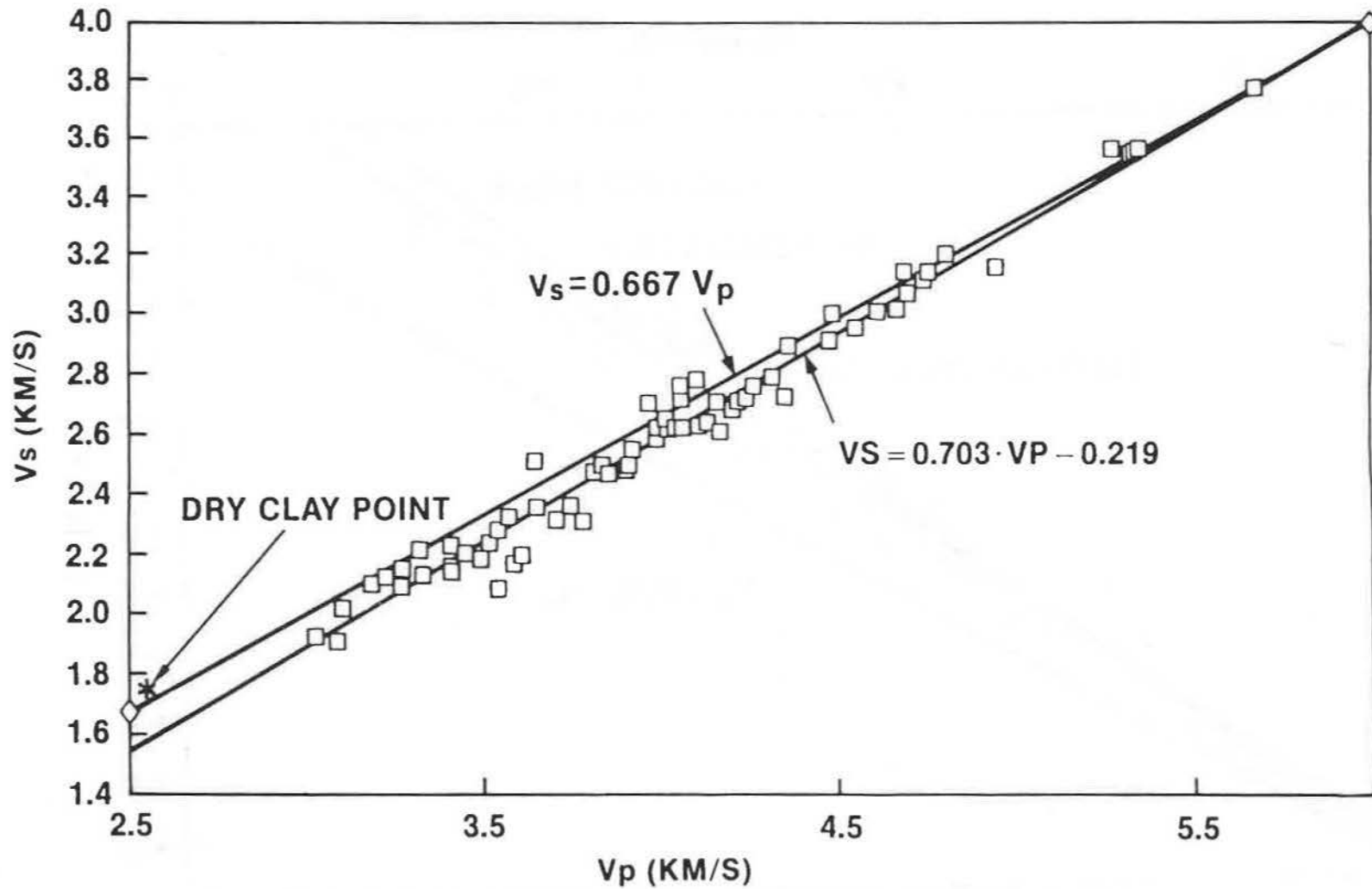


Figure 2b

**FIGURE 2:** Measured Vp and Vs versus porosity for 69 dry sandstones at a confining pressure of 400 Bars. Data show wild scatter which is caused by different clay content, consolidation and other rock parameters (reference to Han, 1987).

# Vs-Vp RELATION FOR 69 DRY SAMPLES (Pd=400 BARS)



**FIGURE 3:** Vs-Vp relation for 69 dry sandstones at a confining pressure of 400 Bars. Data suggest that Vs correlates with Vp. The 'dry clay point' is shown.

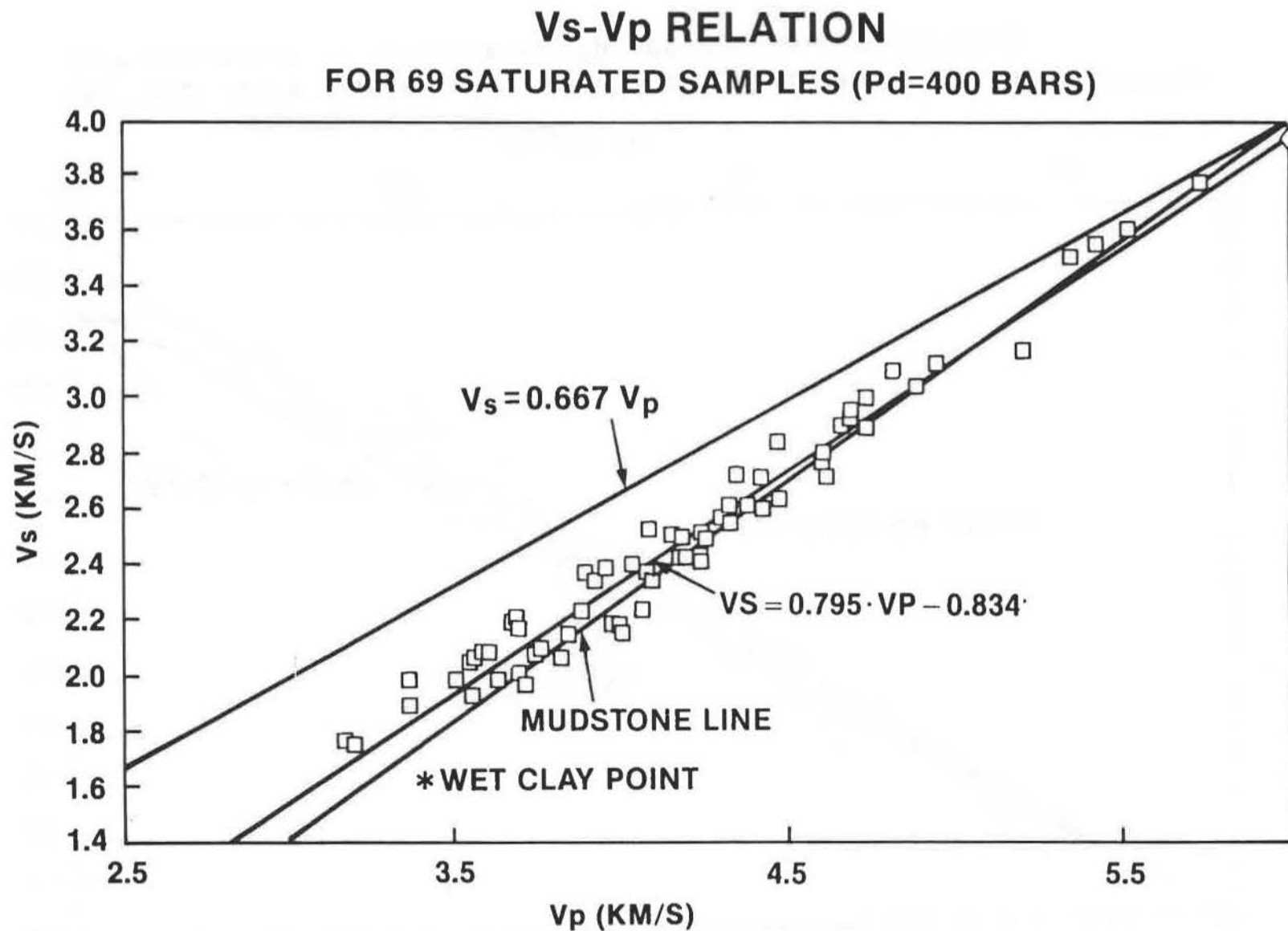


**FIGURE 4:** Vs-Vp relation for 69 sandstones with water saturation at an effective pressure of 400 Bars. The 'wet clay point' is shown.

# Vs-Vp RELATION FOR DRY LIMESTONES (P=400 BARS)

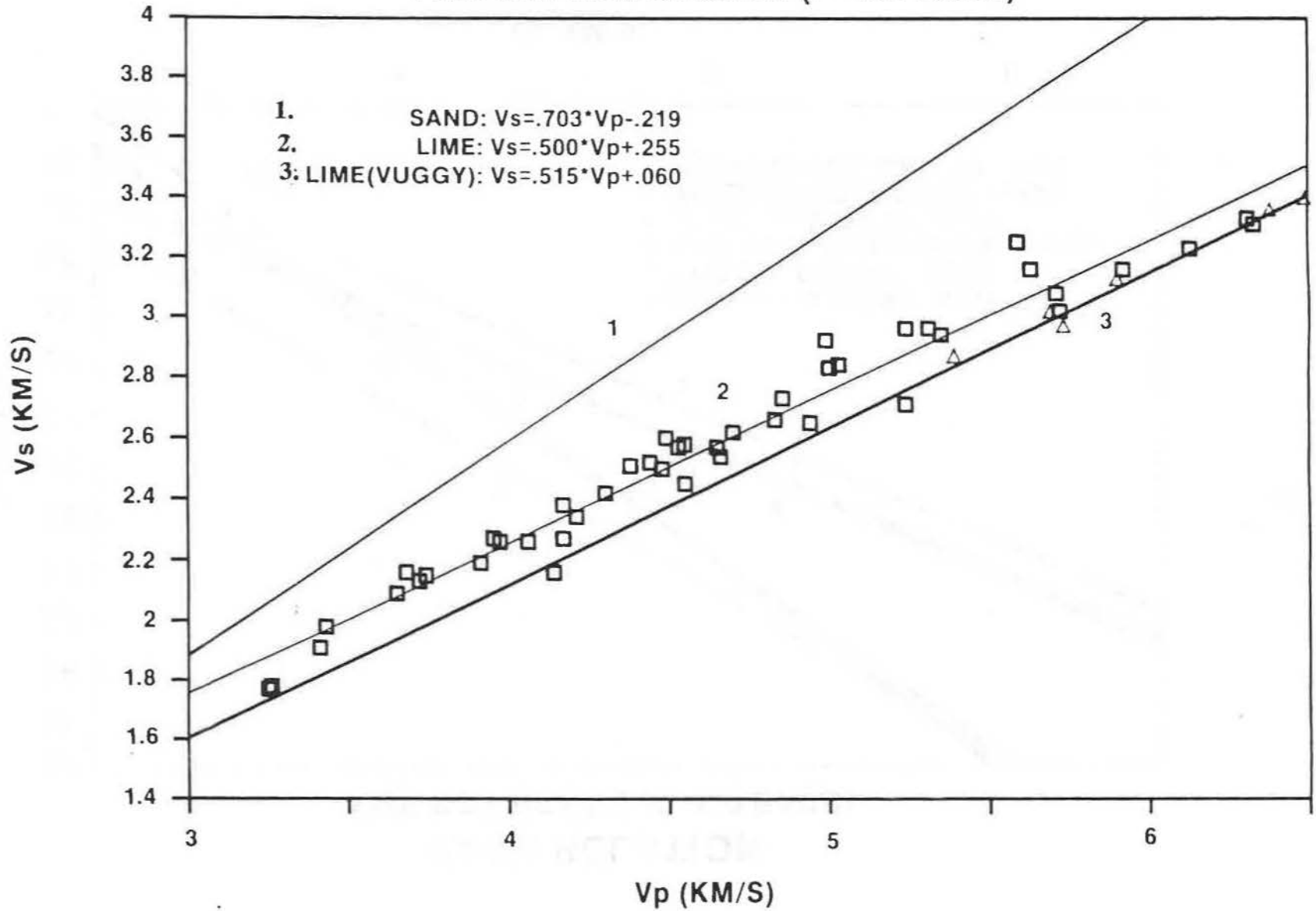


**FIGURE 5:** Vs-Vp relation for dry limestones and limestones with vuggy pores at a confining pressure of 400 Bars.

## Vs-Vp RELATION FOR DRY ROCKS (P=400 BARS)

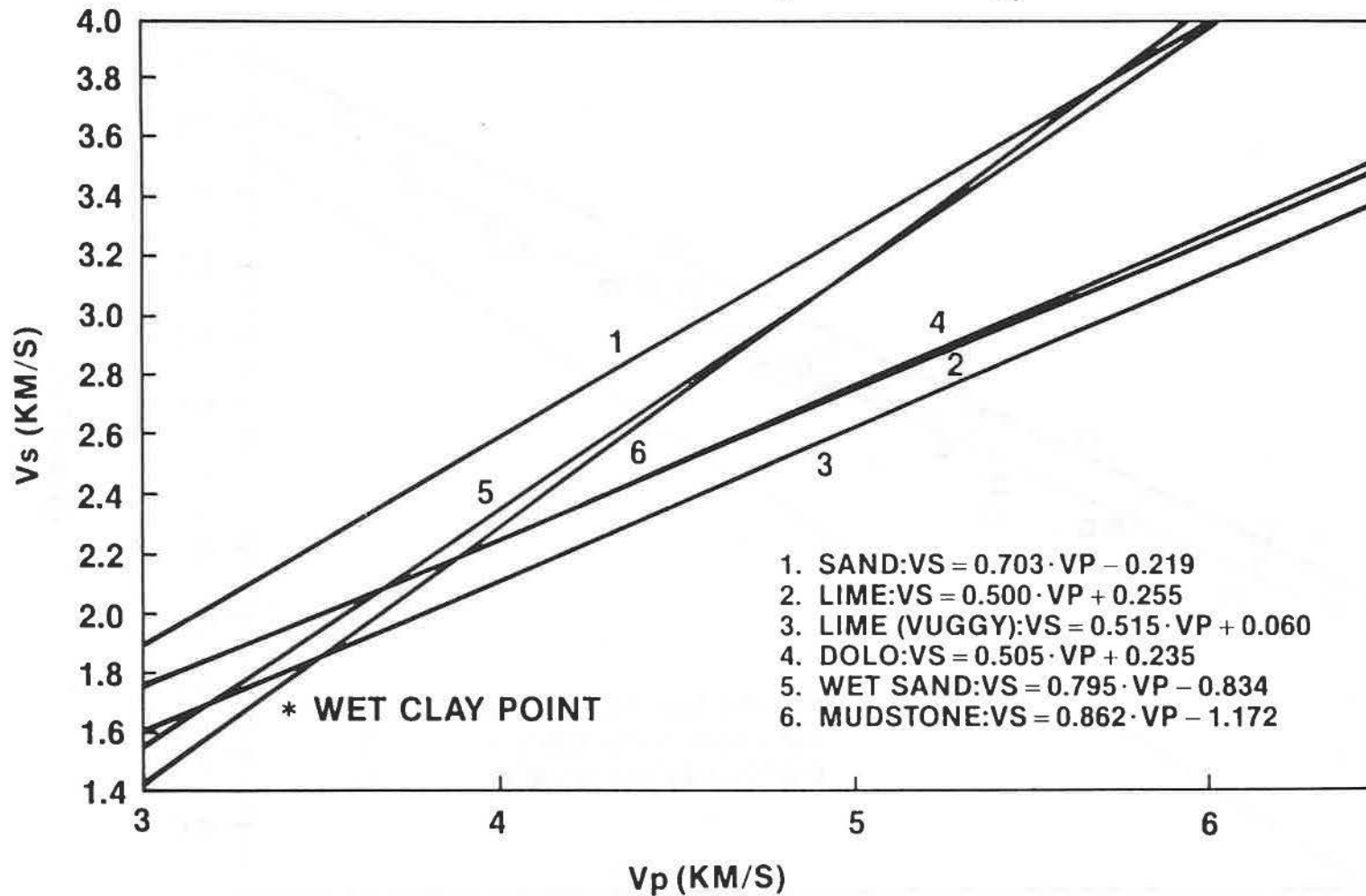


**FIGURE 6:** Vs-Vp relationships for sandstones, limestones and dolomites.

## EFFECT OF CEMENTATION ON THE ELASTIC PROPERTIES OF ROCK

(Expanded Abstract)

Jack Dvorkin, Gary Mavko and Amos Nur

*Stanford University*

The acoustic and mechanical characteristics of sedimentary rocks may be strongly affected by the properties and structure of intergranular bond material. The deformational pattern of cement material and its interaction with elastic grains is important for estimates of stress-strain behavior of granular material, as well as for its failure criteria. Sedimentary rocks of interest with intergranular cementation span a wide range from diagenetic sediments and sand-clay mixtures to tar sands.

Numerous publications on the mechanics of granular media were discussed by Stoll (1989). The theoretical description of granular material has been based on the classical solution for the problem of a normal compression of elastic spheres or disks by Hertz (Johnson, 1985) as well as on the results regarding the oblique compression of elastic spheres and disks (Mindlin, 1949; Walton, 1978). All these models consider the direct contact of elastic bodies. The dimension of a contact zone changes with varying external forces.

The situation is different for the contact of initially cemented grains. In this case the dimension of a contact zone between two bodies is predetermined and does not change in the process of interaction. Bruno and Nelson (1990) examined the inelastic mechanical behavior of cemented granular material using a two-dimensional discrete element procedure. Intergranular interaction through cementation was modeled using a linear spring scheme.

In this paper we concentrate on the description of cement layer deformation as well as on the interaction of elastic grains with an elastic cement layer. To investigate two-dimensional cement layer deformation when the layer is thin and grains are much stiffer than the cement we have derived a simple analytical model. The approach used is similar to those commonly employed in approximate theories of thin plates and shells. This approach was used by Matthewson (1981) to model an axisymmetric contact on thin compliant coatings. The problem of a two-dimensional arbitrarily-shaped cement layer deformation has been reduced to an ordinary differential equation of the second order.

We show that a cement layer under normal compression can be approximately treated as an "elastic foundation" between two grains. Using this result we reduce the two-dimensional problem of interaction between two elastic grains and an elastic cement layer to a linear integral equation. Solving this equation we are able to estimate the elastic modulus of cemented granular material. We also employ the "elastic foundation" approximation to solve the problem of the normal compression of two cemented spherical elastic grains.

The presence of a cement layer dramatically increases the elastic modulus compared to the case of an intergranular Hertzian contact.

The shape of stress distribution between cemented grains is completely different from the classical Hertzian case. This shape dramatically changes depending on the ratio of cement stiffness to grain stiffness.

The stiffness of the cemented system does not depend on the confining pressure.

The stiffness of the cemented system increases with the length of the cement layer and with the relative stiffness of the cement. It significantly exceeds the stiffness of the Hertzian system at low confining pressure.

The small increase of the cementation content results in significant growth of a contact

zone between two contacting grains and, thus, dramatically increases the stiffness of the system.

These theoretical models can be used to predict the influence of cement content and location on the properties of sediments.

#### REFERENCES

1. Bruno, M.S. and Nelson, R.B., "Microstructural Analysis of the Inelastic Behavior of Sedimentary Rock," Chevron Oil Field Research Company, 1990.
2. Johnson, K.L., "Contact Mechanics," Cambridge University Press, 1985.
3. Matthewson, M.J., "Axi-Symmetric Contact on Thin Compliant Coatings," *Journal Mech. Phys. Solids*, Vol. 29, 1981, 89-113.
4. Mindlin, R.D., "Compliance of Elastic Bodies in Contact," *Trans. ASME*, 71, A-259.
5. Stoll, R.D., "Sediment Acoustics," Springer-Verlag, 1989.
6. Walton, K., "The Oblique Compression of Two Elastic Spheres," *Journal Mech. Phys. Solids*, Vol. 26, 1978, 139-150.

# ESTIMATION OF LITHOLOGY FROM ELASTIC PROPERTIES?

Manika Prasad  
202 Oceanic

(This work was conducted at the Institute for Geophysics, Leibnitzstr. 15, 2300 Kiel, FRG)

Correlation between porosity, to some extent grain size, and seismic properties have been studied by various investigators on standard rock samples. Although these interactions are well documented, effects of a large range of lithologic properties on seismics are rare.

We have carried out laboratory experiments on sands of different grain sizes with an aim of correlating the porosity, permeability, static frame compressibility, shear modulus, grain size and shape with velocity and attenuation of P- and S-waves. The seismic experiments were conducted on a Pulse Transmissions Apparatus at 100 kHz. Attenuation values were evaluated using Aluminum as standard reference for the Rise Time and Spectrum Division methods. A comparison between seismic and geologic properties measured on the same sample has yielded interesting results.

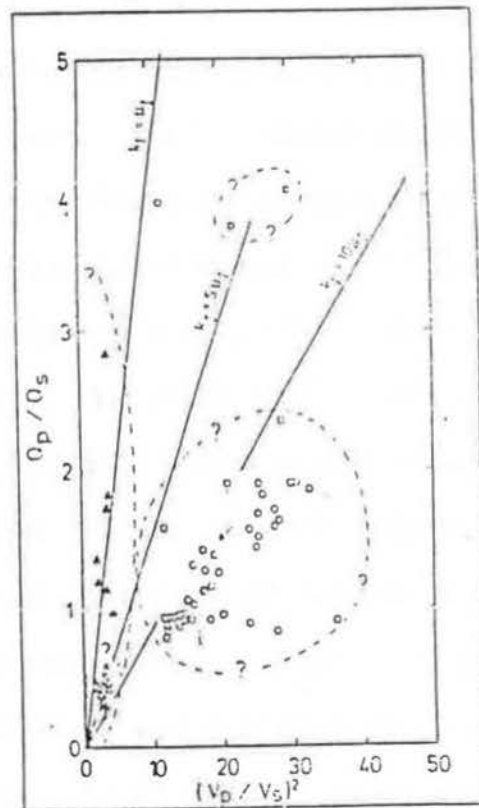
The samples covered a broad range of grain size, angular and round grain shape, and predetermined static frame compressibility and static shear modulus. Porosity, permeability and seismic properties of the dry, or fully water saturated samples were determined at each pressure step.

An interdependency is observed between grain size, shape, porosity, permeability and static frame compressibility. Comparing them with the seismic properties gives the basis for correlation criterion between seismic and lithologic properties. Not only is such a correlation possible, but this comparison also gives us an understanding about the processes taking place within the sediment. The "loss diagram" is a typical example. A clear demarcation of the areas occupied by the different samples is observed. The samples can be sorted not only on the basis of their pore filling (water or air), grain shape also seems to play a major role; angular grains can be separated from the rounded ones.

Our major observations are:

1. Static frame compressibility and P-wave velocity correlate with each other at low pressures. This correlation diminishes with increasing pressures.
2. Coarseness of grains increases the velocity and attenuation of P-waves and the attenuation of S-waves. The S-wave velocity is unaffected by grain size.
3. Angularity of grains causes a decrease in velocity, attenuation and static frame compressibility.
4. Dry grains show high shear losses, whereas saturated grains have predominant bulk losses of seismic energy.

The results show that a combination of P- and S-waves is a powerful tool in predicting lithologic parameters from seismic data. Such a study is also important to understand the physical processes taking place in a sediment and thus lend more credibility to theoretical prediction about its seismic response.



<u>saturated grains</u>	<u>dry grains</u>
○ rounded	× rounded
◊ angular	△ angular
	▲ powdered

"LOSS DIAGRAM":

$(Q_p / Q_s) - (V_p / V_s)^2$  relationship for all samples

## **Effect of Clay Content on Compressional and Shear Wave Velocities and Attenuations in Tight Gas Sand Formations**

**Tutuncu A.N., Podio A.L. and Sharma M.M.  
Department of Petroleum Engineering,  
The University of Texas at Austin,  
Austin, TX 78712**

An attempt has been made to study the relationship between compressional and shear wave velocities, attenuations and mineralogy in tight gas bearing rocks. Ultrasonic measurements (pulse transmission at ~ 1 MHz) have been conducted using fully brine saturated cores with known mineral content and porosity. Simultaneous measurements of compressional and shear wave velocities and attenuations under a biaxial stress state were carried out and frequency and load effects on attenuation were examined using amplitude spectra of P and S waves in the frequency domain.

The clay content of the samples tested varied from 1% to 30%. Compressional and shear wave amplitude data exhibit a shift in peak frequency toward lower frequencies for samples with higher clay content when compared to the data for clean samples. The presence of clay softens the rock grain contacts and causes larger contact area values compared to the values for a nearly clean rock under the same applied load. This effect is accounted for in a modified Hertz contact model developed by introducing the mineral composition into the dry frame moduli. The model also takes into account the interactions taking place between the fluid in the pore space and the grains in contact. This interaction plays a major role in wave propagation and attenuation in sandstones with medium to high clay content.

When scaling the acoustic properties from a core (cm) to a log (m) scale, two problems exist a) depth corrections and b) sampling volumes. The maximum and minimum log arrival times over a depth shift interval determined from high resolution FMS data and

core pictures were read to give a comparison of the changes in log-derived velocities that could be expected due to a depth mismatch between log and core. With these corrections, the trend observed in P and S wave velocities in homogeneous intervals shows that clean sandstone velocities measured in the ultrasonic frequency range deviate systematically from the log derived velocities ( $\sim 20$  KHz). The deviations were correlatable in most cases to the clay content. More random variations between core and log measurements were observed in heterogeneous intervals where the core sampling density is insufficient.

# THE EFFECTS OF NON-WELDED INTERFACES ON SEISMIC WAVE PROPAGATION AND ATTENUATION

*Larry R. Myer*  
Earth Sciences Division  
Lawrence Berkeley Laboratory  
University of California  
Berkeley, CA 94720

*Roberto F. Suarez-Rivera & Neville W.G. Cook*  
Department of Materials Science and Mineral Engineering  
Hearst Mining Building  
University of California  
Berkeley, CA 94720

Rocks contain discontinuities on all scales from microcracks and pores through joints, fractures, and bedding planes to faults. These discontinuities allow rocks to store and transport fluids. Until recently, seismology has been concerned primarily with either welded or free boundaries at discontinuities. Many boundaries, such as cracks and fractures, at effective stresses of engineering interest are, in fact, non-welded. That is, they consist of areas of contact separated by voids. Non-welded boundaries produce discontinuities in the seismic particle displacement or velocity, depending upon the rheology of the boundary. If the wave length of the propagating wave is large compared to the size of the voids then the discontinuity can be represented by an average value.

The boundary conditions for plane wave propagation across a purely elastic non-welded boundary between two elastic half spaces, I and II, are:

$$u_I - u_{II} = \tau/\kappa, \quad \tau_I = \tau_{II}$$

where  $u$  are particle displacements,  $\tau$  are stresses and  $\kappa$  is the specific stiffness of the boundary. These boundary conditions lead to frequency-dependent coefficients for the transmission, reflection and conversion of a seismic wave incident at such a boundary (e.g. Schoenberg, 1980; Pyrak-Nolte et al 1990). They also produce a frequency-dependent group time delay. Results for normal incidence are illustrated in Figure 1. Either increasing frequency or decreasing specific stiffness results in a reduction of the transmitted wave amplitude, but because the boundary is elastic, energy is conserved. The group time delay is greatest at low frequencies and low specific stiffness.

Displacement-discontinuity theory can be used to analyze seismic wave propagation in media in which anisotropy results from multiple, parallel boundaries, such as joint sets or non-welded bedding planes. For normal incidence, the group time delay results in an average group velocity at the zero frequency limit equal to the seismic velocity given by the effective modulus derived from a pseudo-static analysis of the average strain in the media. However, in general, as illustrated in Figure 2 the group velocity derived from the displacement discontinuity theory is frequency dependent and differs as a function of propagation direction from that based on an effective modulus. Laboratory results have shown that the effects on a propagating wave of each discontinuity in a set can be evaluated independently for a discontinuity spacing greater than the spacing between the voids in the fracture planes (Myer et al, 1990). When the discontinuity spacing is small there is interaction between the voids in adjacent discontinuities which changes their specific stiffness.

Laboratory measurements of compressional wave transmission under dry and saturated conditions at frequencies from 100 kHz to 1 MHz across single natural fractures at different normal stress levels produced results in close agreement with predictions given by the displacement discontinuity theory (Figure 3). Displacement discontinuity theory has also been used to model the results of cross-hole measurements at ~25 kHz in unsaturated columnar basalt. The observed anisotropy in both velocity and amplitude of the compressional wave were predicted based on knowledge of the specific stiffness of the dominant fractures and their spacing.

Modeling of laboratory measurements of shear wave transmission, particularly in saturated rock, requires a discontinuity in velocity, as well as in displacement. For a Kelvin-type rheology the boundary conditions are:

$$\kappa(u_I - u_{II}) + \eta(\dot{u}_I - \dot{u}_{II}) = \tau, \quad \tau_I = \tau_{II}$$

where  $\dot{\phantom{x}}$  refers to time derivative and  $\eta$  is specific viscosity. For a Maxwell-type rheology, the boundary conditions are:

$$(\dot{u}_I - \dot{u}_{II}) = \tau/\kappa + \tau/\eta, \quad \tau_I = \tau_{II}$$

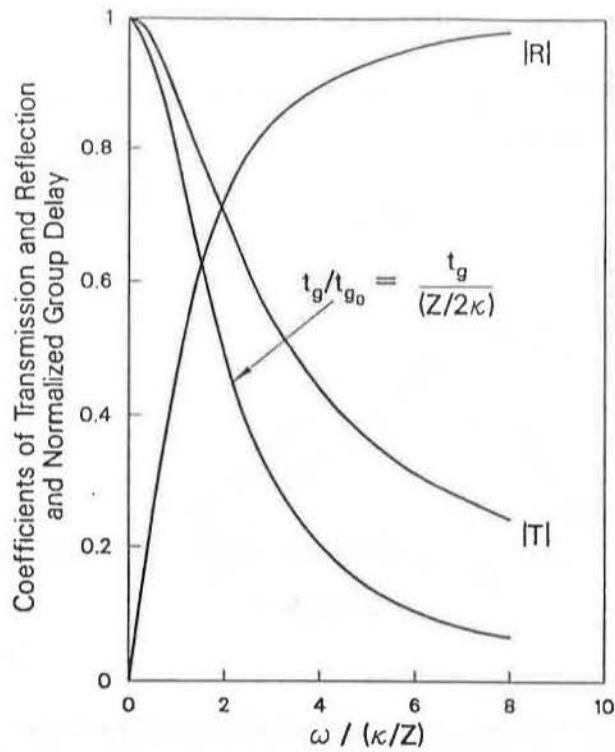
The effect of the velocity discontinuity is to add a frequency independent component to the apparent attenuation of the transmitted wave (Myer et al 1990). Energy is lost at the

boundary due to viscous dissipation. Figure 4 is a comparison of laboratory shear wave measurements at different stress levels on a single fracture with predictions based on a Kelvin rheology.

Finally parallel work on the stiffness and hydraulic conductivity of natural fractures has shown that the apertures of the void spaces between these surfaces are spatially correlated (Pyrak-Nolte et al, 1988). As a result of this the stiffness of a fracture bears a rank correlation to its hydraulic conductivity. Because of the explicit relationship between fracture stiffness and the amplitude and group time delay of a propagating wave, suggests the seismic response of fractures may provide some insight concerning their hydraulic behavior.

## References

- Myer, L.R., L.J. Pyrak-Nolte, D. Hopkins, and N.G.W. Cook, 1990, "Seismic characterization of fracture properties," *Proceedings of First Annual International High-Level Radioactive Waste Management Conference*, American Nuclear Society, vol. 1, pp. 908-914.
- Pyrak-Nolte, L.J., L.R. Myer and N.G.W. Cook, 1990, "Transmission of Seismic waves across single fractures," *Journal of Geophysical Research*, vol. 95, no. B6, pp. 8617-8638.
- Pyrak-Nolte, L.J., N.G.W. Cook, and D. Nolte, 1988, "Fluid percolation through single fractures," *Geophysical Research Letters*, vol. 15, no. 11, pp. 1247-1250.
- Schoenberg, M., 1980, "Elastic wave behavior across linear slip interfaces," *Journal of the Acoustical Society of America*, vol. 68, no.5, pp. 1516-1521.



XCG 8612-12352

Figure 1. Magnitudes of the reflection and transmission coefficients and normalized group time delay for a seismic wave normally incident upon a displacement discontinuity as a function of normalized frequency.

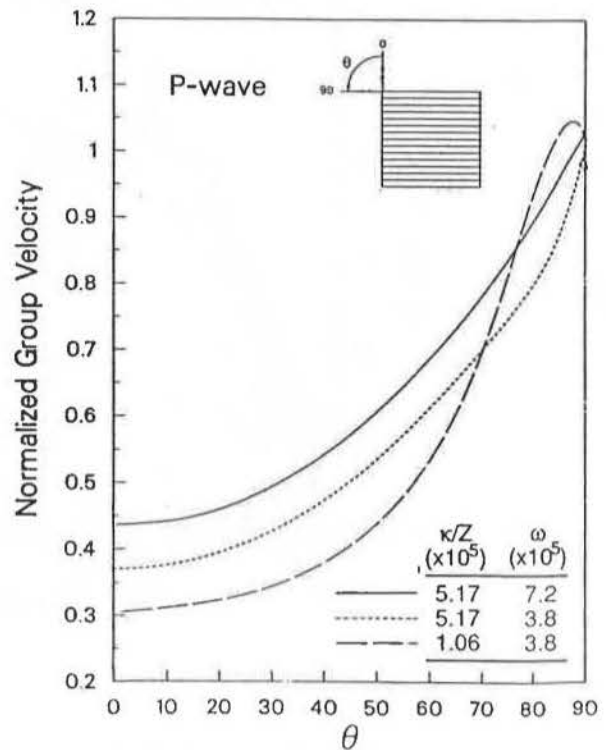
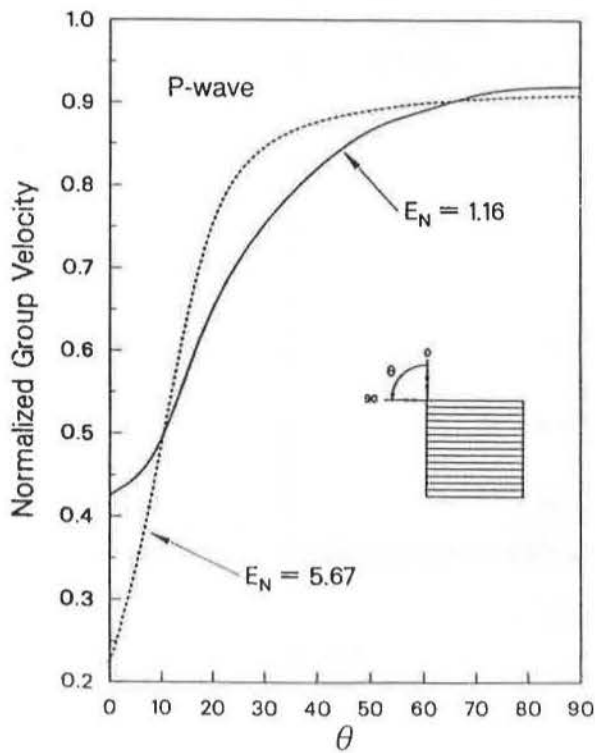


Figure 2. Normalized P-wave group velocity as a function of angle of incidence, plot on left based on effective moduli theory, plot on right based on displacement discontinuity theory. Inset show the angle of incidence and particle motion.

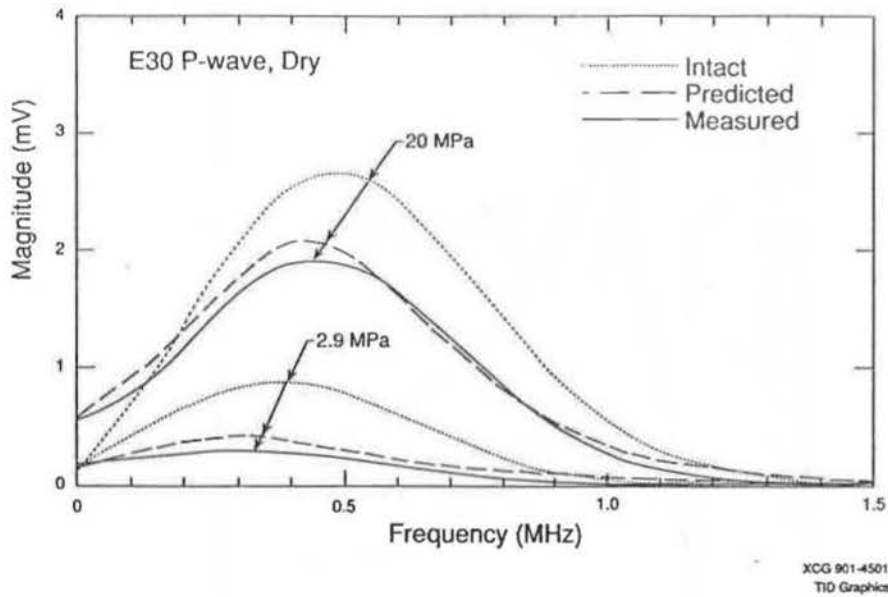


Figure 3. Example results of laboratory tests showing amplitude spectra of P-waves for fractured and intact specimens at the same stress level, and predicted curves based on elastic fracture rheology.

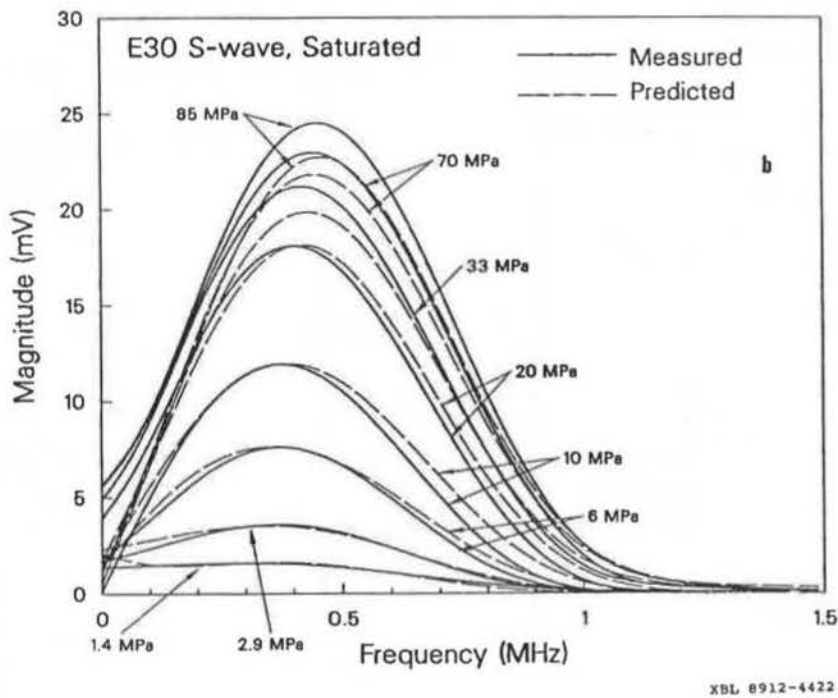


Figure 4. Comparison of measured and predicted spectra of S-waves propagated across a saturated fracture; prediction based on Kelvin rheology.

## **The Effects of Grain Contacts on Elastic Waves in Granular Rock**

*Extended Abstract for the SEG 1991 Summer Research Workshop on Lithology*

*K. T. Nihei\*, N. G. W. Cook\*, L. R. Myer†, and R. Suárez-Rivera\**

### **Introduction**

Theoretical and experimental studies have demonstrated that discontinuities spanning the scale from faults and joints to cracks can significantly alter elastic wave velocities and attenuation. Less well documented are the effects of core scale features such as grain contacts. The purpose of this paper is to show that, in certain granular rocks, grain contacts act as non-welded interfaces similar in nature to faults and joints.

### **Grain Contacts in Granular Rocks**

Scanning electron microscope (SEM) observations of epoxy pore casts of granular rocks, such as sandstone and limestone, show that the regions between grains are composed of both large pores and very fine intergranular spaces between grain contacts. The porosity and permeability of the grain contacts are often negligible, compared with that of the large pore space, but these sub-micron scale features can have a dramatic effect on the velocities and attenuation of elastic waves.

SEM observations also show no evidence of microcracking. Grain contacts are different from what is typically referred to as a microcrack. A grain contact is a region of partial contact between two grains. Stresses are transmitted across the grain contact but vanish on the surfaces of the crack.

### **Laboratory Tests with Low-Melting Point Solids**

---

\*Department of Materials Science and Mineral Engineering, University of California, Berkeley, CA 94720

†Earth Sciences Division, Lawrence Berkeley Laboratory, Berkeley, CA 94720

Laboratory measurements of ultrasonic P- and S-waves were performed on dry and fluid-saturated cores of Berea sandstone. When a hydrostatic stress was applied to the specimen, P- and S-wave velocities increased and attenuation decreased. The changes in attenuation were always larger than the corresponding changes in velocity. These changes in the elastic properties must be associated with the elastic deformation of the highly deformable parts of the pore space, such as the stiffening of the grain contacts.

An alternative approach for stiffening the grain contacts is through the use of low melting point solids such as sulfur, paraffin, and epoxy (wetting fluids). These fluids can be imbibed into the rock until a prescribed saturation is achieved and then solidified in place to effectively weld the grain contacts and other small parts of the pore space (Figure 1). As Figure 2 indicates, the effect of filling 18% of the pore space of a specimen of Berea sandstone with sulfur is to produce a notable decrease in both P- and S-wave attenuation (i.e., an increase in the amplitudes). Because sulfur is a wetting fluid, it is drawn by capillary forces into the smallest pore features, such as the grain contacts. Figure 2 demonstrates that the attenuation is also reduced in a specimen of Berea sandstone saturated with 55% Wood's metal. Wood's metal is a non-wetting fluid and, consequently, must be forced into the pore space by applying a capillary pressure (Figure 1). The Wood's metal will reside in the largest parts of the pore space. Upon solidification, the Wood's metal should effectively eliminate scattering off the large pores, while the sulfur should reduce losses associated with scattering off the grain contacts. Figure 2 suggests that the grain contact attenuation overshadows attenuation resulting from scattering off pores.

### **Grain Contact Scattering**

At present, the micromechanical processes of attenuation associated with grain contacts are not well understood, and a series of experimental and theoretical work is currently in progress. It is likely that attenuation results from a scattering mechanism

at the grain contacts. By increasing the confining stress, we increase the stiffness of the grain contacts, thereby, reducing the scattering and increasing the energy transmitted through the specimen.

To examine the effects of grain contacts on the velocities and attenuation of elastic waves, we use, as a zero-order approximation, the displacement-discontinuity model of a non-welded interface (Shoenberg, 1980; Pyrak-Nolte et al., 1990). If we also ignore multiple and off-angle scattering, the attenuation resulting from scattering off dry grain contacts can be expressed as

$$Q_p^{-1} = \frac{-2c_p}{\omega L} \ln [|T_p(\omega)|] \quad (1)$$

where  $c_p$  is the P-wave velocity,  $\omega$  is the angular frequency,  $L$  is the length of the specimen, and  $|T_p(\omega)|$  is the frequency-dependent transmission coefficient for a non-welded interface given by

$$|T_p(\omega)| = [(\omega Z / 2\kappa)^2 + 1]^{-n/2} \quad (2)$$

where  $Z$  is the P-wave impedance,  $\kappa$  is the stiffness of each grain contact (Figure 3). The stiffness of each grain contact can be estimated from the effective modulus of the rock:  $\bar{M}^{-1} = M^{-1} + N/\kappa$ , and  $N$  is the number of grain contacts,  $n$ , per length,  $L$ . Similar expressions which incorporate a discontinuity in velocity, in addition to the displacement-discontinuity, have been proposed by Pyrak-Nolte et al. (1990) to account for losses resulting from viscous drag in saturated or partially saturated rock.

The predictions of this highly idealized model of a granular rock are compared with laboratory P-wave measurements made on a dry specimen of Berea sandstone confined hydrostatically in Figure 4. The theoretical predictions are in good agreement with the ultrasonic data, indicating that the basic mechanics of the model are correct. The model predicts that attenuation due to grain contact scattering is frequency-dependent and is significant primarily at frequencies in the ultrasonic range. At exploration frequencies, dry grain contacts will have a negligible influence on the

attenuation of seismic waves. However, when the grain contacts are filled with fluid, grain contact viscous drag losses can become significant at exploration frequencies.

### References

- Pyrak-Nolte, L. J., L. R. Myer, and N. G. W. Cook (1990). Transmission of seismic waves across single natural fractures, *J. Geophys. Res.*, 95, 8617-8638.
- Shoenberg, M. (1980). Elastic wave behavior across linear slip interfaces, *J. Acoust. Soc. Am.*, 68, 1516-1521.

### Tests with Low-Melting Point Solids

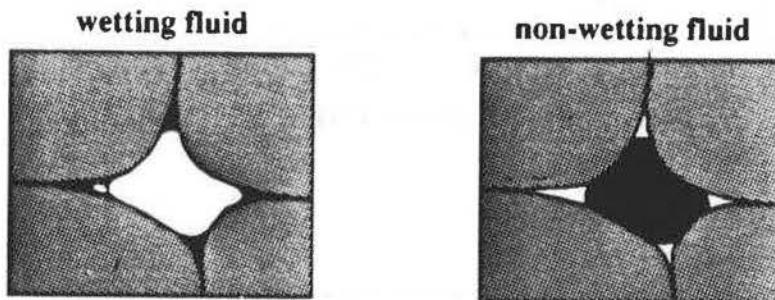


**Figure 1** A fluid with surface tension,  $\gamma$ , can be forced under a pressure,  $P_c$ , into parts of the pore space with radii,  $R$ :  $P_c = \frac{2\gamma}{R} \cos\theta$  (Laplace's Equation). Wetting fluids can be solidified in place to *weld* the grain contacts. Non-wetting fluids can be used to eliminate the large pore spaces.

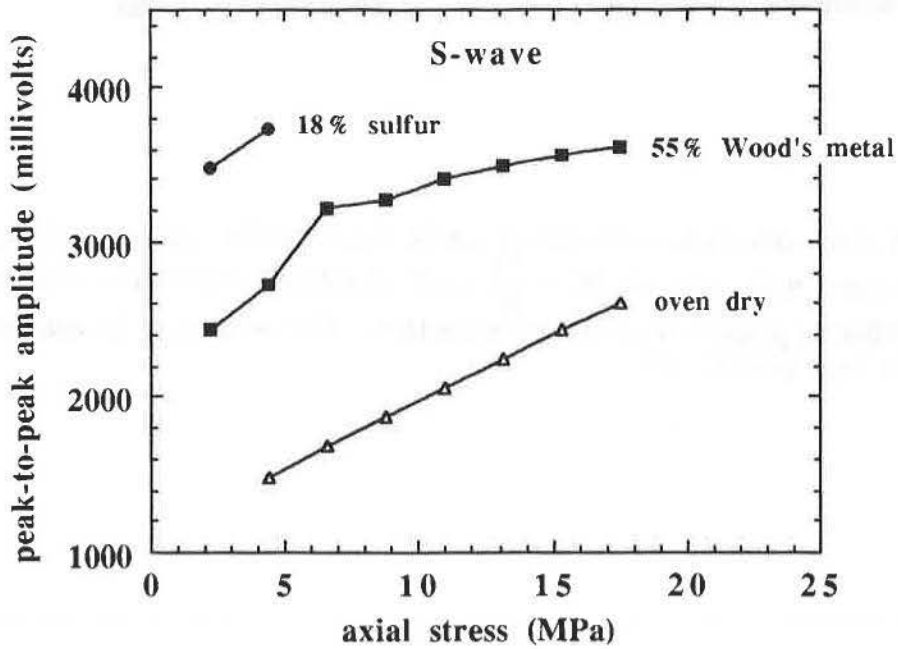
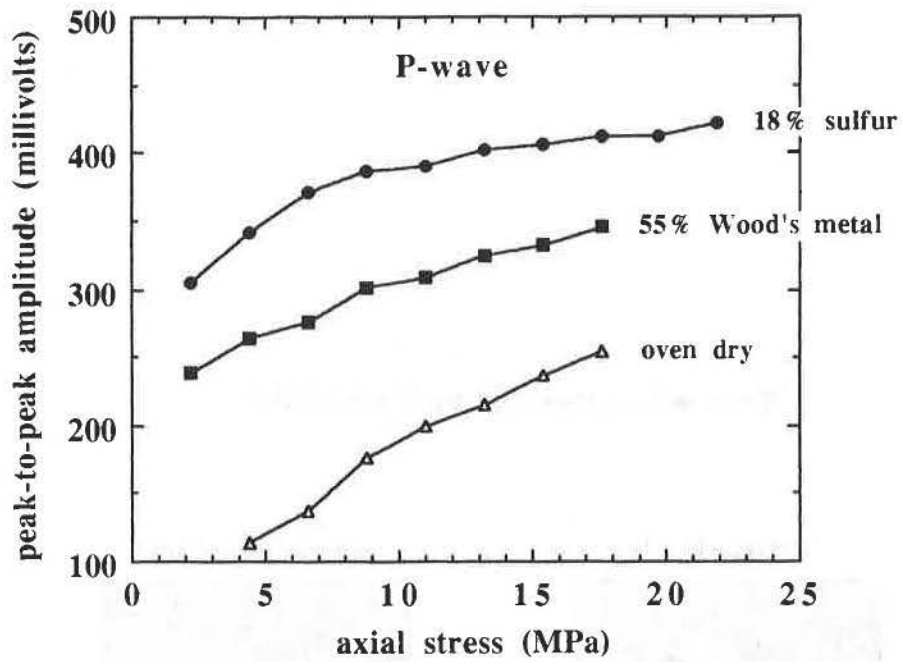


**Figure 2** Peak-to-peak amplitudes of ultrasonic P- and S-waves in Berea sandstone as a function of uniaxial stress. The three curves are for different specimens:  $\Delta$  oven dry,  $\bullet$  18% sulfur, and  $\blacksquare$  55% Wood's metal.

### Contact Stiffness Scattering Model

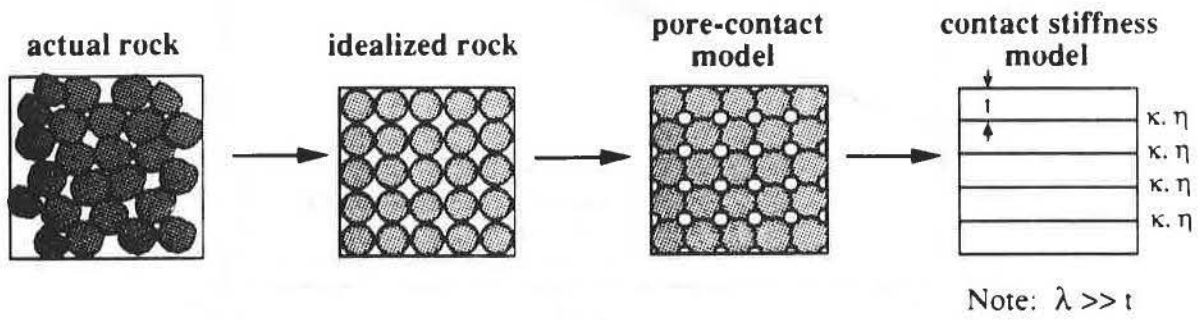


Figure 3 Idealized grain contact scattering model.

### P-wave Attenuation: Theory and Observation

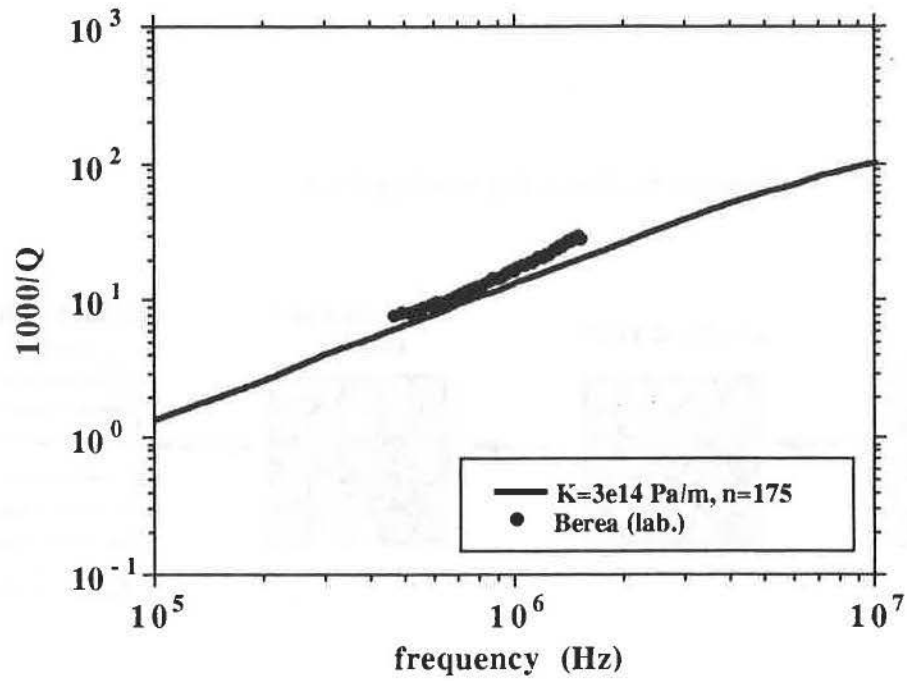


Figure 4 P-wave attenuation versus frequency for dry Berea sandstone: grain contact scattering model and observation.

## Scale-dependent effects of anisotropic mechanisms

Ebrom, D.A.\*, Tatham, R.H.+, and McDonald, J.A.\*

\* University of Houston, Houston, Texas

+ Texaco, Inc., Houston, Texas

To a first approximation, the earth is a layered sequence of isotropic, elastic homogeneous lithological units. Anisotropy may be regarded as a perturbation of this model, given that extremely strong anisotropies (such as are observed in single crystals) have not yet been identified in elastic wave experiments at seismic wavelengths. The relatively weak anisotropies present in the earth arise from several different mechanisms, which are not mutually exclusive. If anisotropy is to be included in an explorationist's earth model, the hope must be that the anisotropy is related to some economic interest. On this basis, there is a motivation to separate those anisotropic effects related to geologic objectives, from those anisotropic effects which are unrelated to geologic objectives *but* whose correction may improve the seismic image.

The most likely mechanisms for causing velocity anisotropy at seismic wavelengths are:

1. background stress (due to regional or local tectonics),
2. aligned crystallographic orientation (as in upper-mantle olivine),
3. aligned micro-clasts (as in shales),
4. aligned micro-cracks (as a response to background stress),
5. aligned layers of alternating lithology (as on the Gulf Coast), and
6. aligned joints or fractures (as in the Austin Chalk).

Of these six mechanisms, only the last is directly relatable to the description of hydrocarbon reservoirs. Mechanisms 1 and 4 may yield useful information about the overall stress state of a lithologic unit, but will not give diagnostic advice concerning the location of particular prospects. Mechanisms 2, 3, and 5 are of concern principally by virtue of their ability to cause depth errors in seismically derived subsurface horizon maps. (Although Winterstein has shown how these stacking velocity/depth conversion anomalies may be inverted to infer gross lithology).

We have been employing scale-model seismology to investigate artificial earth models containing joints (fractures). Our models are on

the centimeter scale length, as opposed to the field case of hundreds of meters, so our scale factor is about 1:10,000. Some of the variables that are controllable in such experiments are:

1. fracture intensity (or number of fractures per unit length),
2. fluid content of the fracture,
3. effective normal stress,
4. surface texture (as quantified by a profilometer and recorded by electron micrography),
5. frequency of elastic waves,
6. polarization of elastic waves, and
7. angle of rays relative to fracturing.

The advantage of the scale-model approach is that a more complete characterization of the experiment is possible than in virtually any actual seismic survey except the most detailed.

Our results to date have suggested some discriminants for separating the effects of joint-induced anisotropy from the other five mechanisms previously mentioned.

1. Mechanisms 1, 2, 3, and 4 are expected to produce the same effective elastic constants at all frequencies from the seismic up to and past the highest logging frequencies (circa 100,000 Hz). Mechanisms 5 and 6 will produce dispersive effects at seismic frequencies whose wavelengths are comparable to layer thickness or joint spacing. For layer thicknesses or joint spacings of a few meters, these frequencies are in the cross-borehole seismic band (50-1000 Hz).

2. Mechanisms 5 and 6 have very different dispersive effects. Our experiments suggest that for mechanism 5, all three wave types (qP, S1, and S2) are dispersive, while for mechanism 6, only the S2 wave type is dispersive. These results are strictly only applicable to wave polarizations that are traveling along rays orthogonal to the symmetry axis (that is, traveling parallel to either the layers or the fractures).

The difference between mechanism 5 and mechanism 6 can be interpreted by means of a modified Backus theory in which the fractures are viewed as a layer of small (but finite) thickness and smaller (but not negligible) elastic constants. Thus, the fracture is seen as a thin and compliant, but fully elastic layer. This model is adapted from the "bed of nails model" (Gangi, 1978), which relates the asperity height distribution

of the fracture interfaces and the normal stress to the elastic properties of the fracture.

To test this model, we have calculated long-wavelength elastic constants by implementation of the averaging procedure described by White (1955). Our model has two layers of unequal thickness. The Plexiglas plates are the thick layer, while the fractured zone is the thin layer. The value used for the thickness of the fracture is constrained by direct profilometer measurements of the asperity distribution on the Plexiglas plate surfaces. The shear modulus and the density of the fractured zone are a small, but non-negligible, fraction of their values for the unfractured Plexiglas, generally between 1% to 20% of the unfractured Plexiglas values. Forward modeling of the frequency dependence of C44 can then be done by the method of Achenbach (1968). These dispersion results are in agreement with the observed dispersion results in our fractured Plexiglas system.

3. In our models, mechanism 6 also produces differential Q effects in which the Q's of the qP and S1 wave are substantially higher than the S2 wave (ca. 30-40 vs. 5). One possible explanation for the higher attenuation of the S2 wave (for a ray parallel to fractures) is the observation by Strick (1970) that attenuation functions and dispersion functions are not independent, but in fact knowledge of one determines the other. This suggests that the S2 wave is not more highly attenuated than S1 for frequencies at which dispersion no longer occurs. (Dispersion only occurs for those frequencies whose wavelengths are comparable to the layering distance, say from 10% to 1000% of the layering distance.)

These results may be most applicable to cross-borehole seismology, an increasingly popular method of reservoir evaluation. The goal, of course, is to be able to relate elastic parameters to some economically meaningful attribute of a lithological unit. The modeling described above is an attempt to describe the anisotropy produced by fractures in terms of observable fracture parameters.

#### ACKNOWLEDGMENTS

I would like to thank Tony Gangi for several conversations regarding his "bed of nails " model for fractures. Ed White suggested the Achenbach dispersion method.

## REFERENCES

Achenbach, J.D., 1968, Wave propagation in lamellar composite materials: Jour. Acoust. Soc. Amer., **43**, 1451-1452.

Gangi, A.F., 1978, Variation of whole and fractured porous rock permeability with confining pressure: Intl. Jour. Rock Mech., **15**, 249-257.

Strick, E., 1970, A predicted pedestal effect for pulse propagation in constant-Q solids: Geophysics, **35**, 387-403.

White, J.E. and Angona, F.A., 1955, Elastic wave velocities in laminated media: Jour. Acoust. Soc. Amer., **27**, 310-317.

## The Effect of Pore fluids and Pressures on the Seismic Velocities in Cracked and/or Porous Rocks

Anthony F. Gangi  
Department of Geophysics  
Texas A&M University  
College Station, TX 77843-3114

Pore fluids under pressure have a strong effect on the seismic-wave velocities in cracked and porous rocks. The Gassmann theory has been used to determine the p-wave velocity variation with depth (or confining and pore pressure) and degree of water and gas saturation in porous rocks by Domenico (1974). An equivalent theory is possible for cracked rocks.

For cracked rocks, the variation of the dry-rock modulus (or velocity) with confining pressure can be determined by using an asperity-deformation model such as the bed-of-nails model (Gangi, 1978; see also, Carlson and Gangi, 1985). To determine the effect of the pore fluids and the pore pressure, it is necessary to know how the pore volume changes with externally applied pressure and with changes of the pore pressure and modulus (or moduli) of the pore fluids. In addition, it is necessary to know whether the permeability of the rock is 'high' or 'low.'

For 'high' permeability, the modulus of the rock/fluid system is the drained modulus (this is also the static and/or 'low'-frequency modulus). In this case, the pore pressure does not change as the confining pressure changes (or pore volume changes) because the permeability is sufficiently "high" or the frequency sufficiently "low" that the pore fluid can flow out of the pore space and cause minimal change in the pore pressure.

For 'low' permeability, the modulus of the rock/fluid system is the undrained modulus (the dynamic or 'high'-frequency modulus). In this case the permeability is so low, or the frequency so high, that the pore-fluid pressure will change as the confining pressure and, consequently, pore volume changes. The undrained modulus is always greater than the drained modulus; consequently, the velocity determined by the the undrained modulus is higher than that determined by the drained modulus. This variation of velocity, caused by the permeability, results in velocity dispersion in fluid-saturated porous and/or cracked rocks.

The variation in the seismic velocity with variations in both the pore and the confining pressure depends upon the effective pressure. That is, if the pore pressure,  $P_p$ , and the confining pressure,  $P_c$ , are varied so that the effective pressure,  $P_e$ , is not changed, then there will be no change in the velocity. There have been a number of different definitions proposed for the effective pressure. The earliest and the simplest is that the effective pressure is the differential pressure; that is, the difference between the confining and pore pressures. This definition is not valid for low-porosity rocks or for rocks under high differential pressure. Another definition for the effective pressure is  $P_e = P_c - nP_p$  where  $n$  is a constant less than 1. When highly accurate data are available, a better expression for the effective pressure has the coefficient of deformation,  $n$ , a function of the differential pressure.

P-wave velocity data for a water-saturated chalk as a function of pore and confining pressure are given in Figure 1a. The same data, plotted as a function of the empirical effective pressure, are shown in Figure 1b. The data almost fit on a single curve, as they should if the proper effective pressure was used. However, some small systematic deviations from a single curve are still apparent.

Theoretical curves based on a force-balance equation and the asperity-deformation model for a different cracked rock are given in Figures 2a and b. In Figure 2a, the pore medium is assumed to be water while in Figure 2b, the pore medium is assumed to be gas. As expected, significant differences in the velocities occur at the same pore and confining pressures when the pore fluid is changed from water to gas. The same characteristic behaviors of the velocity with pore pressure and confining pressure appear in both the theoretical and the experimental curves, demonstrating that the theory accurately describes the effects.

FIGURE 1a

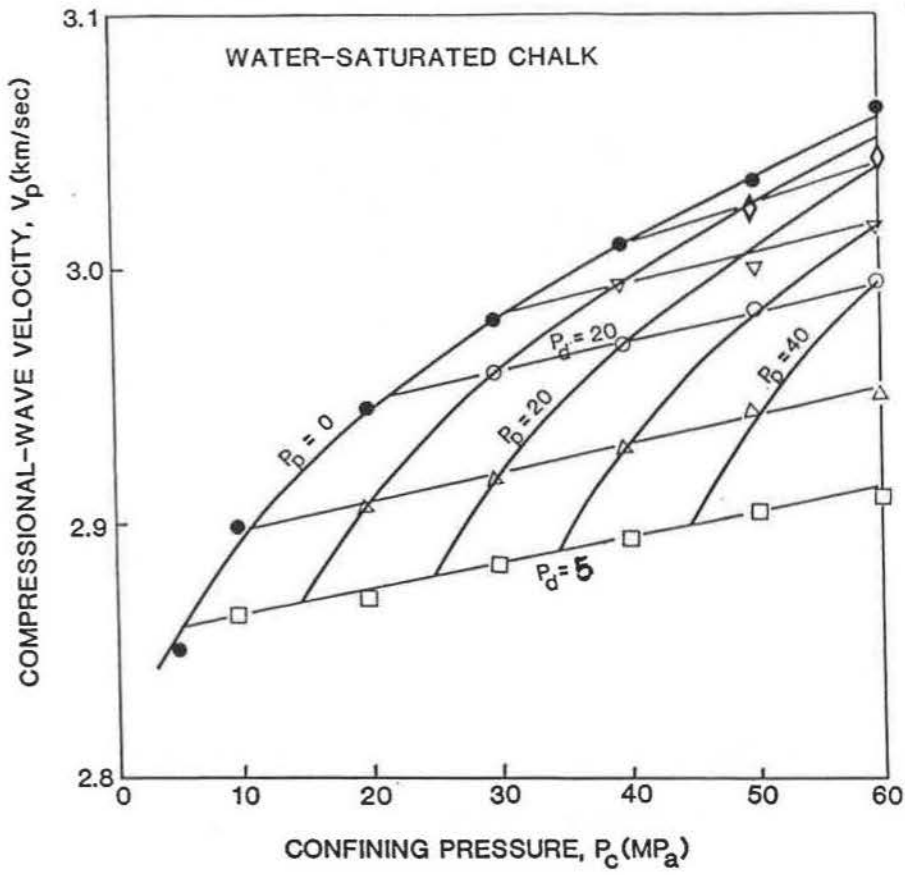
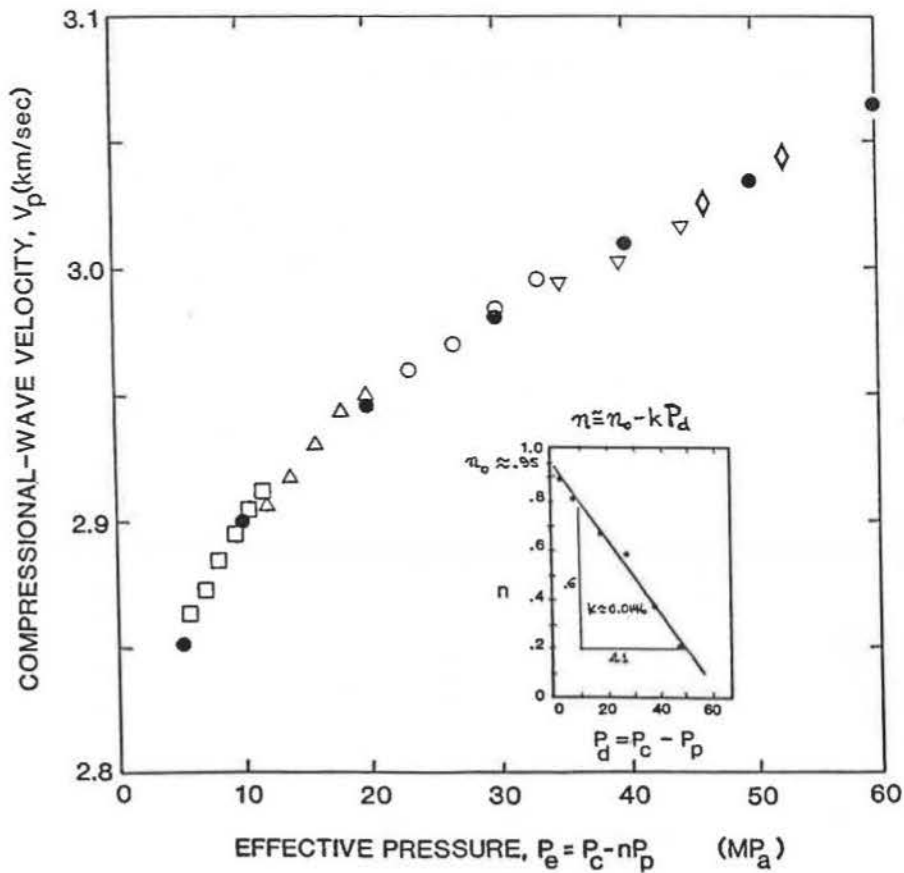
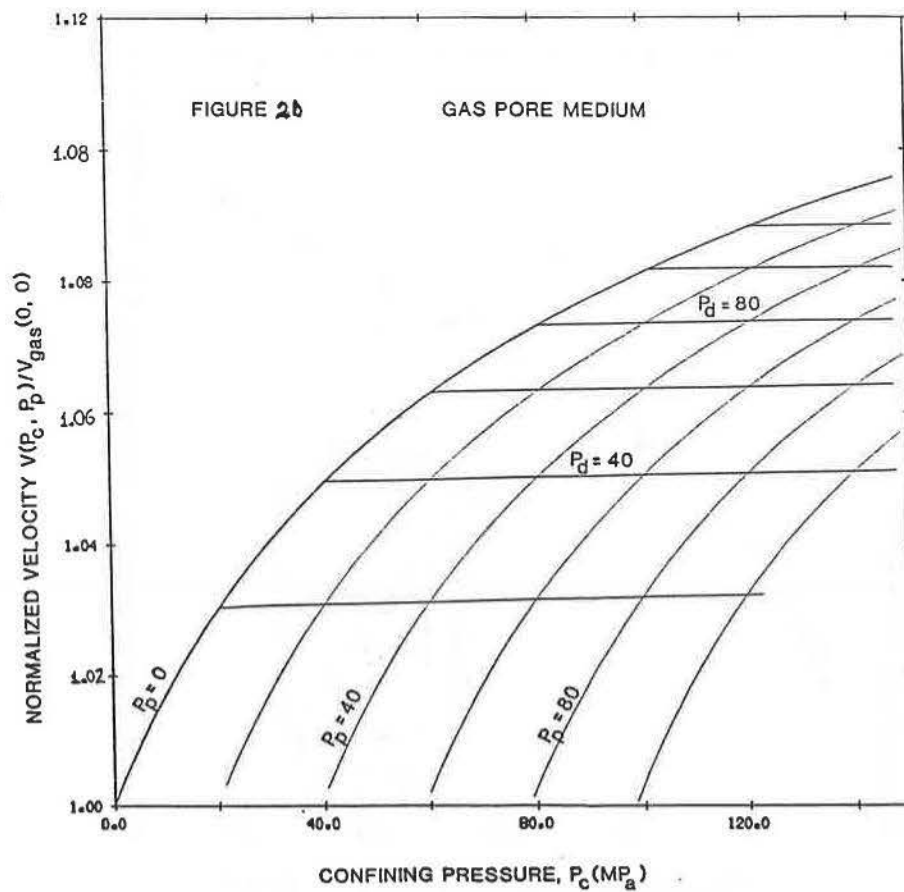
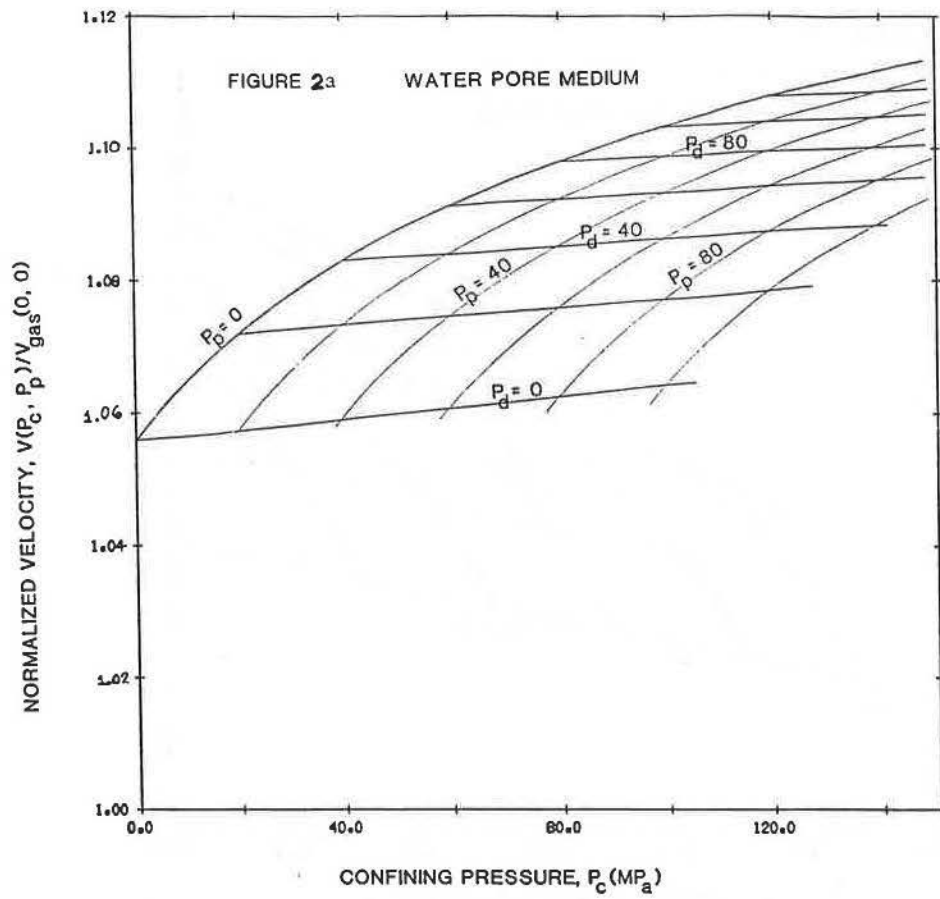


FIGURE 1b





# ANISOTROPIC ACOUSTIC PROPERTIES OF COAL

Ziqiong Zheng and John McLennan  
Terra Tek, Inc, Salt Lake City, Utah

Unlike many other engineering materials, rocks contain numerous heterogeneities, including pores, bedding planes, and fractures as well as variable mineralogy and preferred grain orientations. These heterogeneities gives rise to inhomogeneous and anisotropic properties. Mechanical, rheological and thermal behavior of rocks under different stress, temperature and saturation regimes is often dependent on these heterogeneities. In engineering operations involving excavation in rock, it is important to comprehend the mechanical behavior of a rock in which the excavation is made. For example, knowing the anisotropic behavior of rock can provide guidance criteria for maximizing production and minimizing stress concentration-caused hazards. This is particularly true in coal, especially with the current unprecedented acceleration of drilling for coalbed methane.

Coal usually has two dominant cleat systems which are approximately orthogonal to each other. The major system (face cleats) often has more cleats or better developed apertures and hence is more conductive to fluid (water, gas). The mechanical properties of coal, in directions parallel and orthogonal to a cleat plane, are also very different. The determination of cleat system (face and butt) orientations and dominance impacts well placement schemes, strategies for hydraulic fracturing stimulation and permeability/production forecasting.

Nondestructive fracture (flaw) detection using ultrasonic methods has long been used in the materials industry and in mechanical engineering quality assurance programs. Seismic methods have been used in geophysical exploration for many years to detect mega-scale fractures and faults, formation variations and vertical profiles (VSP). In the laboratory, many researchers have performed rock anisotropy measurements using ultrasonic methods. The

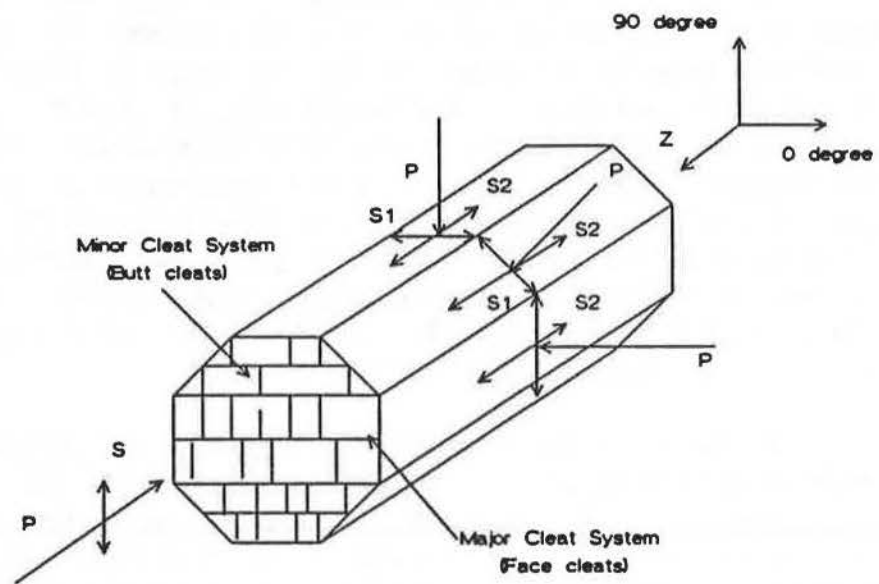


Figure 1. Schematic of testing setup.

same principles, with experimental modifications, have been used on coal samples to

characterize anisotropy. Cylindrical coal samples were cut and ground to configurations with an octagonal cross-section. The axis of the samples was perpendicular to bedding planes and the sides of the octagons were machined parallel, 45 degrees and perpendicular to the major cleat planes. Great care was extended during sample preparation in order to minimize mechanical damage. Description of sample preparation procedures is presented elsewhere<sup>1</sup>. Two samples were tested. The first one (Sample 1) had an apparent porosity of 4.2% and was tested dry. Sample 2 (apparent porosity of 4.0%) was tested under both dry and water saturated conditions. Under benchtop conditions, compressional (P) and shear (S) waves were transmitted through Sample 1 perpendicular to its axis (shown as the z-axis in Figure 1) with S-wave polarization in directions both parallel and perpendicular to the z-axis (as shown in Figure 1). P- and S-waves were transmitted through Sample 2 in directions both parallel and perpendicular to its axis but with S-wave polarization only perpendicular to the axis, under dry and saturated conditions. To assure full contact between the transducers and the samples, a nominal contact stress of 50 psi was applied. Dynamic properties of the samples were calculated from the measured velocities using elastic relationships<sup>2</sup>.

Figure 2a shows calculated values for dynamic Young's modulus and Poisson's ratio for both of the samples tested. With the exception of Sample 2 without fluid in the cleat systems, there is an evident directional anisotropy. The minimum values for modulus align perpendicular to the face cleat direction. Conversely, Poisson's ratio does not show consistent directional trends when the shear wave is polarized in a direction parallel to the sample axis, but does show substantial fluctuation when polarization is perpendicular to the sample axis. This is indicated in Figure 2b.

In addition to the actual presence of the cleat systems, the presence of water in these features altered the dynamic properties dramatically. As an illustration, consider directional variation of Young's Modulus for Sample 2. When the cleats were dry, Figure 2a indicates a modest directional variation ( $E_{max}/E_{min}$ ) of less than 20%. With the cleats nominally saturated with water, directional variation was much more exaggerated; the value normal to the face cleats being approximately seven times less than that normal to the butt cleats and approximately twenty times less than the value determined by axial measurements. Figure 2b demonstrates saturation dependence for Poisson's ratio. The values measured under saturated conditions were substantially higher than when fluid was not present and did not reflect diagnostic directional dependence radially. Axial measurements mimicked dry data more closely.

Evaluation of wave velocity data suggested that substantial reduction in Young's modulus and elevation of Poisson's ratio on saturation coincided with substantial reduction in the S-wave velocity, which almost disappeared in the direction orthogonal to the face cleat planes. P- and S-wave velocities are shown in Figures 3a and 3b. Regardless of the saturation conditions, the directional variation of P-wave velocity was relatively consistent.

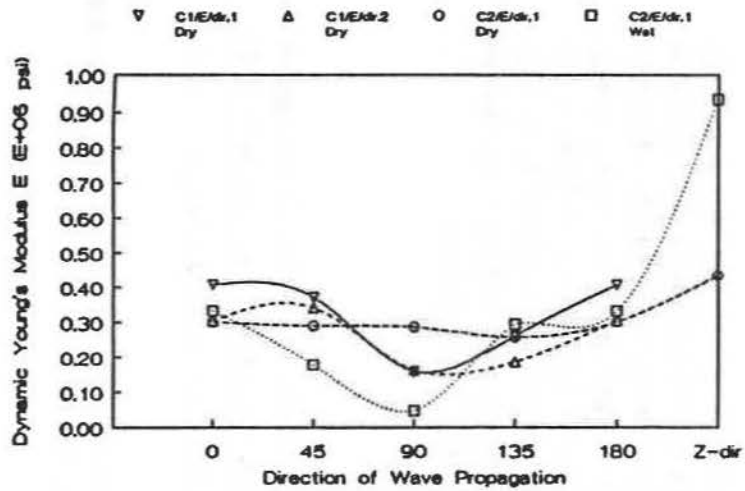


Figure 2a. Dynamic Young's modulus as a function of wave incidence angle ( $0^\circ$  indicates propagation parallel to the face cleats).

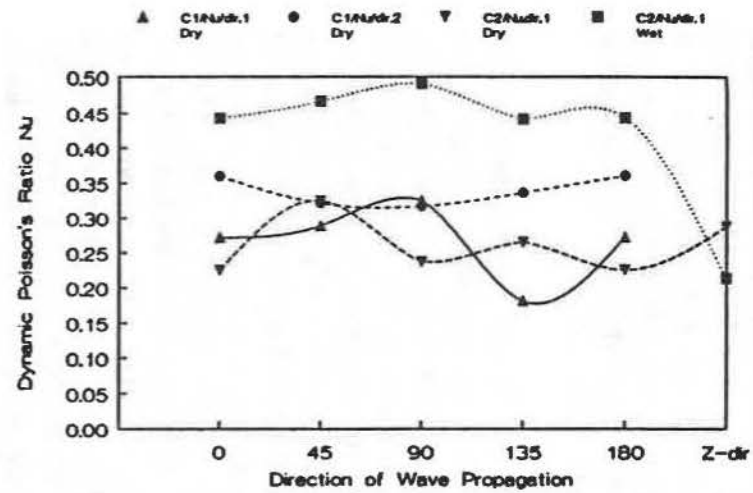


Figure 2b. Dynamic Poisson's ratio as a function of wave incidence angle ( $0^\circ$  indicates propagation parallel to the face cleats).

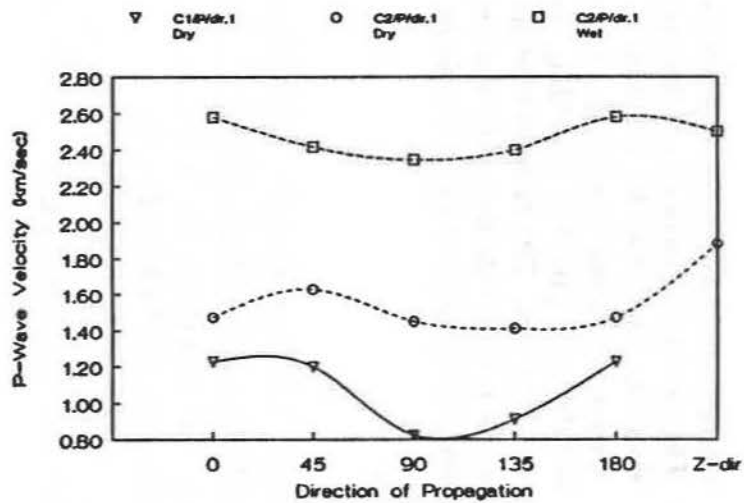


Figure 3a. P-wave velocity as a function of incidence angle.

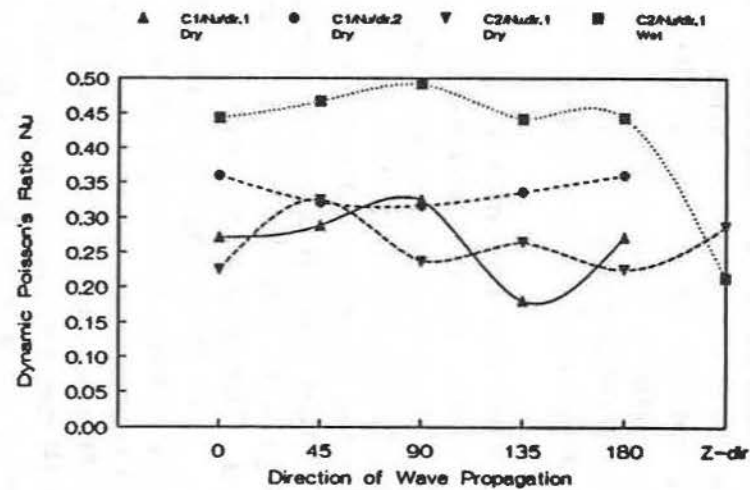


Figure 3b. S-wave velocity as a function of incidence angle.

Under nominal saturation conditions, the average P-wave velocity increased significantly. Shear wave velocities in the dry environment showed sample to sample variability and some modest directional dependence. However, as can be seen for Sample 2, saturation dramatically reduced the S-wave velocity from a value of 825 meter/sec when it is propagating parallel to the face cleats, to a value of 325 meter/sec when it is propagating perpendicular to the face cleats. With such variations, elastic calculations yielded increased values for Young's modulus and depressed values for Poisson's ratio.

Directional and saturation propagation dependence is commonly detected in reservoir materials. Coal is an extreme example because of its propensity for cleat development. The real interest, beyond immediate advantages of directional engineering data for these coals, is speculation on the mechanisms causing the directional and saturation dependent variation. It is hypothesized that the substantial reduction in S-wave velocity stems from viscous resistance of the water in the cleat systems. When a shear wave travels through a dry cleat/microfracture, transmission is afforded through solid to solid contact areas. This solid-solid contact enables particle motion, the mechanism of wave propagation, to be transmitted from one cleat surface to the adjoining face. Under conditions of saturation, a thin layer of fluid between the two cleat faces inhibits intimate solid-to-solid contact. Consequently, shear wave transmission must rely on viscous forces rather than intimate contact. This is particularly true when the normal effective stress is small. Triaxial compression testing<sup>1</sup> has validated that even a very modest increase in the effective normal stress (a few hundred psi) will dramatically alter the shear wave velocity by decreasing cleat aperture with attendant changes in the thickness of the liquid interface. Large reductions in shear wave velocity have also been observed in a simulated single, smooth laboratory joint<sup>3</sup>.

In summary, the anisotropic characteristics of coal can be defined by ultrasonic procedures. The noted precautions are that anisotropy may be most reliably determinable from wave velocities and may be masked by further processing to calculate dynamic properties. Under saturated conditions, S-wave velocity reduction at low stress levels should be anticipated, possibly providing conceptual methodology for inference of directional stress contrast. The reduction in shear wave velocity is hypothesized to be due to the presence of a fluid interface. Under saturated conditions, the validity of predicted dynamic mechanical properties using simplistic elastic relations is in question.

## REFERENCE

1. Zheng, Z., Khodaverdian, M. and McLennan, J. D., "Static and dynamic testing of coal samples", *Proceedings, SCA 1991 Conference*, San Antonio, Texas, August, 1991.
2. Jaeger, J. C. and Cook, N. G. W., *Fundamentals of Rock Mechanics*, Chapman and Hall, London, 1979 (3rd edition).
3. Suarez, F. R., Pyrak-Nolte, L., Cook, N. G. W. and Myer, L., "Transmission of S-wave across a thin fluid layer", *EOS, AGU Trans.* Vol. 69, No. 44, November, 1988.

## **ACKNOWLEDGEMENTS**

The authors gratefully acknowledge the Gas Research Institute, GRI, for their contribution in financially supporting this research effort. Particular thanks is extended to Dr. R. Schraufnagel of GRI.

# **ELASTIC PROPERTY SCALING RELATIONSHIPS: CORE MEASUREMENTS RESULTS AND ACOUSTIC LOGGING EXPERIMENTS**

by

**D. R. Burns, X. M. Tang, and R. J. Martin, III**

**New England Research, Inc.  
76 Olcott Drive  
White River Junction, VT 05001**

## **INTRODUCTION**

In order to maximize production and reserve growth in existing oil and gas fields, an accurate description of the geometry and connectivity of reservoir flow units is needed throughout the field. Heterogeneity in flow units between wells may result in untapped or under-produced reserves. In either case in-fill drilling and field extension can be optimized by having a knowledge of the distribution of flow units in three dimensions. Seismic data, because of its capacity to image the interwell area, is ideally suited to providing more information about the flow unit heterogeneity away from wells. There has been much research devoted to the utilization of seismic data to provide high resolution images of stratigraphic variations (e. g., Payton, 1977; Doyen et al., 1989), to provide information about the nature and distribution of pore fluids (e.g., Ostrander, 1984), and to monitor the production and injection of fluids in reservoir units (Graves and Fulp, 1987; Pullin et al., 1987). Another recent application of seismic data has been to transform seismic travel times to porosity in order to build a detailed 'flow' model of the reservoir (Doyen, 1988; deBuyl et al., 1986). For any of these approaches to be consistent, however, a number of problems need to be overcome. First, the scaling problem must be addressed. The basic premise is that variations in velocity are related to variations in porosity. This basic assumption can be complicated by variations in clay content, pore fluids, and pore pressure. In addition to these complications, however, a major question that remains is the relationship between velocity measurements taken on core samples (volume = 0.001 - 0.05 cubic feet) using a frequency range of 100's of kHz, velocities measured by logging tools (volume = 1 - 10 cubic feet) at 10's of kHz, and seismic measurements (volume = 10,000 - 1,000,000 cubic feet) using frequencies of 50 - 200 Hz. Each of these measurements will be affected by the heterogeneity of the sample, the frequency of the seismic signal used to measure the velocity, and any unique local effects, such as strain relaxation of the core or mud filtrate invasion adjacent to the borehole. How are these different measurements related? In order to quantify seismic measurements we must understand these elastic scaling relationships.

Scaling relationships have been a topic of interest in geophysical (e.g., Stewart et al., 1984; Byun et al., 1988) as well as production engineering (Haldorsen, 1986) research. The relationship between core and well log velocity measurements is a topic which has been discussed in many reservoir studies, but there are many instances of misties, with sampling, borehole conditions, and experimental error being blamed in most cases. The misties between logs and VSP data have also received much attention (Stewart et al., 1984, Stewart, 1989). In these cases dispersion, interbed multiples, and near surface effects are

identified as the most probable causes (Stewart et al., 1984). Finally, the mistie in velocity (or travel time) between synthetic seismograms (generated from well logs) and surface seismic data has also been addressed (O'Doherty and Anstey, 1971; Shoenberger and Levin, 1974, 1978a,b). In all of these cases, calibrations and adjustments are used to get agreement between the different data sets for the purpose of interpretation. Each set of data contain useful information within the context of the scale and frequency range employed. The relationships between different measurements contain information on the heterogeneity scales, the wavelength sampling (equivalent medium properties), mechanisms of attenuation, and local environmental effects.

## **BACKGROUND**

The relationships between velocity and attenuation measurements obtained at different scales are functions of three major factors: 1) physical mechanisms which affect wave propagation, 2) sampling and heterogeneity, and 3) 'environmental' factors related to the sample or measurement technique. Numerous models of mechanisms affecting wave propagation in rock samples have been formulated and presented in the literature (Gassman, 1951; Biot, 1956a,b; White, 1975; O'Connell and Budiansky, 1974; Kuster and Toksoz, 1974; Mavko and Nur, 1979). Measurements at different scales, frequencies, and strain amplitudes can be dominated by different mechanisms. For example, differences between static and dynamic moduli have been postulated to be due to differences in the strain amplitude of the measurements. Also, the effects of fluid motion on velocity and attenuation may play a role in high frequency core measurements, but are generally negligible at seismic frequencies.

The effect of sampling and heterogeneity is most likely the major factor in the relation between sonic or elastic properties at different scales. The key parameter in this factor is the range of heterogeneity scales relative to the wavelength of the measurement. Even in core samples, the amount of heterogeneity can be large. Likewise, field in-situ measurements, from log, crosswell seismic, VSP, or surface seismic data, are affected by the heterogeneity in the sampled volume of earth. At low frequencies (relative to the heterogeneity scales) the sampled volume behaves as a homogeneous medium with some 'average' properties (White, 1983, p.49-56), while at higher frequencies scattering and internal reflections will alter the measured velocity and apparent attenuation (O'Doherty and Anstey, 1971). The distribution of heterogeneities in space within the reservoir controls production and ultimate reserves, and different sonic measurements will sample different portions and scales of that distribution. Relating these measurements and integrating them will maximize our knowledge of the reservoir heterogeneity distribution.

Finally, every measurement is affected to varying degrees by the sampling or measurement process itself. When core is extracted from its in-situ conditions it undergoes changes due to the release of pressure. This strain relaxation process can alter the properties of the sample. Fluids from the drilling process or introduced in the lab could also alter the properties of core relative to the in-situ conditions. Logging data can be affected by mud filtrate invasion or drilling related damage of the near-borehole portions of the formation. Downhole and surface seismic measurements can be affected by the coupling of the source or receiver, and near surface geologic variations can affect surface seismic measurements. Lastly, all measurements can be affected by the instrumentation responses. Most of these environmental factors can be controlled or at least corrected for, but they are factors which must be considered in any comparison between different sets of measurements.

## RESULTS

During the past year, we have focussed on the laboratory measurement of velocity and attenuation over a range of frequencies and sample sizes. The techniques employed include ultrasonic pulse propagation (300kHz - 1MHz), resonant bar (10 - 200kHz), stress-strain hysteresis loops (0.1 - 50Hz), and a low frequency pulse propagation technique (10 - 200kHz) (Tang, 1991). These techniques permit measurements of velocity and attenuation to be made in lab sized samples over a wide frequency range. Examples of such measurements using Sierra White Granite as a calibration material are shown in Figure 1. These results indicate that at laboratory scales the attenuation of compressional waves is roughly equivalent for the frequency range of 0.1Hz - 100 kHz, but is much higher for the ultrasonic frequency range (300 - 800kHz). Furthermore, the ultrasonic values are much closer to field value magnitudes estimated from seismic data. These results are in agreement with Lucet and Zinszner (1988), Blair (1990) and Lucet et al. (1991). It could be, as suggested by Blair (1990), that scattering may be an important mechanism for both the ultrasonic and field seismic measurement scales. This mechanism is supported by finite difference modeling of ultrasonic wave propagation in a core sample. Using a 2-D staggered grid elastic finite difference model, a point source was propagated through a core model with random elastic constant heterogeneities. The numerical model contained no attenuation, so any changes in pulse shape and amplitude are due only to spreading losses and scattering from the heterogeneities. Figure 2 shows a diagram of the heterogeneity distribution of the model. The background compressional (P) wave velocity was 4000m/s, while the shear (S) wave velocity was 2000 m/s. The heterogeneity distribution, constructed using a gaussian correlation function with a correlation length of 0.7 cm and having an elastic constant standard deviation of 20%, is very similar to the core x-ray tomography images measured by Lucet and Zinszner (1988) and similar in size to the 'grain clusters' discussed by Blair (1990). Figure 3 shows the propagating pulse output at two points at a distance of 1 and 3 cm from the source point (the pulse frequency is approximately 700kHz). The estimated  $Q_p$  value is 40 due only to the scattering off elastic constant perturbations. If the sample also has intrinsic attenuation, the total measured  $Q_p$  value would be lower than this value.

During the coming year we will undertake a series of controlled laboratory and field experiments, with support from BP Exploration and the Gas Research Institute, to acquire a data set which can be used to develop elastic property scaling relationships in one dimension. Core measurements similar to those described above, together with in-situ acoustic logging measurements also taken over a range of frequency and sample volume, will form the basis of this effort.

## CONCLUSIONS

The quantification of seismic data in terms of rock properties and, eventually, flow unit distributions within reservoirs, is predicated on the calibration of such data using core and well log measurements. Such calibrations assume that measurements made at different scales and frequencies are somehow related. The specific form of these elastic scaling relationships are needed in order to perform these calibrations and optimize our use of seismic data sets. Laboratory core measurement results indicate that scattering may be an important attenuation mechanism in both ultrasonic core measurements and field seismic data. Future field work will be undertaken to relate log and core acoustic data over a wide frequency range in order to quantify scaling relationships.

## REFERENCES

- Biot, M. A., 1956a, Theory of propagation of elastic waves in a fluid saturated porous rock: I low frequency range, *J. Acoust. Soc. Am.*, v. 28, p. 168-178.
- Biot, M. A., 1956b, Theory of propagation of elastic waves in a fluid saturated porous rock: II low frequency range, *J. Acoust. Soc. Am.*, v. 28, p. 179-191.
- Blair, D., 1990, A direct comparison between vibrational resonance and pulse transmission data for assessment of seismic attenuation in rock, *Geophysics*, v.55, p. 51-60.
- Byun, B. S., Tran, H. V., and Carter, M.D., 1988, An analysis of statistical average velocities in a horizontally layered earth, *Geophysics*, v. 53, p. 1488-1489.
- de Buyl, M. H., Guidish, T. M., and Bell, F., 1986, Reservoir description from seismic lithologic parameter estimation, *J. Petr. Tech.*, 40, p. 475-482.
- Doyen, P.M., 1988, Porosity from seismic data: a geostatistical approach, *Geophysics*, v. 53, p. 1263-1275.
- Gassman, F., 1951, Elastic waves through a packing of spheres, *Geophysics*, v. 16, p. 673-685.
- Graves, R. J. and Fulp, T. J., 1987, Three dimensional seismic monitoring of an enhanced oil recovery process, *Geophysics*, v. 52, p. 1175-1187.
- Haldorsen, H.H., 1986, Simulator parameter assignment and the problem of scale in reservoir engineering, in *Reservoir Characterization*, L. W. Lake and H. B. Carroll, Jr., eds., Academic Press, Inc., Boston, p. 293-340.
- Kuster, G.T. and Toksoz, M. N., 1974, Velocity and attenuation of seismic waves in two phase media, part I, theoretical formulation, *Geophysics*, v. 39, p. 587-606.
- Lucet, N. M. and Zinszner, B. E., 1988, Comparing sonic and ultrasonic attenuation in rocks: the importance of density heterogeneities, *SEG 58th Ann. Mtg. Exp. Abstracts*.
- Lucet, N. M., Rasolotsoaon, P. N. J., and Zinszner, B. E., 1990, Velocity dispersion in rocks under confining pressure: from ultrasonic to sonic frequency band, *SEG 60th Ann. Mtg. expanded abstracts*, p. 823-826.
- Mavco, G. M. and Nur, A., 1979, Wave attenuation in partially saturated rocks, *Geophysics*, v. 44, p. 161-178.
- O'Connell, R. J. and Budiansky, B., 1974, Seismic velocities in dry and saturated cracked solids, *J. Geophys. Res.*, v. 79, p. 5412-5426.
- O'Doherty, R. F. and Anstey, N. A., 1971, Reflections on amplitudes, *Geophys. Prospecting*, v. 19, p. 430-458.
- Ostrander, W. J., 1984, Plane wave reflection coefficients for gas sands at non-normal angles of incidence, *Geophysics*, v. 49, p. 1637-1648.
- Payton, C. E., ed, 1977, *Seismic stratigraphy - applications to hydrocarbon exploration*, AAPG Memoir 26.

Pullin, N., Matthews, L., and Hirsche, K., 1987, Techniques applied to obtain very high resolution 3-D seismic imaging at an Athabasca tar sands thermal pilot, *Leading Edge*, v. 6, p. 10-15.

Schoenberger, M. and Levin, F.K., 1974, Apparent attenuation due to intrabed multiples, *Geophysics*, v. 39, p. 278 - 291.

Schoenberger, M. and Levin, F.K., 1978a, Apparent attenuation due to intrabed multiples, II, *Geophysics*, v. 43, p. 730-737.

Schoenberger, M. and Levin, F. K., 1978b, The effects of subsurface sampling on one-dimensional synthetic seismograms, *Geophysics*, v. 44, p. 1813-1829.

Stewart, R. R., 1989, Integrated seismic analysis: Kidney Area, northern Alberta, Canada, *Geophysics*, v. 54, p. 1240-1248.

Stewart, R. R., Huddleston, P.D., and Kan, T. K., 1984, Seismic versus sonic velocities: a vertical seismic profiling study, *Geophysics*, v. 49, p. 1153-1168.

Tang, X. M., 1991, A waveform inversion technique for measuring elastic attenuation in cylindrical bars, submitted to *geophysics*.

White, J. E., 1975, Computed seismic speed and attenuation in rocks with partial gas saturation, *Geophysics*, v. 40, p. 224-232.

White, J. E., 1983, *Underground sound*, Elsevier, NY.

## COMPARISON OF ATTENUATION VALUES OF SIERRA WHITE GRANITE OBTAINED USING DIFFERENT METHODS

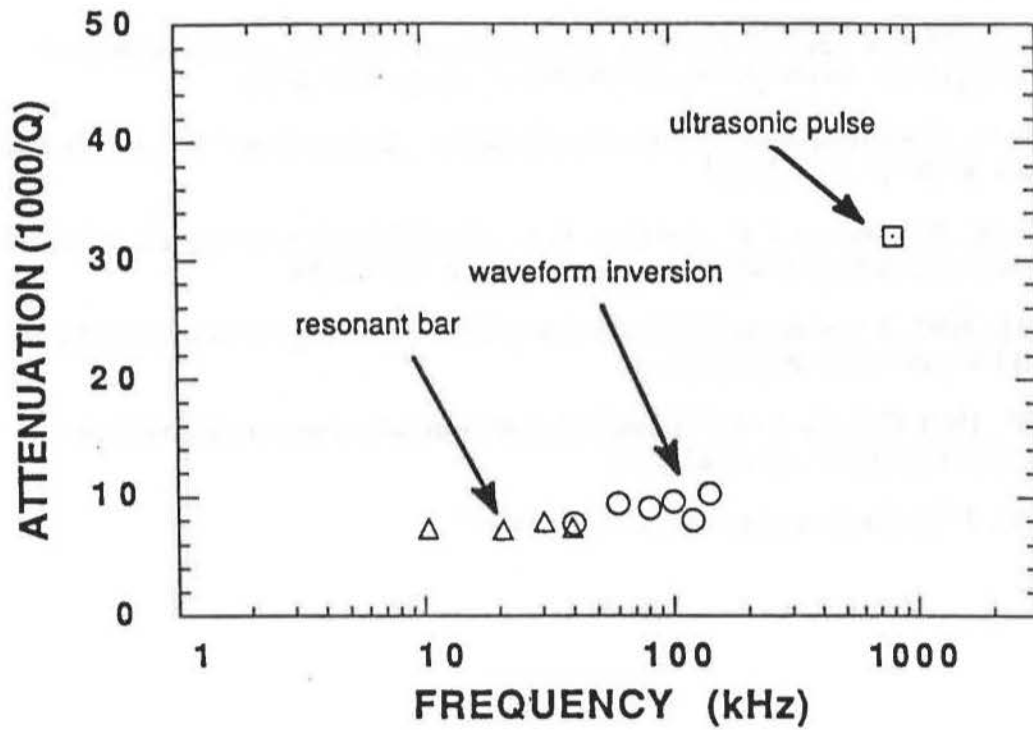
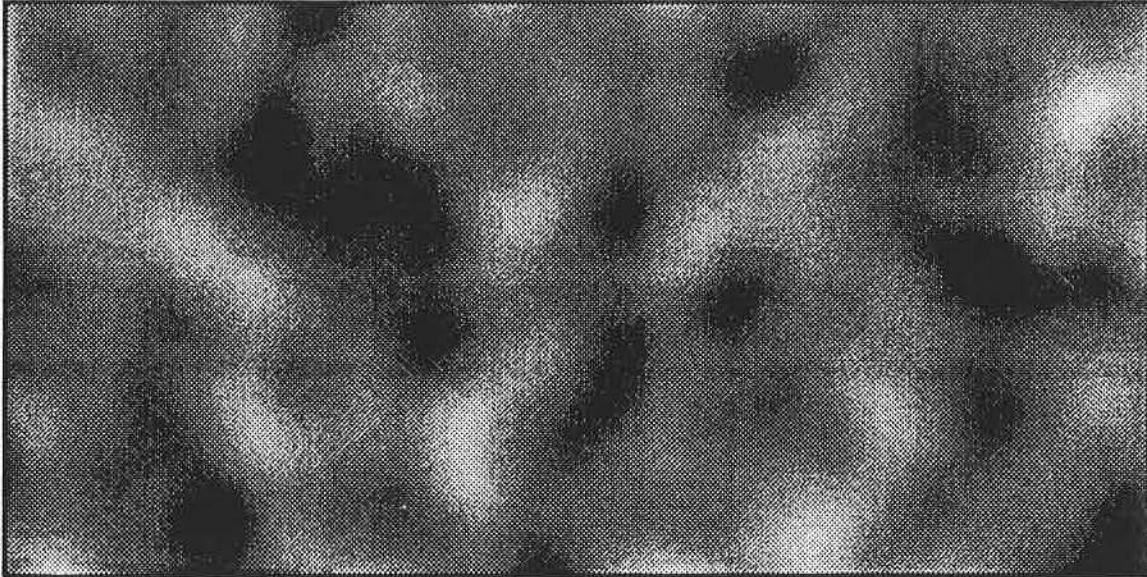
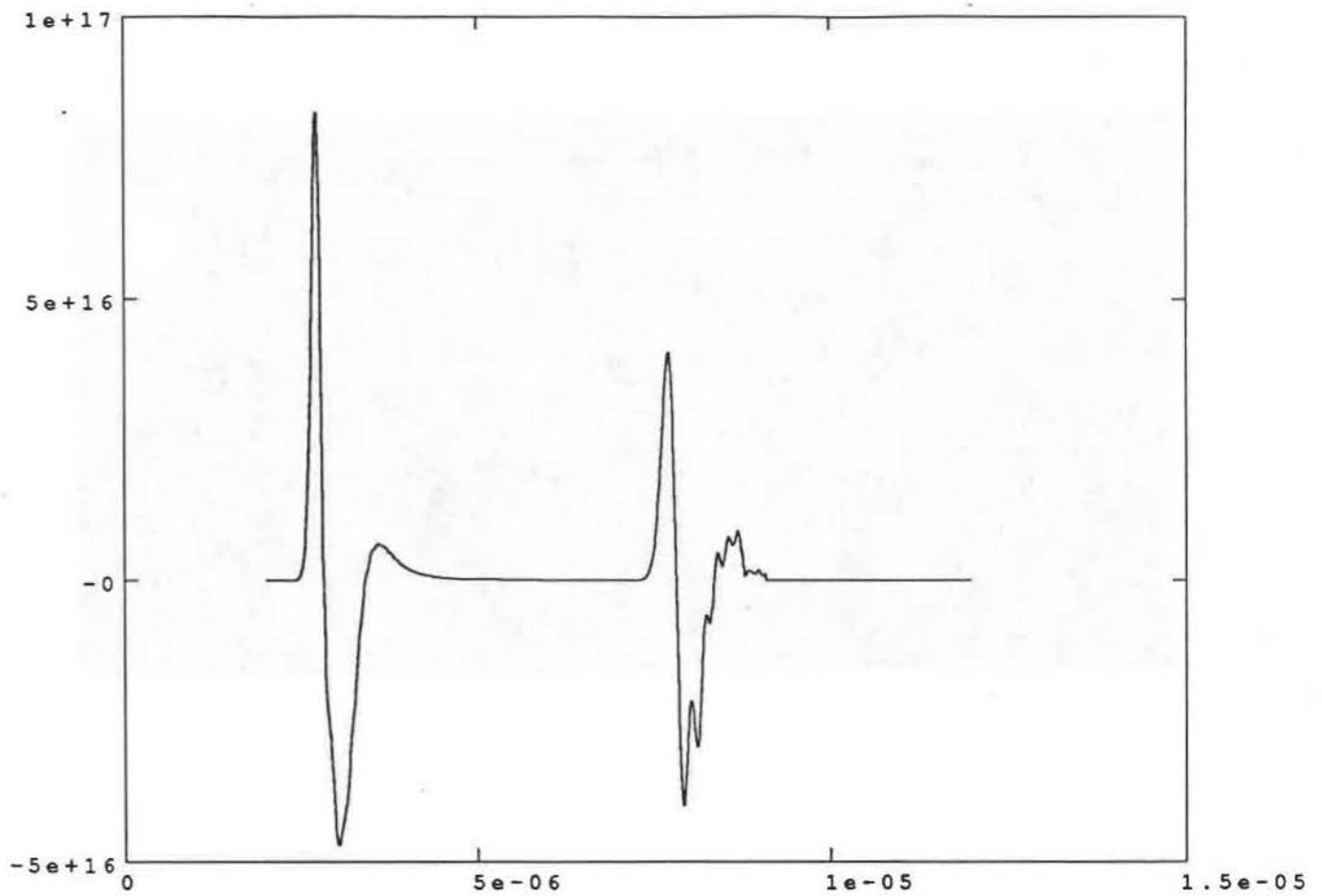


Figure 1: Attenuation ( $1000/Q_e$ ) of dry Sierra White Granite as a function of frequency computed from ultrasonic pulse propagation (spectral ratio), waveform inversion, and resonant bar measurements.



**Figure 2:** Plot of the random elastic constant heterogeneity distribution used in the finite difference wave propagation model. The distribution was constructed using a gaussian correlation function with a correlation length of 0.7 cm. The background P wave velocity is 4000 m/s and the S wave velocity is 2000 m/s. The elastic constant standard deviation is 20%. The model size is 2 cm x 4 cm.



**Figure 3:** Plot of the computed waveforms from the heterogeneous core model of Figure 2. The propagation distances are 1 and 3 cm respectively.

# BOREHOLE STONELEY WAVE PROPAGATION ACROSS PERMEABLE FRACTURES

X.M. Tang, New England Research, Inc.  
C.H. Cheng, M.I.T.

## SUMMARY

This study investigates the propagation of borehole Stoneley waves across heterogeneous and permeable structures. By modeling the structure as a zone intersecting the borehole, a simple one-dimensional theory is formulated to treat the interaction of the Stoneley wave with the structure. This is possible because the Stoneley wave is a guided wave, with no geometric spreading as it propagates along the borehole. The interaction occurs because the zone and the surrounding formation possess different Stoneley wavenumbers. Given appropriate representations of the wavenumber, the theory can be applied to treat a variety of structures. The application to the fluid-filled planar fracture shows that the present theory is fully consistent with the existing theory and accounts for the effect of vertical extent of an inclined fracture. Of special interest are the cases of permeable porous zone and fracture zones. The results show that, while Stoneley reflection is generated, strong Stoneley wave attenuation is produced across a very permeable zone. This result is particularly important in explaining the observed strong Stoneley attenuation at major fractures, while it has been a difficulty to explain the attenuation in terms of the planar fracture theory. In addition, by using a simple and sufficiently accurate theory to model the effects of the permeable zone, a fast and efficient method is developed to characterize the fluid transport properties of a permeable fracture zone.

Several field cases are also modeled and the theoretical results are compared with the field data. It is shown that low- and medium-frequency Stoneley waves (1 kHz data from Moodus, Connecticut, and 5 kHz data from Manitoba, Canada) are very sensitive to the permeability of the fractures and can be used to assess permeability from in-situ logging data, if the fracture porosity and zone thickness can be measured. At high frequencies, however, Stoneley waves are not very sensitive to permeability but are mainly affected by the sum of the fracture openings expressed as the product of fracture zone thickness and porosity in the fracture zone. This finding is demonstrated by a logging data set (Manitoba, Canada) obtained using high-frequency Stoneley waves at 34 kHz.

## INTRODUCTION

Fractures or permeable structures in reservoirs are of great importance in the exploration and production of hydrocarbons. Heterogeneous layers in the formation are of major significance. A very good example of such heterogeneous and permeable structures are the sand-shale sequence found in sedimentary formations. Full waveform acoustic logging offers an effective tool for characterizing these structures. The current technique for modeling borehole acoustic wave propagation is finite difference method. This technique can handle heterogeneity quite easily. However, the implementation of the method to a permeable porous formation is still a topic of research. Although wavenumber integration technique can be used to calculate wave propagation in homogeneous porous formations (Rosenbaum, 1974) it is very difficult, if not impossible, to apply such a technique to treat problems involving porous layer structures. In this study, we will show that if only the low-frequency Stoneley wave is used, the interaction of

acoustic waves with borehole permeable structures can be much simplified. The objective of this study is to develop a theoretical model that can be used to calculate borehole Stoneley wave propagation across heterogeneous and permeable structures. As a result, the properties of such structures can be characterized by means of Stoneley wave measurements.

The Stoneley (or tube) wave has been used as a means of formation evaluation and fracture detection. This wave mode dominates the low-frequency portion of the full waveform acoustic log due to its relatively slow velocity and large amplitude. Because this wave is an interface wave borne in borehole fluid, the Stoneley is sensitive to such formation properties as density, moduli, and most importantly, permeability or fluid transmissivity. It is expected that any change of these properties due to a formation heterogeneity will result in the change of Stoneley propagation characteristics, allowing the heterogeneity to be characterized using Stoneley wave measurements. Borehole fractures are an example of such heterogeneity. Paillet and White (1982) observed that attenuation of Stoneley wave occurs in the vicinity of permeable fractures. Hornby et al. (1989) showed that permeable fractures also give rise to reflected Stoneley waves. In all these models, the analogy of parallel planar fluid layer was commonly adopted to represent the fracture. Laboratory model experiments that comply with this analogy have yielded results that agree with the theoretical results (Tang and Cheng, 1988; Hornby et al., 1989). Although both attenuation and reflection of Stoneley wave are predicted by the plane-fracture model, it takes a rather large fracture aperture (on the order of centimeter) to attenuate the Stoneley wave significantly. However, fractures with such apertures are rarely found in the field (Hornby et al., 1989), but Stoneley wave attenuation (up to 50% or more) across *in situ* fractures is commonly observed (Paillet, 1980; Hardin et al., 1987). Until now, there has not been an effective model to account for the significant Stoneley wave attenuation observed in the field. Paillet et al. (1989) suggested that *in situ* fractures may consist of an array of flow passages or fracture layers, instead of a single fluid layer. In this study, we substantiate this hypothesis by modeling fractures as a permeable zone in the formation. Key parameters that are used to characterize the permeable zone are thickness of the zone, permeability, fracture porosity, and tortuosity. Since the last three parameters are typical parameters of a porous medium, we can use the Biot-Rosenbaum theory (Rosenbaum, 1974) to model the Stoneley wave characteristics in the permeable zone. Tang et al. (1990) have recently developed a simple model for Stoneley propagation in permeable formations. This model yields consistent results as the analysis of Biot-Rosenbaum theory in the presence of a hard formation, but the formulation and calculation are much simplified. The use of this simple theory in modeling the permeable zone will allow the development of a fast and efficient algorithm to characterize the effects of the zone on Stoneley waves. In the following, we develop a theory for the Stoneley wave interaction with a borehole structure.

## THEORY

In this section we describe a theory for calculating Stoneley wave propagation across heterogeneous and permeable borehole structures. The structure is modeled as a zone sandwiched between two

formations of different properties. The theory is able to handle a variety of structures including a fluid-filled plane fracture (horizontal or inclined), an elastic layer, a permeable porous zone, and a permeable fracture zone. In this study, we concentrate on the problem of a permeable fracture zone. We briefly outline the major steps concerning the calculation of a permeable fracture zone. This zone is modeled as thin layer of porous materials which can have very high porosity and permeability. Figure 1 illustrates the configuration of the borehole, a logging tool (modeled as rigid), the permeable zone, and the surrounding formations. As the Stoneley wave encounters the permeable zone, interaction between borehole fluid and permeable fracture zone occurs because of dynamic fluid conduction into the permeable zone. This interaction is governed by the wave propagation characteristics in the zone as well as in the formation. Therefore, the interaction is characterized by two wavenumbers  $k_1$  and  $k_2$ , where  $k_1$  is the Stoneley wavenumber in the surrounding formation (i.e., the incident Stoneley wavenumber) that can be calculated using the borehole period equation. The Stoneley wavenumber in the permeable zone  $k_2$  can be calculated using Biot-Rosenbaum model (Rosenbaum, 1974; Cheng et al., 1987). However, this model is somewhat complicated. By applying the concept of dynamic permeability of Johnson et al. (1987) to acoustic logging in a porous formation, Tang et al. (1990) showed that the complicated Biot-Rosenbaum model can be much simplified to give an explicit expression for the Stoneley wavenumber. The dynamic permeability captures the frequency-dependence of fluid flow in porous media and makes the simplified theory consistent with the exact theory of Biot-Rosenbaum model (Rosenbaum, 1974, Cheng et al., 1987) even at high frequencies (Tang et al., 1990). The transmission and reflection coefficients at the permeable zone are given by

$$TC = \frac{4k_1 k_2 e^{-ik_2 L}}{(k_1 + k_2)^2 e^{-ik_2 L} - (k_1 - k_2)^2 e^{ik_2 L}}, \quad (1)$$

$$RC = \frac{2i(k_2^2 - k_1^2) \sin(k_2 L)}{(k_1 + k_2)^2 e^{-ik_2 L} - (k_1 - k_2)^2 e^{ik_2 L}}, \quad (2)$$

where  $L$  is the thickness of the permeable zone. In addition to the transmission and reflection coefficients, one can also obtain solutions for Stoneley wave motion in the permeable zone. As a result, synthetic seismograms can be computed for any source-receiver locations, which can be used to simulate the Stoneley wave log across the permeable zone.

## APPLICATION

We apply the permeable zone theory to the modeling of Stoneley (tube) wave log across a fracture zone in the Moodus #1 well drilled in east-central Connecticut. The well was drilled into crystalline rocks. A major water-producing zone at depth of about 610 ft was identified. The various log data in the vicinity of the zone have been published in the 1989 SPWLA symposium (Hornby et al., 1990) and are re-presented in Figure 2. Of special interest is the Stoneley wave log in Figure 2a. This log was recorded using a research prototype sonic tool which excites a Stoneley wave with centerband energy around 1 kHz (Hornby et al., 1990). As seen from Figure 2a, Stoneley wave reflections are clearly generated at the fracture zone. The reflection coefficient of about 0.1 was estimated (Figure 2a). In the section across the zone (at the origins of the up- and down-going reflected waves) the transmitted waves show weaker amplitudes compared with the waves outside the section. In other words, Stoneley waves are attenuated across the zone. The borehole televiewer in Figure 2b shows that the thickness of the zone is about 5 ft. The fracture image obtained

using formation microscanner indicates that the zone consists a large number of micro-fractures and the average fracture porosity is on the order of 10%. Although fracture porosity determined by an electrical tool is usually very variable, this porosity value can still be used as an order-of-magnitude estimate for the fracture zone. This data set presents a very good example for our theoretical modeling. It also provides most of the parameters needed for the modeling. The borehole radius is given in Figure 2a as  $R = 8.5$  cm. We assume that the tool radius is  $a = 0.4$  cm. Since the well is in crystalline rocks, we assume that the density, compressional and shear velocities are  $\rho = 2.7$  kg/m<sup>3</sup>,  $V_p = 6$  km/s, and  $V_s = 3$  km/s. The same parameters are also used for the rock matrix of the fracture zone. For the fracture zone, we use a porosity of  $\phi = 10\%$  (Figure 2b) and the tortuosity  $\alpha$  in Eq. (2) is assumed to be 1. The zone and the borehole are filled with water whose density, acoustic velocity, and viscosity are  $\rho_0 = 1$  kg/m<sup>3</sup>,  $V_f = 1.5$  km/s,  $\mu = 1$  cp. The zone thickness  $L$  in Eq. (2) is 1.52 m ( $\approx 5$  ft). The only uncertain parameter in the modeling is the permeability  $\kappa_0$  in Eq. (3). Fortunately, we have the measured Stoneley wave reflectivity (Figure 2a). A permeability of about 4 Darcies was estimated by matching the theoretical reflection coefficient with the measured value.

If the plane fracture theory is used to model the reflection data, the fracture aperture would be 5.6 mm (Hornby et al., 1990), which gives a reflectivity of 0.1 around 1 kHz. This aperture was obtained with a fluid-filled borehole. If a rigid tool of 4 cm radius in the borehole is accounted for, the aperture value reduces slightly to 4.5 mm, which gives the same reflectivity of 0.1 around 1 kHz. It is convenient here to compare the full results from the present theory and the plane fracture theory. To do this, we have computed synthetic Stoneley wave logs across the fracture zone using to the two theories. The seismograms are calculated using a Kelly source with a center frequency of 1 kHz. The source-receiver spacing is 3.06 m (Hornby et al., 1990). Figures 3 and 4 show the results. The seismograms in Figure 4 are computed using the permeable zone theory, while those in Figure 5 are using the plane fracture of 4.5 mm. The two separate figures show the same features for the up- and down-going reflected waves, the amplitudes of these waves being almost equal. However, the waves transmitted across the fracture zone, as indicated by arrow(s) in the figures, are quite different. The permeable zone theory predicts significant attenuation for the transmitted waves, which is supported by the Stoneley wave data across the fracture zone (Figure 2a) Whereas the plane fracture theory shows very slight attenuation.

We also applied the theory to two additional logging data sets (one is 5 kHz and the other is 34 kHz) from Manitoba, Canada. For the 5 kHz data, the theory was found to fit both the transmitted and reflected Stoneley waves fairly well. For the 34 kHz data, it was demonstrated that Stoneley attenuation is not sensitive to permeability, but is primarily controlled by the sum of fracture thicknesses across the fracture zone.

## CONCLUSIONS

In this study, we have tested the new theoretical model for Stoneley wave propagation across permeable fractures by comparing it with field data. Application to the low-frequency data from Moodus #1 well shows that the theory is very sensitive to permeability at low frequencies and can be used to assess fracture permeability from the measurement data. The medium-frequency data from URL-M11 well showed that with reasonable choice of fracture permeability and porosity, the Stoneley wave characteristics in the vicinity of a fracture zone can be satisfactorily modeled.

The case of high-frequency data from Manitoba data set indicates that at very high frequencies, the model is controlled by the parameter  $L\phi$ , or the total fluid volume across the fracture zone. These examples demonstrate that the permeable zone model can be used as an effective method for fracture detection and characterization.

### ACKNOWLEDGEMENTS

We thank Brian Hornby for permitting us to use a figure from his original paper. This research was supported by New England Research, Inc. and by the Full Waveform Acoustic Logging Consortium at MIT and by Department of Energy grant No. DE-FG02-86ER13636.

### REFERENCES

- Cheng, C. H., J. Z. Zhang, and D. R. Burns, 1987, Effects of in-situ permeability on the propagation of Stoneley (tube) waves in a borehole, *Geophysics*, 52, 1297-1289.
- Hardin, E.L., C. H. Cheng, F. L. Paillet, and J. D. Mendelson, 1987, Fracture characterization by means of attenuation and generation of tube waves in fractured crystalline rock at Mirror Lake, New Hampshire, *J. Geophys. Res.*, 92, 7989-8006.
- Hornby, B. E., D. L. Johnson, K. H. Winkler, and R. A. Plumb, 1989, Fracture evaluation using reflected Stoneley-wave arrivals, *Geophysics*, 54, 1274-1288.
- Hornby, B. E., S. M. Luthi, and R. A. Plumb, 1990, Comparison of fracture apertures computed from electrical borehole scans and reflected Stoneley waves: an integrated interpretation, *Trans., Soc. Prof. Well Log Analysts, 31th Ann. Symp.*, Paper L.
- Johnson, D. L., J. Koplik, and R. Dashen, 1987, Theory of dynamic permeability and tortuosity in fluid-saturated porous media, *J. Fluid Mech.*, 176, 379-400.
- Paillet, F. L., 1980, Acoustic propagation in the vicinity of fractures which intersect a fluid-filled borehole, *Trans., Soc. Prof. Well Log Analysts, 21th Ann. Symp.*, Paper DD.
- Paillet, F. L., C. H. Cheng, and X. M. Tang, 1989, Theoretical models relating acoustic tube-wave attenuation to fracture permeability - reconciling model results with field data, *Trans., Soc. Prof. Well Log Analysts, 30th Ann. Symp.*, Paper FF.
- Rosenbaum, J. H., 1974, Synthetic microseismograms: logging in porous formations, *Geophysics*, 39, 14-32.
- Tang, X. M., and C. H. Cheng, 1988, A dynamic model for fluid flow in open borehole fractures, *Geophysics*, 39, 14-32.
- Tang, X. M., C. H. Cheng, and M. N. Toksöz, 1990, Dynamic permeability and borehole Stoneley waves: A simplified Biot-Rosenbaum model, submitted to *J. Acoust. Soc. Am.*

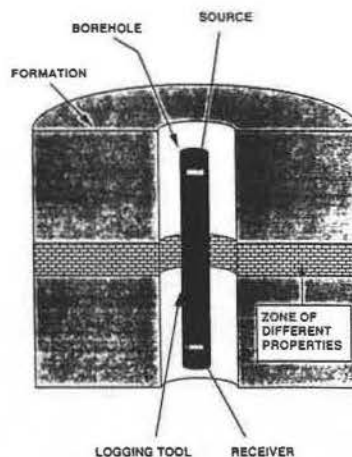


Figure 1: Acoustic Logging across a fracture zone

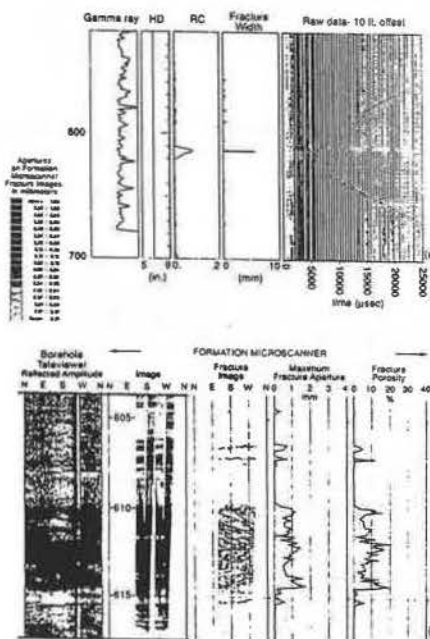


Figure 2: Logs for Moodus #1 well (from Hornby et al. 1990)

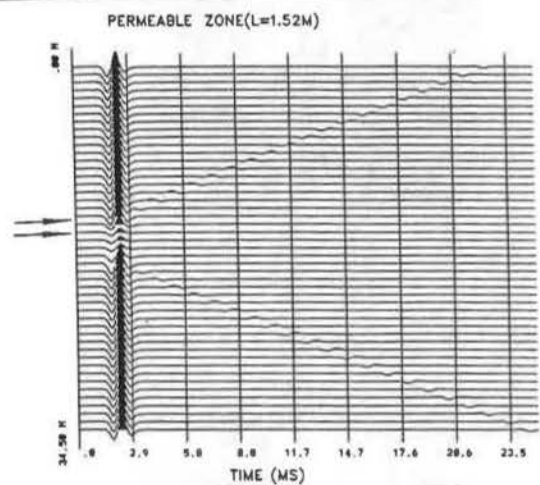


Figure 3: Synthetic Stoneley waveform log across the Moodus #1 well fracture zone from the permeable zone theory.

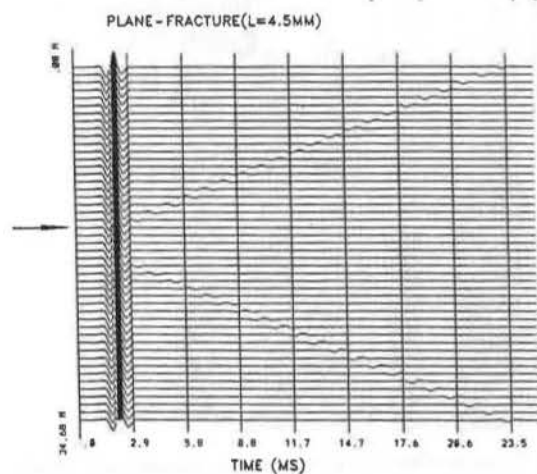


Figure 4: Synthetic Stoneley waveform log across the Moodus #1 well fracture zone from the plane fracture zone theory.

# SCALE OF ANISOTROPY: A THEORETICAL STUDY OF VELOCITY ANISOTROPY FOR MICRO AND MACRO FRACTURES

Batakrishna Mandal and M. Nafi Toksoz, M.I.T.

## SUMMARY

Theoretical calculations are made to compare the anisotropic velocity variations for rock masses having micro and macro fractures. We use two different hypotheses for computing elastic moduli. They are, (a) micro fracture models where fracture dimensions are very small compared to the wavelength (e.g. Hudson, 1980, 1981), and (b) rock mass with large fractures where the stresses are continuous across the fracture but displacements are discontinuous (e.g. Schoenberg, 1980, 1983; Pyrak-Nolte *et al.*, 1990). Both cases show anisotropic velocity variation but they differ in nature. A good example is the qSP wave (polarized (P)arallel to the symmetry axis) propagating parallel to the fractures. *Case a* predicts that both qSP and qSR (wave polarized (R)ight angle to the symmetry axis) have the same velocity for incidence perpendicular to the fractures and qSP wave velocity is same for both perpendicular and parallel to the fractures. On the other hand, model for *Case b* predicts that the qSP wave velocity parallel to the fracture is equal to the velocity of unfractured rock mass. This also holds for P and qSR waves. To compare the anisotropic velocities of the three body waves (qP, qSP and qSR) for the two models we calculate different examples. For *Case a*, we evaluate the dependence on the fracture density ( $CD = N a^3/V$ ) and the aspect ratio ( $AR = d/a$ , where  $N$  is the number of fractures of radius  $a$  and thickness  $d$  in volume  $V$ ). For *Case b*, we investigate the effects of fracture spacing (number of fractures per unit length) and the specific stiffnesses of fractures (the ratio of the incremental stress across the fracture to the incremental displacement that the stress produces). Some of the important features will be discussed as follows: For a fixed crack density, the qSR velocity variations are same for cracks of different aspect ratios. *Case a* predicts less velocity variations for qSR and large variations for qP for increase in aspect ratios. Velocity variations increase with increasing fracture densities. For fixed fracture spacing, *Case b* predicts that as the angle of incidence increases, all three body wave (qP, qSP and qSR) velocities increase and approach the velocity values in the unfractured rock at an angle of incidence of  $90^\circ$  (parallel to the fractures). The intermediate nature of the velocities is controlled by the stiffnesses of the fractures.

## INTRODUCTION

The understanding of seismic anisotropy of various fractured rock masses is important for the successful resolution of many geophysical problems such as exploitation of fractured hydrocarbon and geothermal reservoirs. Discontinuities ranging in

scale from microfractures to faults are common within the Earth's crust. These discontinuities often occur as nearly parallel groups or sets and also control the hydraulic and mechanical behavior of rock mass. To locate such discontinuities from seismic information is of great importance to practical geophysical problems. It is often observed that the presence of such discontinuities displays seismic anisotropy in the elastic properties of the rock mass. In this study, we discuss about two different kinds of crack system. They are, (a) dilute fracture model where wavelengths are large compared to the size of the cracks, and (b) nonwelded fracture model where the stresses are continuous but displacements are discontinuous across the fracture. Both cases show seismic velocity anisotropy. The motivation of this study is to understand the nature of velocity variation with different parameters of the fracture system derived from existing theories.

## DILUTE FRACTURE MODEL

The use of this kind of fracture model is very common to represent crack systems. The theory for computing the effective moduli of a rock mass containing aligned thin fractures or cracks was established by Hudson (1980, 1981). This model assumed that the crack dimension was small compared to the wavelength and that the distribution of parallel penny-shaped cracks was dilute. The effective moduli of the entire rock mass containing such crack systems were established by introducing first and second order perturbations to the isotropic elastic moduli of the uncracked rock mass, and incorporating fracture density, aspect ratio and weakly isotropic filling material. From these effective elastic constants the seismic velocities of the medium containing parallel cracks were determined. Figure 1 shows the azimuthal variation of normalized velocities with different aspect ratios for a crack density 0.1, where the parallel cracks in the rock mass are filled with gas. The  $0^\circ$  represents the wave propagation perpendicular to the crack plane. As the aspect ratio increases the velocity variation also increases for both qP and qSP wave. The qSR wave variation does not depend on aspect ratios (AR). Figure 2 represents the velocity variation with the different crack densities and aspect ratios for the wave propagating along the plane of  $60^\circ$  from the crack plane (i.e.  $30^\circ$  from the perpendicular of the crack plane). In general the velocity anisotropy increases with increase of crack density and aspect ratio, but at higher values of the product of aspect ratio and crack density, it appears that the Hudson's theory produces nonlinear velocity variation. We also present here the anisotropic effect for the other filling material.

## Scale of Fracture Induced Anisotropy

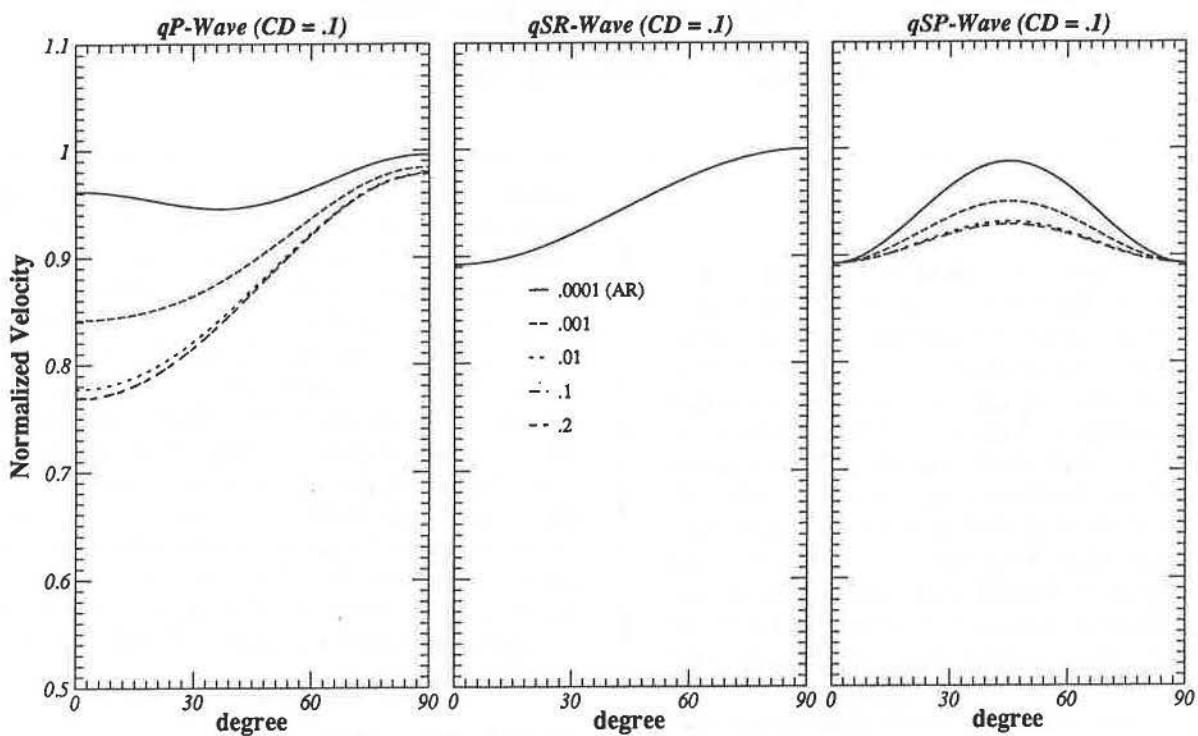
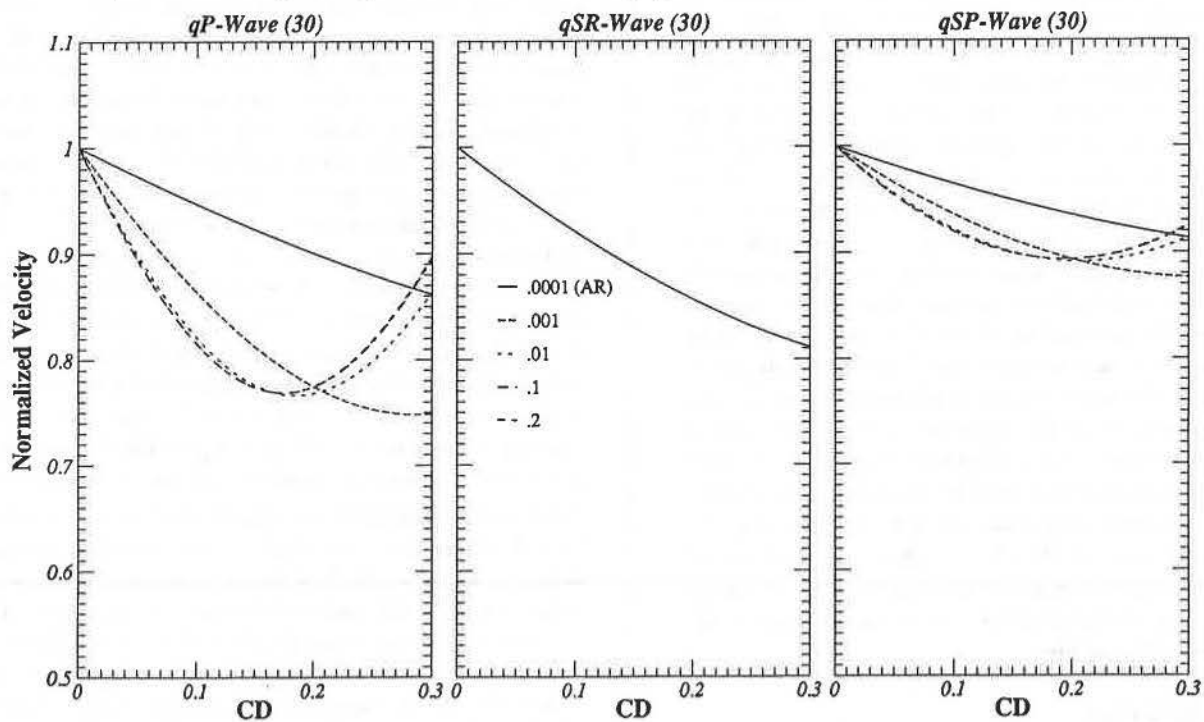


Figure 1: Normalized azimuthal velocity as a function of aspect ratio for a crack density of 0.1 using the Hudson theory. 0° represents the wave incident perpendicular to the fractures.



Host rock :  $V_p = 5000$ ,  $V_s = 2900$  m/sec

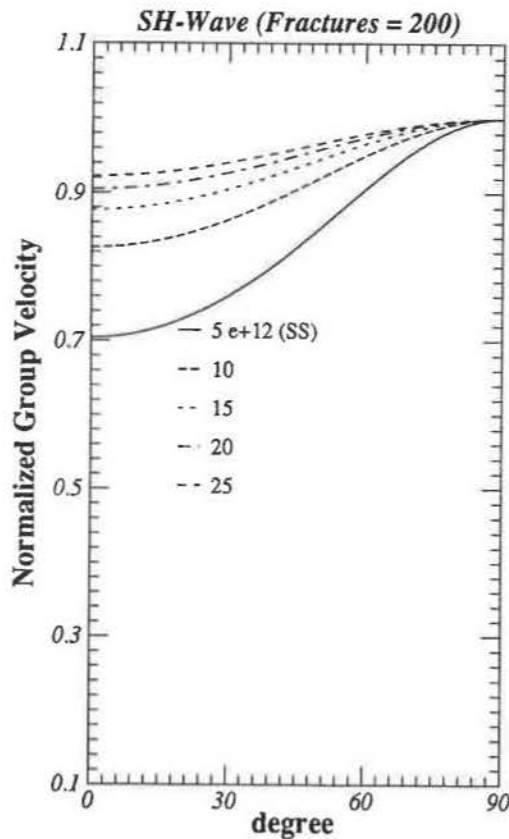
Filling : Gas

Figure 2: Normalized velocity as a function of crack density and aspect ratio for the wave incidence at 30° from the perpendicular of the crack plane.

## Scale of Fracture Induced Anisotropy

### DISPLACEMENT DISCONTINUITY FRACTURE MODEL

This model represents a rock mass containing from a single to a large number of nonwelded interfaces represented by displacement discontinuity boundary conditions in the seismic wave equation. The displacement discontinuity is the ratio of average stress to the specific stiffness of the interface. The stiffness is related to the density of coplanar fractures. The dense fracture population refers to a low fracture stiffness, while the dilute fracture population represents a high fracture stiffness. The specific stiffness is the ratio of the internal stress across the fracture to the incremental displacement that the stress produces. The value of specific stiffness determines the seismic properties of the fractures including the effect of the mechanical coupling between the fracture surfaces on the transmission properties across the fracture. For example, an infinite specific stiffness refers to the welded contact and a zero stiffness represents the free surface. In this model the main constraint is



Host rock :  $V_p = 5000.$ ,  $V_s = 2900$  m/sec

Figure 3: Azimuthal variation of normalized effective group velocity with change of specific stiffness (SS in Pa/m) for a rock mass with 200 fractures per meter.

that the seismic wavelength must be greater than the fracture spacing (i.e., the asperities of contact between the two surfaces of the fracture). Theoretical studies involving the general solution of the seismic wave equation for this kind of fractures are given by Schoenberg (1980), Park-Nolte *et al.* (1990) and others. Park-Nolte *et al.* (1990) also investigated this displacement discontinuity theory in light of the observed laboratory data. This model produces also anisotropic velocity variation which is different in nature than that from the dilute fracture model. For example, we display in figures 3-4 the effective SH group velocity variation with different incident angles to the fracture ( $0^\circ$  represents the incidence perpendicular to the fracture), specific stiffnesses (SS) and number of fracture per unit length. The P-wave velocity variation is similar to SH, but SV-wave suffers a discontinuity in the effective group velocity at the the critical angle as a converted P-wave is generated here by the incident SV-wave. We will discuss this in details.

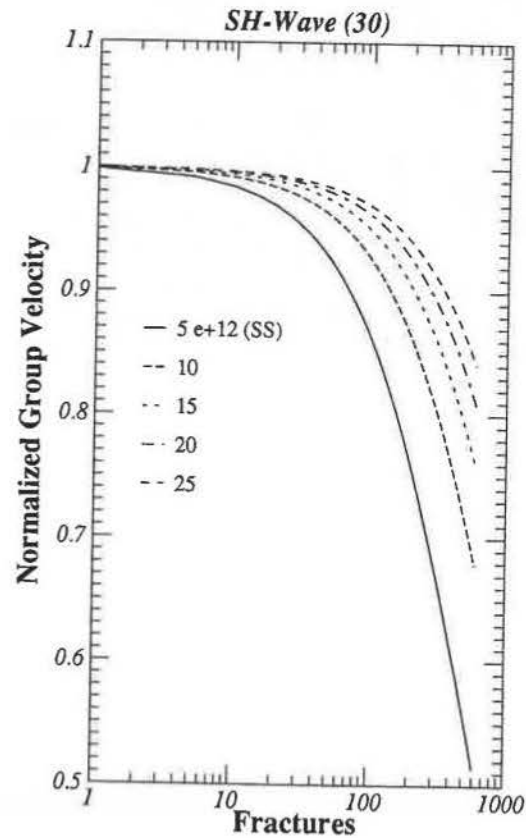


Figure 4: Normalized effective group velocity as a function of number of fractures per unit length and specific stiffness.

## Scale of Fracture Induced Anisotropy

All these three body waves are slow for incidence perpendicular to the fracture. In general, this variation depends on the frequency, but the dependence is negligibly small in the seismic frequency band (0-2000 Hz).

### DISCUSSION

In this presentation we review the anisotropic velocity variations due to aligned fractures distributed evenly in the rock mass. The two different theoretical approaches contribute different velocity variations. Our study needs further experimental data to confirm the theoretical predictions. In general, the difference between the two approaches could result in significantly different interpretations of the field data.

### REFERENCES

- Hudson, J. A., 1980, Overall properties of a cracked solid, *Math. Proc. Cambridge Philos. Soc.*, *88*, 371-384.
- Hudson, J. A., 1981, Wave speeds and attenuation of elastic waves in material containing cracks, *Geophys. J. R. Astron. Soc.*, *64*, 133-150.
- Pyrak-Nolte, L. J., Myer, L. R. and Cook, N. G. W., 1990, Anisotropy in Seismic Velocities and Amplitudes from Multiple Parallel Fractures, *J. Geop. Res.*, *95*, 11345-11358.
- Schoenberg, M., 1980, Elastic wave behavior across linear slip interfaces, *J. Acoust. Soc. Am.*, *68*, 1516-1521.
- Schoenberg, M., 1983, Reflection of elastic waves from periodically stratified media with interfacial slip, *Geophys. Prospect.*, *31*, 265-292.

# Propagation of Seismic Waves Through 2D Random Media: Implications for Travel Times

L.T. Ikelle, M. Schoenberg, C. Chapman and A. Kurkjian <sup>1</sup>

The integration of surface seismic data with borehole seismic data and well-log data requires a model of the Earth which can explain all these measurements. Such a model consists of large and small scale inhomogeneities. The large scale inhomogeneities are the mean characteristics of the Earth while the small scale inhomogeneities are fluctuations from these mean values.

In this paper we consider a model where the large scale inhomogeneities are represented by a homogeneous medium and small scale inhomogeneities are randomly distributed inside the homogeneous medium. The random distribution is characterized by an ellipsoidal autocorrelation function. Thus we can describe media in which the inhomogeneities are elongated in a particular direction or even flattened. Some examples are shown in Figure 1.

We have implemented an elastic finite-difference algorithm to simulate the propagation of seismic waves through media with random distribution of inhomogeneities, in particular to study the effects on travel times. We have looked at two source-receiver configurations: (i) receivers are distributed along a quarter of circle (Figure 2) and (ii) VSP type of geometries (Figure 3).

With the configuration in Figure 2, we can study the scattering dependence with angle. Figure 4 shows finite-difference synthetics for an explosive source propagating through a homogeneous medium (top) and a 1D random medium (bottom). The parameters used are described in Table 1. The results are in agreement with theory.

With the configuration in Figure 3, we can point out the travel time drift between 1D

---

<sup>1</sup>Schlumberger Cambridge Research, P.O. Box 153, Cambridge CB3 OHG, England

and 2D random media. Figure 5 illustrates this travel time drift with respect to receiver depths. Our talk will discuss these results in details.

## Figure Captions

Figure 1. *Random media.* We consider random medium with an exponential autocorrelation  $f(x, z) = \mu^2 e^{-\sqrt{\frac{x^2}{a^2} + \frac{z^2}{b^2}}}$  where the quantities  $a$  and  $b$  represent the "scale size" of inhomogeneities in  $x$  and  $z$  direction respectively.  $(x, z)$  are the cartesian position vector in 2D medium. Using the scale sizes  $a$  and  $b$  we can describe media in which the inhomogeneities are elongated in a particular direction or even flattened. (a)  $a = 0.9\text{ m}$  and  $b = 0.9\text{ m}$ , (b)  $a = 3.6\text{ m}$  and  $b = 3.6\text{ m}$ , (c)  $a = 9.0\text{ m}$  and  $b = 0.9\text{ m}$ , (d)  $a = 18.0\text{ m}$  and  $b = 0.9\text{ m}$ , (e)  $a \mapsto \infty$  and  $b = 0.9\text{ m}$  and (f)  $a = 0.9\text{ m}$  and  $b = 4.5\text{ m}$ .

Figure 2. *Source-receiver configuration used to study the scattering dependence with angle.*

Figure 3. *Source-receiver configuration used to study the travel time drift between 1D and 2D random medium*

Figure 4. *Finite difference synthetics for an explosive source (i.e. only P-wave are generated) propagating through a homogeneous medium (top) and an exponential random medium with  $a \mapsto \infty$  and  $b = 0.8\text{ m}$  (bottom).*

Figure 5. *Finite difference synthetics for an explosive source (i.e. only P-wave are generated) propagating through a 1D random medium with  $a \mapsto \infty$  and  $b = 0.8\text{ m}$  are surimposed on those obtained for a 2D random medium with  $a = 12.0\text{ m}$  and  $b = 0.8\text{ m}$*

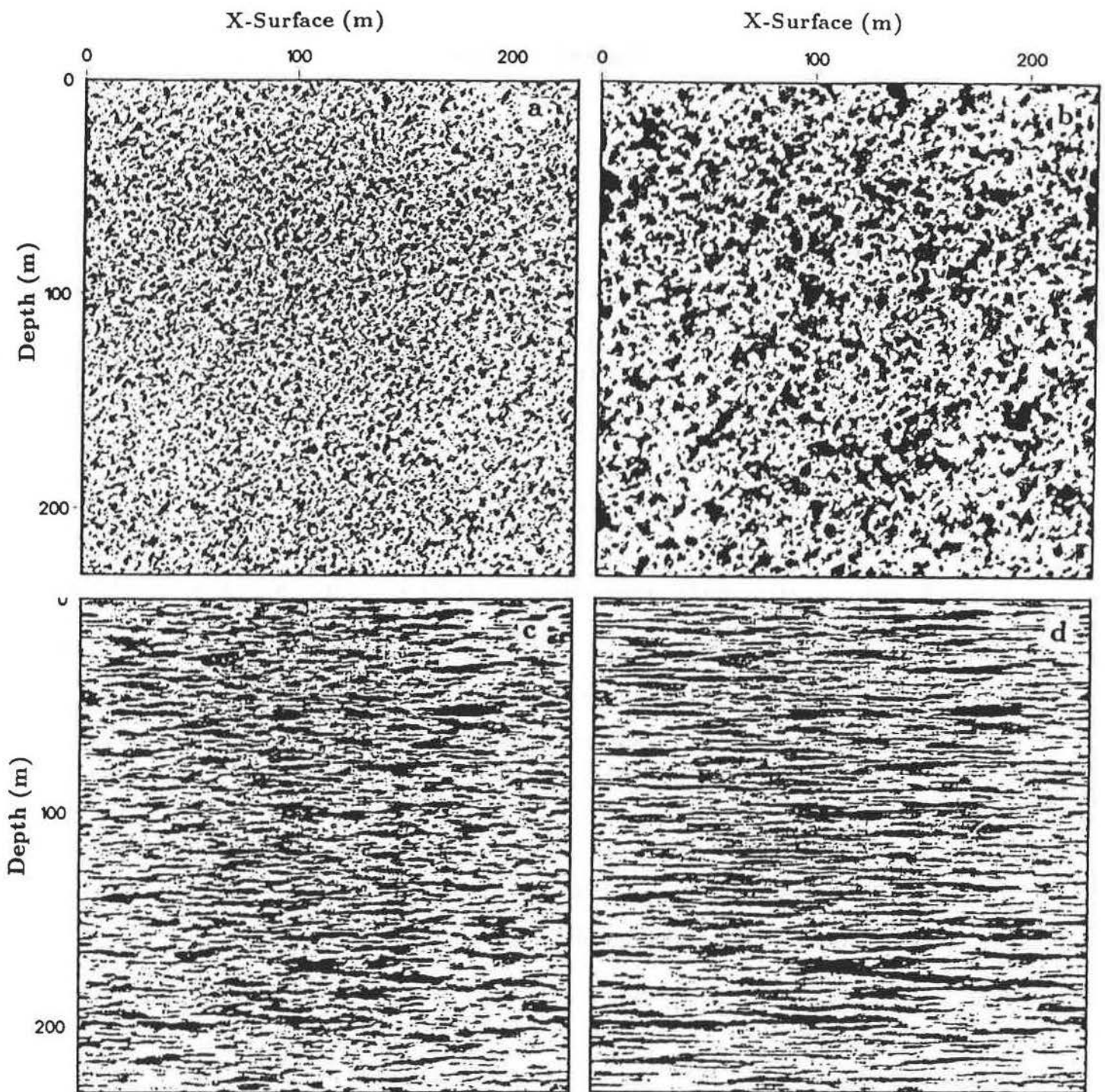


Figure 1

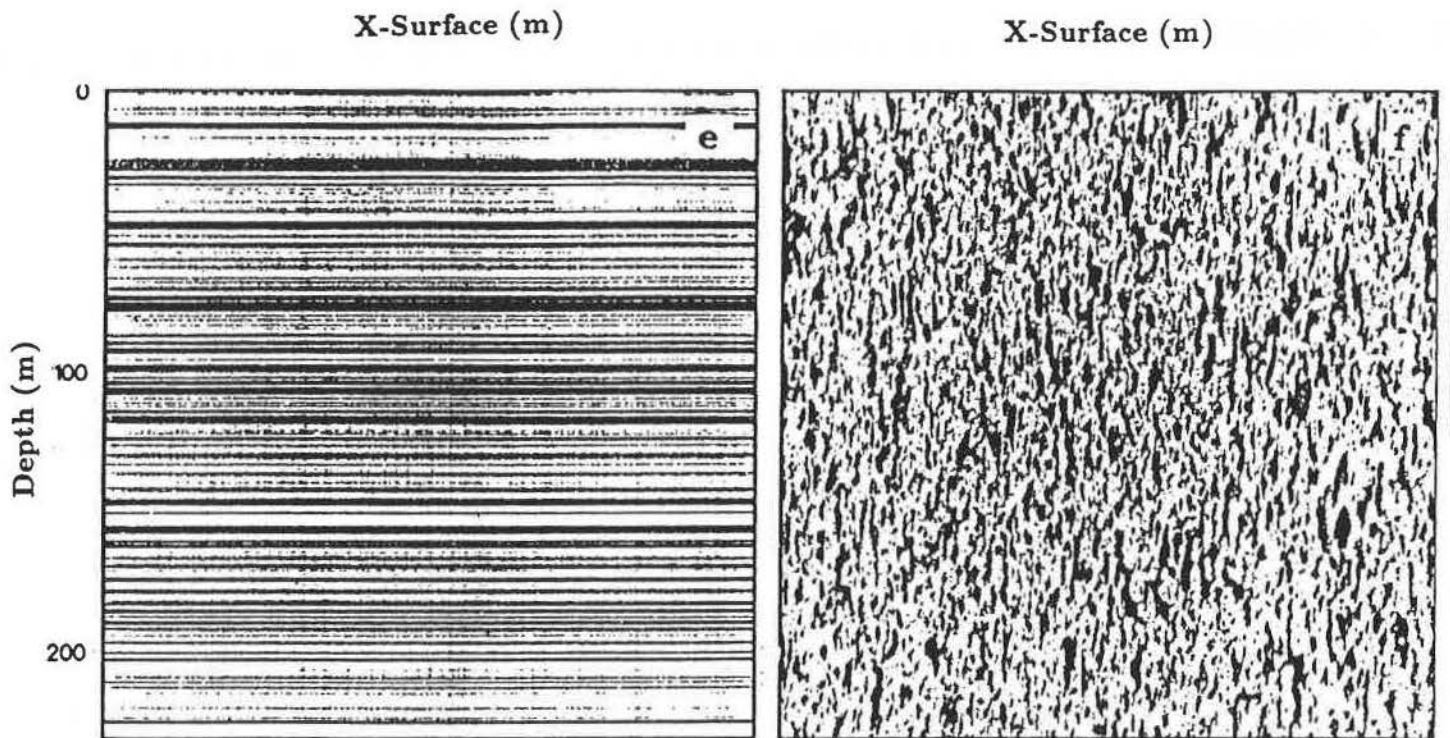


Figure 1

**TABLE 1**  
**Finite-Difference's Parameters**

---

- Spacing (1024x1024)

$$DX = 0.40m \quad DZ = 0.40m$$

- Elastic parameters

$$V_p = 3000ms^{-1} \quad V_s = 2110ms^{-1} \quad \rho = 2.6gcc^{-1}$$

- Standard deviations

$$\sigma_{V_p} = 0.1 \quad \sigma_{V_s} = 0. \quad \sigma_{\rho} = 0.1$$

- Source:

$$Central \ Freq. = 350Hz \quad DT = 60\mu s$$

---

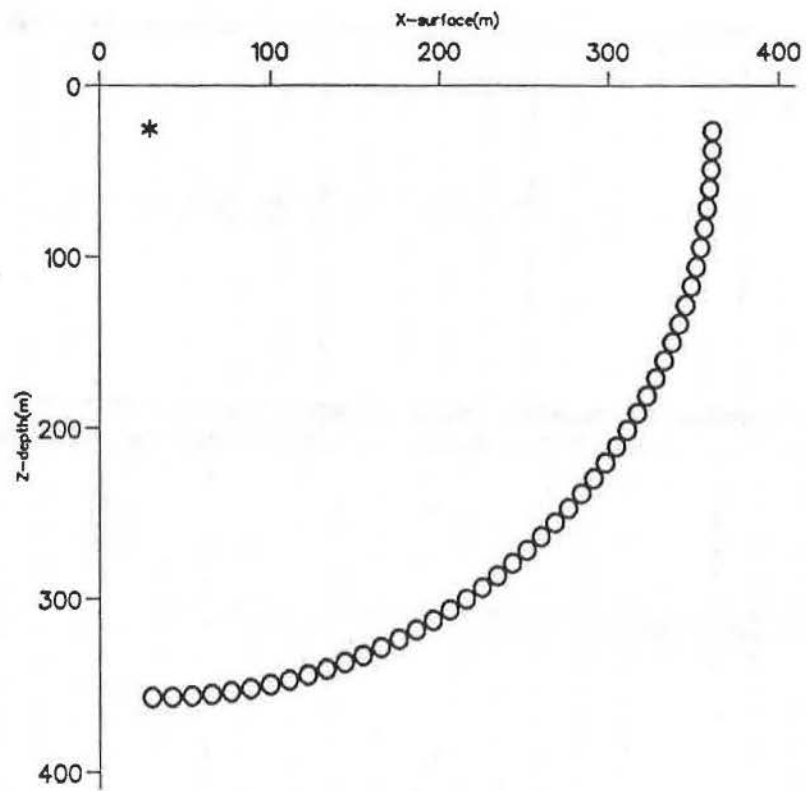


Figure 2

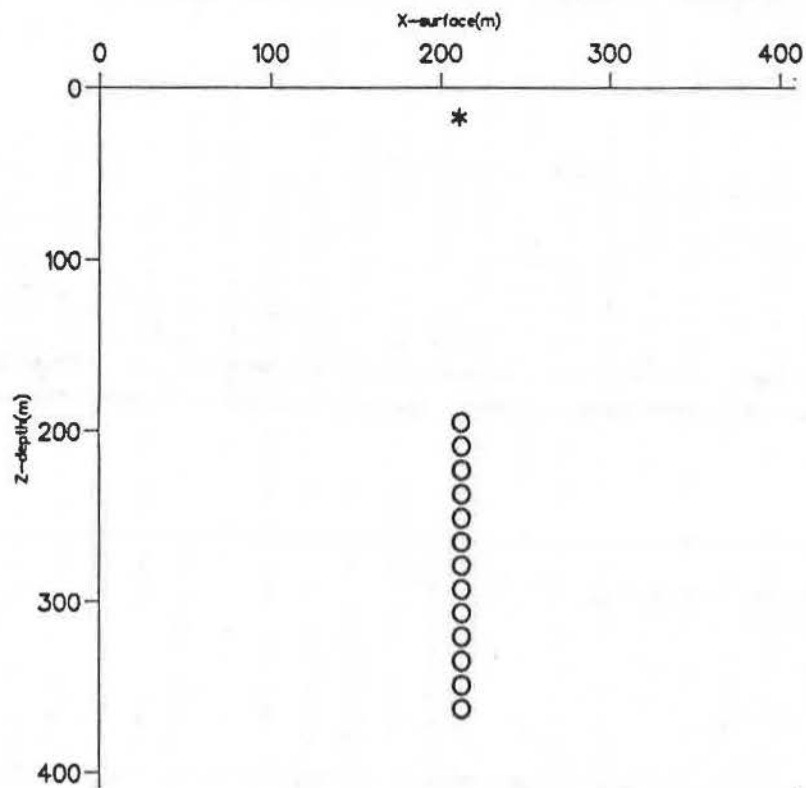


Figure 3

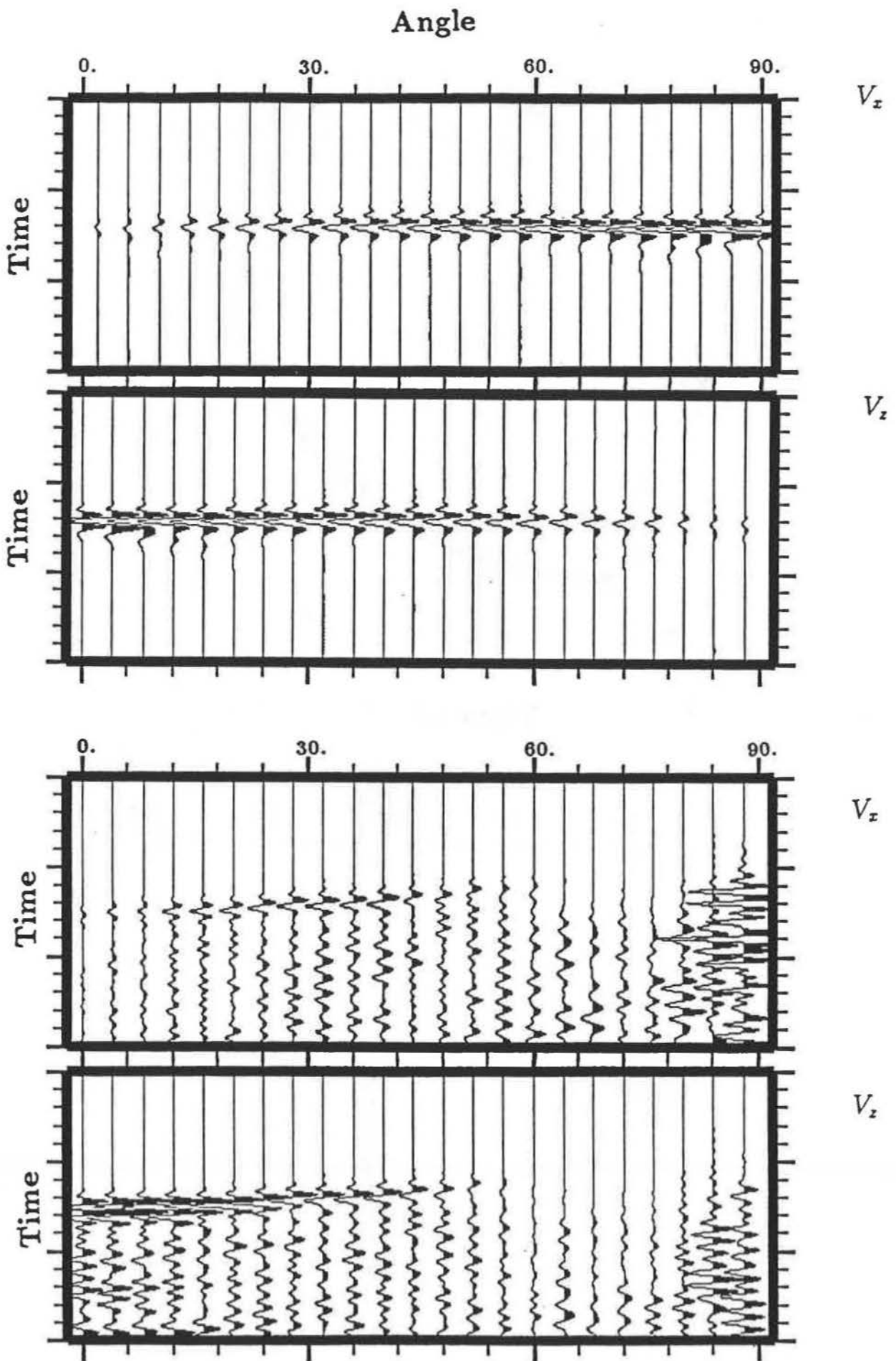


Figure 4

Depth

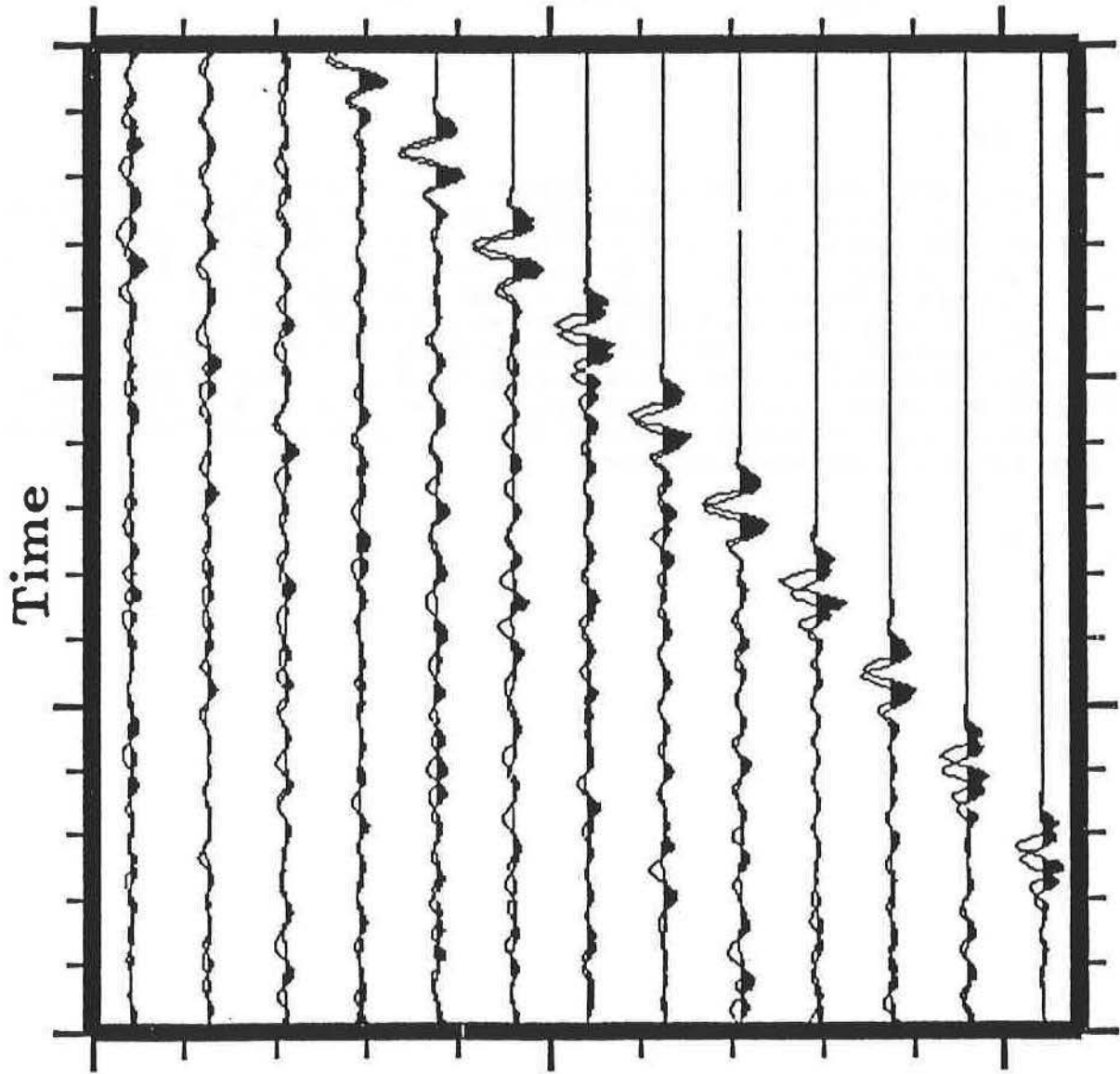


Figure 5

# ACOUSTIC ANISOTROPY OF SYNTHETICS WITH CONTROLLED CRACK GEOMETRIES

**J.S. Rathore, E. Fjaer, R.M. Holt and L. Renlie**  
**Continental Shelf & Petroleum Technology Research Institute**

**L. Thomsen, Amoco Production Company**

## I. INTRODUCTION

The knowledge of crack distributions is of vital importance for the withdrawal of fluids from reservoirs in which cracks exist as penetrating fractures, serving as primary channels for fluid flow. The presence of cracks affects the acoustic wave velocities giving rise to anisotropy. It is important to be able to predict theoretically whether the observed anisotropy is caused by a large number of small, isolated microcracks, or by a few similarly oriented, larger and possibly connected fractures. Several theoretical models for the acoustic behaviour in cracked and jointed media exist (Hudson, 1981, Thomsen, 1986), yet none of them have been confirmed in a controlled experiment, one in which sizes, shapes, amounts and orientational distributions of cracks are known. In geomaterials these are generally unknown parameters. Hence we have undertaken the task of producing a synthetic material in which the above crack parameters are known.

# Modeling Surface Roughness in Porous Media Acoustics

Steve Pride, Dale Morgan, and A.F. Gangi  
Department of Geophysics, Texas A&M.

## Abstract

The presence of half-cylinders on the surface of an otherwise smooth and constant width flow channel has been allowed for in modeling the drag due to flow induced both by a time-harmonic pressure gradient and by time-harmonic shaking of the walls. Such a drag analysis allows one to determine the complex inertial flow operator in Biot's theory of wave propagation. It is shown that when the flow fields about the bumps on either side of the flow channel do not interact, then the predicted drag does not correlate with the pore-surface to pore-volume ratio and, further, that there is little difference compared to a smooth-walled model. When the bumps across the channel begin to interact there is, of course, an enhancement in the drag. However, this enhancement does not directly correlate with the pore-surface to pore-volume ratio.

## Introduction

Biot's equations controlling the average linear dynamics of an isotropic, porous, fluid-saturated material can be written as

$$\rho_B \frac{\partial \dot{\mathbf{u}}}{\partial t} = -\rho_f \frac{\partial \dot{\mathbf{w}}}{\partial t} + \nabla \cdot \bar{\boldsymbol{\tau}}_B \quad (1)$$

and

$$\rho_E \frac{\partial \dot{\mathbf{w}}}{\partial t} = -\rho_f \frac{\partial \dot{\mathbf{u}}}{\partial t} - \nabla \bar{p} \quad (2)$$

where  $\dot{\mathbf{u}}$  is the average particle velocity of the solid frame, and  $\dot{\mathbf{w}}$  is the average relative fluid/solid velocity or "filtration velocity". Equation (1) is a force balance on a bulk volume of the material.  $\bar{\boldsymbol{\tau}}_B$  is the average stress tensor in this bulk volume and is related to the average stresses in the solid ( $\boldsymbol{\tau}$ ) and fluid ( $-\bar{p}\mathbf{I}$ ) by  $\bar{\boldsymbol{\tau}}_B = (1-\phi)\boldsymbol{\tau}_s - \phi\bar{p}\mathbf{I}$  where  $\phi$  is the porosity.  $\rho_B$  is the bulk density given by  $\rho_B = (1-\phi)\rho_s + \phi\rho_f$ . Equation (2) represents a force

balance on the fluid in relative motion. The inertial operator  $\rho_E$  has within it all induced mass and frictional flow resistance effects associated with the average relative motion. Proper modeling of  $\rho_E$  is crucial if estimates of the relative flow (and, therefore, estimates of the importance of the slow wave) are to be accurate.

Biot (1956b) analytically modeled the frequency dependence of  $\rho_E$  by considering the medium to consist of banks of parallel constant-width flow channels. Pride (1991) has generalized this model to allow for flow channels possessing variable widths. To obtain analytical results, two restrictions on the variable-width channels were required: 1) the constriction lengths (i.e., the axial distance between two adjacent "throats") must be larger than the average channel width; and 2) the slope of the channel walls (with respect to the channel axis) must be less than one.

Both in this work and in Pride (1991), the effect on  $\rho_E$  of allowing for bumps on the surface of an otherwise smooth and constant-width flow channel is considered. Such bumps will, in general, violate both of the conditions given above for the validity of the variable-width model and, therefore, a different analysis is required. The restriction for which the analysis of this work is valid is that the viscous boundary layers associated with the time-harmonic relative flow must be smaller than the bump sizes.

It has been suggested by Johnson et al. (1987), Warner and Beamish (1987), and Klimentos and McCann (1988), that when the frequencies become so large that the viscous boundary layers are of the size of (or smaller than) the surface roughness on the grains of a porous material, then frictional resistance to the flow will be enhanced compared to flow through materials with no surface roughness. Our modeling will demonstrate that, at least for the case where the bump heights are much smaller than the channel widths, there are only small differences in the friction drag associated with bumpy and smooth walled models even though the bumpy walls have as much as 50% greater area. Accordingly, the usefulness of pore-volume to pore-surface ratios in defining the  $\rho_E$  operator is brought into question.

By directly volume averaging the linear force-balance equation (Cauchy's first law) controlling the fluid motion within a porous material, Pride (1991) obtains

$$i\omega \frac{\rho_f}{\phi} \dot{\mathbf{w}} - \mathbf{d} = -\nabla p - i\omega \rho_f \dot{\mathbf{u}} \quad (3)$$

where  $\mathbf{d}$  is the drag force defined by

$$\mathbf{d} = \frac{1}{V_f} \int_{S_w} \mathbf{n} \cdot \boldsymbol{\tau}_f dS \quad (4)$$

and  $\boldsymbol{\tau}_f$  are the actual, non-averaged, fluid stresses acting on the wall surfaces  $S_w$  within a unit macroscopic volume of the porous material.  $V_f$  is the volume of fluid within this macroscopic volume, and  $\mathbf{n}$  is the normal to the walls directed from the fluid into the solid.  $\nabla p$  and  $i\omega\rho_f\dot{\mathbf{u}}$  are the two forces driving the relative flow and are associated with the peaks and troughs of a compressional wave and the shaking of the pore walls respectively. From simple linearity arguments as well as the assumption of macroscopic isotropy we must have the relation

$$\mathbf{d} = \nu (\nabla p + i\omega\rho_f\dot{\mathbf{u}}) \quad (5)$$

where, for the time-harmonic case,  $\nu$  is a complex, frequency-dependent function independent of the applied forces. Combining equations (2), (3), and (5) then gives

$$\rho_E = \frac{\rho_f}{\phi} \frac{3}{1 - \nu}. \quad (6)$$

The factor of 3 comes from the fact that only roughly one third of the pore space is conducting fluid in a macroscopically isotropic porous medium. The other two-thirds of the porespace can be thought to consist of flow channels perpendicular to the direction of the macroscopic flow. By actually solving for the tractions  $\mathbf{n} \cdot \boldsymbol{\tau}_f$  operating on the surface of the bumpy walled flow channels and integrating these tractions over the surface  $S_w$  according to equation (4), analytical expressions for  $\nu$  can be developed from which  $\rho_E$  is obtained through equation (6).

### Modeling the Fluid Stresses

The detailed and fully developed modeling of the fluid stresses has been given by Pride (1991). In what follows simply the basic idea of the modeling is outlined.

For time-harmonic relative flow, a boundary layer develops whenever the frequencies become so large that the inertial forces of the fluid dominate the viscous shear forces. When this begins to occur, the fluid in the center of the channel behaves as if the fluid were inviscid. However, since the fluid must have zero relative velocity at the wall there is always a region near the wall — called the viscous boundary layer — in which the shear forces

dominate the inertial forces. The thickness of the boundary layer is of the order

$$\delta = \sqrt{\frac{\mu}{\omega \rho_f}} \quad (7)$$

where  $\mu$  is the fluid's shear viscosity.

As stated above, the fundamental assumption of the modeling is that  $\delta$  is smaller than some characteristic length  $\ell$  associated with the bumps on the walls. For an elliptical bump as shown in Figure 1, this characteristic length  $\ell$  can be taken as the smallest radius of curvature ( $= L^2/R$ ) so that the condition  $(\delta/\ell)^2 < 1$  can be expressed as

$$\omega = 2\pi f > \frac{\mu}{\rho_f} \frac{R^2}{L^4}. \quad (8)$$

Taking  $R = L$  for simplicity, we see that for water ( $\mu/\rho_f = 10^{-6} \text{ m}^2\text{s}^{-1}$ ), condition (8) becomes  $f > 10^5 \text{ Hz}$  if bump lengths are on the order of a micron (e.g., clays). Alternatively, if the bumps are envisioned to be grains on the order of 100 microns, then condition (8) becomes  $f > 10 \text{ Hz}$ .

If condition (8) is fulfilled, then the flow can be approximately modeled in the fashion of Landau and Lifshitz (1987, pp. 86-87). If  $v_t$  is the tangential component of the flow velocity about the bump, then Landau and Lifshitz obtain

$$v_t = v_t^{(\infty)} \left( 1 - \exp\left(-i^{1/2} \frac{\chi}{\delta}\right) \right) \quad (9)$$

where  $v_t^{(\infty)}$  is the ideal flow field ( $\mu = 0$ ) that prevails outside the boundary layer and that is approximately constant across the width of the boundary layer.  $\chi$  is a local coordinate measuring distance normal to the bump surface.

If  $\tau_t$  is further denoted as the local component of the viscous shear traction acting tangentially on the wall, we have

$$\tau_t = \mu \left. \frac{\partial v_t}{\partial x} \right|_{x=0} = i^{1/2} \frac{\mu}{\delta} v_t^{(\infty)}. \quad (10)$$

Because flow in the boundary layer is locally plane to the wall, there can be no large variation in the pressure across the boundary layer (e.g., Jones and Watson, 1963, pp. 198-203) so that the pressure is everywhere the pressure associated with ideal flow

$$p = p^{(\infty)} \quad (11)$$

Since  $p$  and  $\tau_t$  are the two stresses involved in the drag integral, the problem of obtaining  $\rho_E$  is reduced to solving the ideal flow problem.

Pride (1991) has considered both elliptical half-cylinders and circular half-cylinders as the bumps on the surface of the channel (see Figure 2). In the numerical results that follow, we only consider the circular half-cylinder case. To solve for the ideal flow field about a circular cylinder oscillating perpendicular to its axis we can use the result of Lamb (1945, p. 64) that the flow field is equivalent to if a fluid dipole source were located on the cylinder axis and oriented in the direction of the oscillations. If the ideal velocity is represented in terms of a velocity potential, and if the fluid is modeled as being incompressible (which is acceptable so long as  $f < 10$  MHz), then the potential obeys Poisson's equation with a dipole source term. This problem has a well-known solution. To find the total velocity potential due not only to one particular half-cylindrical bump on the wall, but due to all the surrounding bumps as well, each bump can be replaced by a fluid dipole source, and the potential response from each dipole can simply be summed to obtain the total potential field.

Doing this alone will violate the condition that no flow can penetrate the bump surface. Therefore, image dipoles must be appropriately placed that cancel any flow through the bump surfaces, and the potential response from all such image dipoles must be added into the total response as well. In the numerical results that follow, the flow field from all the dipoles shown in Figure 2 have been allowed for. Within the central cylinder of Figure 2 there is an image dipole corresponding to each of the displayed dipoles. Integrating the ideal pressure field and viscous shear traction over the pore walls within the dashed box of Figure 2, then leads to an analytical expression for the  $\nu$  function (and, therefore,  $\rho_E$ ). Due to the complicated nature of this  $\nu$  function, the reader is deferred to Pride (1991) for its explicit form.

## Numerical Results

It is convenient to express the drag integral of equation (4) as the sum of two terms:

$$\mathbf{d} = \mathbf{d}^{form} + \mathbf{d}^{fric} \quad (11)$$

where,

$$\mathbf{d}^{form} = -\frac{1}{V_f} \int_{S_w} \mathbf{n} p_f dS \quad (12)$$

and

$$\mathbf{d}^{fric} = \frac{1}{V_f} \int_{S_w} \mathbf{n} \cdot \boldsymbol{\tau}_f^D dS. \quad (13)$$

$p_f$  is the actual fluid pressure induced in the fluid by the flow, and  $\boldsymbol{\tau}_f^D$  are the deviatoric (or shear) stresses acting on the wall. If a material consists of constant-width parallel flow channels (a Biot model) then the normal to the walls ( $\mathbf{n}$ ) will be perpendicular to the average flow direction and no form drag will exist. In the bumpy pore model considered in Figure 2, form drag is dominant. Thus, large differences between the smooth walled and bumpy walled cases can be expected in the modeling of  $\rho_E$ .

In Figure 3, we compare *only* the friction drag from the bumpy-walled model  $d_{bumpy}^{fric}$  to the friction drag from a smooth-walled model  $d_{smooth}^{fric}$ . Both models have the same channel width ( $2DR$ ) where  $D = 10$ . We have chosen a large  $D$  value so that we may investigate whether the pore-surface to pore-volume ratio in and of itself is an important parameter in the determination of  $\rho_E$ . We see from the figure that when the bumps are just touching ( $B = 1$ ), the friction drag from the bumpy-walled model is roughly 20% greater than from the smooth-walled model. This is because the channel has been effectively reduced in width. For larger  $B$  values there is slightly less friction drag in the bumpy-walled models than in the smooth-walled models. This is because even though the shear tractions on top of each bump are greater than the tractions on the smooth wall, the shear tractions on the side of the bumps and on the wall between the bumps are less than in the smooth-walled case. Thus, depending on how the bumps are placed on the wall, there can either be a slight increase or slight decrease in the friction drag due to the bumps. Thus, no simple relation between friction drag and the pore-surface to pore-volume ratio exists for this example.

In Figure 4, we investigate the effect of bringing the walls together keeping the bump-height fixed. Both the real and imaginary parts of  $\rho_E$  are plotted. A value of  $\delta/R = 0.1$  was chosen for this example. Although the friction drag is directly proportional to  $\delta/R$ , the form drag is independent of  $\delta/R$  and, therefore, independent of frequency. Over eighty percent of the real part of  $\rho_E$  is due to form drag. The form drag does not contribute to the imaginary part of  $\rho_E$ . The real part of  $\rho_E$  corresponds to the effective inertia of the fluid in motion, while the imaginary part is proportional to

the friction (heat generating) flow resistance. It is seen that for small values of  $D$  (i.e., the bumps on either side of the channel close to each other) there can be large value for  $\rho_E$ .

In conclusion, it has been shown that the pore-surface to pore-volume ratio does not directly correlate with the frictional drag resistance for the case in which the bumps across the channel from each other do not significantly interact. However, when the bumps across the channel do interact, then large increases in  $\rho_E$  can be expected. Although this latter result is intuitively expected, we have provided an analytic means to model  $\rho_E$ .

### References

Biot, M.A., 1956b, Theory of propagation of elastic waves in a fluid-saturated porous solid. II—Higher-frequency range: *J. Acoust. Soc. Am.*, *28*, 179-191.

Johnson, D.L., Koplik, J., and Dashen, R., 1987, Theory of dynamic permeability and tortuosity in fluid-saturated porous media: *J. Fluid Mech.*, *176*, 379-402.

Jones, C.W., and Watson, E.J., 1963, Two-dimensional boundary layers in Laminar Boundary Layers: L.Rosenhead, Oxford, Clarendon Press.

Klimentos, T., and McCann, C., 1988, Why is the slow compressional wave not observed in real rocks?: *Geophysics*, *53*, 1605-1609.

Lamb, H., 1945, Hydrodynamics: New York, Dover.

Landau, L.D., and Lifshitz, E.M., 1987, Fluid Mechanics, 2nd edition: New York, Pergamon Press.

Pride, S.R., 1991, Linear Vibrations of Porous Media: PhD. dissertation, Texas A&M University.

Warner, K.L., and Beamish, J.R., 1987, Ultrasonic attenuation and pore microstructure in a liquid-<sup>4</sup>He-filled ceramic: *Phys. Rev. B*, *36*, 5698-5701.

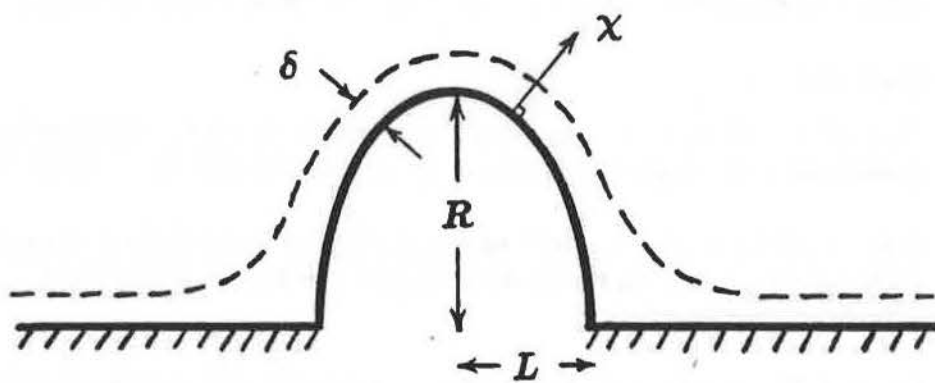


Figure 1: A bump on a wall.

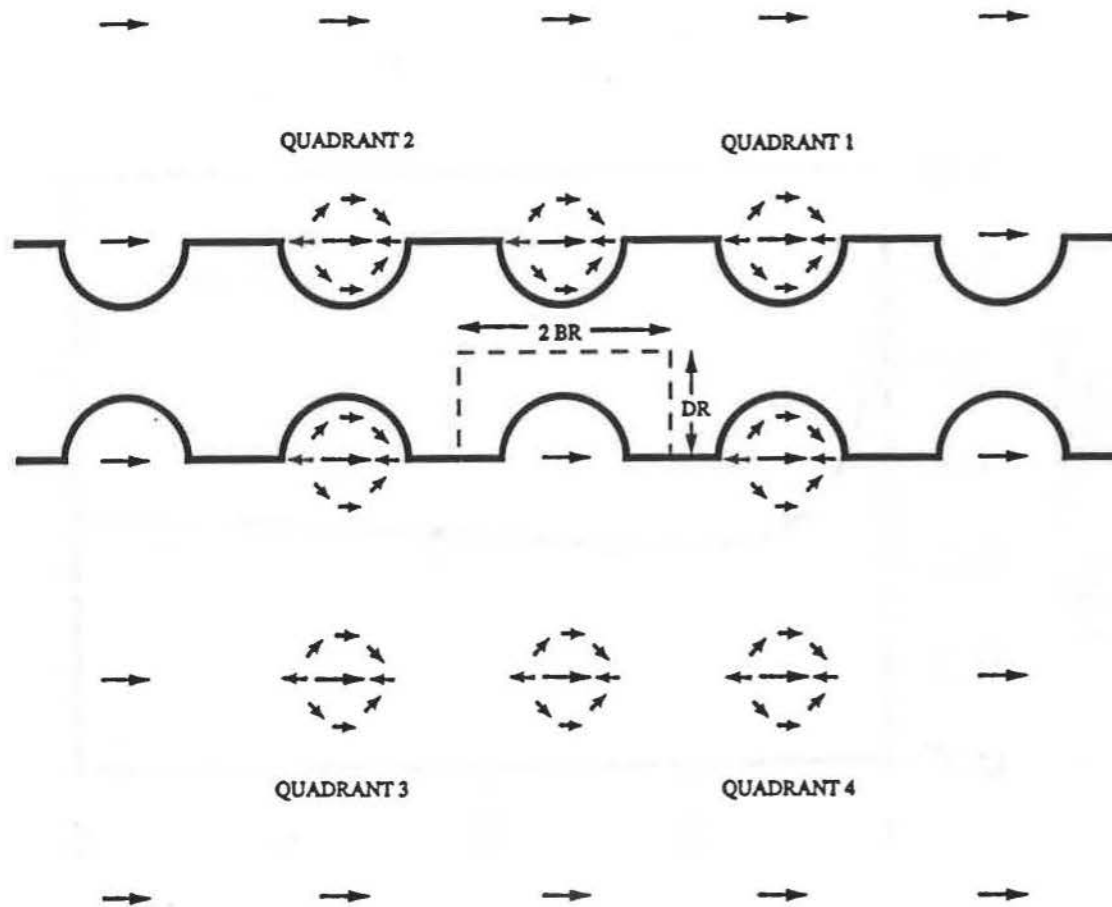


Figure 2: The dipole modeling of the ideal flow field. 177 dipoles up to order  $(2B)^{-2}$  and  $(2D)^{-2}$  have been allowed for. Within the central cylinder, there is an image dipole corresponding to each of the displayed dipoles.

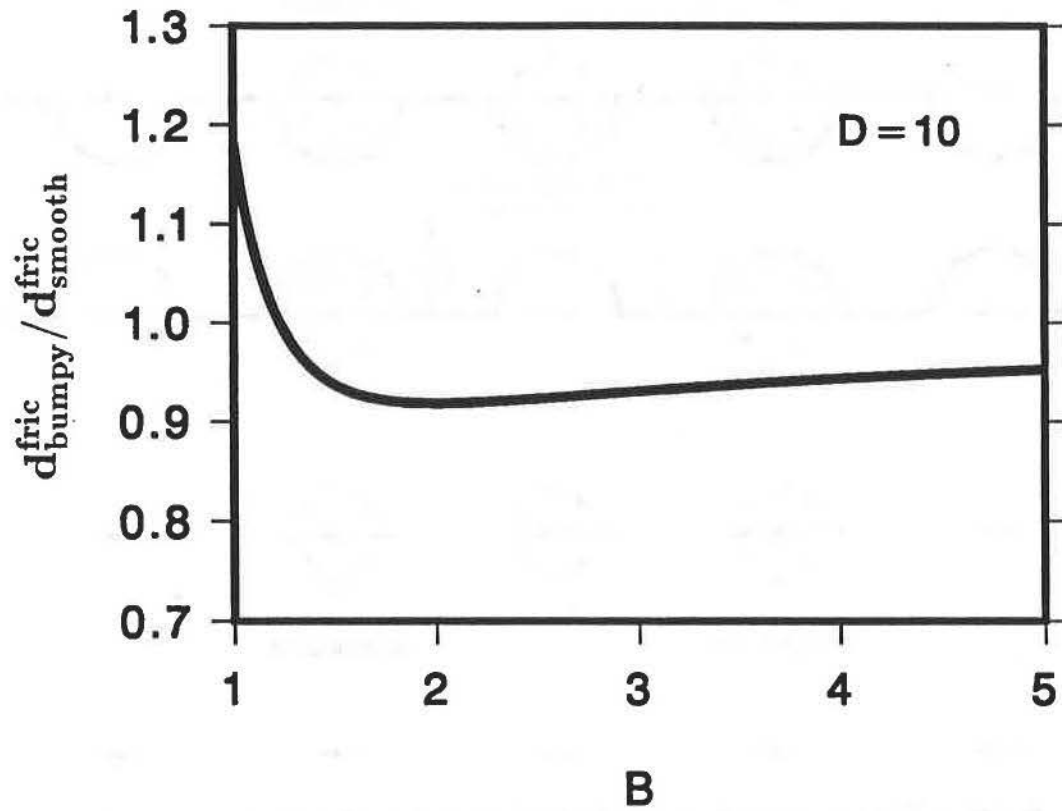


Figure 3: The ratio of friction drag from a bumpy-walled model to friction drag from a smooth-walled model. Both models have the same channel width ( $= 2DR$ ).

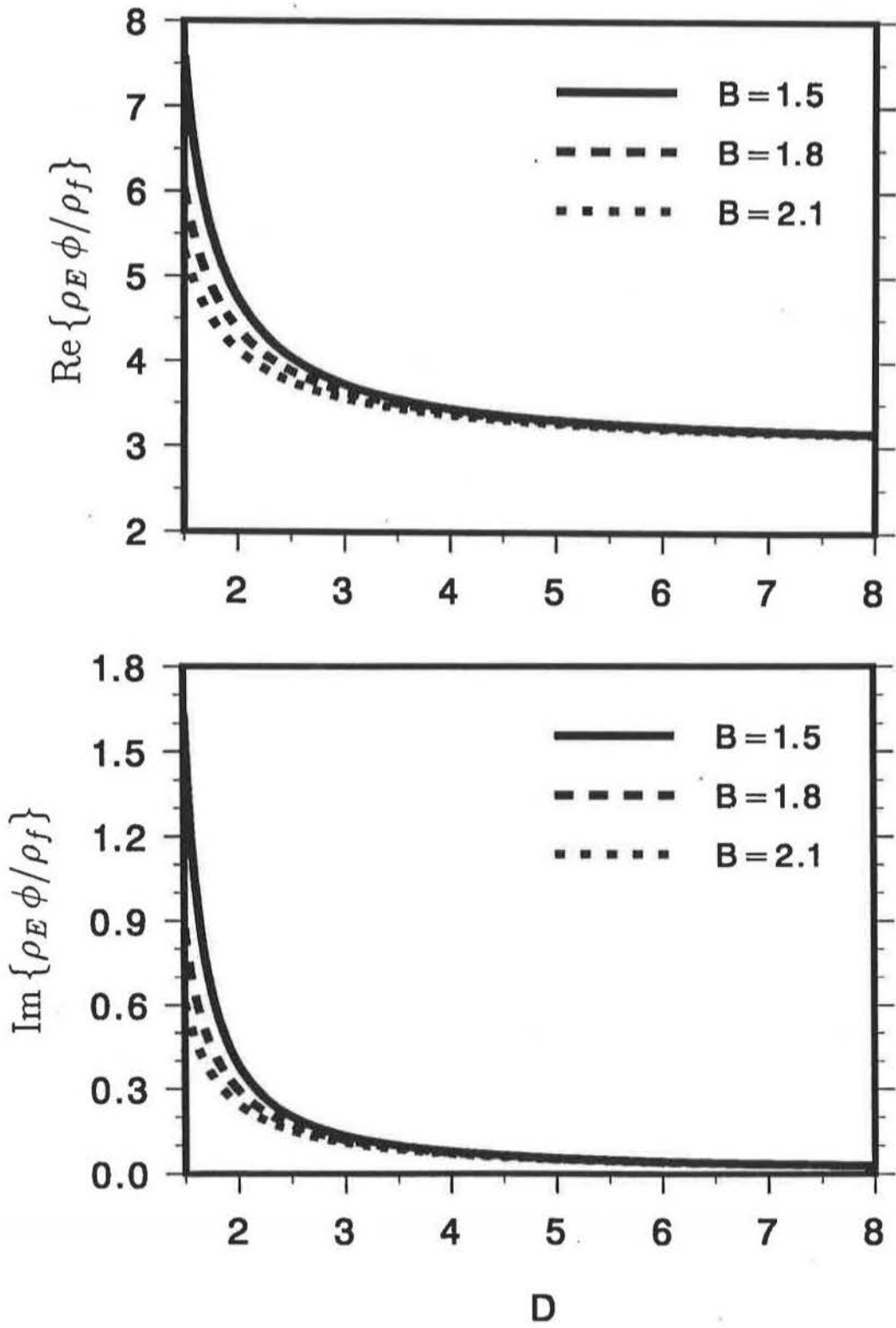


Figure 4: The real and imaginary parts of the dimensionless quantity  $\rho_E \phi / \rho_f$ .

**SESSION 2**

**DEVELOPMENT AND PRODUCTION**

Monday Afternoon  
Session Co-Chairmen: E. Witterholt and T. Stark

## **Relating Rock Physics from the Laboratory to an in situ Velocity Tomogram**

**Gary Mavko, Nathalie Lucet, Mark VanSchaack  
Department of Geophysics  
Stanford University**

We are exploring ways of applying laboratory-derived relations between seismic measurements and rock properties to data obtained in the field -- in particular, well logs and the high quality velocity images obtained with cross well seismic tomography. A specific goal is to derive the best possible images of porosity and shaliness from the velocity tomogram, as well as estimates of their uncertainty.

In a particular Gulf Coast example, we have found that using well logs, velocity can be related empirically to porosity and clay volume, with very high correlation. This is very similar to our observations in the laboratory, except that the regression coefficients differ due to the lower degree of consolidation in the field.

Three general approaches are used for creating porosity images:

- Geostatistical techniques - in which velocity, porosity, and shaliness are considered to be random fields, and we make no a priori assumptions about the physical relation between them. Instead we derive their statistical relation (auto and cross correlations) from the velocity and well log data.
- Laboratory rock physics - in which we use various laboratory and theoretical relations between velocity, porosity, and clay to deterministically map the tomogram, point by point, to rock properties.
- Combination of rock physics and geostatistics - in which we apply theoretical, laboratory, and log-based velocity-porosity-clay relations to the tomogram using statistical tools

As expected, ordinary kriging using only the porosity logs gives a fairly detailed image of porosity very near to the wells, but a low resolution, low accuracy image in the interwell region beyond the correlation range. Adding velocity information via cokriging gives slightly more detail in the interwell region. The use of the pure rock physics techniques gives porosity images with interwell features that mimic the velocity image; however, they do not reflect the uncertainty of velocity-porosity relations, and they do not match the measured porosities at the wells. The images that combine rock physics and geostatistics have the best features from both methods.

# The Effect of Permeability Heterogeneity on Oil-Water Displacement in Porous Media

D.W. van Batenburg, H. Bakken, J. Bruining, and G.G. Drijkoningen

Faculty of Mining and Petroleum Engineering, Delft University of Technology, Mijnbouwstraat 120, 2628 RX Delft, The Netherlands

## Abstract

Conventional work on permeability heterogeneity focusses on viscous flow ignoring the effect on capillary pressure. We show however that small-scale permeability variations may lead to capillary trapping of one phase in a two-phase system, in our case oil in a water-oil system. It illustrates the fact that we must properly account for processes occurring on a macroscopic scale (few cm's), in a mesoscopic world (m's).

## Introduction

Waterdrive is an important recovery mechanism for hydrocarbon reservoirs. Some of the most prolific oil fields in the world have been produced or are operating under waterdrive condition.

This paper focusses on the description of a two phase flow where the presence of macroscopic heterogeneities induces additional capillary forces [1]. As elaborated by King [2], we use a probabilistic simulation method based upon the streamline approach, where capillary forces are included. Using such an approach, we can study the effect of capillary forces in the presence of permeability heterogeneities with regard to displacement characteristics and small-scale entrapment of oil. Such a probabilistic simulation appears to be robust, in particular for viscous unstable systems, although it is acknowledged that from the computational point of view, it is rather time consuming.

## The initial state

Consider a square horizontal porous medium of height  $h$  and length  $L_1$  with permeability  $k_1$ . Within it, there is a block of the same height  $h$  and length  $L_2$  with permeability  $k_2$ , as shown in Figure 1. The porous medium contains water at connate water saturation  $S_{wc}$  and oil at a saturation of  $(1 - S_{wc})$ . Water is injected from the left and oil and water are produced on the right. The other two sides of the medium are considered as no-flow

boundaries. Oil and water are considered incompressible and immiscible. Gravity forces are excluded but could also be introduced without much difficulty.

The parameters determining the flow in the heterogeneous model are described by two dimensionless numbers. The first one is the macroscopic capillary number  $N$  which is a scaled ratio of the viscosity  $\mu$  and the root of the permeability  $k$ :

$$N = \frac{\mu_o q}{\sigma \sqrt{k}},$$

in which  $\sigma$  denotes the interfacial tension between oil and water and  $q$  the total flux; the subscript  $o$  refers to oil. The other parameter determining the flow, is the ratio of the viscosities:

$$M = \frac{\mu_o}{\mu_w},$$

where the subscript  $w$  refers to water. As an aid we shall also use the ratio of the permeabilities  $\beta$ :

$$\beta = \sqrt{\frac{k_2}{k_1}}.$$

Relative permeabilities quadratic with respect to reduced saturations were used. For the capillary pressure  $p_c$ , Leverett's [3], empirical relation was used, i.e.,

$$p_c(\vec{r}, S_w) = \sigma J(S_w) \sqrt{\frac{\phi}{k(\vec{r})}} \quad (1)$$

where  $\phi$  denotes the porosity,  $\vec{r}$  denotes the position vector in space and  $J(S)$  is the Leverett J-function. We have taken for  $J$ :

$$J(S) = (1 - S)(2S^2 - 2S + 1) \quad (2)$$

## Flow relations

The model equations (here given as (8) and (11)) are derived as follows. The mass balance equations for each phase is given by

$$\phi \frac{\partial S_\alpha}{\partial t} + \vec{\nabla} \cdot \vec{u}_\alpha = 0, \quad \alpha = o, w, \quad (3)$$

where  $\vec{u}_\alpha$  is the specific discharge (Darcy velocity) of phase  $\alpha$ . Adding the two equations and recognizing that  $S_o + S_w = 1$ , we obtain the following condition for the total specific discharge  $\vec{u} = \vec{u}_o + \vec{u}_w$ :

$$\vec{\nabla} \cdot \vec{u} = 0. \quad (4)$$

For the equation of motion Darcy's law for multiphase flow is applied

$$\vec{u}_\alpha = -\lambda_\alpha \vec{\nabla} p_\alpha, \quad \alpha = o, w, \quad (5)$$

where  $\lambda_\alpha$  is the mobility of phase  $\alpha$ . Assuming the difference in pressure between the oil and water phase is given by the capillary pressure, i.e.,  $p_c = p_o - p_w$ , we obtain by adding the two last equations:

$$-\vec{\nabla} p_w = \frac{\vec{u}}{\lambda_{tot}} + \frac{\lambda_o}{\lambda_{tot}} \vec{\nabla} p_c, \quad (6)$$

in which the abbreviation  $\lambda_{tot} = \lambda_o + \lambda_w$  is used. We now define the stream vector  $\vec{\Psi}$  by:

$$\vec{u} = \frac{q}{L} \vec{\nabla} \times \vec{\Psi}. \quad (7)$$

We take the curl of the one-but-last equation and substitute the definition of the stream vector. Assuming all quantities are independent of  $z$ , we obtain for the  $z$ -component  $\Psi_z$  of the stream vector (2D-stream function formulation):

$$\frac{q}{L} \vec{\nabla} \cdot \left( \frac{1}{\lambda_{tot}} \vec{\nabla} \Psi_z \right) = \frac{\partial}{\partial x} \left( \frac{\lambda_o}{\lambda_{tot}} \frac{\partial p_c}{\partial y} \right) - \frac{\partial}{\partial y} \left( \frac{\lambda_o}{\lambda_{tot}} \frac{\partial p_c}{\partial x} \right). \quad (8)$$

It can be shown that the right hand side of (8) becomes zero when the capillary pressure function only depends on the saturation i.e. in the absence of heterogeneities. Substitution of equation (1) with position dependent permeability into (8) leads to a source term on the right hand side of (8)

$$\frac{d}{dS} \left( \frac{\lambda_o}{\lambda_{tot}} \right) \sigma J(S_w) \sqrt{\phi} \left[ \vec{\nabla} S \times \vec{\nabla} (k^{-1/2}) \right]_z \quad (9)$$

This means that the flow is not rotational free when the source term is non-zero. Such a non-zero source term induces a vortex motion. It is noted that the source term is only non-zero if the saturation gradient and the permeability gradient have different directions. In a homogeneous permeability field this term is always zero.

Also in the presence of capillary forces, we assume we can write  $\vec{u}$  as  $f_w \vec{u}$  where  $f_w$  is the fractional flow function; this is the streamline approach. We can then write equation (3) for the water phase as:

$$\phi \frac{\partial S_w}{\partial t} = -\vec{u} \cdot \vec{\nabla} f_w, \quad (10)$$

We used equation (4). In the direction of flow  $\xi$ , i.e. in the direction of the specific discharge vector  $\vec{u}$ , one obtains

$$\phi \frac{\partial S_w}{\partial t} = -u_\xi \frac{\partial f_w}{\partial \xi} = \frac{q}{L} \frac{\partial \Psi}{\partial \zeta} \frac{\partial f_w}{\partial \xi}, \quad (11)$$

where equation (7) was used in the coordinate system  $\xi, \zeta, z$ ;  $\xi$  is the coordinate in the direction of flow and  $\zeta$  is the coordinate perpendicular to the flow direction. In the streamline approach one derives

$$f_w = \frac{\lambda_w}{\lambda_{tot}} + \frac{\lambda_w \lambda_o}{\lambda_{tot} u_\xi} \frac{\partial p_c}{\partial \xi} \quad (12)$$

The boundary conditions for the flow are given by:

$$\begin{aligned} \Psi_z &= 0 & \text{for } 0 \leq x \leq L, y = 0; \\ \Psi_z &= 1 & \text{for } 0 \leq x \leq L, y = L; \\ \frac{\partial \Psi_z}{\partial n} &= 0 & \text{for } x = 0, 0 \leq y \leq L; \\ & & \text{for } x = L, 0 \leq y \leq L. \end{aligned}$$

## Numerical implementation

For the simulations a staggered grid is used. The saturation dependent variables such as capillary pressure, fractional flow and mobility are defined in the centre points of squares. The stream function values are then assigned to the points located on the corners of the square. For calculation of the normalized stream function, the saturation dependent properties are averaged over the relevant sides of the squares. Equation (8) is discretized using a conventional five point molecule [4].

A time step starts by calculating the value of the normalized stream function,  $\Psi$ , on the corners of each square. To this end the discretized form of equation (8) is solved iteratively. Saturation dependent properties are considered constant during stream function calculation. Subsequently two independent random numbers are generated. The two numbers determine the location in the grid where "the walker"  $\Delta S$  will be trapped. The location is found by following the streamline corresponding to the first random number until the fractional flow value for the current block "equals" the second random number. The procedure is repeated until the required number of pore volumes has been injected.

## Results and discussion

Figure 2 shows the comparison between the cases for two different capillary numbers, a small and a large one, being represented by the left and the right column, respectively. The different rows correspond to different pore volumes injected. In the figure we show the streamlines with the water front, illustrated by water saturation values between 0.5 and 0.7.

Let us concentrate on the first column of figure 2. The first picture shows the features when the water front is just about to reach the heterogeneity, while the next one in the column shows what happens when the water front has just reached the heterogeneity. By looking close at the streamline pattern, we can see that the pattern is less dense than before the water entered the zone. This implies that the total flux through the entrance of the region has changed, indicating that capillary forces try to prevent the water from entering the region. This effect is caused by the term in equation (9).

Now we concentrate on the comparison of the first column with the second column. The difference between the two lies in a different capillary number, being larger in the second column. Actually, the capillary number in the second column is so large that viscous effects are dominant over capillary effects and so can be interpreted as neglecting the capillary-forces effect. The first observation is about the streamline distribution: we can observe that the capillary number has hardly any effect on that. What we do see however is that the distribution of the water saturation is totally different. After one pore volume injected some oil is still trapped at the entrance of the high permeable zone. The difference in saturation distribution is mainly caused by the additional term in the fractional flow equation (12).

In the next figure(3) we show the saturation distributions. The effect of capillary forces is pretty well pronounced in these pictures as can be seen by the depression in the distribution even after the whole heterogeneity is flooded. Also, the picture shows that the heterogeneity is not swept uniformly. This last feature is even better illustrated in the last picture in the column. The entrance of the heterogeneity is still less swept than the rest of the zone, as can be seen by the smaller values of the water saturation.

## Conclusions

1. In a simple heterogeneous model saturation jumps occur across boundaries of regions with different permeabilities.
2. Capillary forces influence the streamline pattern and the saturation distribution in a simple model with permeability heterogeneity. These effects are originating from the local permeability gradients.

## Acknowledgements

Scholarships given by The Norwegian Institute of Technology, NTH, and The Norwegian Council for Science and The Humanities, NAVF, made H. Bakken's stay at Delft University of Technology possible. A research grant from Delft University of Technology for the project "Free boundary problems for multiphase flow in porous media", supplied the computer on which the simulations were carried out.

## References

- [1] Kortekaas, T.F.M., "Water/Oil Displacement Characteristics in Crossbedded Reservoir Zones," *SPEJ*, (December 1985), pp. 917-926.
- [2] King, M.J., "Probability approach to multiphase and multicomponent fluid flow in porous media," *Physical Review A*, (1985), 35, No. 2, 929-932.
- [3] Leverett, M.C., "Capillary Behavior in Porous Solids," *Trans. AIME* 142, 152, (1941), 152-169.
- [4] Ames, W.F., *Numerical Methods for Partial Differential Equations*, 2nd edition, Academic Press, (1977), pp. 98-161.
- [5] Bakken, H., "The effect of Capillary Forces in Heterogeneous Reservoirs, a Streamline Approach", M.Sc.Thesis Dietz Laboratory, Delft University of Technology, (March 1991).

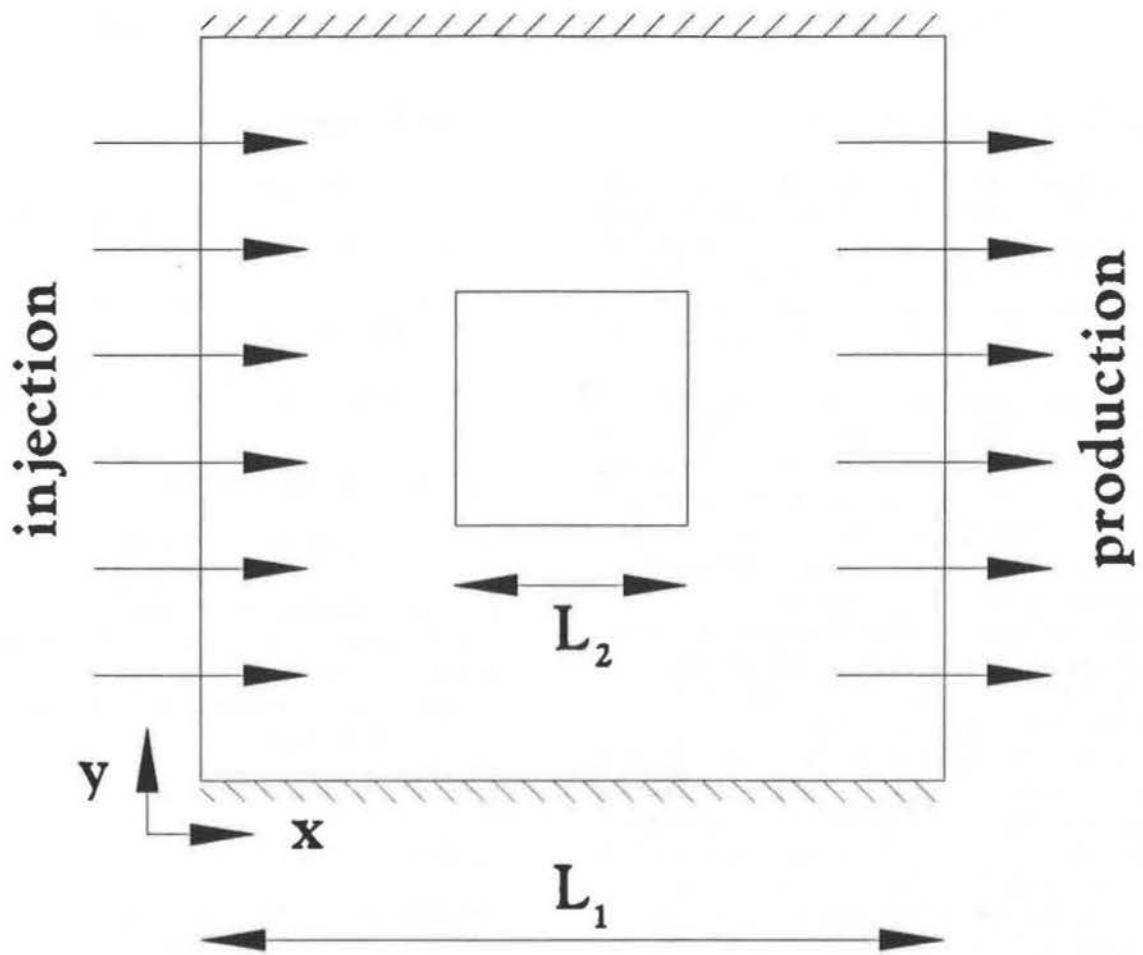


Figure 1: Schematic representation of flow unit.

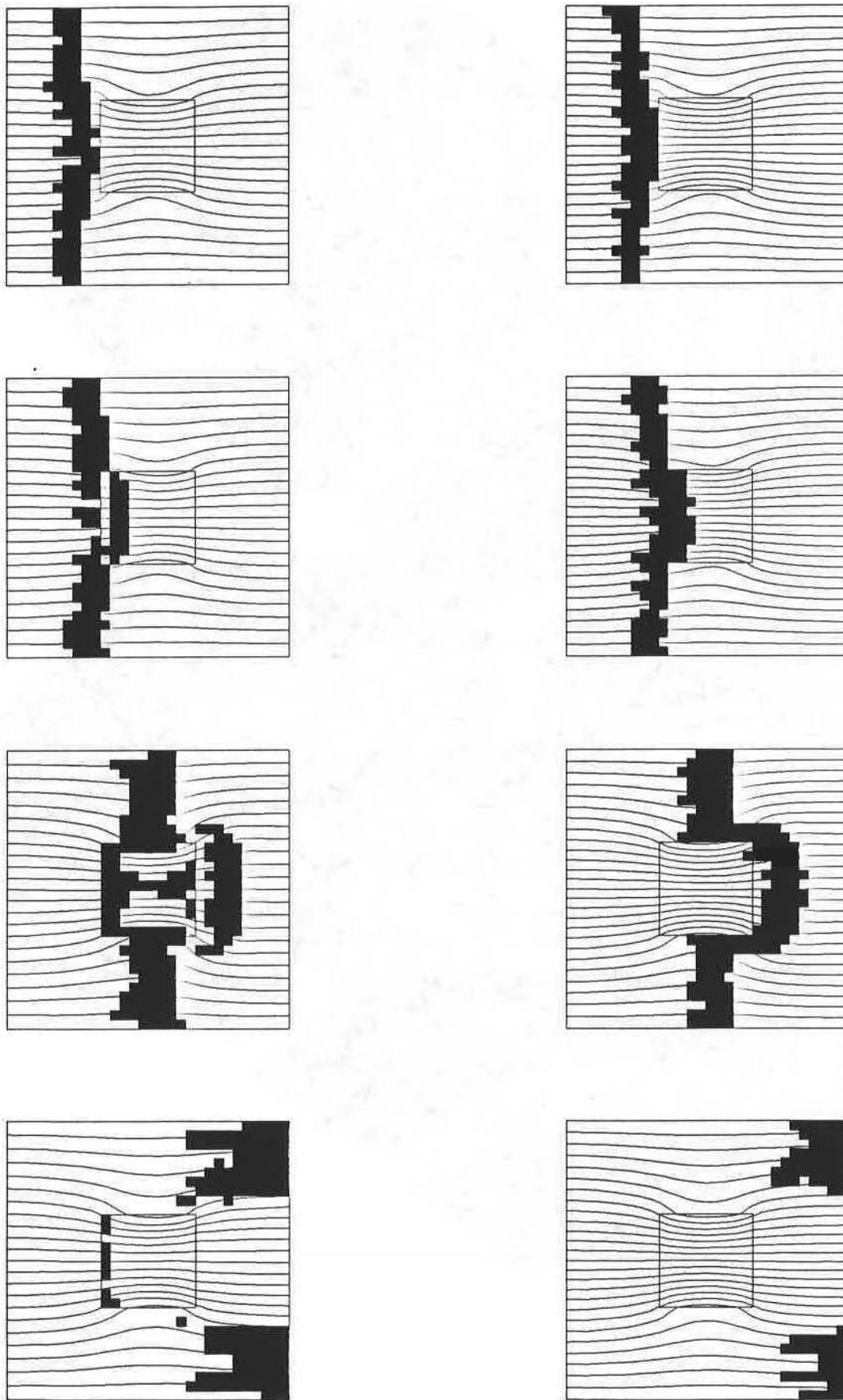


Figure 2: Comparison of streamlines and part of the water saturation distributions with low ( $N=1$ , left column) and high capillary number ( $N=10$ , right column);  $l_1/l_2 = h_1/h_2 = 3$ ,  $M = 0.5$ ,  $\beta = 2$ . Injected pore volume (a) 0.23, (b) 0.33, (c) 0.55, (d) 1.0.

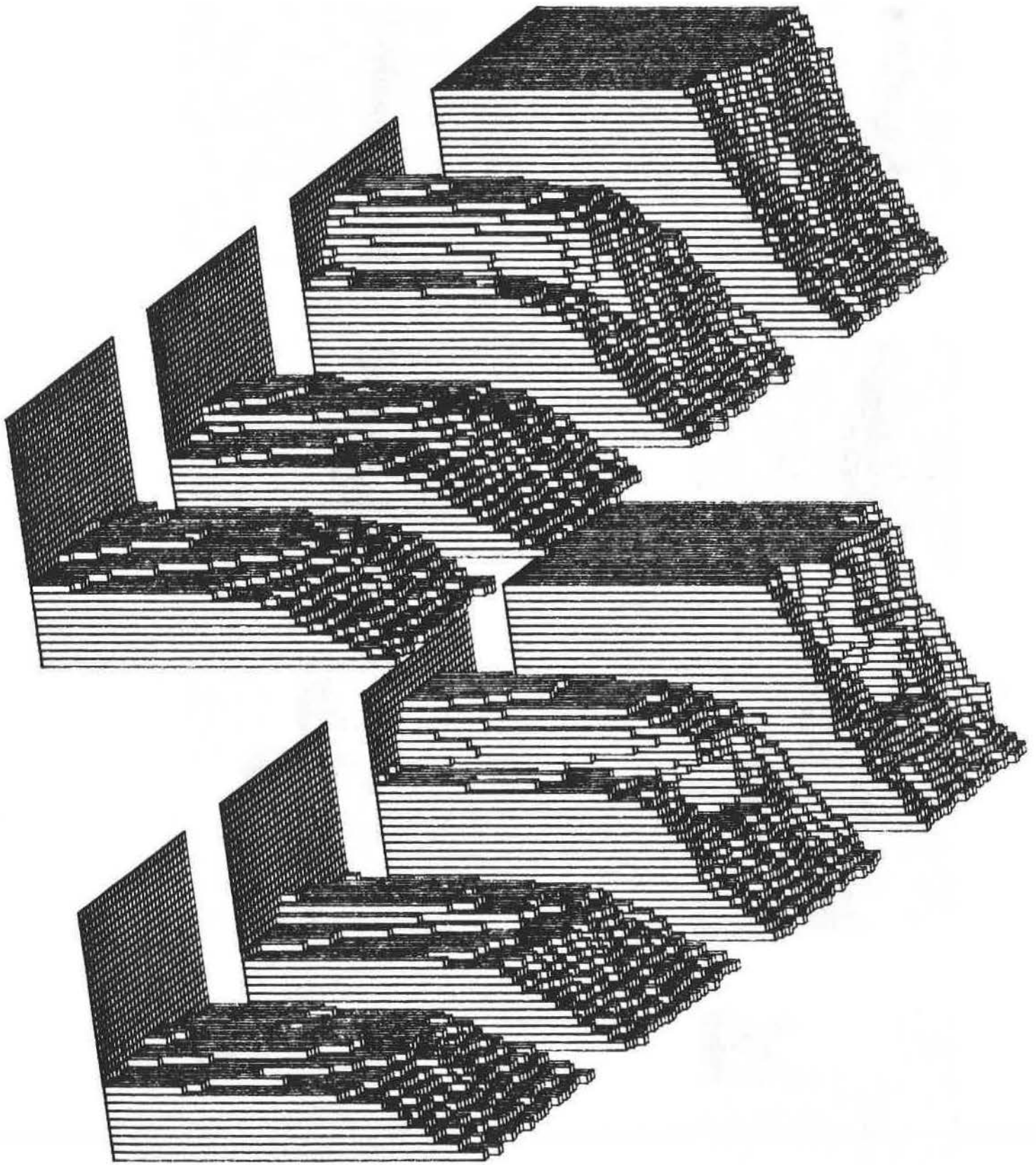


Figure 3: Comparison of water saturation distributions with low ( $N=1$ , right) and high capillary number ( $N=10$ , left);  $l_1/l_2 = h_1/h_2 = 3$ ,  $M = 0.5$ ,  $\beta = 2$ . Injected pore volume (a) 0.23, (b) 0.33, (c) 0.55, (d) 1.0.

# A CASE STUDY OF RESERVOIR HETEROGENEITY IN A FLUVIAL SANDSTONE: THE GYPSY SANDSTONE OF OKLAHOMA

J.D. Doyle, M.L. Sweet, D.J. O'Meara, V. Langlais  
B.P. Exploration

Reservoir simulation models based on detailed outcrop description provide a means to evaluate the importance of various types of heterogeneity on reservoir performance. To better understand the effects of heterogeneity on fluvial reservoirs, three dimensional reservoir simulation models were constructed based on descriptions of the lithofacies, internal architecture, and porosity and permeability distribution of a multistoried fluvial sequence, the Pennsylvanian Gypsy sandstone, at a study site 25 miles west of Tulsa, OK. A detailed two dimensional description of the exposure also provides a basis for measuring the spatial variability of reservoir properties and for assessing and calibrating geostatistical methods which have been proposed for use in developing reservoir models.

Reservoir models based on the outcrop use deterministic mapping of channel sandbodies together with stochastic representation of facies as a basis for assigning reservoir properties. Results of simulation of simple, incompressible, two-phase flow with various well configurations are discussed in comparison to models with constant, averaged permeability.

To prepare the models, the fluvial architecture of six channel sandbodies was mapped on the parallel walls of a 300 m roadcut using photomosaics. Macroforms identified within sandbodies are lateral accretion deposits modified by chute channels. Channel sandbodies decrease in size upward from 200 m wide and 10 m thick to 60 m wide and 3 m thick. Erosional surfaces comprising the bases of the lower three channels could be traced longitudinally 330 m into a grid of 22 boreholes; lower order features could not be correlated. Laterally, the channel sandbodies thin into floodplain mudstone and siltstone.

Each channel-fill sequence is comprised of up to 5 sandstone facies in addition to laterally and vertically adjacent mudstones and siltstones. All of these facies were extensively sampled to determine their porosity and permeability characteristics. Spatial distribution of these facies is variable, and their lateral extent is commonly less than the spacing between borings. Therefore a stochastic representation of facies was chosen for the models.

# INTEGRATION OF GEOLOGY AND GEOPHYSICS IN STOCHASTIC MODELS

**A. GALLI , C. RAVENNE and Heresim Group**

To build an accurate stochastic model of a reservoir we need to integrate all the data (wells, seismic) and the available geological information.

The Heresim model for reservoir description is based on the idea that heterogeneities are partly controlled by sedimentology. So that we first simulate the architecture of the reservoir in terms of lithofacies. This first simulation is computed after our accurate sequence stratigraphy study of the data which provides the sequential ordering of the lithofacies, the boundaries of the sequence and the chronostratigraphic markers. Then inside these lithofacies we reconstitute the spatial variability of petrophysical parameters such as porosity and permeability.

Because of the flexibility of this model we can integrate both geological knowledge, and seismic information.

The geological knowledge gives the general depositional environment. It also provides precise ideas of the vertical splitting of the reservoir into units which are homogeneous from a geological point of view, mainly using sequence stratigraphy concepts. This also give ideas of chronostratigraphic markers which can be used as reference levels for statistical computation and geostatistical simulations. This together with the wells provides precise vertical knowledge and depending on the number of wells and their separations some lateral knowledge, quantified by means of variograms and of vertical proportions (i.e : at each vertical level probability to have a given lithofacies). The seismic data gives less vertical information but increases the lateral information available.

This can be used at different levels in the modelling :

- more precise determination of some unit boundaries
- general knowledge of lateral variations of the geological environment, and/or quantification of the horizontal anisotropy by means of variogram computation on amplitudes.
- If there is a reasonable relation between some seismic attribute and lithologies we can obtain the probability to have a given lithofacies in between wells from the seismic data or in some cases the sand shale ratio over the thickness of the reservoir. Both can be incorporated as constraints in Heresim by means of what we call horizontal proportion curves (which are probabilities to have a given lithofacies on the thickness of the reservoir). Note however that this lateral evolution has to be combined with the vertical evolution obtained using the wells.

Here, we just want to illustrate some new constraints brought by seismic data, mainly ranges of horizontal variograms and modification of proportion curves.

For the geological studies, the basic concepts are provided by sequence stratigraphy. For seismic studies, the basic tool is seismic stratigraphy as described by

"Vail et al. in AAPG memoir 26. Vail et al. (1977) demonstrated that primary seismic reflections follow geological time lines and thus seismic sections show chronostratigraphy at the resolution of the seismic data plus or minus the breadth of one half of a reflector". (Vail, preprint 1990). As we work in the stratigraphic frame work, and as all the geostatistical parameters must be computed parallel and perpendicular to the reference level, the first step is to flatten the seismic section, that is to say to horizontalize one selected reflector in the reservoir area, and of course to delete the effects of post-sedimentary faults.

Several trials must be carried out before getting the best flattening and often, the reservoir zone, even on seismic data must be split in different seismic units with different flattening markers.

In seismic stratigraphy, seismic facies units (see Sangree and Widmier, 1977) can be defined in the depositional sequence. One unit is characterized by a certain set of values of the seismic parameters (amplitude, continuity, ..... ) which is different in other units. After the full seismic stratigraphy analysis, these units can be interpreted in lithologies.

In this case study, the seismic facies units are based on amplitude values. Sandstone can be found in both positive or negative amplitude values. Horizontal variograms have been computed along all the lines (vertical sampling : 2 m sec).

The first set of simulations shows three types of 3D simulation conditioned by the same wells. These simulations differ by the computations of proportion curves and mainly by the computation of variograms used after for these simulations.

In the first one, the range of the fitted variogram is provided by geologists (based only on geological knowledge), in the second one this range is obtained from the geostatistical analysis performed on the 33 available wells and in the third one, this range is obtained from the geostatistical analysis carried out on the flattened seismic section, giving of course a shorter range.

Some geostatistic tools are also presented, namely the experimental variogram calculation and its fit. This presentation emphasizes the interest of this tool. Remember that it characterizes the spatial correlation for the data, which are point data or convoluted data. The model which gives a good fit of the experimental variograms is then used to make (punctual or convoluted) estimation or simulation. The first one is the best linear unbiased estimation, the second one gives more variable values honoring the fitted model.

As the shape of the experimental variogram depends on the spatial correlation of the data, the hypothesis of stationarity, regularization can be refuted or not regarding the variogram. In the same way, the cross-variogram between two variables can show some cross-correlation behaviour. On the two experimental variograms of two seismic amplitude fields, one is valid with the conceptual model commonly used in inversion seismic, the other one is not, at least at this observation scale.

Thus, knowing the experimental spatial correlation of the data, it is possible to simulate a given variable with the same structural behaviour. And if you add correlation between two variables or more, it is possible to elaborate a geostatistical model which honor what you know on your data. That is what is shown on the third part of the presentation. Two types of geostatistical model are tested. These two examples are 2 dimensional and non conditional but it is easy to make them 3D and conditional. All two work by gaussian values simulations truncated by adequate thresholds. The first

one assumes that the facies are in relationship with a seismic attribute. This model needs the correlation spatial model of the underlying gaussian variable, the seismic attribute given by the geophysicists and the correlation coefficient between these two variables. In the presented example two correlation coefficients are used: .8 gives a lithofacies section which is very correlated with the seismic attribute and .25 gives a lithofacies section which is similar to the seismic attribute but with more variations.

The second one is based on the Heresim 3D software. The seismic attribute is transformed into a section of lithofacies proportions which gives the thresholds section. These lithofacies are seismic facies and the probability curves have to be calculated on experimental data. The two simulations presented are obtained with two possible proportion curves of the lithofacies versus seismic attribute.

The presented works already show that to obtain best reservoir simulations it is possible to use the links which exist between seismic attributes and lithofacies. For these first approaches, the seismic sections have been used after geological interpretation in term of seismic facies. For the future, it will be interesting to test other seismic variables.

# CLOSING THE LOOP: How Reservoir Testing, Production, and Simulation Results Feed Back to Seismic Reprocessing and Interpretation

Lisa Stewart\*

May 30, 1991

## Summary

A study was made of the Helm Reservoir in the North Sea to determine if the reservoir model could be enhanced and the production history matched by the combined interpretation of core, log, seismic and production data. The regional tectonic history of the North Sea was examined to place constraints on the structures and depositional environments of the formations sampled by the logs and seismic. Surface seismic lines were reprocessed using a variety of schemes; the optimum scheme was chosen to be the one giving images that fit both the VSP and the continuity requirements of the production history match. The structural model of the reservoir was modified based on the new seismic images, along with dipmeter, well logs, and pressure decline in the wells. The revised structural model is consistent with the 3-D irregular grid reservoir model that was history matched using pressure test and production data. The revised reservoir model suggests that potential target zones exist for future development.

---

\*Schlumberger Doll Research, Ridgefield, CT 06877. Submitted to the SEG Research Workshop on Lithology: Relating Elastic Properties to Lithology at all Scales, St. Louis, Missouri, July 28 - August 1, 1991

## Introduction

Our understanding of a reservoir often follows a "one-way street", starting with a *static* description, involving the interpretation of geological and geophysical data, and ending with a *dynamic* model of reservoir performance. A great deal of the work on the methodology of reservoir characterization (e.g., Haldorsen, 1986; Weber, 1986) recognizes the need for quantifiable input from many disciplines and on many scales, with the dynamic reservoir model as the ultimate product. Within any one step of the static reservoir description or dynamic production simulation there will be several iterations: lithology, porosity, and saturation estimates from logs may be enhanced by core data; seismic velocities may be refined with input from sonic or VSP data; the reservoir simulator grid may be updated with revised permeabilities from core data. The reservoir model, however, need not be the end of the chain. The dynamic behavior of the reservoir will invariably provide information about its geologic structure, as depicted by two way arrows on many reservoir characterization flow diagrams (e.g. Worthington, 1991), but there are few documented cases that this information has been cycled back through the processing and interpretation of the geological and geophysical data.

Testing and production data and simulation results can measure phenomena on volumetric or length scales similar to seismic measurements, and so should be compatible. These results are also quantifiable, to the extent that they indicate regions in space where flow is continuous or discontinuous, and by inference, where formation properties are relatively homogeneous, or inhomogeneous or cut by faults or other structures. The Helm Reservoir in the Dutch sector of the North Sea provides an example of the use of well test data, production data and reservoir behavior simulations to influence acquisition and reprocessing parameters and constrain interpretations of surface seismic and VSP data.

The Helm is a faulted anticlinal structure containing layered oil and gas sands separated by shales. A reservoir model was built based on initial seismic, log and core data. However, a consistent interpretation of the multiwell dynamic reservoir performance data required several features that were not included in the initial interpretation of the seismic data, such as juxtaposition of different sands across both sealing and non-sealing faults, and hydraulic isolation of individual fault blocks that had been interpreted as continuous structures on the seismic sections. In order to address some of the problems encountered in matching the production history to the reservoir production simulations, new borehole seismic data were acquired and the existing surface seismic data were reprocessed and reinterpreted. Several processing schemes were tested over the key seismic line with the most in-line well control. The optimum reprocessing was chosen to be the one that gave a section whose interpretation was consistent with the logs, VSP image, pressure testing, and simulation requirements. All the seismic lines crossing the crest of the structure

were reprocessed using the optimum scheme, and reinterpreted. The new interpretation features repositioned faults that satisfy the requirements of the production history match and some undrained areas that may be potential targets.

### Reservoir Description

The history of the exploration, development, and characterization of the Helm Reservoir has been detailed by Hastings et al., [1991] and so will only be summarized here. The exploration well, Q-1/3, and the appraisal well, Q-1/5, confirmed the hydrocarbon potential and producibility of oil from Lower Cretaceous sands at about 1200-1300 m depth. 2-D development seismic lines trending NE-SW across the structure were acquired and processed in 1979; from the interpreted seismic, maps of tops and bases of four sand layers were prepared, including major faults. Figure 1 shows a contour map of the top of the thickest sand, called F/A 4-3 (for Facies Associations 4 and 3). A cross section across the crest of the dome (along seismic line 32 of Figure 1) is shown in Figure 2.

Simulation studies were conducted to investigate the production behavior of the field. The optimum well configuration to drain the field appeared to be one vertical well at the crest of the dome surrounded by four deviated wells. Each well encountered the unexpected. The vertical well discovered two gas zones, and the first deviated well intersected only half the expected pay thickness, due to a major fault. Production commenced after four wells had been drilled. Over the next four years four more wells were drilled, and again, each yielded surprising information. Each well showed RFT<sup>1</sup> pressure profiles which indicated different pressure declines in the four sand bodies, and the inflow performance could not be matched using the current reservoir description. For example, the expected and actual inflow performance for well Q/A-8 are plotted in Figure 3. In order to match the pressures and production measured in the field, barriers were introduced between most pairs of wells, and the fluid transmissibility across those barriers was varied to fit the observations. In order to confirm the possibility of barriers to flow, the seismic data were revisited with the production and testing results in mind as constraints.

### Revising the Reservoir Model

The reservoir was believed to contain heterogeneities at all scales. The largest scale features are faults, which modify the communication and pressure declines within sand layers and vary the pressure support from the regional aquifer. At an intermediate scale, bioturbation and crossbedding within the sands created permeability anisotropy; these effects were studied through permeability measurements and CT scans on cores. Relative permeabilities varied with scale; measurements on cores indicated mixed-wettability

---

<sup>1</sup>Mark of Schlumberger

which further complicated the interpretation.

In order to refine the large scale model, a borehole seismic experiment (VSP) was conducted in one of the deviated wells, and the key surface seismic line was reprocessed using the parameters obtained from the VSP [Miller and Stewart, 1988]. The criteria for evaluating the image quality of the surface seismic data were 1) that the surface seismic image match the VSP image at the well, and 2) that the surface seismic image indicate faults or discontinuities that seem reasonable given the requirements of the production history match. Figure 4 shows the match between the VSP and the surface seismic line. The processing that gave the best image used interval velocities derived from the VSP in a pre-stack migration. Figure 5 shows the image from the reservoir portion of the key seismic line. The same processing was applied to the lines that had no VSP control, and these lines were interpreted, again with the production requirements in mind.

An example of this process is the isolation of the Q/A-5 well: the early structure map (i.e., Figure 1) showed Q/A-5 to be isolated from Q/A-6 by a fault, but there was no major discontinuity between Q/A-5 and either Q/A-1 or Q/A-2 (these correspond to well numbers on Figure 1). The pressures calculated by simulation were higher than those measured by the RFT<sup>2</sup> in Q/A-5, indicating the levels producing into Q/A-5 were isolated from those at other wells. Depending on the processing method, some of the new seismic images showed a fault on line 32 between Q/A-1 and Q/A-2, and (probably) the same fault on line 33 just west of Q/A-5. This fault has been included in the new structure map of Figure 6. If such a fault were a sealing fault, Q/A-5 would be effectively isolated from all the other wells in the field. The new map in Figure 6 indicates many of the same faults as the early map, but some of the faults have shifted or extended.

### Concluding Remarks

The premier lesson to be learned from the Helm study is the impact of new information from one type of data on interpretation of other types of data. We are all aware of the need to synthesize data from similar physical experiments made at differing scales, such as permeabilities from core and from well testing, or velocities at sonic frequencies and at seismic frequencies; however, there is additional valuable correlative information to be obtained from physical experiments of different natures made on the same volumetric or length scales. The example of using information about fluid flow behavior to help evaluate surface seismic data interpretation should not be as surprising as it appears to be at the current time.

---

<sup>2</sup>Mark of Schlumberger

## Acknowledgments

I would like to thank the management of Unocal, Nedlloyd Energy, and Schlumberger for permission to publish this paper, and my co-authors on the previously published works on this study (A. Hastings, D. Miller, and P. Murphy) for their contributions.

## References

- Haldorsen, H.H., 1986, Simulator Parameter Assignment and the Problem of Scale in Reservoir Engineering, in Lake, L.W. and Carroll, H.B.Jr., Eds., Reservoir Characterization, Academic Press, pp. 293-340.
- Hastings, A.F., Murphy, P., and Stewart, L., 1991, A Multidisciplinary Approach to Reservoir Characterization: Helm Field, Dutch North Sea, in Spencer, A. M., Ed., Generation, accumulation and production of Europe's hydrocarbons, Special publication of the European Association of Petroleum Geoscientists, No. 1, pp. 194-202, Oxford University Press.
- Miller, D. and Stewart, L., 1988, Reservoir Imaging Using VSP-Derived Velocities: A Case Study, SEG 58th Annual Meeting Expanded Technical Abstracts, pp. 534-536.
- Weber, K. J., 1986, How Heterogeneity Affects Oil Recovery, in Lake, L.W. and Carroll, H. B. Jr., Eds., Reservoir Characterization, Academic Press, pp. 487-544.
- Worthington, P., 1991, Reservoir Characterization at the Mesoscopic Scale, in Lake, L. W. et al, Ed., Reservoir Characterization II, Academic Press, pp. 123-165.

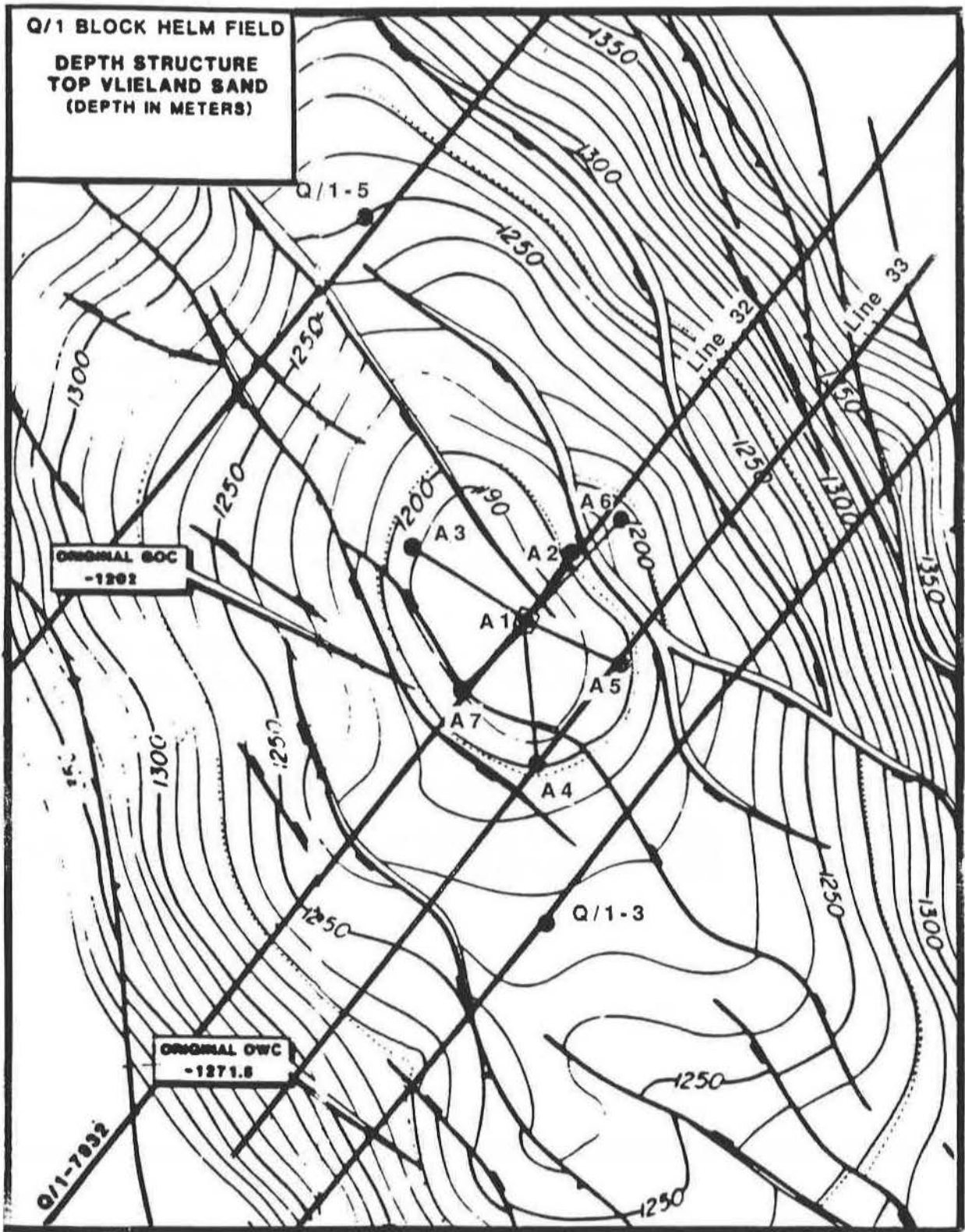


Figure 1.

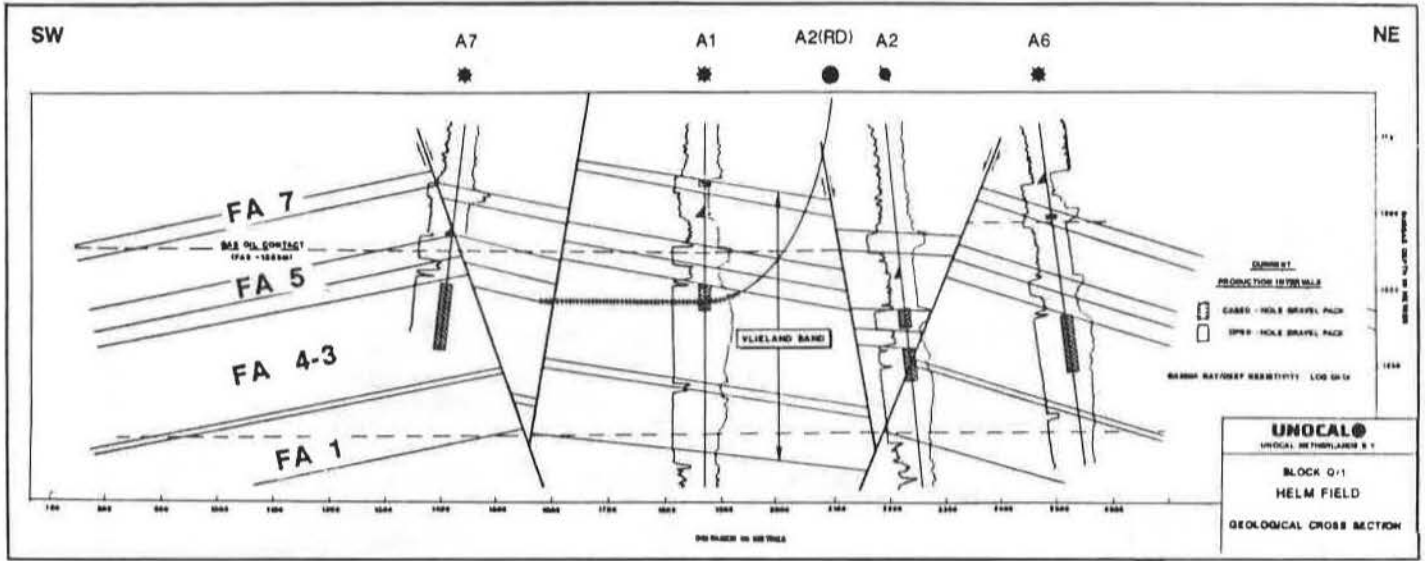


Figure 2.

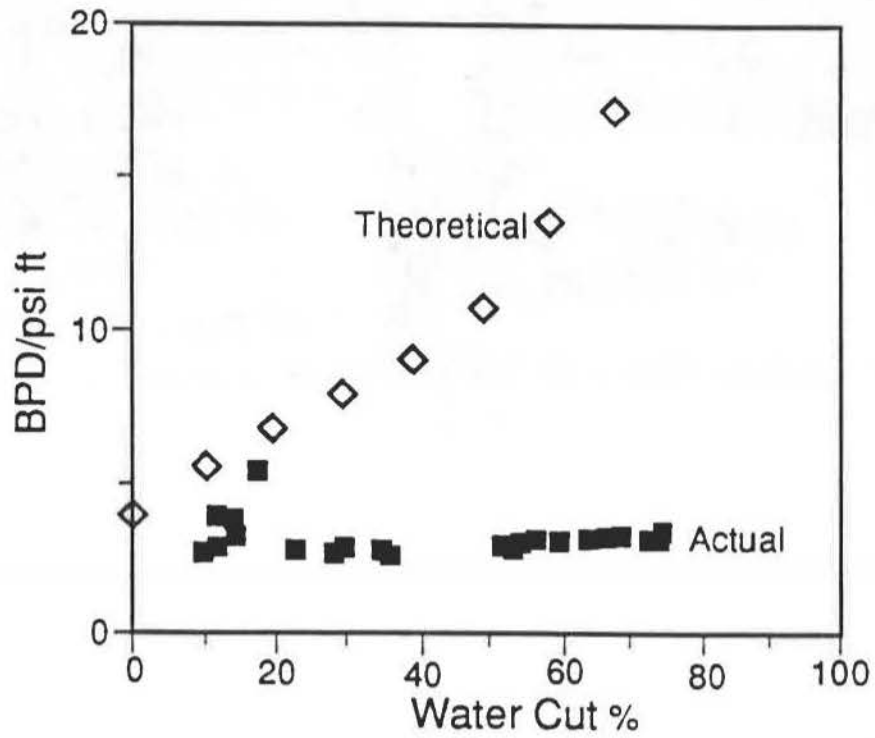


Figure 3.

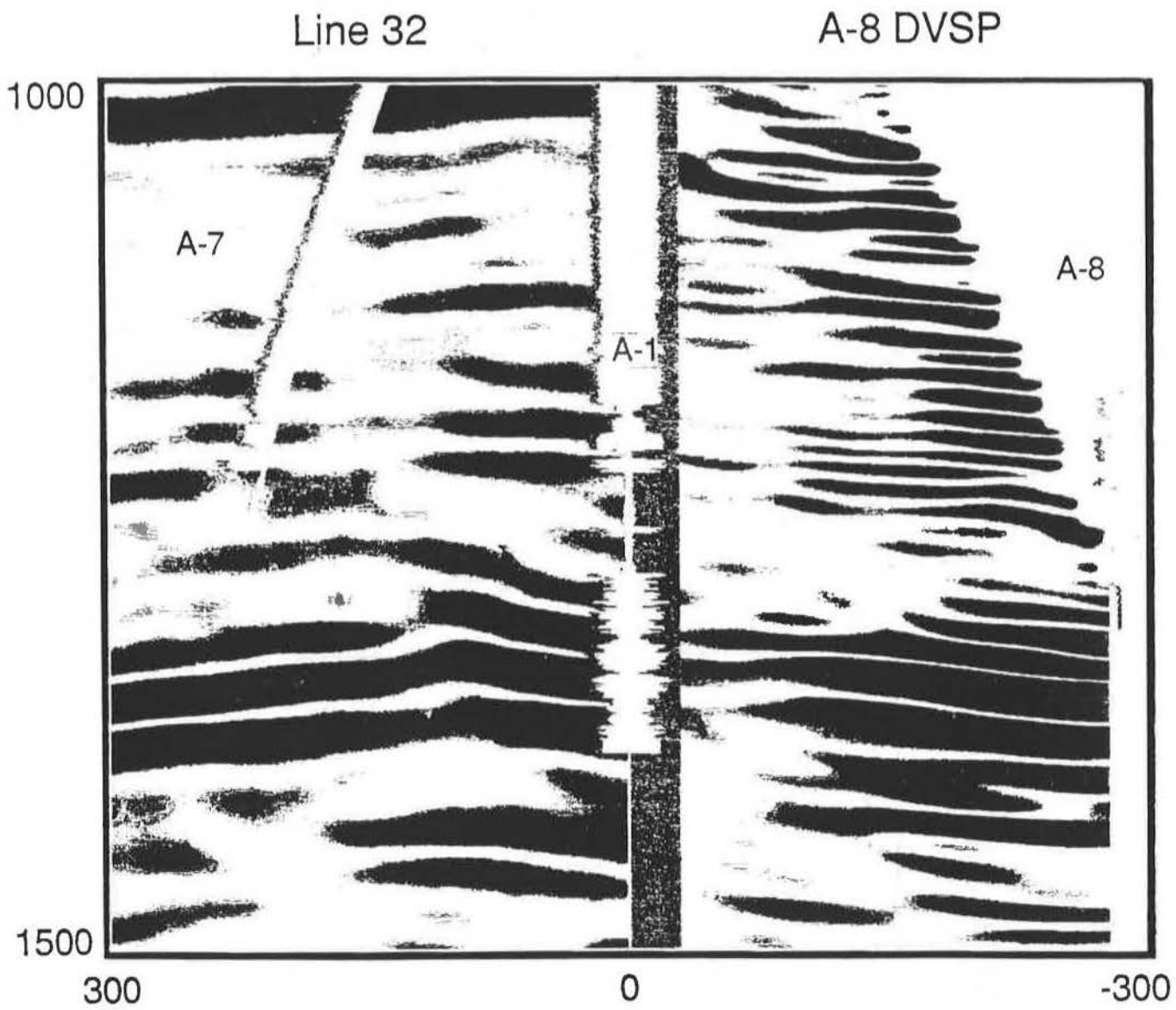


Figure 4.

Seismic Line 32

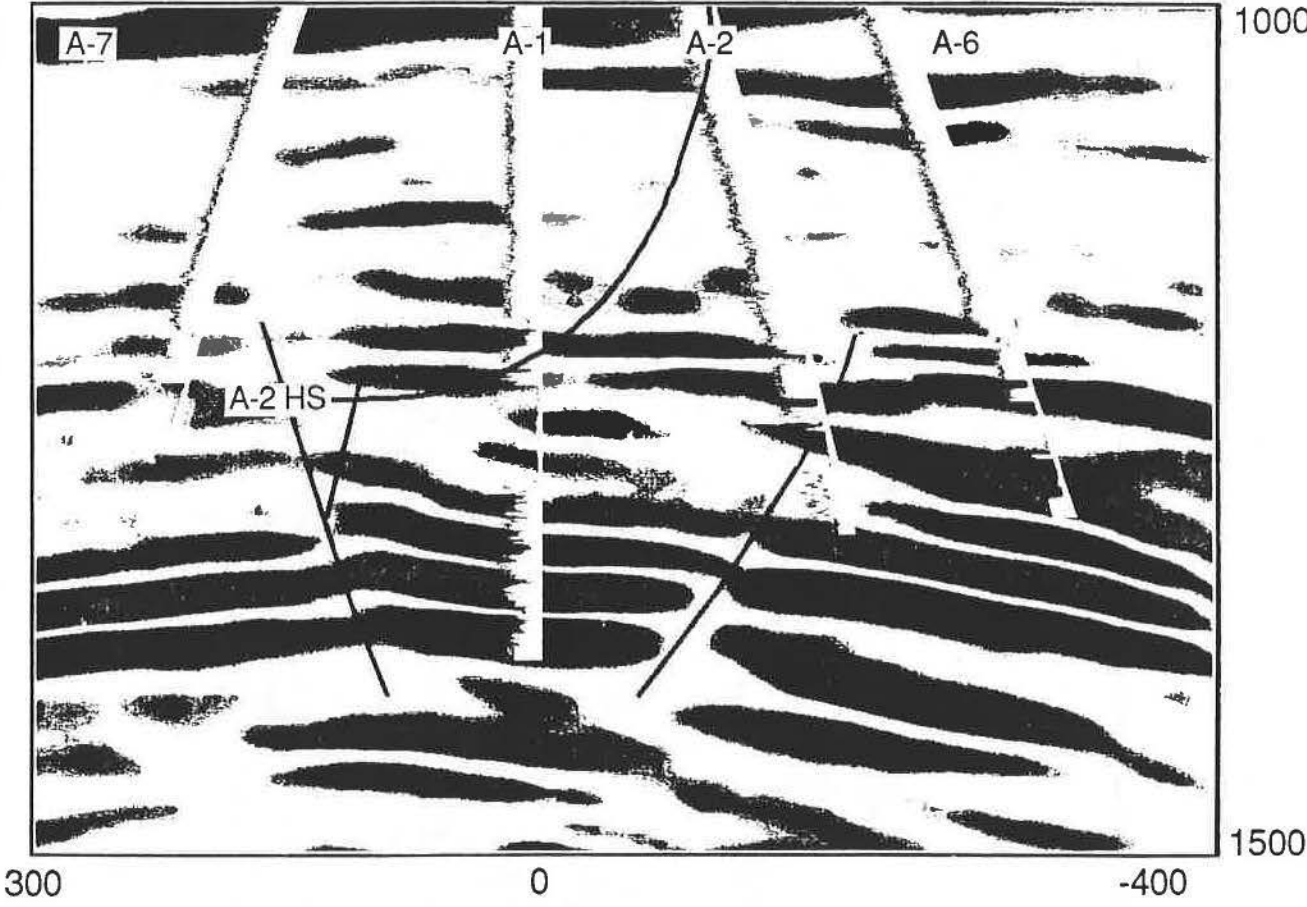


Figure 5.

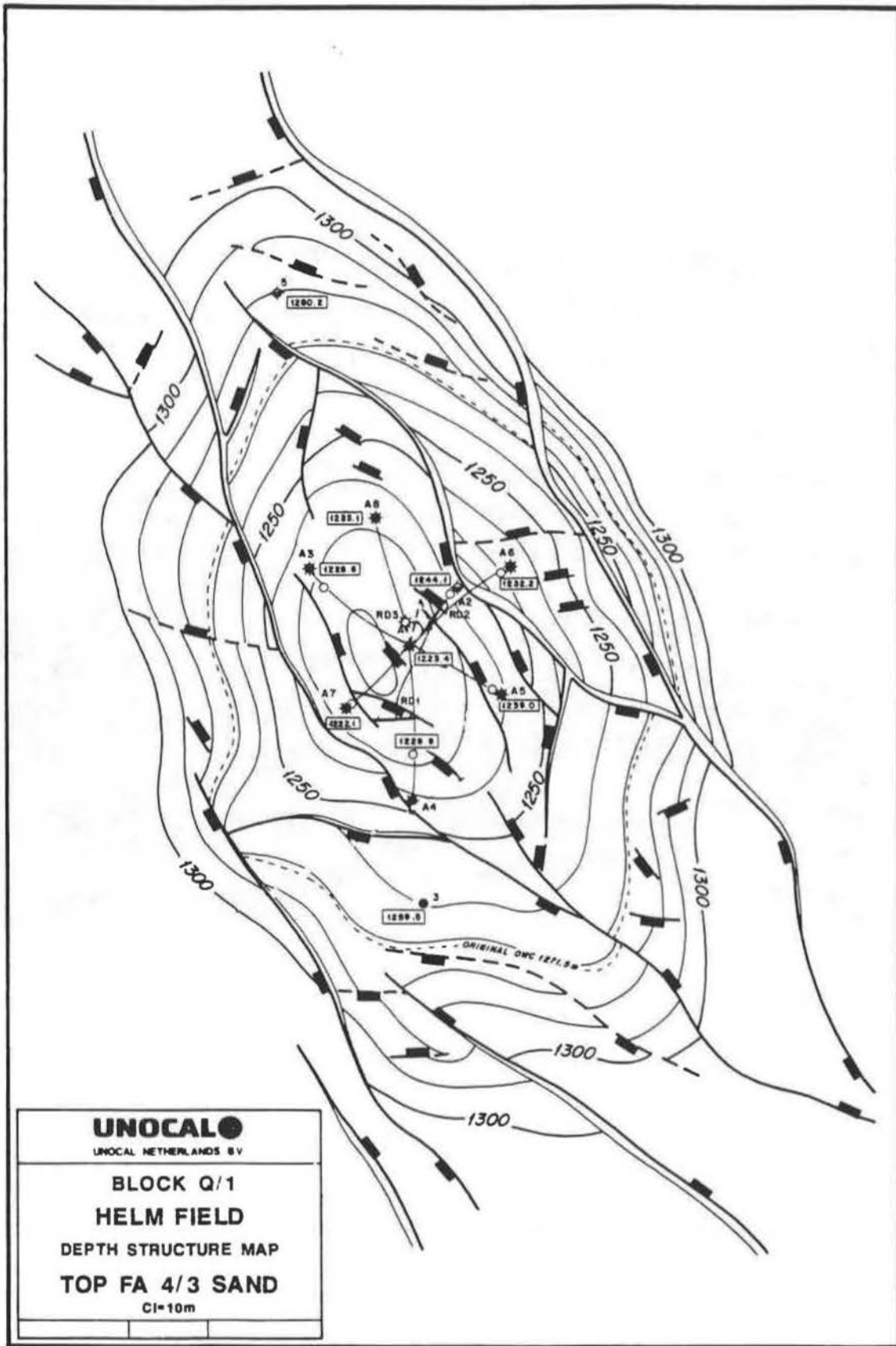


Figure 6.

# MULTICOMPONENT VERTICAL SEISMIC PROFILES FOR RESERVOIR CHARACTERIZATION, SOUTH CASPER CREEK FIELD, NATRONA COUNTY, WYOMING

D. Kramer and T. Davis, Colorado School of Mines

## Abstract:

To further evaluate the role of multicomponent seismology in reservoir characterization, the Colorado School of Mines Reservoir Characterization Project, Phase III, carried out an integrated study in the South Casper Creek Field, Natrona County, Wyoming. The purpose of the study was to image zones of heterogeneity and identify anisotropy in a structurally complex reservoir. As part of this project, multicomponent vertical seismic profiles (VSPs) were recorded in the UNOCAL 10-6-3 well. Shear-wave birefringence measurements determined from the multicomponent VSP data along with wire-line logs, three-dimensional (3-D) surface seismic data and geological information were incorporated in the study.

Faults and associated open fractures were determined to be the dominant cause of velocity anisotropy for vertically propagating shear-waves in the South Casper Creek field. Polarization of the fast shear-wave from the near-offset VSP is parallel to the strike of several of the faults interpreted from the surface 3-D seismic data. Three isolated zones of velocity anisotropy between the surface and 2700 ft were determined from shear-wave birefringence measurements. These zones correspond with a decrease in tube wave amplitude (indication of open fracturing) determined from a full waveform sonic and are associated with brittle rock units such as limestones and sandstones. Cores taken from the producing interval (Tensleep Sandstone) and a Formation Microscanner<sup>†</sup> survey indicate open fractures with a dominant strike direction nearly parallel to the fast shear-wave polarization direction.

Far-offset VSP shear-wave birefringence measurements indicate a variability in polarization direction. Further studies are being pursued to determine if South Casper Creek has a more complicated symmetry system generated by multiple fracture directions or if non-vertical propagation of shear-waves caused a change in polarization direction of the fast shear-wave.

## Introduction:

Integrating geological, geophysical, geochemical and petroleum engineering data can reduce economic risk in petroleum exploration and enhance recovery efficiency in reservoir development. Petroleum reservoirs are heterogeneous, and often contain lithologic, stratigraphic and structural barriers that impede the flow of hydrocarbons. Previous studies of the Reservoir Characterization Project at the Colorado School of Mines have focused on characterizing a deep flat lying fractured chalk reservoir in the Silo Field, Wyoming (Martin and Davis, 1987; Davis and Lewis, 1990). The purpose of this study was to develop processing and interpretation techniques for multioffset, multicomponent VSPs and incorporate wire-line logs, surface seismic data and geological information with the VSPs in order to image zones of reservoir heterogeneity and identify anisotropy in a structurally complex, folded and faulted sandstone reservoir, the South Casper Creek Field, Wyoming. Processing procedures

for the VSP data will be discussed in a separate paper entitled: Multicomponent, Multioffset VSP Processing.

Shear-waves propagating through an azimuthally anisotropic medium (generated by parallel vertical cracks) will have components of displacement parallel and perpendicular to the fractures. The shear-wave component parallel to the fracture direction will propagate faster causing the polarized shear waves to split and to be recorded at different times. The resulting separation of shear-waves with different polarizations is known as *shear-wave birefringence* or *shear-wave splitting*. A multicomponent VSP provides the opportunity to record downward propagating shear-waves at different levels so that zones of anisotropy can be identified in situ.

## Geologic Background:

The South Casper Creek Oil Field is located on the Casper Arch in Natrona County approximately 24 miles west of Casper, Wyoming (Figure 1). The field was discovered in 1918 when gas was found in the Jurassic Sundance Sandstone. Oil was discovered in the underlying Pennsylvanian Tensleep Sandstone Formation in 1922. The South Casper Creek field is a structural/stratigraphic trap with two doubly plunging anticlines (*domes*). Dips on the limbs of the fold structure vary up to 30 degrees. Locally, the Tensleep is an eolian dune and sheet sand, folded, faulted and fractured through several episodes of tectonic activity (Ray and Keefer, 1985; Skeen and Ray, 1983). Porosity in the Tensleep Formation at South Casper Creek ranges between 18 and 33%, and permeability varies from 10 to 3200 md (Tanean, 1990). The producing Tensleep interval has 580 ft of closure and is at a depth of 2400 to 2600 ft. Although oil has been produced for 67 years, only 10 MMbbls of an estimated 70 MMbbls in place have been recovered. The cause of such low recovery is reservoir heterogeneity and the heavy oil (15 API) in the reservoir.

Late in the Laramide Orogeny the principle stress direction was southwest-northeast (Gries, 1983). "Two left-lateral shear zones divided the Casper Arch into three distinct styles of deformation" (Skeen and Ray, 1983). To the south release of this stress generated left stepping enechelon folds, two of which are identified as the Poison Spider and South Casper Creek Oil fields (Figure 2a). Parallel vertical faults, wrench faults and multiple fracture sets observed locally are caused by brittle failure of the rocks and support the conceptual diagram showing the formation of enechelon folds presented in Figure 2b.

## Data Acquisition:

The UNOCAL USA 10-6-3 well, located in the southwest portion of the northeast corner of Section 3, Township 33 North, Range 83 West, (SW/NE-SEC3-T33N-R83W) was the site for acquisition of wire-line logs and a multioffset multicomponent VSP survey. A three-dimensional (3-D) multicomponent surface seismic study was also conducted over a portion of the southern dome centered about the 10-6-3 well. Figure 3 shows the location of the 10-6-3 well, the VSP source positions and areal

<sup>†</sup> Trademark of Schlumberger

coverage of the 3-D multicomponent surface seismic survey overlain on a structural contour map of the Tensleep Sandstone.

Multicomponent VSPs were acquired with vertically polarized (P-wave) and two orthogonal, horizontally polarized (S-wave) energy sources recorded into a three-component (3-C) receiver sonde. The resulting nine-component survey was recorded at one 300-ft, near-offset location and two orthogonal, 1092-ft, far-offset locations. Source locations were chosen down-dip from the structure so that when the S-wave sources vibrated either radial or transverse to the borehole their polarization directions would be oblique to the anticipated axis of fracturing determined from a nearby UNOCAL 2-D seismic line (Cameron, 1987) in an attempt to observe shear-wave birefringence from each source. Accelerometers attached to each S-wave vibrator base plate were used to determine the starting polarity direction and the S-wave vibrators were then oriented so that all positive polarities conformed to a right-hand coordinate system with positive "z" downward (Figure 4).

Two strings of casing were cemented in the borehole. The first, from the surface to 1400 ft and the second, from the surface to 2770 ft. A cement bond log was run in the well prior to the VSP to insure coupling between the surrounding formation and casing. Data were recorded at depth increments of 25 ft, from 2700 to 900 ft for the near-offset VSP. From 900 to 700 ft recordings were made every 50 ft and from 700 to 300 ft, recordings made at 100 ft levels. This large depth increment resulted, essentially, in a checkshot survey from 700 to 300 ft. For the far-offset VSP, a full nine-component recording was made at depth increments of 25 ft from 2700 ft to 1975 ft. Sweep parameters used for the vibrators were as follows:

P-wave: 10-122 Hz, 14-s sweep, 500-ms taper, 7 sweeps/level,  
S-wave: 6-83 Hz, 14-s sweep, 500-ms taper, 7 sweeps/level.

#### Analysis:

Modeling studies were used to determine the most effective processing procedure to identify the polarization direction of the fast shear-wave. The four-component rotation technique (Alford, 1986) was more robust than hodogram analysis and was used to transform data recorded from the orthogonal S-wave sources on the horizontal receivers into a natural (fast and slow shear-wave) coordinate system.

Analysis of the near-offset VSP survey revealed three isolated zones of velocity anisotropy (Figure 5). These anisotropic zones are associated with specific lithologic units in the subsurface. Competent rocks such as limestones and sandstones exhibited azimuthal anisotropy while ductile rocks such as shales and evaporites showed no measurable shear-wave birefringence for a vertically propagating shear-wave. Velocity anisotropy is estimated between 4 to 6 percent in the first zone which begins in the near surface and continues to a depth of 850 ft. Fractured Cretaceous sandstones, some of which crop out in South Casper Creek, are the probable cause of velocity anisotropy in this zone. The predominant direction of surface fractures is 114 degrees from north, paralleling the polarization direction of the fast shear-wave as determined from the VSP. Velocity anisotropy is estimated between 11 and 14 percent in a second zone which extends from 1372 ft in the Triassic Alcova Limestone to 1600 ft in the Red Peak Shale. A third zone exhibits velocity anisotropy ranging between 4 and 11 percent. This zone encompasses from the top of the Permian Minnekatha

Limestone Member (2294 ft) of the Goose Egg Formation to the Pennsylvanian Amsden Formation (2719 ft) and includes the Pennsylvanian Tensleep Sandstone (reservoir). For vertical shear-wave propagation all three zones have a natural polarization direction (fast shear-wave) of 119 degrees from north, parallel to the long axis of the dome.

Shear-wave birefringence from the far-offset VSP (1092 ft northwest of the well) indicates a natural polarization direction of 124 degrees from north which compliments the near-offset VSP birefringence measurements. However, for the southwest far-offset VSP, located 1092 ft down-dip from the well, a polarization direction for the fast shear-wave was estimated at 77 degrees from north. The variability in polarization direction along with considerable coherent energy on the off-diagonal components, after four-component rotation, suggests that the polarization of fast and slow shear-waves may not be orthogonal when propagating at non vertical incidence angles or that a more complicated anisotropic symmetry system, possibly orthorhombic or triclinic exists. Further analyses of the multicomponent 3-D surface seismic and anisotropic modeling are required to determine the cause of the disparity in polarization directions as measured from the far-offset VSPs.

Faults and associated fractures in brittle rock units are considered to be the principal cause of velocity anisotropy at South Casper Creek. The 3-D surface seismic data indicates numerous faults in the vicinity of the 10-6-3 well. These faults are predominantly aligned at 120 degrees from north, paralleling the axis of the South Casper Creek anticline. A fault trend oriented 80 degrees from north is also noted at the reservoir level near the well. A full waveform sonic from the 10-6-3 well exhibits almost complete attenuation of tube wave amplitudes (an indication of fracturing) in each of the aforementioned anisotropic zones. Cores taken in the well from the Tensleep Sandstone are highly fractured and data from a Formation Microscanner<sup>†</sup> survey over the reservoir level indicates the dominant direction of fracturing to be oriented 100 degrees from north. Figure 6 is a Tensleep structure map indicating natural polarization directions determined by shear-wave birefringence from near- and far-offset VSPs along with the orientation of dominant surface and subsurface fractures.

#### Conclusions:

Reservoir development and enhanced oil recovery projects can benefit by integrating multicomponent VSP, 3-D seismic and geological data into the overall framework of reservoir characterization. Recording the down-going wave fields from a multicomponent VSP allows in situ measurements of shear-wave birefringence and velocity anisotropy. These measurements can be used to determine the orientation of reservoir fracture sets so that injector and production wells may be located to optimally sweep the reservoir. Velocity anisotropy is caused by the presence of open fractures at South Casper Creek. Based on the results of this study, multicomponent seismology should be an integrated procedure for future reservoir characterization and development.

#### Acknowledgements:

The authors wish to thank the corporate sponsors of the Reservoir Characterization Project, Phase III for funding of this research: Advance Geophysical Corporation, AGIP, AMOCO.

Associated Geophysical Analysts, Canadian Hunter, Chinese Petroleum Corporation, CGG American Services Incorporated, CNG Development, Conoco, Gas Research Institute, Golden Geophysical, H & H Star Energy, Halliburton Geophysical Services, INTEVEP, South America, Japan National Oil Corporation, Japan Petroleum Exploration Company Limited, Marathon Oil Company, Meridian Oil Company, Mesa Limited Operating Partnership, Mobil Research and Development Corporation, Northern Geophysical of America, ORYX Energy Company, PETROBRAS, Santa Fe Minerals, Incorporated, Schlumberger Well Services, Shell, Texaco Incorporated, UNOCAL, and Union Texas Petroleum

**References:**

Alford, R. M., 1986, Shear data in the presence of azimuthal anisotropy: Dilley, Texas: Presented at the 56th Annual International SEG Meeting, Houston, Expanded Abstracts, 476-479.

Cameron, Jack, 1987, Multi-component seismic data, Casper Creek, Wyoming: An unpublished report of Union Oil of California (UNOCAL).

Davis, Thomas L., and Lewis, Catherine, 1990, Reservoir characterization by 3-D, 3-C seismic imaging, Silo field, Wyoming: Geophysics: The Leading Edge of Exploration, 9, 22-25.

Gries, Robbie, 1983, North-south compression of Rocky Mountain foreland structures: Rocky Mountain foreland basins and uplifts, published by RMAG Denver Colorado, editors James D. Lowell and Robbie Gries, 9-32.

Martin, Marshall A. and Davis, Thomas L., 1987, Shear-wave birefringence: A new tool for evaluating fractured reservoirs: Geophysics, The Leading Edge of Exploration, 6, 22-28.

Ray, Randy R. and Keefer, W. R., 1985, Wind River Basin, Central Wyoming: Seismic exploration of the Rocky Mountain Region, RMAG and DGS Publication, Robbie Gries and Robert Dyer editors, 201-212.

Skeen, Riley C. and Ray, Randy R., 1983, Seismic models and interpretation of the Casper Arch Thrust: Application to Rocky Mountain foreland structure: Rocky Mountain foreland basins and uplifts, published by RMAG Denver Colorado, James D. Lowell and Robbie Gries editors, 99-124.

Spencer, Edgar W., 1977, Introduction to the structure of the earth, second edition, McGraw-Hill Book Company, New York, 75-97.

Tanean, Hondiro, 1990, Reservoir characteristics of the Tensleep Formation, South Casper Creek Field, Natrona County, Wyoming: Masters Thesis T-3827 Colorado School of Mines, Golden, Colorado.

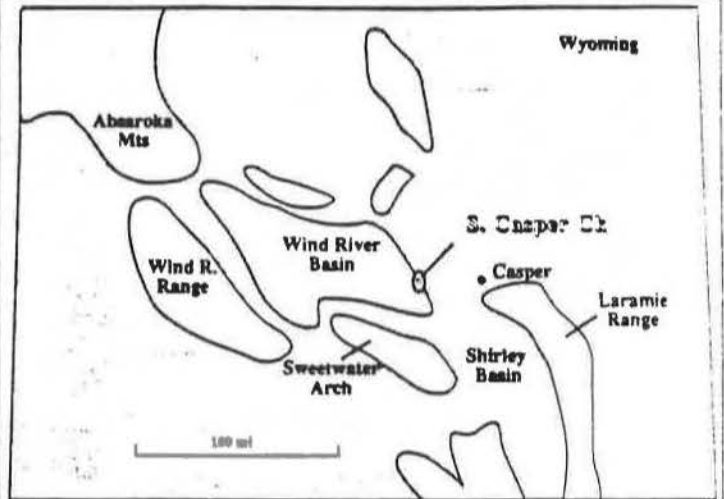


Figure 1: Location map, South Casper Creek Oil Field, Natrona County, Wyoming

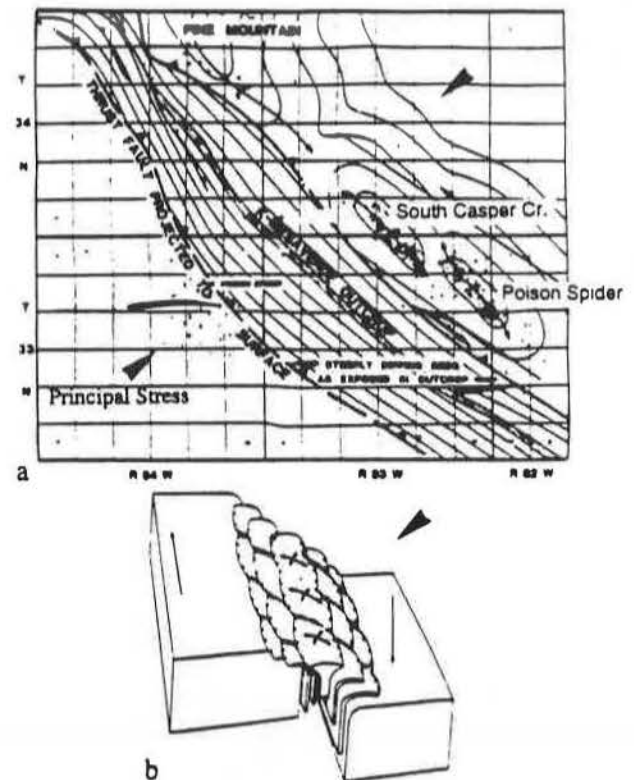


Figure 2: Left stepping enechelon folds generating dome features due to applied stress. a) Form-line structure map of Poison Spider and South Casper Creek fields (after Skeen and Ray, 1983). b) Conceptual diagram showing formation of enechelon folds. The upthrusts are not necessarily as symmetrically disposed as shown, and the deeper faults may tend to coalesce and braid rather than be parallel (after Spencer, 1977).

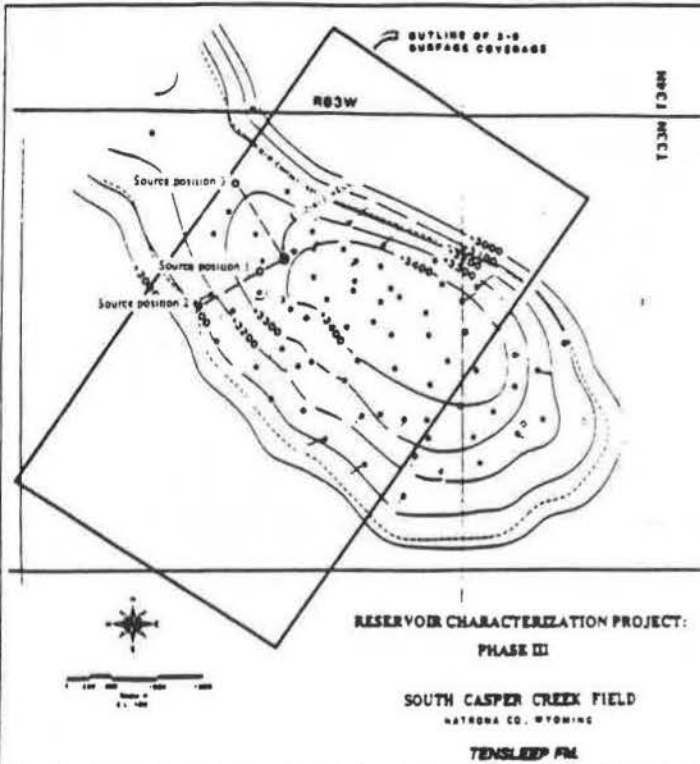


Figure 3: Structural contour map of the Tensleep Sandstone, South Casper Creek Field, indicating VSP source positions, areal coverage of the 3-C 3-D surface seismic and the UNOCAL 10-6-3 well.

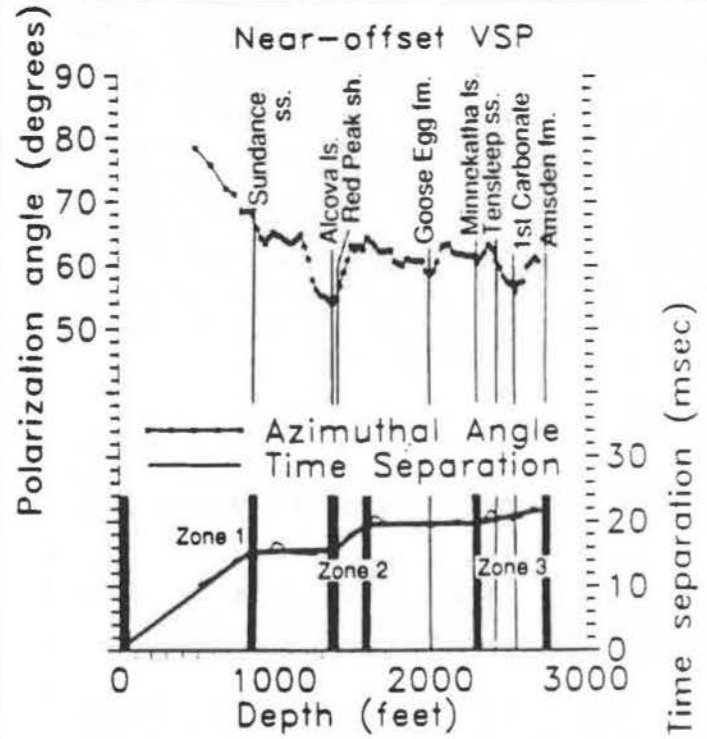


Figure 5: Natural polarization angles between the source-receiver plane and particle displacement of the fast shear-wave (upper curve). Cross-correlation time lags between fast and slow shear-waves representative of shear-wave splitting (lower curve).

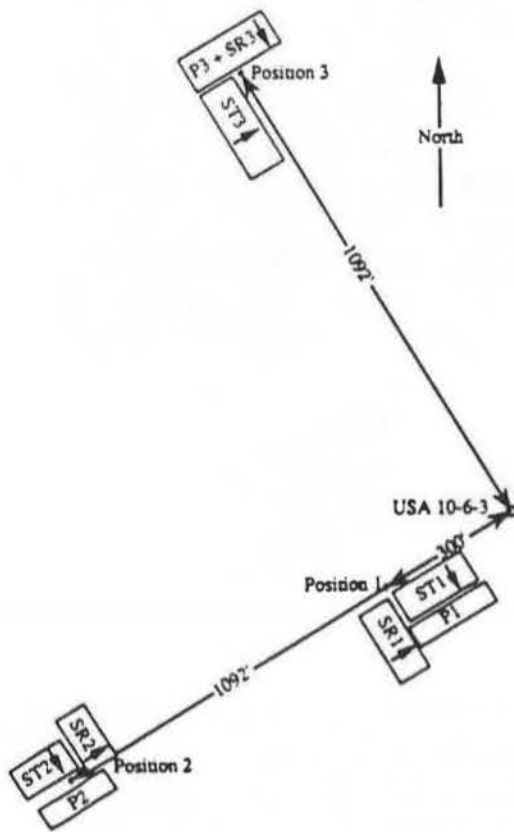


Figure 4: Vibrator locations with respect to the 10-6-3 well. Vibrators are labeled by their polarization (vertical (P), horizontal radial (SR), and horizontal transverse (ST)) and by their offset position (1, 2, or 3).

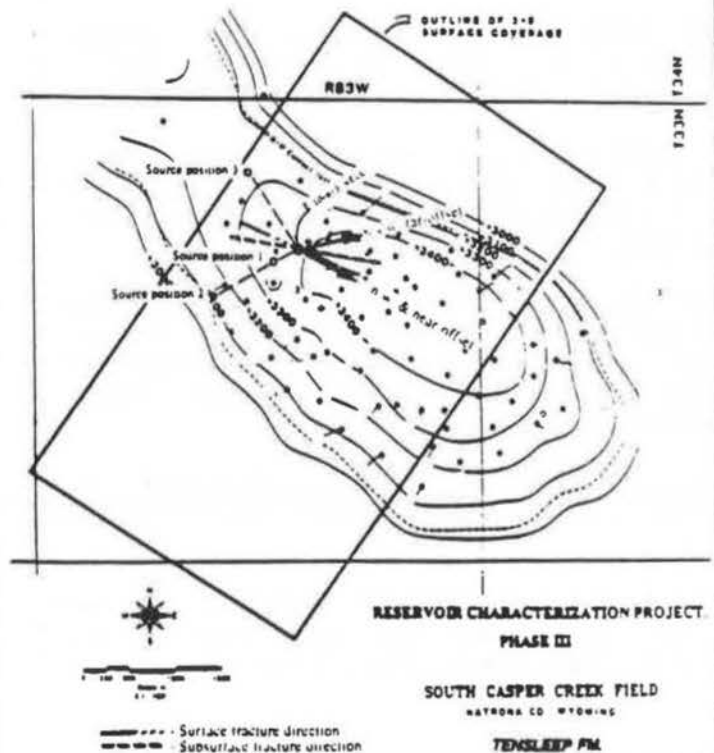


Figure 6: Natural polarization direction of fast shear-waves determined from VSP data (arrows). Orientation of fractures determined from surface geology and wire-line surveys (dashed lines). Base map courtesy of UNOCAL.

## SHEAR-WAVE POLARIZATION ANALYSIS AS A TOOL FOR DEDUCING SUBSURFACE ROCK PROPERTIES

D. F. Winterstein and M. A. Meadows  
*Chevron Oil Field Research Company*

### SUMMARY

Analysis of shear-wave (S-wave) birefringence in vertical seismic profile (VSP) data provides information about certain rock properties that are important for reservoir development. These properties are the direction of maximum horizontal stress or the orientation of aligned fractures and the variation of these quantities as a function of depth. The magnitude of S-wave birefringence contains information about the effects of unequal horizontal stresses on subsurface rock. Because use of S-wave birefringence is relatively new, there are many unanswered questions that only further use and supplementary experiments are likely to answer. Our focus on VSP data in contrast to surface reflection seismic data evidences our concern for having the best possible control at these early stages of application; however, many of the quantities available from VSP data are in principle also available from surface seismic data.

We recorded a number of nine-component VSPs suitable for analysis of S-wave birefringence in California and Texas. In every case we found measurable S-wave birefringence and also significant variation of the S-wave polarization azimuths with depth. These polarization azimuths, although typically consistent over large depth intervals, changed abruptly at various depths in every area. A simple layer-stripping technique made it possible to follow the polarization changes and determine the S-wave birefringence over successive depth intervals. The variations with depth are particularly interesting because they indicate changes of principal stress or fracture orientation.

At a few depth levels S-wave birefringence was negligible. While such cases may seem uninteresting, they provide potentially useful information. For example, hydraulic fractures in such zones will probably proceed more in the manner of a random walk than along well-defined planes, and reservoir engineers need to know that.

The purpose of the nine-component VSP data sets was to determine anisotropic properties of the subsurface by calculating S-wave polarization azimuths and the lags between the S waves. Data from the Lost Hills field of California show that the polarization of the fast S

wave was aligned with the direction of maximum horizontal compressive stress as determined from analysis of tiltmeter data. Tiltmeters monitored fractures that were hydraulically induced in or near the VSP wells. When fractures were induced in one of the VSP wells, fracture azimuths as determined from tiltmeter data were N 53° E and N 56° E, respectively, in two different depth zones; in the same zones the fast S-wave polarization directions were N 58° E and N 59° E. When fractures were induced in a well 537 ft from the second VSP well, tiltmeter data indicated a mean fracture strike of N 59° E, while the fast S-wave polarization direction in that case was N 40° E. S-wave polarization directions were determined by minimizing energy on off-diagonal components of the 2x2 S-wave data matrix, accomplished by computationally rotating sources and receivers by the same angle.

S-wave polarizations from two concentric rings of offset VSPs at Lost Hills were consistent in azimuth with one another and with polarizations of the near offset VSP. The S-wave polarization pattern in offset data fits a model of vertical cracks at N 55° E in a weakly transversely isotropic matrix with infinite-fold symmetry axis tilted 10° from the vertical towards N 70° E, a monoclinic model.

In this paper we also show details of S-wave birefringence analyses of data from the Elk Hills oil field of California and from an oil field in south Texas. The Texas data demonstrate that major changes in S-wave polarization azimuths occur also in areas far removed from major contemporary fault systems.

## INTRODUCTION

Conventional vertical seismic profiles (VSPs) typically make use of compressional wave reflections to image subsurface structures. This paper presents a completely unconventional use of VSP data in that only shear-wave (S-wave) direct arrivals from S-wave sources at the surface are used, and the quantities of interest are the S-wave polarization azimuths and the differences in arrival times (lags) between the faster and slower S waves.

In simple cases the polarization of the faster S wave in birefringent rock lies along the direction of maximum horizontal stress or dominant fracture strike. This direction is readily available from polarization analysis of S-wave VSP data. The lag gives the magnitude of the birefringence and is a direct measure of the effect of oriented fractures or of horizontal

compressive stress on rock. Such information on stress or fracture orientation can be important for secondary recovery, horizontal drilling and infill drilling.

We document major changes in S-wave polarization azimuth with depth in oil fields in California and Texas. Our analysis of such changes uses a layer stripping technique. Lefeuvre et al. (1989) and Cox et al. (1989) used propagator matrices or transfer functions instead of layer stripping. Recently Lefeuvre applied his propagator matrix method to some of our data and obtained variations in S-wave polarization with depth that were closely similar to our results from layer stripping (Lefeuvre et al., 1991).

Exactly how to interpret the S-wave birefringence is not always clear. In most cases, however, the birefringence almost certainly results from unequal horizontal stresses such as those from plate tectonics. Such stresses cause what are thought to be predominantly microscopic strains in large volumes of rock, making it anisotropic to seismic waves. In some cases the birefringence may result from oriented macroscopic fractures. The effectiveness of these fractures presumably is related also to principal stress orientation. That is, fractures perpendicular to the maximum horizontal compressive stress are likely to close and hence be less effective in causing anisotropy than those parallel to the maximum horizontal stress.

Two current models of the effects of stress on rock are the extensive dilatancy anisotropy (EDA) model and the Nur model. EDA was proposed by Crampin et al. (1984) to explain earthquake precursors and vertical S-wave birefringence. According to this model, compressive stresses open vertical cracks parallel to the maximum stress direction and perpendicular to the minimum stress direction, where maximum and minimum stresses are both horizontal. We call this configuration of EDA cracks the standard EDA model to distinguish it from configurations where the minimum stress direction is not horizontal. A key feature of the standard EDA model is that planes of induced cracks are parallel. Hence, if the rock had been isotropic before stressing, it becomes transversely isotropic (TI) after inducing cracks, with its infinite-fold symmetry axis normal to the crack planes. Many theoretical formulations, such as those of Hudson (1981, 1986) and Nishizawa (1982) are available for modeling such a system.

The Nur model was invoked by Nur and Simmons (1969) to explain laboratory observations of stress effects on Barre granite. According to this model, rock has a

uniform distribution of randomly oriented cracks and is isotropic in the absence of stress. Unequal compressive axial stresses close cracks perpendicular to stress directions, making the rock anisotropic. Uniaxial stress causes transverse isotropy, while triaxial stress in general makes the rock orthorhombic. Nur (1971) provided a theory for modeling this system.

Anisotropy from sets of oriented, macroscopic fractures is a study in itself (see Winterstein, 1990). How much such fractures contribute to vertical S-wave birefringence is unknown but likely to vary greatly from formation to formation. Martin (1987) attributed vertical S-wave birefringence to oriented macroscopic fractures in his Silo field, Woming, study, as did Becker and Perelberg (1986) in their study of Austin Chalk, and Lynn and Thomsen (1990) in their analysis of reflection data from Pennsylvania. A single set of planar, parallel, macroscopic fractures or joints would be indistinguishable from EDA at wavelengths appreciably in excess of the fracture spacing.

Crampin and Bush (1986) pointed out that S-wave birefringence might provide a useful tool for reservoir development. The polarization direction of the fast S wave in simple cases gives the direction of maximum horizontal stress, a quantity much in demand by those who hydraulically fracture reservoirs. Results presented here from the Lost Hills field reinforce the notion that vertical S-wave birefringence can be caused by horizontal stresses, and that the polarization direction of the fast S wave may lie in the direction of maximum horizontal compressive stress.

#### DATA ACQUISITION

Data sets were from nine-component VSPs, but for birefringence analysis we treat only data of the 2x2 S-wave data matrix, that is, data from x and y sources and receivers, or four of the nine components. In most cases we used a single ARIS (ARCO Impulsive Source) and downhole receivers with the Gyrodata gyrocompass attached. We typically recorded at increments of 100-200 ft from maximum depths ranging from greater than 10 000 ft to less than 2000 ft. Where possible our shallowest depths were no greater than 100 ft below the surface. The wells often were nearly vertical cased and cemented holes which had not yet been perforated, but in a few cases they were older, perforated holes that were temporarily taken off production. In one case we recorded in an open hole.

## METHODS AND MODELS

The objective of S-wave data analysis was to quantify subsurface S-wave birefringence or, in other words, to find the natural polarization directions of the two S waves and the time delays or lags between them. The purpose of the analysis was to correlate birefringence effects with formation properties such as direction of maximum horizontal stress.

To determine natural polarization directions of the subsurface rock, we found the source-receiver coordinate frame rotation angle at which S-wave energy on off-diagonal components of the 2x2 S-wave data matrix was a minimum (Alford, 1986), a method we call the "Alford rotation" method. We implemented Alford rotations by choosing time windows that included only the leading portions of the first arrival S waves and then calculating energy (sums of squares of amplitudes) on the off-diagonal components at rotation angle increments of one degree.

Data analysis showed convincingly that S-wave polarization directions varied with depth. We developed a layer stripping method specifically to analyze such changes. Layer stripping involves simply subtracting off anisotropy effects in a layer in order to analyze anisotropy effects in the layer immediately below. If polarization varies with depth, polarization analysis will be confused if there is no compensation for the variation. To subtract off effects from above the depth at which polarization change occurs--i.e., down to the bottom of the upper layer, we rotate source and receiver coordinate frames of all the data from below that depth by the azimuth angle determined down to that depth. We then apply a static shift to data from all greater depths to remove the lag between the two S waves at the bottom of the upper layer. The process simulates putting a source at the bottom of the upper layer, such that the simulated source polarizations are oriented along natural polarization directions (assumed orthogonal) of the upper layer. After layer stripping, rotation analysis is repeated as before, and further layer stripping (i.e., "downward continuation") is applied if indicated by cues in the data.

## RESULTS

Offset data from the 1-9J well of the Lost Hills field gave remarkably consistent S-wave polarization azimuths. For modeling of offset polarization azimuths we assumed a single homogeneous anisotropic layer whose stiffnesses came from crack sets of various

orientations. Crack set properties were from Hudson's first order approximation (Hudson, 1981) for cracks filled with weak material. Our best fit was obtained with a monoclinic medium created by introducing vertical cracks at N 55° E into a weakly anisotropic TI matrix with infinite-fold symmetry axis tilted 10° from the vertical towards N 70° E. Because our model fits available geologic knowledge, it is probably accurate.

Analyses of tiltmeter data obtained during hydraulic fracturing were performed for the 1-9J well and for the nearby 12-10 well. The calculated fracture orientation agreed closely with the polarization azimuth of the fast S wave, well within expected error, for the 1-9J well. There was a 20° discrepancy, however, for the 11-10X well, about 500 ft from the 12-10. The discrepancy was thought to result from changes in subsurface structures such as faults. In general the close agreement indicates that the polarization azimuth of the fast S wave gives the direction of maximum horizontal compressive stress at Lost Hills.

Polarization azimuths of the fast S-wave in the uppermost anisotropy layer for VSP wells in the southwest San Joaquin basin of California range from N 43° E to N 60° E, which, if interpreted as directions of maximum horizontal compressive stress, are in good agreement with the "fault normal compression" noted by Zoback et al. (1987). The consistency suggests that tectonic stresses which formed the Lost Hills and neighboring anticlines apparently persist today. Maximum horizontal compressive stress is thus, by this interpretation, roughly perpendicular to the San Andreas fault, which trends N 40° W ten to twenty miles to the southwest. However, in layers below the uppermost, this consistency of polarization direction vanishes, and at the present time it is not possible to fit all observations into a simple pattern.

In some cases, for example, in the Elk Hills data set, initial Alford rotation analyses of near offset VSP data gave S-wave polarization azimuths that were nearly constant over the entire VSP depth range. This constancy, however, is illusory, generated by the inertia in polarization azimuth determinations when one makes use of seismic wavelets in the analysis without eliminating the effects of travel in shallower birefringent layers. The S-wave lags, after the initial Alford rotation, presented a truer picture of the actual subsurface variability in birefringence; the slopes of lag-vs-depth curves showed large variations. After layer stripping analysis, the S-wave polarization angles were revealed to have considerable variation with depth.

Our deepest anisotropy layer in the Elk Hills well, from 8300 ft to 9950 ft, showed no S-wave birefringence. Scatter in calculated azimuth angles was very large, and S-wave lags were small and patternless. The most likely explanation for the absence of birefringence is that, in that layer, horizontal stresses are isotropic and there is no set of open, vertical fractures. Hence hydraulically induced fractures would probably propagate randomly rather than along a well-defined plane.

An interesting feature of the Texas VSP is that the data set was acquired by two different contractors partly in open hole and partly in cased hole. Despite these major differences in acquisition, both the polarization angles of the fast S-wave and the magnitudes of the S-wave lags blended smoothly from open to cased hole and from data of one contractor to those of the other. That the data sets matched smoothly testifies to the robustness of S-wave birefringence analysis.

## DISCUSSION

The reasons for the observed changes of fast S-wave polarization direction with depth are not known, but analogous evidence for change of stress direction with depth suggests that they may be indicating changes in stress directions. Hickman et al. (1988) observed changes in stress direction over a 500-900 ft interval in the Hi Vista well in the Mojave desert. They point out that rapid variations of stress magnitude and direction with depth have been observed elsewhere but have seldom been adequately explained. They suggest that a major stratigraphic discontinuity or slip on a fault might abruptly change stress magnitude or orientation. A recent study of relatively continuous wellbore breakouts in the Cahon pass scientific well indicated large variations of maximum horizontal stress direction with depth (Shamir, 1991). Such variations in stress direction could easily result from inhomogeneities, especially when rocks are sedimentary. For example, if relatively incompressible rock alternates with compressible rock, the incompressible rock will bear the horizontal stress. Then the geometric distribution of the incompressible rock will determine the orientation of local compressive stress vectors. At this stage, however, we should also not rule out the possibility that some of the larger trends may result from actual changes in regional stress direction with depth.

Magnitudes of vertical S-wave birefringence near the San Andreas fault are generally larger than they were in the VSP of the south Texas well, a circumstantial indication that stresses associated with the San Andreas contribute to the birefringence. Nevertheless, both

significant birefringence and major changes of polarization azimuth with depth were clearly evident in the Texas data, indicating that changes of polarization azimuth with depth are not confined to the vicinity of a major fault system.

### CONCLUSIONS

Analysis of S-wave birefringence in multicomponent VSP data gives important information about subsurface rock properties. At the moment there are unanswered questions about exactly what the birefringence means, but as we record and analyze more data and do appropriate supplementary experiments, the interpretation should become clear. At Lost Hills field we have clear evidence that the fast S-wave polarization direction corresponds to the direction of maximum horizontal compressive stress. There are good reasons for thinking that this correspondence should prevail in most places.

Two major observations are noteworthy so far. First, measurable S-wave birefringence occurs everywhere we have looked for it with VSPs (see also Willis et al., 1986). Second, significant changes of S-wave polarization directions as a function of depth have occurred everywhere we have looked. We believe these observations have just scratched the surface of what is likely to be a very useful and robust way of gaining information about subsurface rock properties.

### ACKNOWLEDGMENTS

We thank Chevron operating companies, Chevron Oil Field Research Company and the DOE for supporting this research and for permission to publish the results.

## REFERENCES

- Alford, R.M., 1986, Shear data in the presence of azimuthal anisotropy: Dilley, Texas: 56th Ann. Internat. Mtg., Soc. Explor. Geophys., Expanded Abstracts, 476-479.
- Becker, D. F., and Perelberg, A. I., 1986, Seismic detection of subsurface fractures: 56th Ann. Internat. Mtg., Soc. Explor. Geophys., Expanded Abstracts, 466-468.
- Cox, V. D., Rizer, W. D., Anno, P. D., and Queen, J. H., 1989, An integrated study of seismic anisotropy and the fracture system in the Spraberry sandstone, Pembroke, field, Upton and Reagan Counties, Texas: Presented at the SEG Summer Research Workshop on Recording and Processing Vector Wave Field Data, Snowbird, Utah.
- Crampin, S., and Bush, I., 1986, Shear waves revealed: Extensive-dilatancy anisotropy confirmed: 56th Ann. Internat. Mtg., Soc. Explor. Geophys., Expanded Abstracts, 481-484.
- Crampin, S., Evans, R, and Atkinson, B. K., 1984, Earthquake prediction: A new physical basis: *Geophys. J. Roy. Astr. Soc.*, **76**, 147-156.
- Hickman, S. H., Zoback, M. D., and Healy, J. H., 1988, Continuation of a deep borehole stress measurement profile near the San Andreas fault: 1. Hydraulic fracturing stress measurements at Hi Vista, Mojave Desert, California: *J. Geophys. Res.*, **93**, 15183-15195.
- Hudson, J. A., 1981, Wave speeds and attenuation of elastic waves in material containing cracks: *Geophys. J. Roy. Astr. Soc.*, **64**, 133-150.
- Hudson, J. A., 1986, A higher order approximation to the wave propagation constants for a cracked solid: *Geophys. J. Roy. Astr. Soc.*, **87**, 265-274.
- Lefevre, F., Winterstein, D., Meadows, M., and Nicoletis, L., 1991, Propagator matrix and layer stripping methods: A comparison of shear-wave birefringence detection on two data sets from Railroad Gap and Lost Hills fields: to be presented at 61st Ann. Internat. Mtg., Soc. Explor. Geophys., Houston.
- Lynn, H. B., and Thomsen, L. A., 1990, Reflection shear-wave data collected near the principal axes of azimuthal anisotropy: *Geophysics*, **55**, 147-156.
- Martin, M. A., 1987, Three-component seismic investigation of a fractured reservoir, Silo field, Wyoming: PhD thesis, Colorado School of Mines.
- Nishizawa, O., 1982, Seismic velocity anisotropy in a medium containing oriented cracks--transversely isotropic case: *J. Phys. Earth*, **30**, 331-347.
- Nur, A., 1971, Effects of stress on velocity anisotropy in rocks with cracks: *J. Geophys. Res.*, **76**, 2022-2034.
- Nur, A., and Simmons, G., 1969, Stress-induced velocity anisotropy in rock: *J. Geophys. Res.*, **74**, 6667-6674.
- Shamir, G., 1990, Crustal stress orientation profile to a depth of 3.5 km near the San Andreas fault at Cahon pass, California: PhD Thesis, Stanford University.
- Willis, H. A., Rethford, G. L., and Bielanski, E., 1986, Azimuthal anisotropy: Occurrence and effect on shear-wave data quality: 56th Ann. Internat. Mtg., Soc. Explor. Geophys., Expanded Abstracts, 479-481.
- Winterstein, 1990, Velocity anisotropy terminology for geophysicists: *Geophysics*, **55**, 1070-1088.
- Zoback, M. D., Zoback, M. L., Mount, V. S., Suppe, J., Eaton, J. P., Healy, J. H., Oppenheimer, D., Reasenber, P., Jones, L., Raleigh, C. B., Wong, I. G., Scotti, O., and Wentworth, C., 1987, New evidence on the state of stress of the San Andreas fault system: *Science*, **238**, 1105-1111.

# TRANSVERSE ISOTROPY: AN INDICATOR OF HORIZONTAL MICROFRACTURES

J. Cameron, Unocal

## Transverse Isotropy: An Indicator of Horizontal Microfractures

A detailed seismic study of the near surface material was conducted on the southwest flank of the Casper Creek Anticline in Wyoming. A mini-spread of 80 3-component seismometers was concentrated in the "weathered" layer, with an 8 ft. horizontal and vertical spacing. Inhole dynamite and horizontal vibrator sources were recorded at several offsets, off both ends of the mini-spread.

Compressional and shear wave velocities were measured within the weathered layer. Lateral changes in the  $V_p/V_s$  ratio, due to lithology changes within this zone, were observed. Along a 312 ft. interval changes were found that would produce significant variations in shear wave reflection statics, without associated changes in compressional wave statics.

The Frontier Sandstone was encountered at a depth of 55 ft. This thick high velocity formation served as a refractor for seismic energy from all source locations. The horizontal vibrators were oriented crossline, inline, and at  $45^\circ$  to the spread, at an offset distance of 1898 ft. The shear wave energy refracted through the Frontier Sandstone exhibited an  $S_H$  velocity of 4000 ft./sec. and an  $S_V$  velocity of 2985 ft./sec. This remarkable case of transverse isotropy was confirmed by the recordings from the horizontal vibrator oriented  $45^\circ$  to the line, FIGURE 1. That source orientation generated both  $S_H$  and  $S_V$  modes, which were recorded on the crossline and inline receivers, respectively. At an offset of 1898 ft., the time separation of the two shear modes is 150 ms.

Nearby outcroppings of the Frontier Sandstone show that it is lithologically homogeneous but highly fractured. The transverse isotropy which was observed is believed due to horizontal microfractures. This formation was uplifted during the creation of the Casper Creek structure. Several thousand feet of overlying material has been eroded, resulting in a decrease of the vertical stress. The vertical stress relief is presumed to be the reason for the development of a prominent horizontal microfracture system that produces the exceptional transverse isotropy characteristics of this formation.

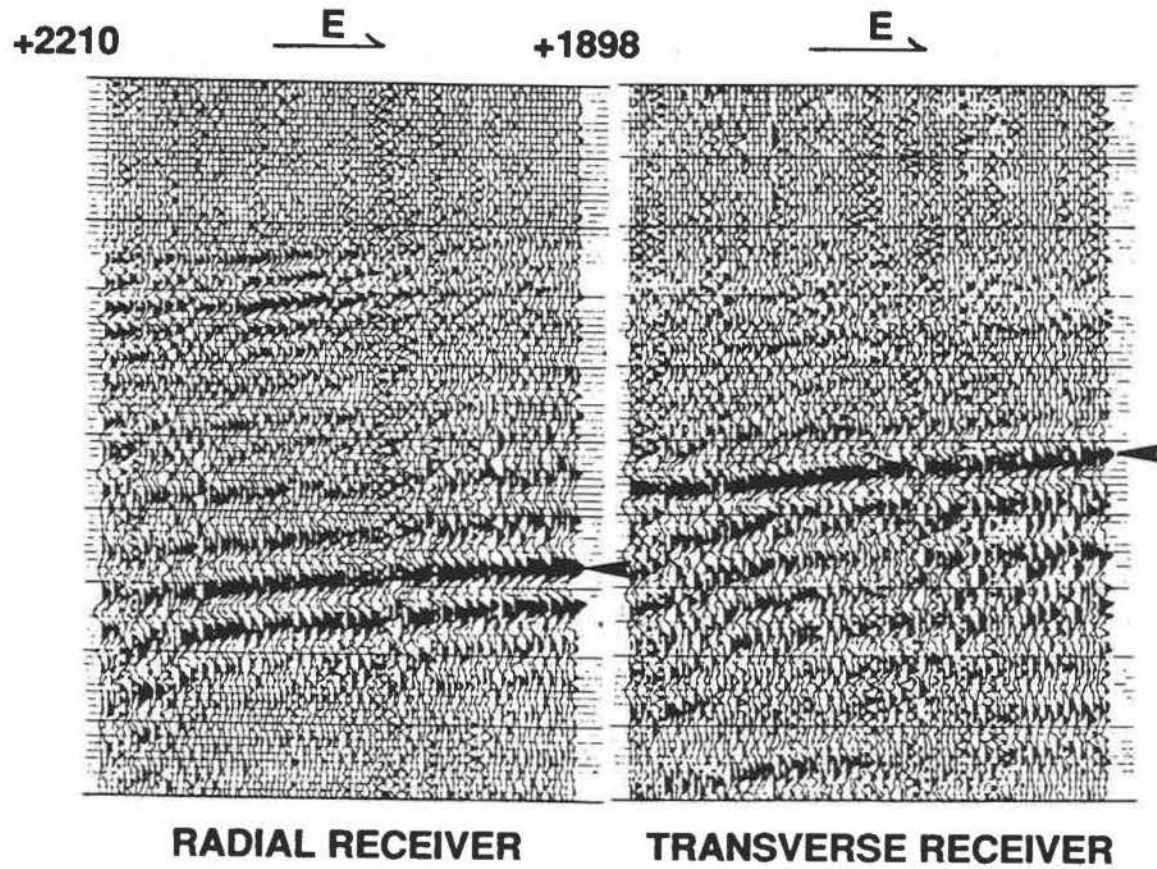


Figure 1  
RECORDINGS FROM VP5 WITH STATICS APPLIED  
SOURCE ORIENTED AT 45°

# Characterizing Hydraulically Fractured Reservoirs Using Induced Microearthquakes

Michael Fehler

MS D443  
Geoengineering Group  
Los Alamos National Laboratory  
Los Alamos, N.M. 87545

## Summary

Hydraulic fracturing is a common method employed to increase the production of oil and gas fields. Recently, there has been increased interest in monitoring the microearthquakes induced by hydraulic fracturing as a means of obtaining data to characterize reservoir changes induced by the injection. Two types of microearthquakes have been observed during hydraulic fracturing. Tensile events have been observed and modeled as the parting of the surfaces of a fracture. A majority of the events observed have been shear-slip events, where two sides of a fault plane slip parallel to each other but in opposite directions. The locations of the microearthquakes can be analyzed to determine regions where significant seismic energy was released, which presumably are regions where injected fluid penetrated into the rock along pre-existing fractures or zones of weakness. The spatial patterns in the locations can be analyzed to find regions where events cluster along planes, which are interpreted to be the dominant fluid flow paths. Imaging methods can also be applied to the travel time and waveform data to obtain direct evidence for the locations of the fractures or fracture zones.

## Introduction

Hydraulic fracturing is frequently used to increase the productivity of oil and gas wells, as well as in the development of geothermal resources. Microearthquakes accompany many hydraulic injections [Albright and Hanold, 1976, Albright and Pearson, 1982; Pine and Batchelor, 1984; Sarda et al., 1988] as well as production from some gas fields [Pennington et al., 1986; Doser et al., 1991] and geothermal fields [Block, 1991]. Observations on a small scale (less than 10 meter samples) have been made by Majer and Doe [1986], Niitsuma et al. [1987], and Masuda et al. [1990]. Observations in larger scale environments, up to 1 km, have been reported by Pine and Batchelor [1984], Sarda et al. [1988], and Talebi and Cornet [1987]. Most of the observations have led to the conclusion that the seismic events are caused by shear slip along fault planes [House et al., 1985], although Bame and Fehler [1986] reported observations of events that they interpreted to be due to the tensile opening of fractures. More recently, Ferrazzini et al. [1990] have modeled these tensile events and estimated the dimensions of the open fractures through which fluid is in easy communication. The dimensions of the shear fractures have been reported by Pearson [1982] and Fehler and Phillips [1991].

Investigators working on the Department of Energy Hot Dry Rock Geothermal Energy Project have observed microearthquakes accompanying many of the hydraulic stimulations of the man-made geothermal reservoir [Albright and Pearson, 1983; Keppler et al., 1983; Fehler, 1989]. Since these microearthquakes occur throughout the volume of the reservoir, they have the potential to provide information about the fracture structure and changes that occur in the reservoir as the reservoir is stimulated. Figure 1 shows the locations of a subset of the microseismic events determined by House [1987] to accompany a massive hydraulic fracturing operation conducted in

the Fenton Hill hot dry rock reservoir. Locations of more than 11,000 events that occurred during this massive hydraulic fracturing operation have been determined. Fehler [1989] has summarized the locations of microseismic events found to accompany other recent hydrofracturing operations in the Fenton Hill reservoir.

Much can be learned by studying the seismicity induced by hydraulic fracturing. Since the microearthquakes occur in direct response to fluid pressure in the reservoir, the locations of the events provide information about the volume of the reservoir in which fluid pressures are elevated. The temporal evolution of the zone in which microearthquakes occur can be used to make inferences about the permeability of the reservoir rocks (Pearson, 1981). Fehler et al. [1987] have presented a statistical scheme to determine planes along which the earthquakes cluster and interpreted these planes to be major flow paths in the reservoir. Both the travel times of the direct P and S waves and the waveforms themselves contain information about the spatial heterogeneity of the rock. In addition, the portions of the waveforms after the first arrivals (termed coda) consist of conversions and reflections from fractures or other heterogeneities in and near the reservoir and may be analyzed to obtain direct information about the locations of large fractures in the reservoir.

### Locations of Microearthquakes

Figure 1 shows locations of some of the events accompanying a 130,000 barrel injection into granitic rock at Fenton Hill whose permeability is on the order of one nanodarcy. The figure shows that the events are confined to a roughly tabular zone with dimensions of 950 m along strike, 850 m down dip and 150 m thick (House, 1987). The thickness of the zone is significantly larger than the estimated precision in the locations (20 m) so the thickness of the zone is considered to be real. Thus, no single hydraulic fracture was formed. Instead, we now believe that the water permeated into a zone of rock and that the microearthquakes occurred along pre-existing zones of weakness in the rock (Murphy and Fehler, 1986). The view of the seismicity looking to the east in Figure 1 shows that the seismicity occurs in zones, with few events occurring in the "quiet" spots located between the zones.

Figure 2 shows the distance of each event from the injection point plotted as a function of the time between initiation of injection and the time the event occurred. The figure shows that the maximum distance of events from the injection point increases with increasing time during the injection with a roughly square root of time dependence, hinting at a diffusion-like process.

Fehler et al. [1987] and Fehler [1989] used a statistical method to analyze the locations to determine spatial clustering of microearthquakes along planes. These planes were interpreted to be dominant fluid flow paths in the reservoir. They identified several planes for each hydraulic injection and found that planes with one common orientation occurred most frequently. Fehler [1989] argued that the orientation of this set of planes was controlled by the orientation and magnitude of the regional *in situ* stress field. Dreesen et al. [1987] analyzed well logs and found anomalies that correlated with the locations where the planes determined from the seismicity intersected the wellbores. They thus concluded that the fractures determined from the seismicity are major fluid paths in the reservoir.

### What are the microearthquakes?

Since hydraulic fracturing involves the forceful injection of fluids into a rock, it is natural to assume that many of the seismic events accompanying hydraulic fracturing are tensile, e.g. due to the parting of rock faces. Field data indicates that a majority of the events are actually shear-type events, where the motion is parallel to the fracture plane and there is little motion perpendicular to the fracture plane (Cash et al., 1983; House et al., 1985; Ohtsu, 1991). Fault plane solution

information and the ratio of shear wave to compressional wave energy for most events show clearly that a majority of the microearthquakes are shear slip along the fracture. Bame and Fehler [1986] identified waveforms of events that occurred only during the early phases of the fluid injection that were clearly different from the waveforms of the later occurring shear slip events. The waveforms of these early events were extremely small in amplitude and the locations of the events could not be determined. Based on their similarity to waveforms observed at volcanoes, these early events have been termed long-period events and we believe that they represent tensile fracturing occurring only during the initial portion of the injection.

### **Sizes of the Microearthquakes**

Pearson [1982] and Fehler and Phillips [1991] studied the spectra of the shear microearthquakes to determine the sizes of the plane over which slip occurred. Fehler and Phillips [1991] found that the source radius ranged between 1.5 m and 100 m although smaller and larger events were not analyzed. Smaller events were detected at too few stations to allow locations to be reliably determined and larger events had recorded waveforms that were unsuitable for analysis.

Ferrazzini et al. [1990] analyzed the waveforms of the long period events observed by Bame and Fehler [1986] using a tensile crack model developed by Chouet [1988]. They found that the frequencies at which peaks occur in the spectra of these events are related to the physical size of the crack over which fluid can easily flow. They showed that the spacing between the frequencies at which the peaks occur is well explained by the model of Chouet [1988]. Using Chouet's model they found that the size of the open crack is approximately 3m by 1m by 3mm. This size is significantly smaller than the size of the fault plane determined for the shear slip events by Fehler and Phillips [1991]. The tensile fracture events are the opening of fractures while the shear events occur due to a change in the stress field induced by the pore fluid pressure. Fluid flow along all of the shear fault planes should be enhanced relative to what it was prior to the event but these planes may not have the high permeability found along the planes of the tensile events.

### **Imaging The Reservoir**

Imaging provides a means to determine reservoir characteristics in three dimensions. We are taking two approaches for inferring the properties of the fracture system in a hydraulically fractured reservoir from microearthquake data: tomography and waveform stacking. The tomographic method is being applied to the arrival times of P and S waves from the microearthquakes to simultaneously locate the microearthquakes and determine the P and S wave velocity structure of reservoirs in three dimensions (Block et al., 1990; Block, 1991). In addition, waveform stacking is being applied to determine the P and S wave velocities within selected regions of the hydraulically fractured rock. We will also apply waveform stacking to determine locations of inhomogeneities, such as fluid-filled fractures, that produce coherent large-amplitude signals in the coda. These methods are being applied to the data collected at Fenton Hill (Fehler et al., 1991). We are finding a clearly delineated low-velocity zone in the vicinity of the injection zone with velocities increasing with distance away from the injection zone. By calculating the volume of reduced velocity, we can obtain an estimate of the volume of the fractured reservoir created by the fluid injection.

### **Conclusions**

Monitoring of the microearthquakes that accompany hydraulic fracturing provides data that may be useful for determining where the injected fluids traveled in the rock. Numerous methods have been developed for analyzing data collected during hydraulic fracturing. The locations of the

events show where rock failed in response to changes in stress field induced by the injections and may provide direct information about the locations of the dominant fluid flow paths. Imaging techniques can be used to determine a three-dimensional image of the rock properties in the reservoir and to determine where the fluid has permeated.

## REFERENCES

- Albright, J., and R. Hanold, 1976. Seismic mapping of hydraulic fractures in basement rocks, *Proc. 2nd ERDA Enhanced Oil and Gas Recovery Symposium*.
- Albright, J.N., and C.F. Pearson, 1982. Acoustic emissions as a tool for hydraulic fracture location: experience at the Fenton Hill hot dry rock site, *Soc. Petr. Eng. J.*, 22, 523-530.
- Bame, D. and M. Fehler, 1986. Observations of long period earthquakes accompanying hydraulic fracturing, *Geophys. Res. Letters*, 13, 149-152.
- Block, L., 1991. Joint hypocenter-velocity inversion of local earthquake arrival time data in two geothermal regions, PhD Thesis, Massachusetts Institute of Technology.
- Block, L., C.H. Cheng, M. Fehler, and W.S. Phillips, 1990. Inversion of microearthquake arrival time data at the Los Alamos Hot Dry Rock Reservoir, Society of Exploration Geophysicists, Expanded Abstracts of the 1990 Technical Program, 1226-1229.
- Cash, D., E. Homuth, H. Keppler, C. Pearson, and S. Sasaki, 1983. Fault plane solutions for microearthquakes induced at the Fenton Hill Hot Dry Rock Geothermal Site: Implications for the state of stress near a Quaternary volcanic center, *Geophys. Res. Lett.*, 10, 1141-1144.
- Doser, D., M. Baker, and D. Mason, 1991. Seismicity in the War-Wink gas field, Delaware basin, west Texas, and its relationship to petroleum production, preprint.
- Dreesen, D., M. Malzahn, M. Fehler, and Z. Dash, Identification of MHF fracture planes and flow paths: a correlation of well log data with patterns of induced seismicity, *Trans. Geotherm. Res. Council*, 11, 339-348, 1987.
- Fehler, M., 1989. Stress control of seismicity patterns observed during hydraulic fracturing experiments at the Fenton Hill Hot Dry Rock geothermal energy site, New Mexico, *Int. J. Rock Mech. Mining Sciences and Geomech Abstr.*, 26, 211-219.
- Fehler, M., L. House, and H. Kaieda, 1987. Determining planes along which earthquakes occur: Method and application to earthquakes accompanying hydraulic fracturing, *J. Geophys. Res.*, 92, 9407-9414.
- Fehler, M. and W. S. Phillips, 1991. Simultaneous inversion for Q and source parameters of microearthquakes accompanying hydraulic fracturing in granitic rock, *Bull. Seism. Soc. Am.*, 81, 553-575.
- Fehler, M., L. House, W.S. Phillips, L. Block, and C.H. Cheng, 1991. Imaging of reservoirs and fracture systems using microearthquakes induced by fluid injections, Expanded abstract of talk to be presented at 1991 meeting of Geothermal Resources Council in Reno Nv, Oct., 1991.
- Ferrazzini, V., B. Chouet, M. Fehler, and K. Aki, 1990. Quantitative analysis of long-period events recorded during hydraulic fracturing experiments at Fenton Hill, New Mexico, *J. Geophys. Res.* 95, 21871-21884.
- House, L., H. Keppler, and H. Kaieda, 1985. Seismic studies of a massive hydraulic fracturing experiment, *Trans. Geotherm. Res. Council*, 9 (part II), 105-110.
- House, L., 1987. Locating microearthquakes induced by hydraulic fracturing in crystalline rock, *Geophys. Res. Lett.*, 14, 919-921.
- Keppler, H., C. Pearson, R. Potter, and J. Albright, 1983. Microearthquakes induced during hydraulic fracturing at the Fenton Hill HDR site: the 1982 experiments, *Trans. Geotherm. Res. Council*, 7, 429-433.
- Masuda, K., O. Nishizawa, K. Kusunose, T. Satoh, M. Takahashi, and R. Kranz, Positive feedback fracture process induced by nonuniform high-pressure water flow in dilatant granite, *J. Geophys. Res.*, 95, 21,583-21,592.

- Majer, E., and T. Doe, 1986. Studying hydraulic fractures by high frequency seismic monitoring, *Int. J. Rock Mech. Min. Sci. and Geomech. Abstr.*, 23, 185-199.
- Murphy, H. and M. Fehler, Hydraulic fracturing of jointed formations, Soc. of Petr. Engineers, Intl. Meeting on Petroleum Engineering, Beijing, China, SPE paper 14088, 1986.
- Niitsuma, H., N. Chubachi, and M. Takanohashi, 1987. Acoustic emission analysis of a geothermal reservoir and its application to reservoir control, *Geothermics*, 16, 47-60.
- Ohtsu, M., 1991. Simplified moment tensor analysis and unified decomposition of acoustic emission source: application to *in situ* hydraulic fracturing test, *J. Geophys. Res.* 96, 6211-6221.
- Pearson, C., 1982, Source parameters and a magnitude-moment relationship from small local earthquakes observed during hydraulic fracturing in crystalline rock, *Geophys. Res. Letters*, 9, 404-407.
- Pearson, C., 1981, The relationship between microseismicity and high pore pressure during hydraulic stimulation experiments in low permeability granitic rocks, *J. Geophys. Res.* 86, 7855-7864.
- Pennington, W., S. Davis, S. Carlson, J. DuPree, and T. Ewing, 1986. The evolution of seismic barriers and asperities by the depressuring of fault planes in oil and gas fields of south Texas, *Bull. Seismol. Soc. Am.*, 76, 939-948.
- Pine, R.J., and A.S. Batchelor, 1984. Downward migration of shearing in jointed rock during hydraulic injections, *Int. J. Rock Mech. Min. Sci. & Geomech. Abstr.*, 21, 249-263.
- Sarda, J.-P., P.J. Perreau, and J.-P. Deflandre, 1988. Acoustic emission interpretation for estimating hydraulic fracture extent, SPE paper 17723, presented at SPE Gas Technology Symposium, Dallas, TX, June 13-15.
- Talebi, S., and F. Cornet, 1987. Analysis of microseismicity induced by a fluid injection in a granitic rock mass, *Geophys. Res. Letters*, 14, 227-230.

Figure 1. Three orthogonal views showing locations of events accompanying the massive hydraulic fracturing experiment as found by House [1987]. Upper left: plan view. Lower left: vertical cross section projected onto an east-west plane. Lower right: vertical cross section projected onto a north-south plane. There is no vertical exaggeration in the figures. The trajectory of the injection wellbore, EE-2, and a second nearby wellbore, at the time of the hydraulic fracturing operation are shown. The open hole injection zone in EE-2 is labeled.

Figure 2. Distance of events from injection zone versus time from the start of injection. Each microearthquake is represented by one point. As time progresses, the events get further from the injection zone. Gaps are periods in time where we have not analyzed data. The injection was terminated at 61 hours and venting began. Note the paucity of seismicity near the injection zone during venting.

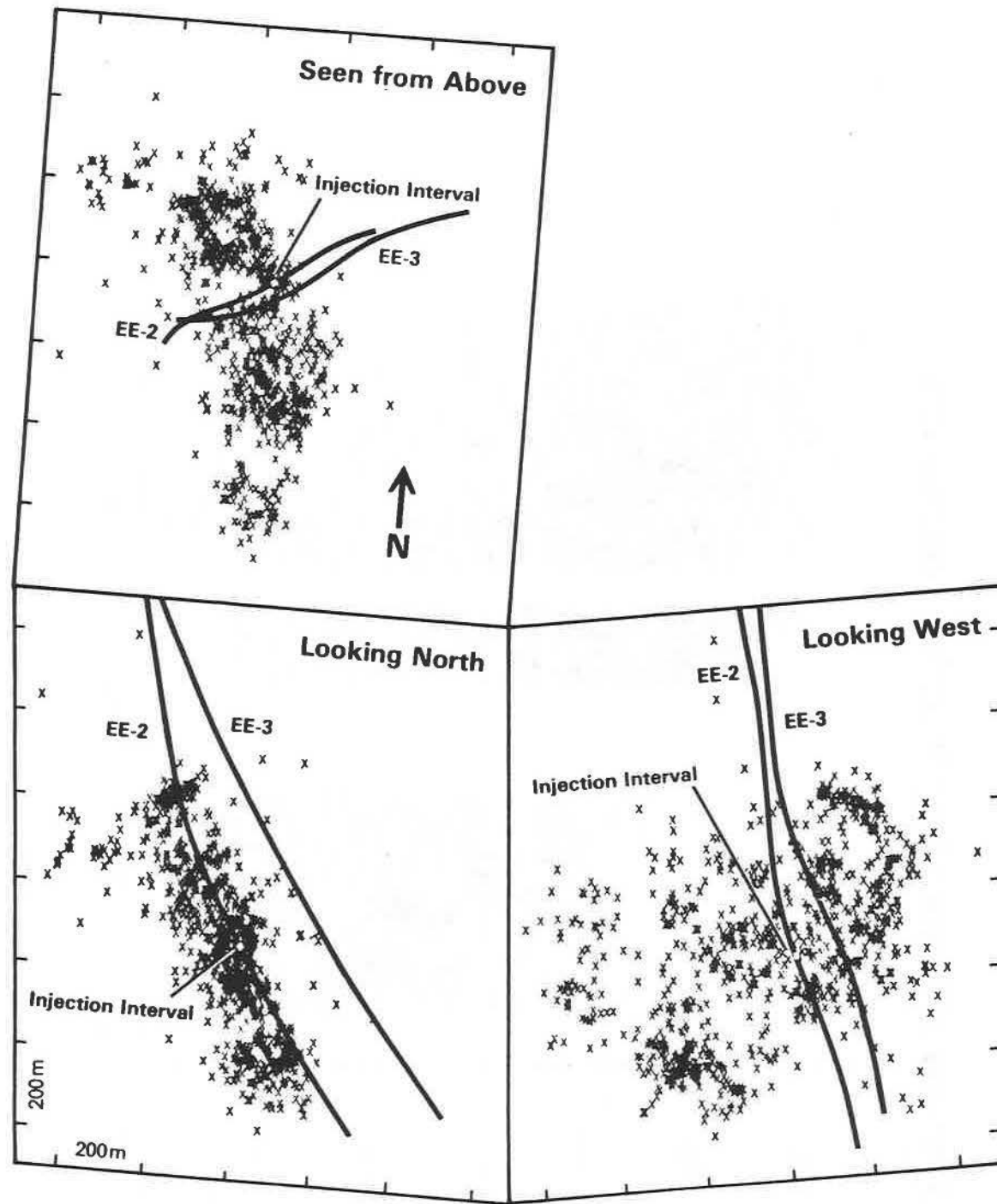


Figure 1

### Distance of Events from Injection Zone vs Time

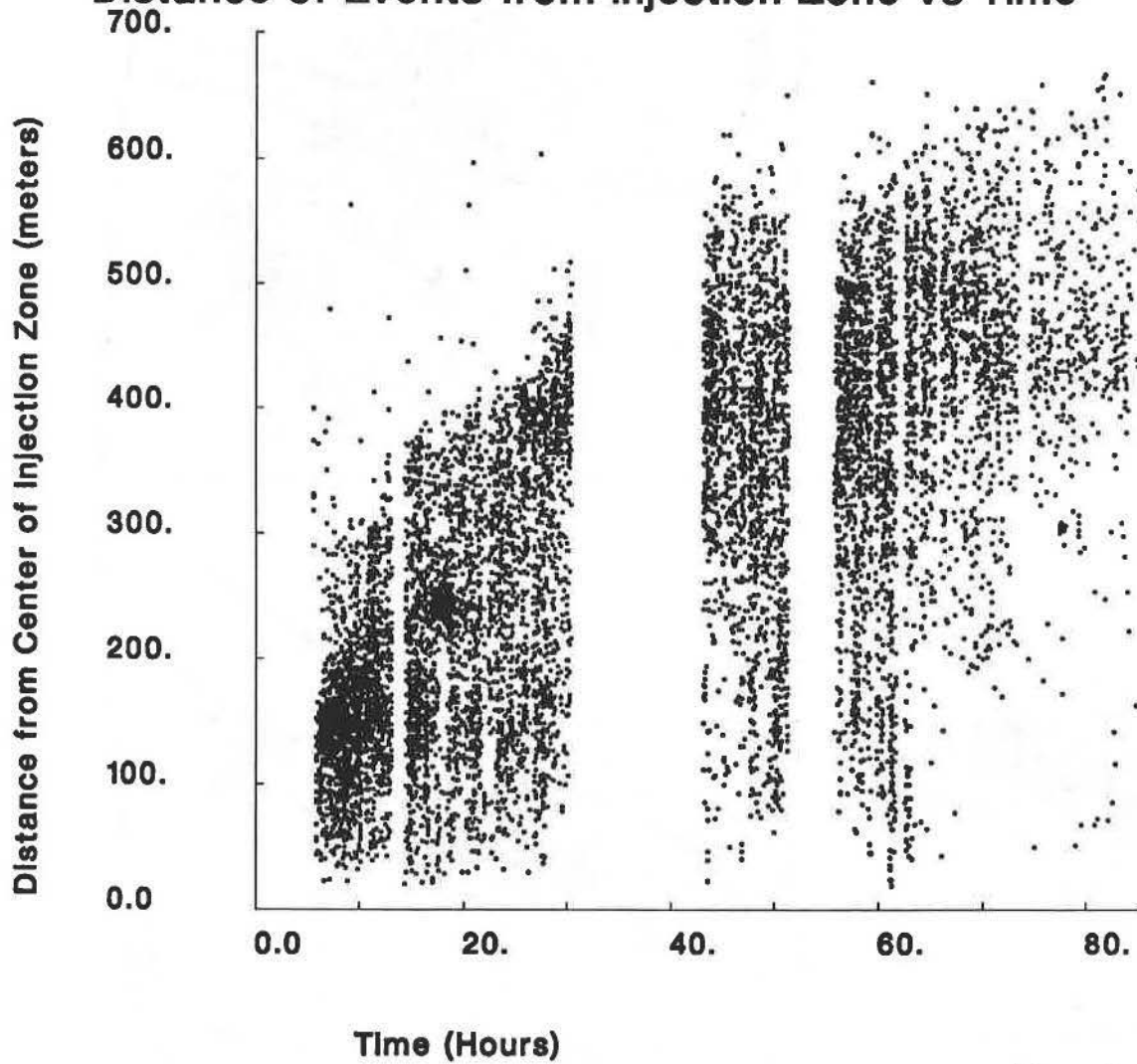


Figure 2

**SESSION 3**

**MATURE EXPLORATION**

Tuesday Morning  
Session Co-Chairmen: A. Cheng and T. Keho

## **Implications of thin layers in extracting lithology using amplitude versus offset**

Christopher Juhlin, Curtin University of Technology, Dept. Exploration Geophysics, GPO Box U1987, Perth, WA 6001, Australia

Roger Young, University of Oklahoma, School of Geology and Geophysics, Energy Center Building, 100 East Boyd Street, Norman, OK, 73019-0628, USA

### **Introduction and Summary**

Amplitude versus offset (AVO) analyses of seismic reflection data are becoming increasingly popular in the exploration industry (Ostrander, 1984; Pinchin and Mitchell, 1991; Mazzotti and Mirri, 1991) and also in scientific studies of the Earth's crust (Juhlin, 1990 and Milkereit et al, 1991). In the exploration industry, AVO analyses are particularly suitable for detection and mapping of gas zones since reservoirs often consist of more plastic shale with high Poisson's ratio (high  $v_p/v_s$ ) overlying a gas bearing sand with low Poisson's ratio (low  $v_p/v_s$ ). Under these conditions there will be an increase in the magnitude of the reflection coefficient with angle of incidence or offset. Other combinations of rock types will also show a similar increase in magnitude such as shale over hard limestone, but the sign of the reflection coefficient will be positive in most of these cases. Therefore, if the polarity of the reflection can be determined to be negative and there is an increase in the amplitude of the reflection with offset, then this is highly indicative of gas.

In this paper we show how thin bed tuning affects the AVO response of a high velocity limestone imbedded in shale versus a low velocity gas sand. We find that high velocity layers, relative to the surrounding rock, distort the normalized AVO response to a much greater degree than low velocity layers. This is also true for analyses of frequency versus offset (FVO). These observations indicate that thin layer effects are less important in low velocity rocks which are of the most interest to the petroleum industry. In addition we compare the AVO results from three different modeling routines and find generally good agreement between the three, however, caution must be used when extracting detailed amplitude information. Finally, the importance of including transmission losses for thin coal layers is considered. We find that when transmission losses are not included in the modeling of a thin (1.8288 m) coal bed there will be an increase in AVO for intermediate or shallow angles of incidence. However, when transmission losses are included no such increase is observed.

### Thin layer tuning effects

The effects of thin layers on reflection amplitudes for normal incidence waves have been studied in detail (Widess, 1973; Kallweit and Wood, 1982). Its presence results in a change in both the amplitude and the waveform of the reflected wave. For layers less than about  $1/8$  of the wavelength corresponding to the peak frequency of the incident wave the amplitude of the reflected wave is less than what would be expected from a simple interface (Figure 1). At a thickness of 0.192 of the wavelength corresponding to that of the peak frequency component in the incident Ricker wavelet (Kallweit and Wood, 1982) constructive interference from the reflection off the top of the layer and that off the bottom is at a maximum resulting in the greatest increase in peak amplitude in the composite waveform. In this study we define a thin layer as being less than or equal to this thickness. The exact thickness for which maximum tuning occurs will depend upon the shape of the incident waveform and the velocity of the layer itself. It is first at layer thickness greater than half of that of the incident wavelength where the peak amplitude is the same as for a simple interface.

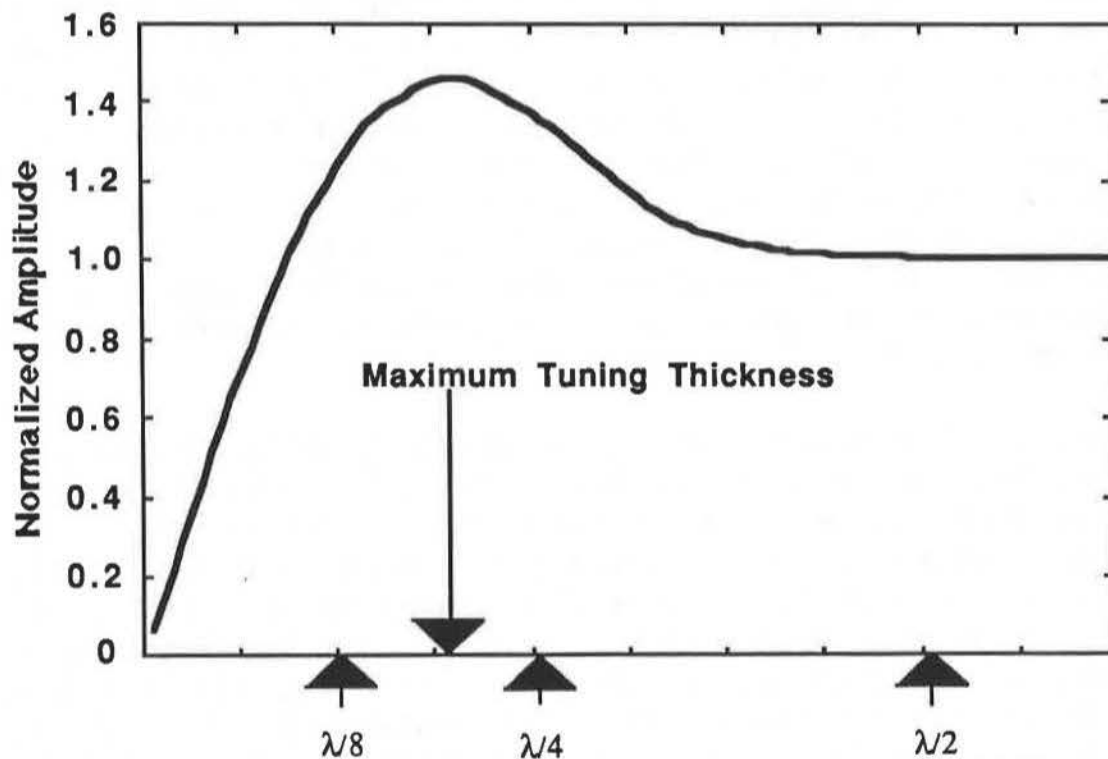


Fig. 1. Peak amplitude as a function of layer thickness for normal incidence waves. The incident waveform is a Ricker wavelet and transmission losses have been neglected. Wavelength  $\lambda$  is relative to the peak frequency of the Ricker wavelet (After Kallweit and Wood, 1982)

### Effect of thin layers on AVO

When non-normal incidence angles are considered the difference in traveltime for plane wavefronts reflecting off the bottom of the layer from those reflecting off the top is given by

$$dt = 2h \cos(\theta) / v \quad (1)$$

where  $h$  is the thickness of the layer,  $\theta$  is the angle of the transmitted wave in the layer determined by Snell's Law, and  $v$  is the velocity of the layer. Eq. 1 governs the thin layer tuning effects for shallow incidence angles provided the amount of converted shear energy is small.

Since the thickness of a layer will have a pronounced effect on the amplitude of the reflected wave for normal incidence waves it is natural to suspect similar behaviour for non-normal incidence ones. Two cases are considered here, (i) the thin layer has a P-wave velocity significantly greater than that of the surrounding rock and (ii) the thin layer has a P-wave velocity significantly less than the surrounding rock. In both cases the amplitude increases strongly with angle of incidence for a simple

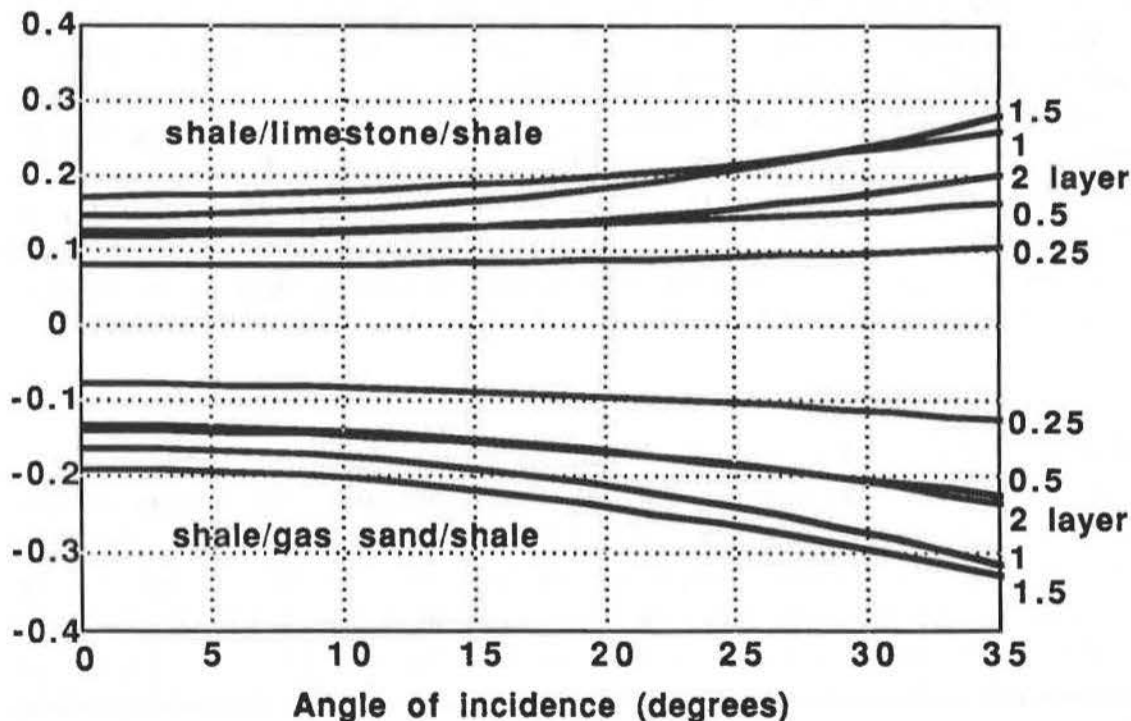


Fig. 2. AVO response of thin layers and a simple interface for shale-limestone-shale lithology (top half of figure) and shale-gas sand-shale lithology (bottom half). The input wavelet is a Ricker wavelet where the maximum tuning thickness is 0.192 of the peak wavelength. For the gas sand using a 40 Hz peak frequency this corresponds to a thickness of 9.4 m where maximum normal incidence amplitude is observed. The values to the right of the curves refer to the thickness of the layer relative to the maximum tuning thickness at normal incidence. The 2 layer curve is the simple interface.

interface (Figure 2) using the assumed velocities and densities. However, it will be shown that the AVO response of the high velocity thin layer deviates the most from that of the simple interface.

Table 1. Elastic properties of rocks used in this study.

Rock Type	$v_p$ (m/s)	$v_s$ (m/s)	$\rho$ (g/cc)	Poisson's ratio	ref.
Shale	2307	942	2.15	0.4	Shuey (1985)
Gas Sand	1952	1300	1.95	0.1	Shuey (1985)
Limestone	4600	1805	2.62	0.41	modified from Nur and Simmons (1969)
Coal	2286	1064	1.40	0.36	Treadgold et al (1990)
Sand	3658	2097	2.33	0.26	Treadgold et al (1990)

### Modeling algorithm used

The AVO response is calculated along the lines outlined by Meissner and Meixner (1969) which assumes plane waves are impinging on a thin layer. The traveltimes for the primary reflections along with conversions and multiples are calculated using Snell's Law and then convolved with an input wavelet. Each contribution is successively added to the seismogram taking into account time shifts less than the sampling rate. The peak amplitude is then picked from the composite seismogram. As reported by Meissner and Meixner (1969), it is found that the primary contributions to the reflected waveform comes from the reflection off the top of the layer and that off the bottom of the layer. The contributions from interbed P-wave multiples, interbed S-wave multiples and interbed P-S conversions are small, but are, nevertheless, included for P-wave multiples to order 2, S-wave conversions and multiples to order 2, and P-S-P-P and P-P-S-P conversions. In all figures shown in this paper regarding thin layer models the angle of incidence refers to the top of the thin layer.

### Results

The normalized AVO response of shale-limestone is approximately the same as shale-gas sand (Figure 3). However, introducing thin layers results in significant differences between the two different lithologies. For the limestone layer the normalized amplitude at 35° varies from about 1.3 to 1.9. The variation for the gas sand is about 1.6 to 1.95, a factor of about two less than for the limestone layer. Layers which are 1.5 times the maximum tuning thickness produce the strongest AVO response while layers which are 0.5 produce the weakest. It is also interesting to note that the AVO response for gas sand layers corresponding to the maximum tuning thickness is nearly identical that of the simple interface (Figure 3). In general, the effect of thin layers on the AVO for the gas sand lithology is much less than the corresponding effect for limestone lithology.

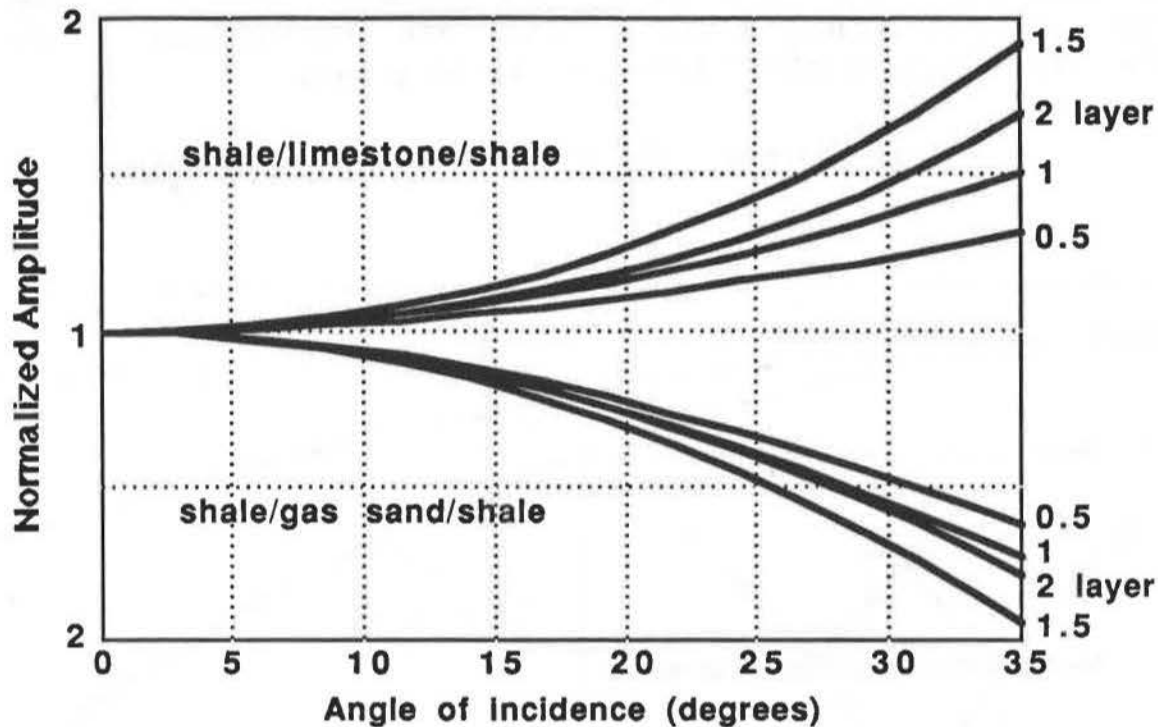


Fig. 3. Normalized AVO response of thin layers and simple interface for shale-limestone-shale lithology (top half of figure) and shale-gas sand-shale lithology (bottom half) where the amplitude for the reflection from each layer has been normalized by the zero offset amplitude. Note that the vertical scale is centered at a value of 1 and increases to 2 both in the up and down direction. The values to the right of the curves refer to thickness of the layer relative to the maximum tuning thickness at normal incidence.

### Delay functions

The observation that the layer thickness is of less importance for gas sands than for limestone layers can be explained by the difference in the velocity contrast shale-gas sand and shale-limestone. The high velocity limestone relative to the shale results in the ray spending proportionately more time in the limestone as the angle of incidence increases compared to that of the gas sand (Figure 4). Regardless of the velocity of the thin layer the wave reflecting off the bottom of the layer will always arrive progressively earlier relative to the reflection off the top as offset increases. This is the major reason for the decrease in the normalized AVO response of reflections from thin layers compared to that of a simple interface when the layer is less than the tuning thickness. From Figure 1, it is seen at time differences less than maximum tuning the trend will always be to reduce the amplitude as the waves arrive closer together in time. On the other hand, for layers which are thicker than the maximum tuning thickness the strength of the reflection will, initially at least, trend towards increased amplitudes as the waves arrive closer in time. These observations are valid for all velocity contrasts and the slower the velocity in the thin layer the less the thin layer normalized AVO response will differ from the simple

interface response. Only when shear wave converted energy becomes significant or when critical reflections occur will this reduction in the normalized AVO response of the thin layer not be present.

### Event Time Difference versus Angle

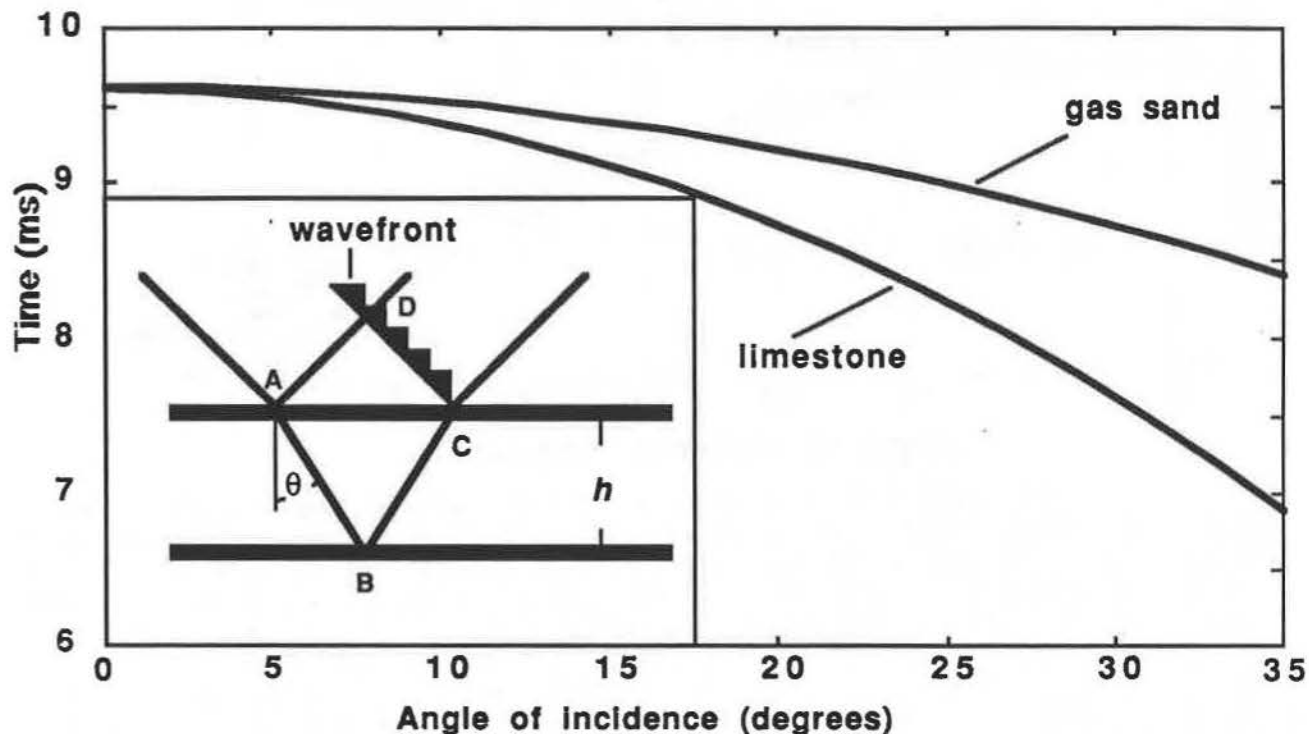


Fig. 4. Time difference (ABC-AD shown in inset) in traveltimes as a function of incidence angle for a reflection off the bottom of a layer and for one off the top of the layer. Velocities used in the calculations are listed in Table 1. The curves are for maximum tuning thickness for normal incidence waves, for gas sand this corresponds to 9.4 m and for limestone to 22.1 m.

#### Effect of thin layers on Frequency versus offset (FVO)

Eq.1 implies the time difference between the reflection off the top of the thin layer from that off the bottom decreases with increasing angle of incidence or offset. This is equivalent to the effective thickness of the layer decreasing. It is known as the layer decreases in thickness that the mean frequency of the reflected wave increases (Robertson and Nogami, 1984). Therefore, one would expect an increase in the mean frequency of the reflected wave as the angle of incidence increases (Figure 5). This increase will occur regardless of whether the velocity contrast of the thin layer to the surrounding rock is positive or negative. Instead, the increase is a function of the velocity of the thin layer, the higher the velocity of the thin layer the more pronounced will the increase in mean frequency be with offset. In the case where the rock above the thin layer has different elastic properties from the rock below, Lange and Almogharbi (1988) found that

the frequency does not necessarily have to increase with offset. They also found that the peak frequency decreases with decreasing layer thickness in some cases when the bounding lithologies are dissimilar.

### Mean Frequency versus Angle

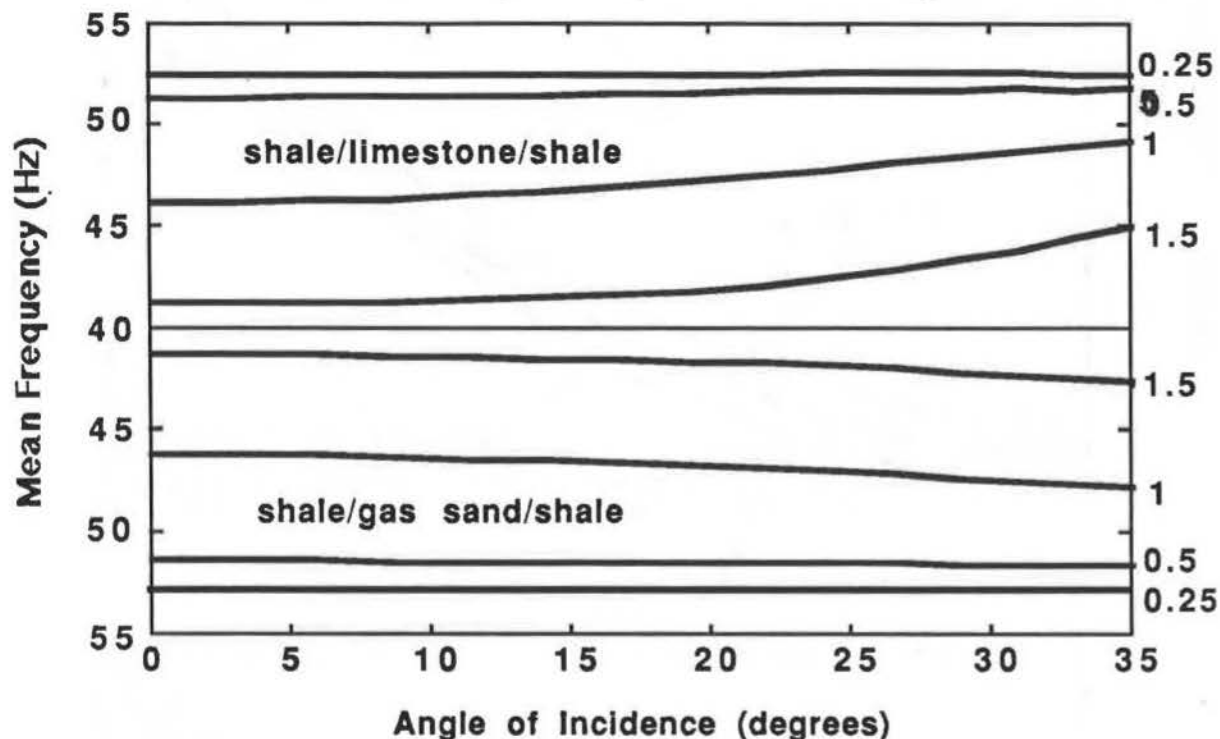


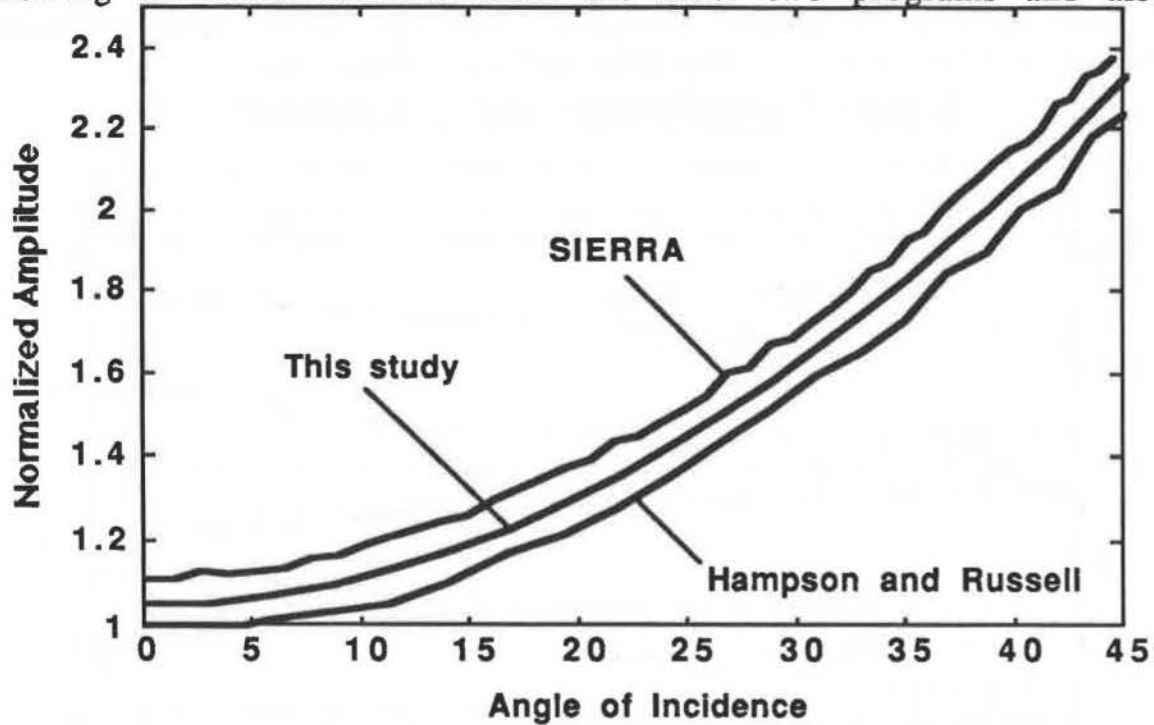
Fig. 5. Mean frequency (which differs from peak frequency) as a function of angle of incidence for thin layers of limestone and gas sands imbedded in shale.

#### Program testing

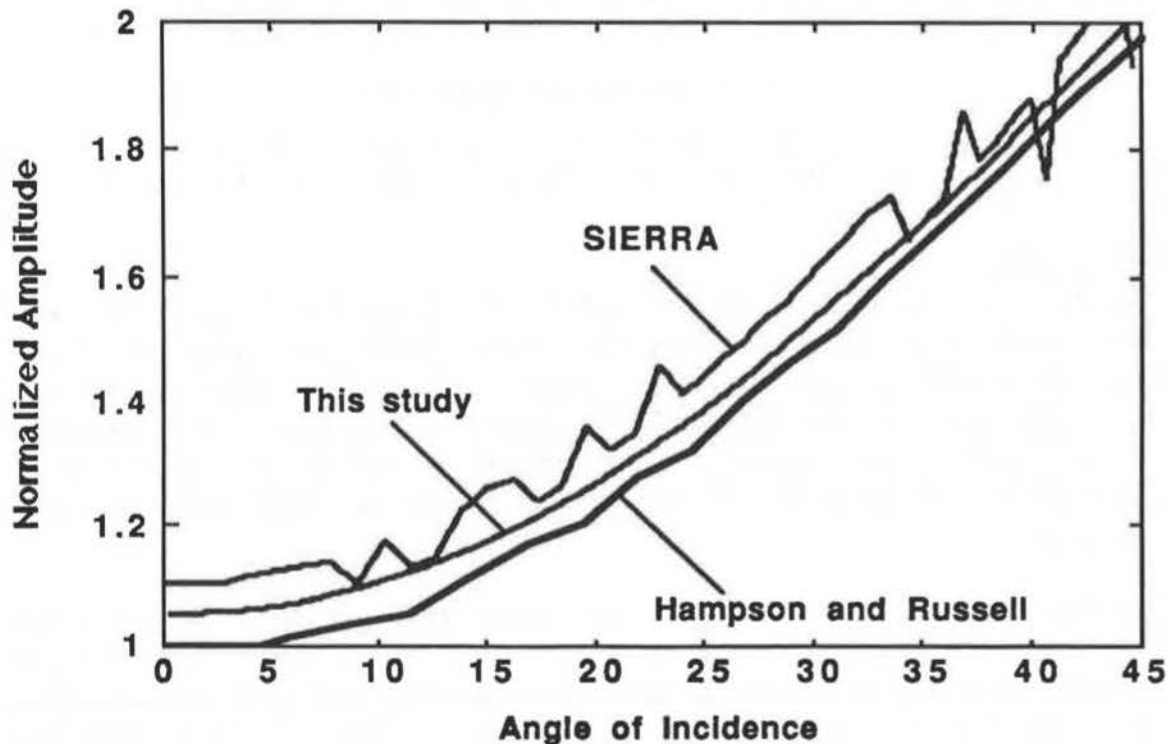
It is valuable to test routines developed to calculate AVO responses with other programs, especially commercial ones. Here we present results comparing our program with the AVO program from Hampson and Russell and the Sierra Geophysics QUIKSHOT program. Hampson and Russell's program also calculates synthetic seismograms based on the plane wave assumption while the QUIKSHOT program is based on WJKB theory using spherical waves.

Results for a simple interface (Figure 6a) show that all three programs for calculating amplitudes give similar results. For the SIERRA results the ray capture radius was set to 7.5% of the CMP spacing and a 1 ms sampling rate was used, the amplitudes were then corrected for spherical spreading losses and angle of emergence to allow comparison of results from the other two programs. In the second test case a 5.8 m thick gas sand in shale is modeled (Figure 6b). Here the results from the modeling diverge to a higher degree than for the simple interface with the SIERRA amplitudes

showing the most deviation from the other two programs and also the



(a)



(b)

Fig 6. AVO response from a (a) simple interface and (b) a 5.8 m thick gas sand imbedded in shale (b) for the programs Sierra, Hampson and Russell and the one used in this study. The results from Sierra have had a constant shift of 0.1 added and the results from this study have had one of 0.05 added to allow separation of the curves which otherwise would plot on top of one another.

most erratic amplitude behaviour. In the comparison all input parameters were held constant such as layer thickness, peak frequency of Ricker wavelet, velocities, densities and inclusion of transmission losses.

By holding the quantity peak frequency times layer thickness constant, the effects of sampling interval on the modeling can be studied since the ratio of wavelength to layer thickness is then constant. Further testing of the SIERRA program shows as higher frequency Ricker wavelets are input, which in effect results in the wavelets being sampled less frequently, the reflected amplitudes become more and more erratic (Figure 7). This is due to the time shifts, as defined in eq. 1, approaching the sampling interval resulting in the wavelets not being sampled adequately enough.

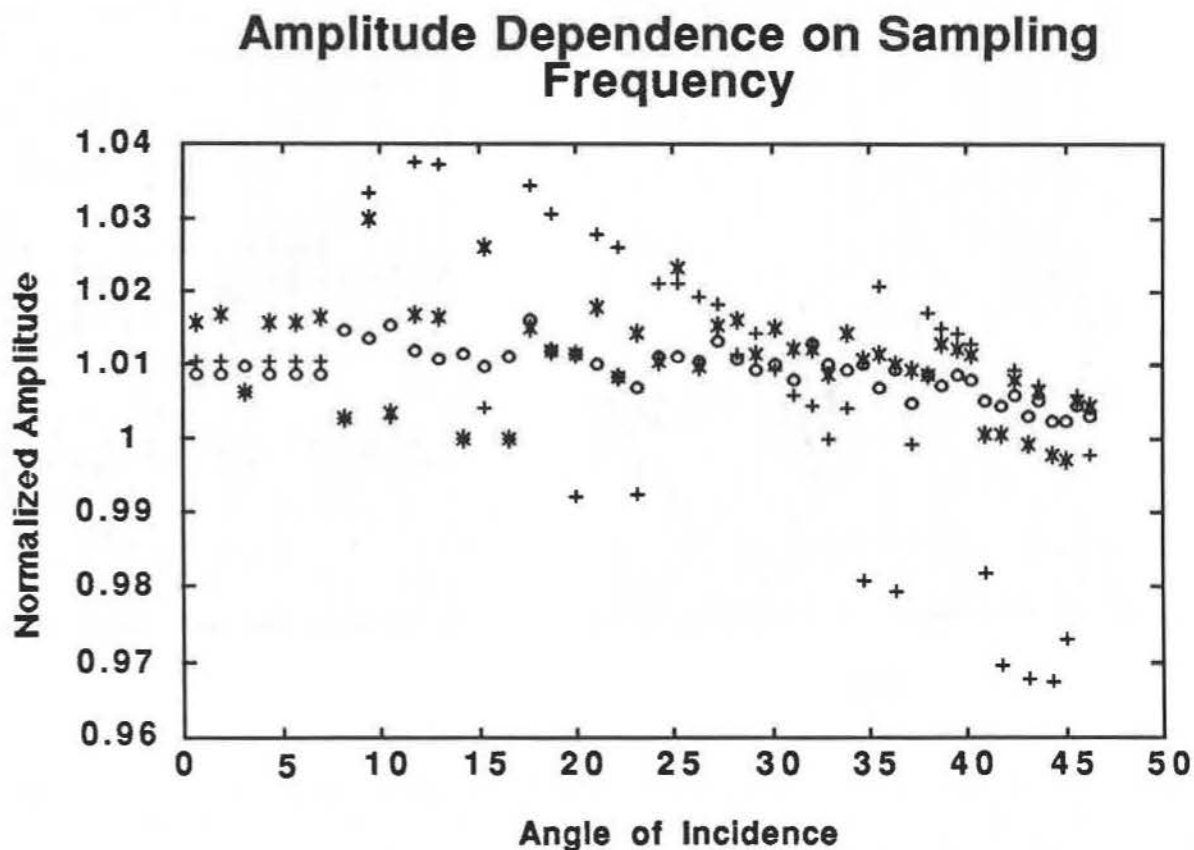


Fig. 7. Picked amplitudes from the Sierra program normalized by the amplitudes from a 10 Hz Ricker wavelet impinging on a 46.8 m thick gas sand imbedded in shale. (+) 80 Hz Ricker wavelet impinging on a 5.8 m thick gas sand, (\*) 40 Hz Ricker wavelet impinging on a 11.7 m thick gas sand, and (o) 20 Hz Ricker wavelet impinging on a 23.4 m thick gas sand.

#### Importance of transmission losses

Treadgold et al (1990) present AVO modeling results from a .9144 m (3 feet) thick coal seam imbedded in a sand where the elastic properties differ markedly (Table 1) leading to a normal incidence reflection

coefficient for the sand-coal interface of close to -0.5. The AVO response they present shows an increase in amplitude with offset which can, as pointed out by the authors, be erroneously interpreted as a direct hydrocarbon indicator. The AVO response of a simple sand-coal interface is one of decreasing amplitude with offset and the authors attribute the increasing AVO response of the thin layer to constructive interference. We

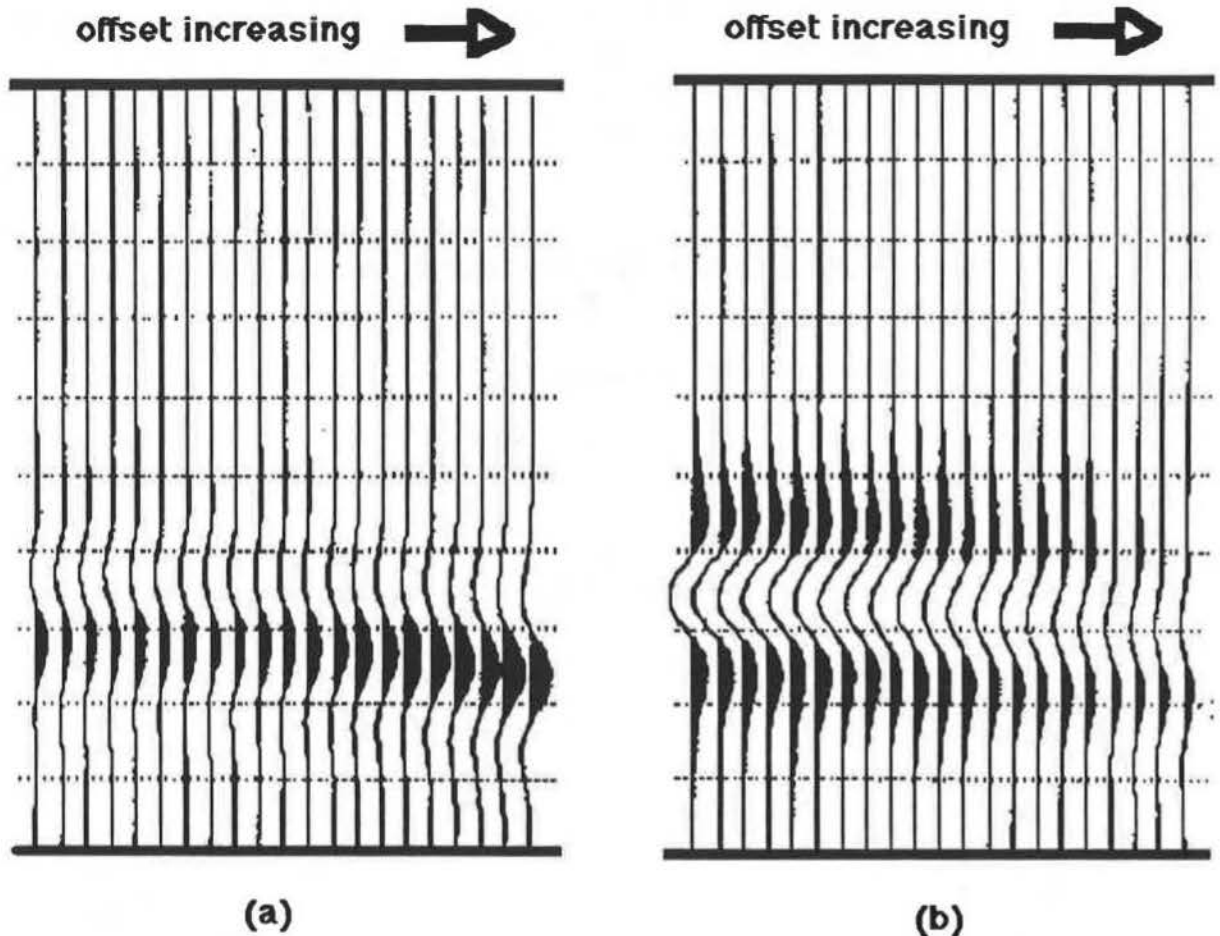


Fig 8. (a) Modeled response of a 15 Hz Ricker wavelet reflecting off a 1.8288 m (6 feet) thick coal seam where transmission losses have not been accounted for. (b) As (a), but now transmission losses have been taken into account and the seismograms have been gained by a factor of 2.5 relative to (a). Angles of incidence at the far offset are close to  $30^\circ$ .

have modeled the coal seam with the same ratio of peak wavelength to layer thickness using the AVO program of Hampson and Russell and find that we can reproduce the results of Treadgold et al (1990) if we do not include transmission losses in the modeling (Figure 8a). However, if we include transmission losses there is no increase in amplitude versus offset, instead there is a decrease with the overall reflection being significantly weaker (Figure 8b). It is only at angles greater than about  $30^\circ$  that the

amplitude starts to increase, this being due to converted wave energy interfering constructively.

### Acknowledgements

This work was carried out under the Seismic/Lithology Project at Curtin University of Technology (MERIWA Project 125 and APIRA Project P274) sponsored by BHP Petroleum, WAPET, Western Mining Corp, Woodside Offshore Petroleum and MERIWA. Sierra Geophysics and Hampson and Russell are gratefully acknowledged for providing Curtin University of Technology with their software.

### References

- Juhlin C., 1990, Interpretation of reflections in the Siljan Ring area based on results from the Gravberg-1 borehole, *Tectonophysics*, 173, 345-360.
- Kallweit R.S. and Wood L.C., 1982, The limits of resolution of zero-phase wavelets, *Geophysics*, 47, 1035-1046.
- Lange J.N. and Almogharbi H.A., 1988, Lithology discrimination for thin layers using wavelet signal parameters, *Geophysics*, 53, 1512-1519.
- Mazzotti A. and Mirri S., An experience in seismic amplitude processing, 1991, *First Break*, 9(2), 65-73.
- Meissner R. and Meixner E., 1969, Deformation of seismic wavelets by thin layers and layered boundaries, *Geophys. Prosp.* 17, 1-27.
- Milkereit B., Percival J.A., White D., Green A.G. and Salisbury M.H., 1991, Seismic reflectors in high-grade metamorphic rocks of the Kapuskasing uplift: results of preliminary drill site surveys, in press, *J. Geophys. Res.*
- Ostrander W.J., 1984, Plane-wave reflection coefficients for gas sands at nonnormal angles of incidence, *Geophysics*, 49, 1637-1648.
- Pinchin J. and Mitchell A.B., 1991, Seismic AVO analysis of Permian gas sand at Kerna Field, Cooper Basin, SA, presented at the 8th ASEG Conference and Exhibition, Sydney, February, 305-308.
- Nur A. and Simmons G., 1969, The effect of saturation on velocity in low porosity rocks, *Earth and Planetary Science Letters*, 7, 183-193.
- Robertson J.D. and Nogami H.H., 1984, Complex trace analysis of thin beds, *Geophysics*, 49, 344-352.

Shuey R.T., 1985, A simplification of the Zoeppritz equations, *Geophysics*, 50, 609-614.

Treadgold G.E., Dey-Sarkar S.K., Smith, S.W. and Swan H.W., 1990, Amplitude versus offset and thin beds, paper presented at *SEG 60th Annual International Meeting and Exhibition, San Francisco, September*, 1463-1466.

Widess M.B., 1973, How thin is a thin bed?, *Geophysics*, 38, 1176-1180.

# LITHOLOGY PREDICTION IN CLASTIC SEDIMENTARY ROCKS USING SEISMIC VELOCITIES

Lev Vernik and Amos Nur

*Stanford Rock Physics Laboratory*

## ABSTRACT

An extensive database of petrophysical measurements at 40 MPa effective pressure on a variety of rock types encountered in clastic sedimentary sequences was used to develop a petrophysical classification of rocks and derive new empirical models that describe velocity versus porosity relations in these rocks. Based on optical microscopy, SEM, and experimental data five major petrophysical groups are distinguished. Four of them comprise reservoir and other non-source rocks: 1) clean arenites (clay content  $C < 2\%$  vol.), 2) altered arenites and arkoses ( $2\% < C < 15\%$ ), 3) wackes ( $35\% > C > 15\%$ ), 4) sandy shales ( $C > 35\%$ ). The fifth group is represented by kerogen-rich hydrocarbon source-rocks, normally referred to as black shales. Each of these petrophysical groups is characterized by its distinct mineralogy, texture, structural position of clay or organic matter.

Most important result is the recognition of the clay content at about 15% as a threshold between grain-supported (clean arenite and arenite) and matrix-supported (wacke and sandy shale) lithologies. This is consistent with some of the modern petrologic classifications (e.g., Greensmith, 1989) that take into account the primary composition and amount of matrix in sedimentary rocks. Thus, our petrophysical classification and empirical relations should be generally independent of regional peculiarities. The difference between arenites and wackes consists not only in gross amount of clay, but also in its structural position. The border between wacke and sandy shale is less clearly defined.

The compressional and shear velocity versus porosity relations for each of the nonsource-rock groups is found to be linear with very high correlation coefficients (0.90 to 0.99) enabling remarkably accurate porosity estimates and lithology prediction from sonic logs, compared to the time average equation (Wyllie et al., 1956) or the linear regression by Han et al., 1986, both of which neglect the structural position of clay in the rock fabric. Most important feature of these new transforms is that their utilization does not require the exact knowledge of clay content, but simply a general range of its variation which is readily available from logging data and/or cuttings analysis.

The linear dependence of velocities on porosity in each petrophysical group breaks down only at the transition to unconsolidated sediments. This breakdown is attributed to the marked increase in shear modulus during the processes of incipient lithification of sediment. The incipient lithification takes place on the background of minor porosity reduction and gradual increase in bulk compressibility. These features allow us to consider the petrophysical analysis, encompassing ultrasonic measurements and petrographic observations, as a major tool that aids in tracing and quantifying subtle features associated with formation, physical compaction, and chemical diagenesis of clastic sedimentary rocks.

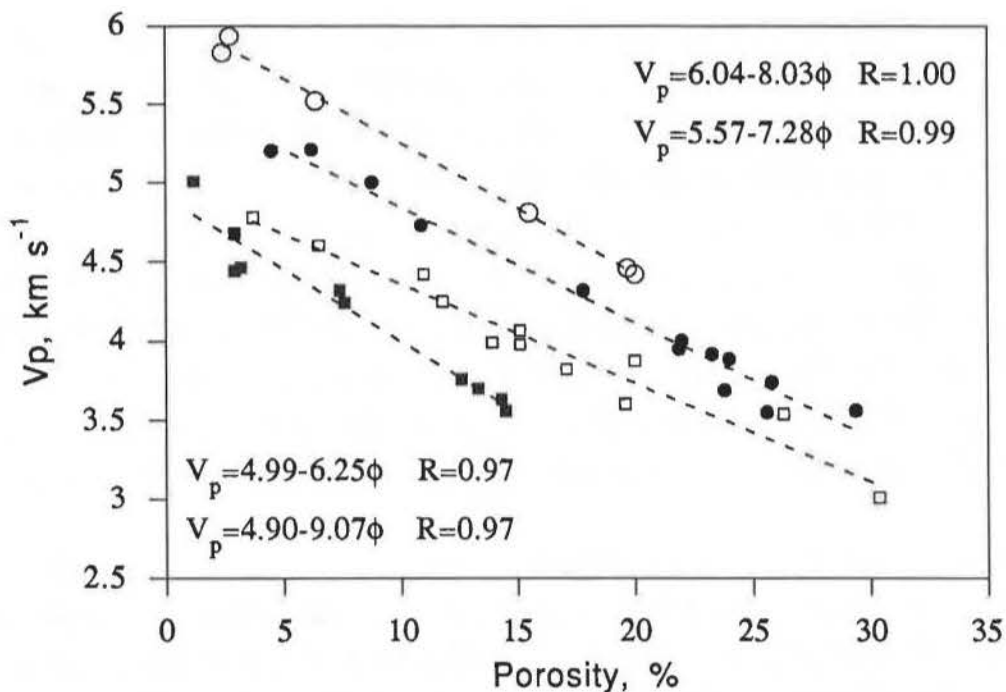


Figure 1. Empirical relations between  $V_p$  and porosity derived after new petrophysical classification of clastic sedimentary rocks. From the top downwards: (1) clean arenite, (2) arenite, (3) wacke, and (4) sandy shale.

A most remarkable feature of kerogen-rich black shales consists in extremely low velocities normal to bedding as compared to other lithologies of comparable porosity. This gives rise to a strong anisotropy even at high confining pressures. We find that these characteristics are fairly unique features of this petrophysical group and primarily reflect kerogen content, microstructure, and maturation level of black shales. The anisotropy parameters  $\epsilon$  and  $\gamma$  governing P- and SH-wave velocity anisotropy of these rocks vary from 0.24 to 0.46. The anisotropy parameter  $\delta$  (apparent anisotropy) indicating the P-wave velocity indicatrics behavior at small incidence angles (to  $25^\circ$ ) may be quite small ( $0.01+0.1$ ) making it difficult to study anisotropy in situ using solely compressional waves.

Conversely, the apparent anisotropy  $\delta'$  that governs SV-wave velocity at small angles is high ( $0.28 + 0.80$ ) and should be used as a major indicator of strong anisotropy when interpreting surface seismics or VSP data.

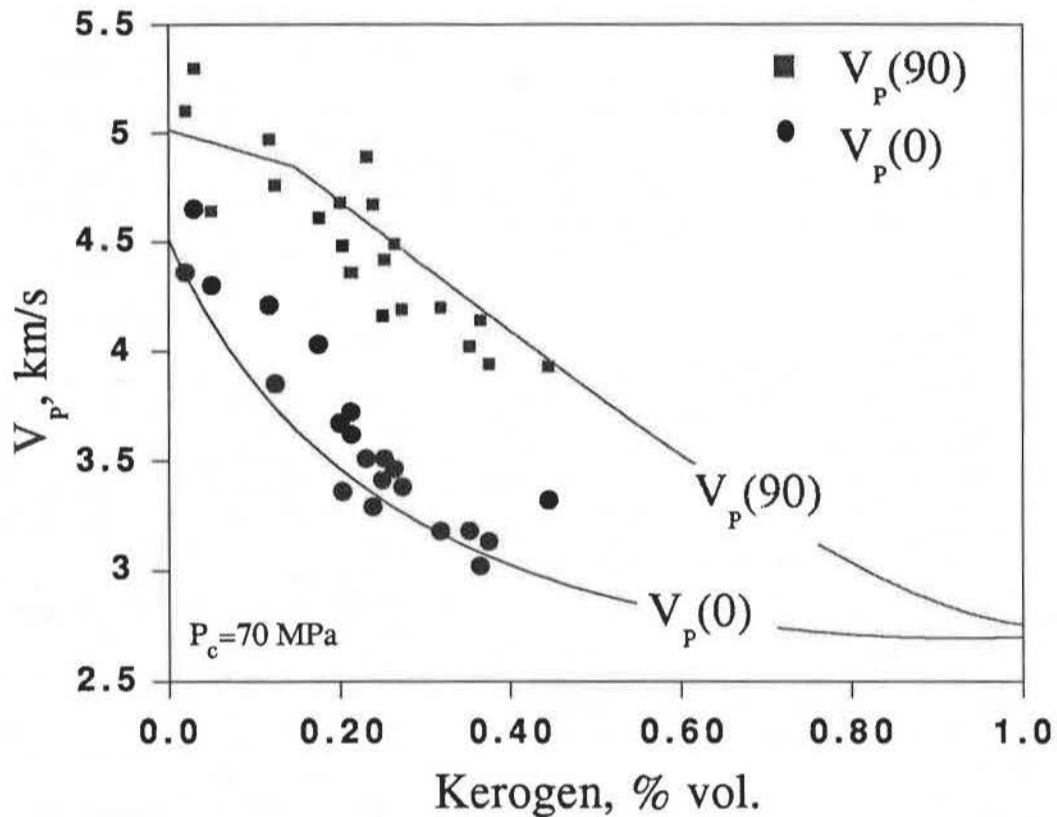


Figure 2. Compressional velocity vs. kerogen content for propagation normal  $V_p(0)$  and parallel  $V_p(90)$  to bedding measured at 70 MPa confining pressure. The data are compared with anisotropy prediction based on Backus (1962) model modified to account for the observed discontinuity of clay layers in black shales containing more than about 15% vol. kerogen.

We find also that microcracks inferred from ultrasonic velocity measurements occur only in mature shales. These microcracks are parallel to the bedding plane and further enhance strong intrinsic anisotropy of these rocks, notably at low effective pressure. This observation may be of special importance in source-rock formations overpressured due to the ongoing process of maturation and hydrocarbon generation. Our results show that on a small scale kerogen-rich shales are transversely isotropic rocks and can be effectively modeled using the thin-layer composite concept modified to account for the specific distribution of organic matter in the rock fabric.

**SUMMARY**

Zero/near-offset VSP synthetic and field data are studied to investigate conditions which are appropriate for the detection of the anisotropic constituents of a reservoir zone. Theoretical studies using synthetic seismograms show the detection abilities of two different analysis techniques and the experimental inaccuracies which may arise. These are complemented by field data analyses from several different survey regions.

**INTRODUCTION**

Estimates of shear-wave splitting may yield valuable information about the stress- and crack- geometries within reservoirs for hydrocarbon production (Crampin et al. 1986). Shear-wave splitting is currently being used to monitor the orientation of cracks at depth in the Earth from a variety of acquisition geometries, this approach being especially useful when the simple geometry of a zero-offset, or near-offset, VSP is employed. Determining the polarization of the leading split shear-wave for vertical or sub-vertical raypaths, may give direct information about the strike of these parallel, aligned vertical cracks, the time-delay between the arrival of the first and second split shear-waves may be related to the maximum differential anisotropy of the medium, from which crack density may be inferred.

To understand those factors which contribute to misunderstandings and errors in the splitting estimates, a variety of seismograms are analysed, ranging from synthetic seismograms in an ideal uniform medium, to field data propagating through a complicated velocity structure. Firstly, a sequence of relatively 'noise-free' response curves are produced by processing synthetic seismograms generated from a variety of different anisotropic models. The analysis is then repeated on seismograms which are further complicated by introducing noise, and correspond to velocity structures obtained from well-log or inversion data from different survey regions. Finally, field data from these regions is analysed using the synthetic results to guide the selection of a suitable strategy to interpret and detect the anisotropy, and determine whether or not it is practical to resolve depth variations in the crack properties.

**RESOLUTION STUDY USING SYNTHETICS****Response curves for analysis techniques**

The expected response of two analysis techniques is studied under ideal conditions. The polarization direction of the

leading shear-wave, and the time-delay between split shear-waves are determined for synthetic seismograms from a zero-offset VSP, under 'noise-free' conditions. Synthetic seismograms are computed for shear-waves propagating vertically through Earth models with an anisotropic reservoir layer embedded in a background of anisotropic material. The waves are excited by in-line and cross-line source, generating a zero-phase wavelet with a peak-frequency of 15Hz.

Two techniques (PMM and AIR) are used to extract the estimates of shear-wave splitting. PMM derives anisotropy values from two neighbouring geophones, using the horizontal displacements from two orthogonal, horizontal source polarizations. It is a frequency domain method. This effectively determines the anisotropy between the geophones using source rotation at depth (Zeng, private communication). AIR obtains anisotropy estimates for the medium between the source and geophone, using the horizontal displacements acquired from two orthogonal, horizontal source polarizations (MacBeth and Crampin, 1991; Zeng and MacBeth, 1991). It is a time domain method. The techniques are fast as they are solved analytically. The techniques are chosen as they estimate the anisotropy in different ways, and are effected by errors arising from noise, local fluctuations and geophone misorientations in different ways.

Figures 1(a) and (b) illustrate different estimation results from PMM and AIR techniques respectively. In this example, zero-offset recordings are simulated for geophones distributed down a vertical borehole which passes through a 120m-thick reservoir layer lying at 690m in a uniform background anisotropic material. The background medium has an isotropic matrix velocity of 1.65km/s. Geophone recordings are made every 30m, starting at 420m, and ending at a depth of 990m. The sets of curves for each technique are for various crack-strike changes relative to background orientation ( $5^\circ$  to  $40^\circ$  in steps of  $5^\circ$ ) given a constant crack-density of 0.04, and for different crack-densities in the reservoir (from 0.04 to 0.20 in steps of 0.02) given a constant crack-strike of  $90^\circ$ .

The polarization estimates from the PMM method (Figure 1(a)) remain at a constant value until the reservoir, at the top of which there is a rise (rate depends on crack density) to the value in this layer, followed by a decrease beyond the bottom of the layer. The sharpness of this response can be enhanced by choosing spectral measurements grouped closer to the peak frequency of the

signal. The time-delay curves provide a better definition of the reservoir layer. The inter-geophone time-delay remains constant up to the reservoir zone, at the top of which there is a sharp change to the value in the reservoir, followed by a sharp decrease at the bottom of the layer back to the background value. The maximum values of crack-strike and crack-density are close to true model values. Increasing the crack-density, in addition to changing the crack-strike direction in the reservoir layer, improves the resolution of the crack-strike change.

The results for AIR are shown in Figure 1(b). The AIR method produces a polarization direction at the source (dotted lines) and a polarization direction at the geophone (solid lines). As these polarization estimates are averaged over the entire pathlength, there is a slow increase in polarization with a maximum of about  $10^\circ$ , followed by a slow decrease outside the reservoir zone. The source orientation stays at a constant value below the reservoir. The time-delay for this technique increases linearly due to the 4% background anisotropy. At the top of the reservoir layer there is an increase in gradient. At the bottom of the layer, this gradient recovers back to the background value. When the crack strike and density vary together, then the change of polarization estimate is more noticeable, but the shape of the curves remains similar to that above.

For both techniques, the time-delay profiles can be readily translated into a differential velocity anisotropy, and hence an estimate of crack-density, by using an estimate of the group delay of the wavelet at each geophone. AIR estimates can be changed into inter-geophone measurements, and divided by the appropriate differential group delay values. Anisotropy values computed in this way for both techniques, agree in both magnitude and position with the model parameters.

#### Resolution of thin anisotropic layers

How thick does a layer of anisotropy need to be before it can be resolved? Synthetic seismograms are constructed for a range of different geophone spacing and reservoir thicknesses. Peak frequency of the wavelet is also considered as a variable. Results are used to tackle a forward design problem for a seismic experiment in a clay reservoir, to be carried out in the Caucasus, USSR. The zone of interest lies at 1700m depth, and is 30m thick. Synthetic seismograms are constructed using the well logs from a neighbouring site (less than 2km away). Response curves for PMM and AIR methods define the ranges of

differential anisotropy, and maximum geophone spacing, which make this layer seismically visible.

#### Minimum geophone spacing

PMM time-delay variations arise due to the measurement of small time-delays between two geophone levels. This is taken further to investigate the effect of geophone spacing on results for different anisotropies. Different wavelet peak frequencies and noise levels are considered.

#### FIELD DATA ANALYSES

Zero- or near- offset data from a variety of different survey regions are analysed using theoretical results to interpret output from analysis techniques. The particular example shown here is for the BP Divine test site in Texas. The reservoir zone in this case is an Austin Chalk layer of about 220m thick, lying at 695m. Geophone recordings are made from 240m to 990m, at intervals of 8m. Data from two sources with orthogonal and horizontal polarizations are acquired. The source offset is 119m. The peak frequency of the wavelet is 10Hz. The results of applying the PMM and AIR methods on data from a near-offset VSP are shown in Figure 2(a) and (b) respectively.

The PMM results in Figure 2(a) show a roughly constant polarization azimuth of down to about 575m, where there is a transition zone, to another constant level at  $9^\circ$  from the previous value. The depth response of PMM in Figure 1(a) suggests that this may be interpreted as a change in crack-strike orientation. Data from other zero- and near-offset VSPs for this area do not show this step. There is no transition in polarization within the reservoir zone. The time-delays obtained using this technique show considerable scatter. It can be shown by using synthetic seismograms that this is a consequence of the geophone spacing and the velocity structure. The gross trend of these time-delays appears to suggest a constant value of about 7.5ms down to the reservoir zone, and a decrease to 3ms within the Austin chalk. The velocity structure determined from well logs suggests that the likely cause of this decrease is an increase in the shear-wave velocities within this zone.

The polarization results (geophone) for the AIR method are roughly constant, at the same value as the upper region of PMM results. As expected, the time-delays show much less scatter than for the PMM method. The time-delay increases linearly from 8ms at the first geophone (corresponding to 3% differential anisotropy in the upper 240m), to 12ms at the top of the Austin Chalk, where there may be a slight change in the gradient of the linear trend.

The first linear portion gives 0.8% differential anisotropy. The change in the slope of the second portion of the data could be related to the increased shear-wave velocity in the reservoir layer.

#### DISCUSSION AND CONCLUSIONS

As yet not enough data has been published from a wide range of geological situations to be certain of how crack parameters vary with depth and geological setting. In some cases it appears that crack orientation remains constant with depth, in others there may be a progressive increase with depth, or possibly abrupt changes in crack strike with depth. This study addresses the requirement, by analysing zero/near-offset VSP data from several different survey regions, with diverse geological settings. Guidelines for the interpretation of the output from estimation techniques are obtained from the analysis of synthetic seismograms, to investigate the detection limits of a reservoir zone and the effect of geophone spacing. There is some evidence for changes in crack strike and time-delay.

#### REFERENCES

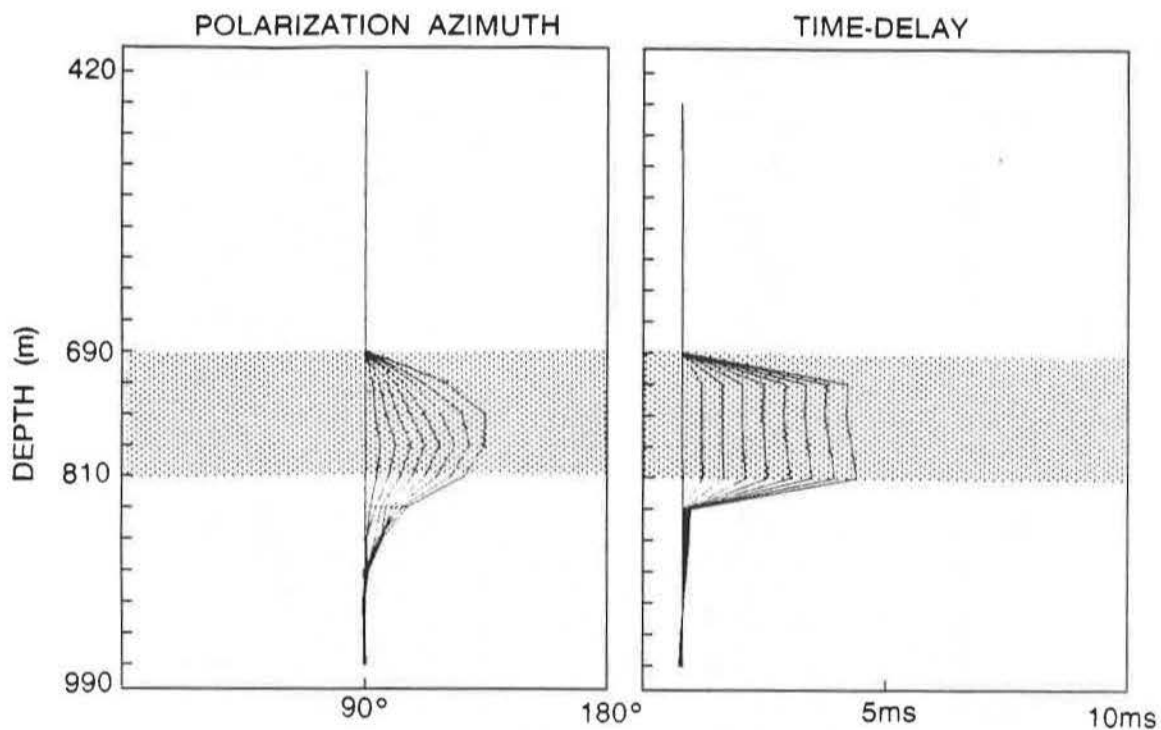
Crampin, S., Bush, I., Naville, C. and Taylor, D.B., 1986. Estimating the internal structure of reservoirs with shear-wave VSPs. *The Leading Edge*, **5**, 11, 35-39.

MacBeth, C. and Crampin, S., 1991. Automatic processing of seismic data in the presence of anisotropy. *Geophysics*, in press.

MacBeth, C., and Yardley, G., 1991. Optimum estimation of crack-strike. *Geophys Prosp.* submitted.

Zeng, X. and MacBeth, C., 1991. Analytical processing for shear-wave anisotropy. *Quarterly Report of Edinburgh Anisotropy Project*, EAP 91 6.

a)



b)

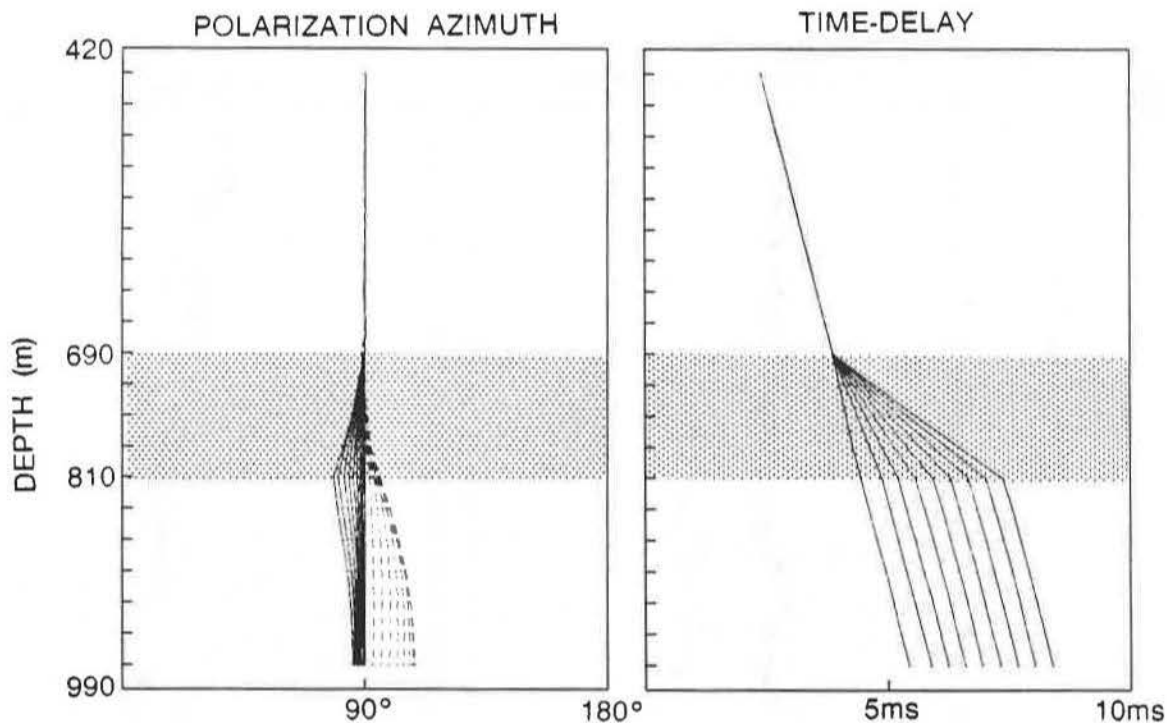


FIGURE 1. Results from applying (a) PMM, and (b) AIR techniques to zero-offset VSP synthetic data. The Earth model consists of a uniform anisotropic material, with a constant isotropic matrix velocity of 1.65km/s. A reservoir zone of 120m thick is embedded at 690m. It is marked by a change in crack-strike ( $5^\circ$  to  $40^\circ$  in steps of  $5^\circ$ , constant crack-density of 0.04), and then crack-density (0.04 to 0.20 in steps of 0.02, constant crack-strike of  $90^\circ$ ). The surrounding medium has a crack-strike of  $90^\circ$  and a crack-density of 0.04. Source polarization directions (dotted lines), and geophone polarization directions (solid lines) are shown for (b).

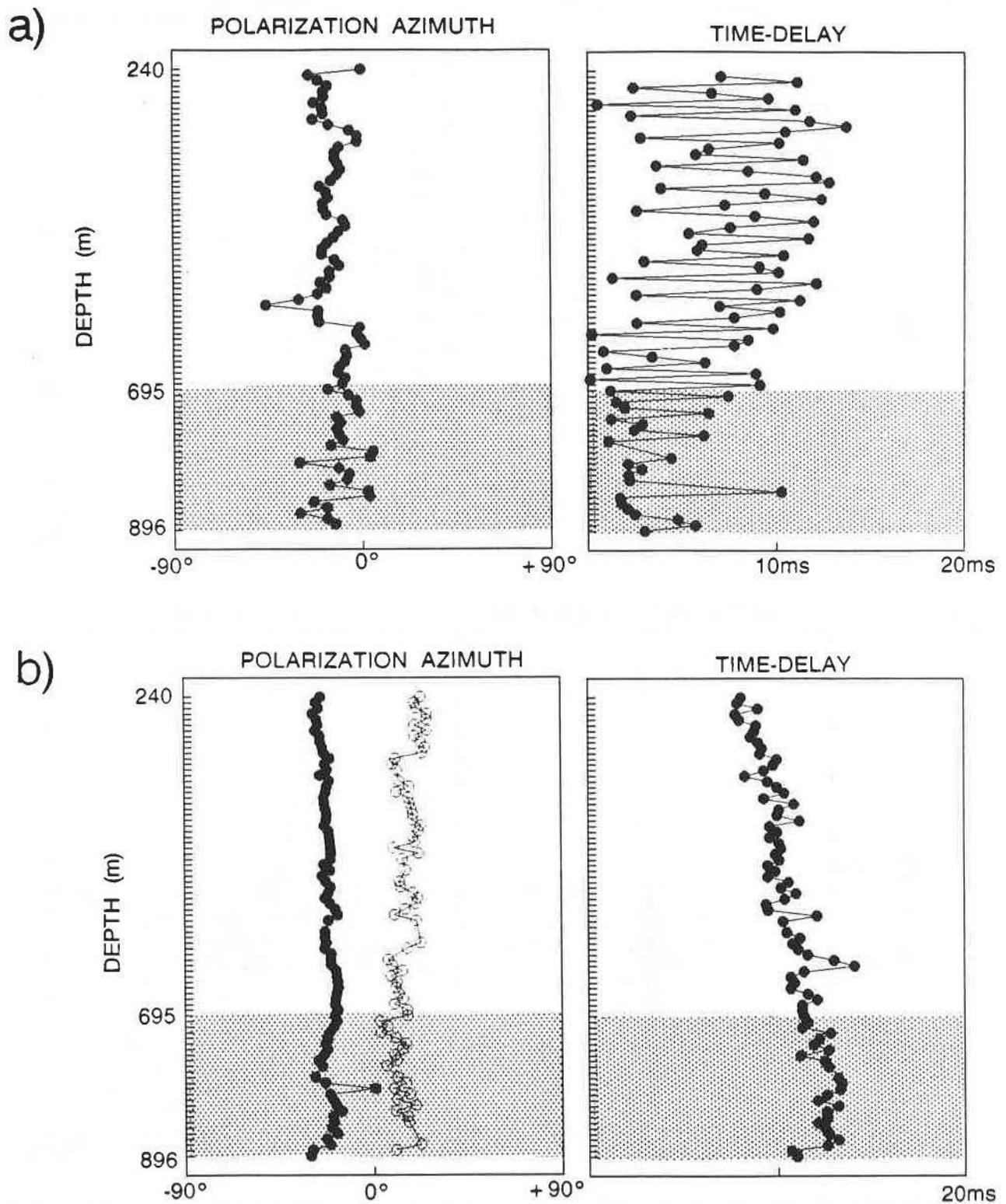


FIGURE 2. Results from applying (a) PMM, and (b) AIR techniques to zero-offset field data from BP Divine test site. Reservoir zone (roughly 220m thick) lies at a depth of 695m. Estimates show a consistent polarization azimuth for both techniques. Time-delays are considerably scattered for PMM, but record a distinct linear trend for AIR. Source polarization directions (open circles), and geophone polarization directions (solid circles) are shown for (b).

# PREDICTING LITHOLOGY FROM ELASTIC PROPERTIES USING DISCRIMINANT ANALYSIS

C. S. Burns, Geophysical Development Corporation

A discriminant analysis of lithology is presented using the variables of compressional transit-time, shear transit-time,  $V_p/V_s$ , and bulk density. The derived discriminant criterion is used to classify the measurements of elastic properties into previously defined lithologic groups.

Generally, discriminant analysis is concerned with developing a discriminant criterion to classify an unknown object containing one or more quantitative variables into one of two or more distinct groups. Assuming that the prior probability of an observation is known and the group probability density function at that observation can be estimated, discriminant analysis determines the posterior probability of an observation belonging to a particular group. The set of measurements of an observation can be presented as a point in a  $p$ -dimensional vector space which is partitioned into regions  $R_i$ . A point is classified as coming from group  $i$  if it lies in region  $R_i$ .

An example is taken from part of a larger study of predicting sand/shale lithology, porosity, and pore fluid from an amplitude-versus-offset inversion of CDP gathers. A discriminant analysis is conducted on known lithologies and their associated elastic properties to establish a local database in order to classify the results of the inversion into 6 lithologic groups: gas-sand, clean water-sand, shaly sand, very shaly sand, sandy shale, and shale. The lithologic description of the training set is obtained from a volumetric analysis of the well-log measurements in conjunction with core analysis. The variables of the lithologic groups are the shear transit-time (from a di-pole sonic), compressional transit-time,  $V_p/V_s$ , and bulk density.

Various tests are conducted on estimating the probability density function for the lithologic groups, and on variable selection. A quadratic discriminant function (assuming a multivariate normal distribution) is contrasted to a nonparametric kernel method used to derive classification criteria. To facilitate graphical presentation of the various tests, the dimension of the elastic variables are reduced to the first two canonical variables. The canonical variables are the linear combinations of the elastic variables that summarize between-lithologic-group variation in a similar way that principal components summarize total variation.

The discriminant criterion is based on the data from one well (sampled every 1ft) and is evaluated on three data sets: 1) original well, 2) original well converted into time (sampled every 4ms), and 3) a nearby well. Each data set was independently interpreted for lithology. A few misclassified observations contaminate the training set. To reduce bias on evaluating the original well, the classification was based on crossvalidation (treating  $n-1$  observations as a training set for the observation left out). Appraisal on the performance of the various classification criteria is somewhat subjective--a "misclassified" observation can be a minor one-level change in lithology and in some instances a possible correction of the original classification.

# RELATING ROCK PHYSICS TO SEISMIC LITHOLOGY IN A NORTH SEA RESERVOIR

J.P. Blangy and S.Strandenes, Stanford University

## Summary

The key to locate, develop and effectively produce oil and gas reserves is a thorough understanding of depositional environment, geological history and geophysical parameters. This leads to the development of depositional, geological and geophysical models that form the basis both for detailed seismic interpretation and eventually for the development and production of the field. In trying to relate seismic data to reservoir quality, an important and often neglected step, is to establish a rock physical model of the reservoir. Knowledge of how the seismic data is affected by variations in lithology can only be obtained from systematic studies of the reservoir rock.

The rock physical model typically consist of a detailed description of the rock in terms of porosity, permeability, pore geometry, mineralogy, cementation, temperature, pore fluids, pore pressure and confining pressure, and how these variables in turn affect the compressional and shear velocities in the rock. Elastic velocities were measured on 38 core samples under varying conditions of effective pressure, fluid type, and temperature. The reservoir sands consist of loosely consolidated sub-arkosic to sub-lithic sands, occur at a relatively shallow depth of 1500m, and are saturated with both oil and gas. Core porosities are comprised between 25% and 40%, and permeabilities vary from 1D up to 30 D. Mineralogy of individual cores was obtained from thin section analyses and related to velocity changes.

The ultrasonic measurements, together with petrographic analysis, provides a detailed knowledge of the rocks at the micro scale. We then propose a method for upscaling and integration with data at different scales. Once the rock physical model has been established, the petrophysical-based micro model can be up-scaled to sonic and seismic frequencies, to provide the important and necessary link between lithologic parameters and seismic data. Log and core data were integrated to yield a synthetic and continuous pseudo-shear velocity record. Elastic parameters on a 0.15m interval were then scaled-up and properly averaged to seismic frequencies, according to the method of Backus (1961).

Ultrasonic, sonic, and seismic data were then combined to better characterize the quality of the reservoir sands from the Troll field in the North sea. A 3-D seismic survey was interpreted and provided the structural and stratigraphic framework for detailed integrated seismic analyses. Detailed pre-stack models were also carried-out to evaluate the effects of mica content, and carbonate "bones" on the seismic response.

## 1. Petrophysics

We measured compressional and shear velocities in 38 rock samples from the Troll field in the North Sea. The samples range from unconsolidated coarse grain sands to loosely consolidated fine grained sandstones with porosities at atmospheric pressure varying between 25 % and 38.5 %.

These measurements give new and useful insight into the effects of cementation on elastic moduli in porous rocks. We use ultrasonic laboratory measurements in combination with petrographic analysis to obtain a rock physical model of weakly cemented unconsolidated reservoir rocks with porosities between 25% and 38.5%.

### (i) Experimental procedures

The rocks under study are weakly cemented, high porosity unconsolidated sandstones. To prevent the samples from falling apart, the cores were cut under liquid nitrogen to a length

between 3 cm and 5 cm and a diameter of 2.5 cm, and were then jacketed in lead sleeves with metal screens at both ends. Porosities were measured with a helium porosity-meter. The standard pulse transmission technique was used to obtain the ultrasonic velocities. Due to the loose consolidation of the samples, corrections for elastic and inelastic deformation were important, and were implemented at all effective pressures.

(ii) Mineralogy of the sands

One thin section from each of the core samples was analyzed, and revealed that the quartz content is generally comprised between 50-80 %, the mica content between 0-30 % and that the amount of feldspar show less variation and generally takes a value of approximately 20 % of the rock volume. It was found that the lowest porosity samples contain a high amount of mica and a low amount of quartz, and that on the average the amount of quartz increases and the amount of mica decreases for increasing porosities. The grain sizes range from fine to coarse grains (< 0.1 mm to 0.5 mm). The highest porosities are found within the mica free medium grained sands.

(iii) Ultrasonic velocities

Dry and water saturated compressional and shear velocities were measured as a function of effective pressure. Figure 1 shows the results for the dry and water saturated samples at 30 MPa effective pressure. At 30 MPa effective pressure, the dry p velocities range from 2100 m/s at the highest porosities (37 %) up to about 2800 m/s for the lowest porosities (22 %). The corresponding variations in dry shear velocities are 1300 m/s - 1800 m/s. The water saturated p velocities range from 2500 m/s at the highest porosity up to 3100 m/s at the lowest porosity, while the corresponding s velocities take values between 1100 m/s - 1600 m/s.

In general there is a good linear relationship between the compressional and shear velocity, with a different slope for the dry and the water saturated case. The ratio between the compressional and shear velocity increases with increasing porosity (and thus decreasing consolidation), in particular for the water saturated case (figure 2). A weak pressure dependence is also present, and in the dry case the  $v_p/v_s$  ratios are on the average 1.55 at 30 MPa effective pressure decreasing to about 1.45 at 5 MPa effective pressure. The  $v_p/v_s$  ratios in the water saturated samples lie between 1.9 - 1.95 at the lowest porosities increasing to 2.2 at the highest porosities. The pressure dependency for the saturated  $v_p/v_s$  ratios is opposite that of the dry case, meaning that the lowest ratios are obtained at the highest effective pressure.

Because the presence of mica is known to restrict the fluid flow at Troll, the mapping of micaceous zones is crucial for an optimal production of the field. The data analysis indicates that a high amount of mica marginally increases the dry compressional velocities compared to the clean sands. High amounts of feldspar can lower the velocities due to the presence of small amounts of clay. This velocity change is on the order of 100 m/s. There is no systematic variation in the amount of feldspar with porosity or grain size, indicating that effects of weathered feldspar may occur within all of the lithologies. Because of this, it is not possible, for a given porosity, to deduce mineral composition of the rocks from the velocity alone. However, since the amount of mica is related to porosity, it is possible to establish a velocity-mica relationship. This relationship gives a linear increase in velocity for increasing mica content.

The measured ultrasonic velocities in the water saturated samples are very similar to those computed from the Biot low frequency expressions, both at low and high effective pressures. This indicates that the pore fluids in these measurements are still relaxed, and that the data can be regarded as being in the low frequency regime. The difference between the low and high frequency results from the Biot expressions are negligible, indicating that the measurements obtained in this experiment can be used in direct comparison between sonic and seismic measurements.

#### (iv) Comparison to other data

A comparison between the measurements of our rocks to measurements in other sandstones can be viewed in figure 3. The large variations are caused by differences in petrophysical characteristics of the rocks. We conclude that the velocities in unconsolidated sandstones have a weaker dependency on porosity compared to those in well cemented sands. The data comparison also shows that the absence of cement can have a stronger effect on the velocities than the presence of clay; the velocities in clean Troll sands are lower than in samples containing a substantial amount of clay. We propose that the absence of cement is the major reason behind these observations.

We have established a detailed rock physical model of weakly cemented, unconsolidated sandstones from Troll. The model is of great importance in reservoir characterization studies, and provides a bridge between disciplines. Next, we integrate these results with other data at different scales, in an attempt to predict reservoir quality between wells.

## 2. Up-scaling and averaging

We have seen that the Troll velocities depend on the intrinsic properties of the mineral constituents, on the in-situ state of the rocks, and on fluid content. We designed an integrated deterministic modeling approach, whereby a suite of properties (mineralogical content, porosity, fluid content, effective pressure, clay content, state of consolidation) are integrated and used quantitatively to arrive at the velocities of the sediments under investigation; the method is based on well responses and includes four steps: the establishment of lithologic boundaries, a classification scheme, a calibration step, and an upscaling procedure. The upscaling method is based on previous work by Backus (1962) and Helbig (1981). This method is then applied to obtain the elastic properties of reservoir sands from calibrated logs and seismic, and is used in sensitivity analyses for the seismic characterization of a North sea reservoir.

## 3. Seismic Interpretation

Two objectives were sought: first, to map the exact gas/oil contact, and its evolution through time as the field is produced; second, to identify areas of high permeability.

Careful mapping and interpretation of a high resolution 3-D seismic survey provided the structural and stratigraphic framework for a detailed integrated seismic analysis. Seismic picks of Formation tops were based on several well control points, and were correlated across the field. The best reservoirs consist of clean, medium grained sands, which were deposited in a shallow marine environment. Lesser quality reservoir sands consist of micaceous sands, which were deposited under a lower energy marine environment, and appear as sands with a generally high and blocky to serrated gamma ray log response. In general, the reservoir sand sequences are cyclic, with a basal more micaceous layer, gradually coarsening upward into clean sands at the top. Key rock properties from the petrophysical analysis provide the link to the seismic stratigraphic interpretation.

A series of sensitivity analyses were then carried-out on pre-stack synthetic forward models. In particular, the A.V.O. responses of good and bad gas sands, and of a good and bad oil sands, were compared. Geological parameters were changed in accordance with depositional models, and petrophysical parameters were varied according to empirical observations; these were then used to calibrate the effects of porosity changes, mineralogy, and fluid type. We make

an attempt at characterizing the seismic response of high permeability sands and to identify them seismically. This is done by integrating petrophysical data such as empirically derived porosity-permeability relationships for each facies and by up-scaling petrophysical properties from the microscale to seismic wavelengths.

(i) Analysis of stacked data

The structural and stratigraphic framework for detailed integrated seismic analyses is provided by the interpretation of a recent high resolution 3-D seismic survey. Seismic picks of formation tops based on several well control points, are tied-in to the seismic and correlated across the field.

Sedimentological analyses indicate that the best reservoirs consist of clean, medium to coarse grained sands, which were deposited in a high energy, shallow marine environment. They are characterized by a generally low and blocky gamma ray log response. Lesser quality reservoir sands consist of micaceous sands, which were deposited under a lower energy marine environment, and appear as sands with higher and blocky to serrated gamma ray log response. In general, the reservoir sand sequences are cyclic, with a basal more micaceous layer, gradually coarsening upward into clean sands at the top.

Stratigraphic relationships relate the energy of the depositional environment to the cyclicity of the reservoir sands, and can be identified through key petrophysical properties such as sorting, grain size, and mica content.

(ii) Preliminary pre-stack Modeling

Log and core data are first correlated as shown in figure 4. This provides a calibration of the well-log derived properties to the rock properties, at the microscale. Velocity dispersion (Biot, 1956, Winkler, 1985, Liu et al, 1976, O'Connell and Budiansky, 1977, Jones, 1986) can be neglected to a first order in these sands. The petrophysical information is then integrated further to yield a synthetic and continuous pseudo-shear velocity record. Elastic parameters at a log scale of approximately 0.15 m interval are then scaled-up and properly averaged to seismic frequencies, according to the method of Backus (1962), and long wavelength transversely isotropic equivalent parameters are derived using Thomsen's (1986) notation.

A series of sensitivity analyses are then carried-out on pre-stack synthetic forward models. Exact reflection coefficients for transversely isotropic layers are calculated using the expressions of Daley and Hron (1977). Geological parameters are changed in accordance with depositional models, and petrophysical parameters are varied according to empirical observations which are used to calibrate the effects of porosity changes, mica content, and fluid type. Changes in amplitude responses are observed on the synthetic gathers and compared to the data. In particular, the A.V.O. responses of good and bad gas sands, and of a good and bad oil sands, are compared (Gassman, 1951, Gregory, 1976, Domenico, 1976). Because the sediments are loosely consolidated and exhibit a relatively small amount of diagenesis, we then relate the permeability of the reservoir sands to the seismic, through porosity and textural information (figure 5).

In a final step, the effects of changes in the petrophysical properties of the seal and its thickness are assessed. The effects of changes in the amount of transverse isotropy (Wright, 1987, Samec and Blangy, 1990, Thomsen, to be published) induced by fine layering of calcite cemented "bones" within the reservoir are also evaluated by comparisons of pre-stack responses.

#### **4. Conclusions**

This work is above all a feasibility study for understanding the effects of parameter changes on seismic pre-stack responses. A technique was presented to systematically integrate different kinds of geophysical/geological data, and to quantitatively determine petrophysical parameters at seismic scales. The technique was then used in sensitivity analyses for the seismic characterization of a North sea reservoir.

#### **Acknowledgements**

This work was supported by the S.R.B. project and the Gas Research Institute. The authors also thank Norsk Hydro a.s. for supplying the data and for their support of this project. The Triple Society is acknowledged for moral support.

#### **References**

- Backus, S., 1962, Long-wave elastic anisotropy produced by horizontal layering, J.G.R., vol. 67, pp. 4427-4440.
- Biot, M.A., 1956a, Theory of propagation of elastic waves in a fluid saturated porous solid.I. Low frequency range: J.Acoust.Soc.Am.,28,168-178
- Biot, M.A., 1956b, Theory of propagation of elastic waves in a fluid saturated porous solid.II. Higher frequency range: J.Acous.Soc.Am.,28,179-191
- Daley, P., F., and Hron, F., 1977, Reflection and transmission coefficients for transversely isotropic media: Bull., Seis. Soc. Am., 67, 661,675
- Domenico, S.N., 1977, Elastic properties of unconsolidated porous sand reservoirs : Geophysics, 42,1339-1368
- Gassmann, F., 1951: Elasticity of porous media: Vier. der Natur. Gesellschaft in Zurich, Heft I.
- Gregory, A. R., 1976, Fluid saturation effects on dynamic elastic properties of sedimentary rocks: Geophysics, 41, 895-921
- Han, D., Nur, A., Morgan, D., 1986, Effects of porosity and clay content on wave velocities in sandstones: Geophysics, 51, 2093-2107
- Han, D., 1986, Effects of porosity and clay content on acoustic properties of sandstones and unconsolidated sediments: Ph.D. Thesis Stanford University, Stanford Rock Physics Report vol. 28
- Klimentos, T., McCann, C., 1990, Relationships among compressional wave attenuation, porosity, clay content and permeability in sandstones: Geophysics, 55, 998-1014
- Samec, P., and Blangy, J.P., 1990, Effects of Viscoelasticity and Anisotropy on A.V.O. Interpretation: Paper presented at the annual International SEG meeting in San Francisco.
- Thomsen, L., 1985, Biot-consistent elastic moduli of porous

- rocks: Low frequency limit: Geophysics, 50, 2797-2807
- Thomsen, L., 1986, Weak elastic anisotropy:  
Geophysics, 51, No. 10, 1954, 1966
- Thomsen, L., Weak anisotropic reflections:  
manuscript prepared for "Offset dependent reflectivity" to be published.
- Winkler, K., 1985, Dispersion analysis of velocity and attenuation in Berea sandstone:  
J. Geophys. Res., 90, 6793, 6800.
- Wright, J., 1987, Short note: The effects of transverse isotropy on reflection amplitude  
versus offset: Geophysics, 52, no. 4, 564, 567.
- Yin, H., Han, D-H., Nur, A., 1988, Study of velocities and  
compaction on sand - clay mixtures: Stanford Rock  
Physics Report Vol. 33

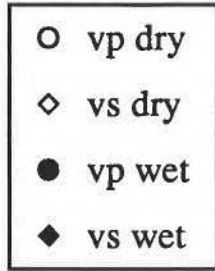
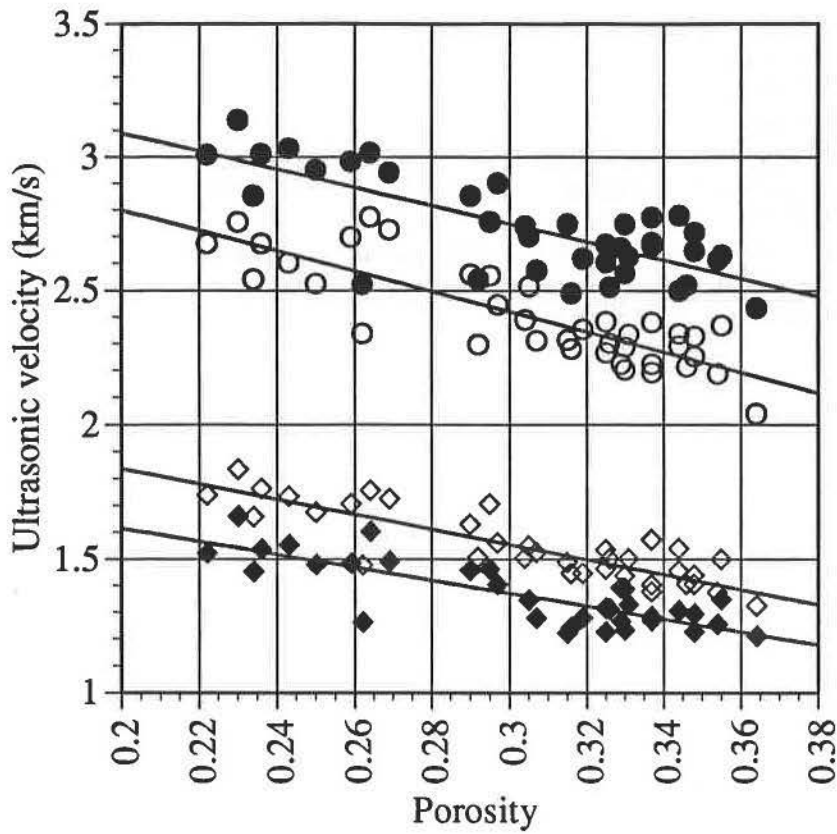


Figure 1 :  
Dry and water saturated  
compressional and shear velocities  
at 30 MPa effective pressure

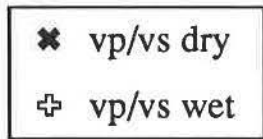
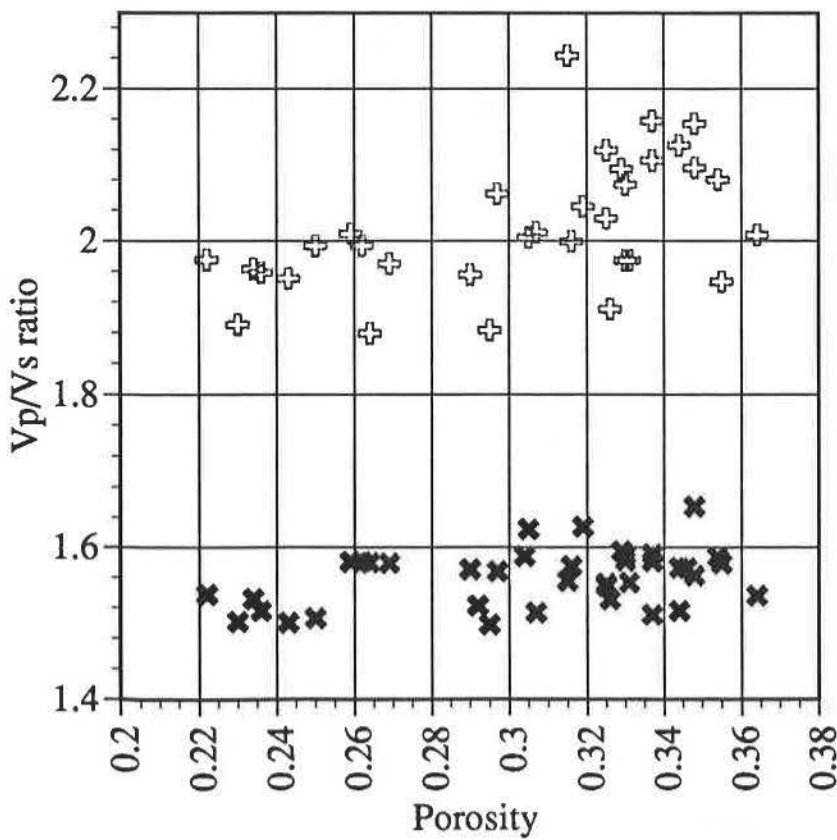


Figure 2 :  
Vp/Vs ratios in dry and water  
saturated samples at 30 MPa  
effective pressure

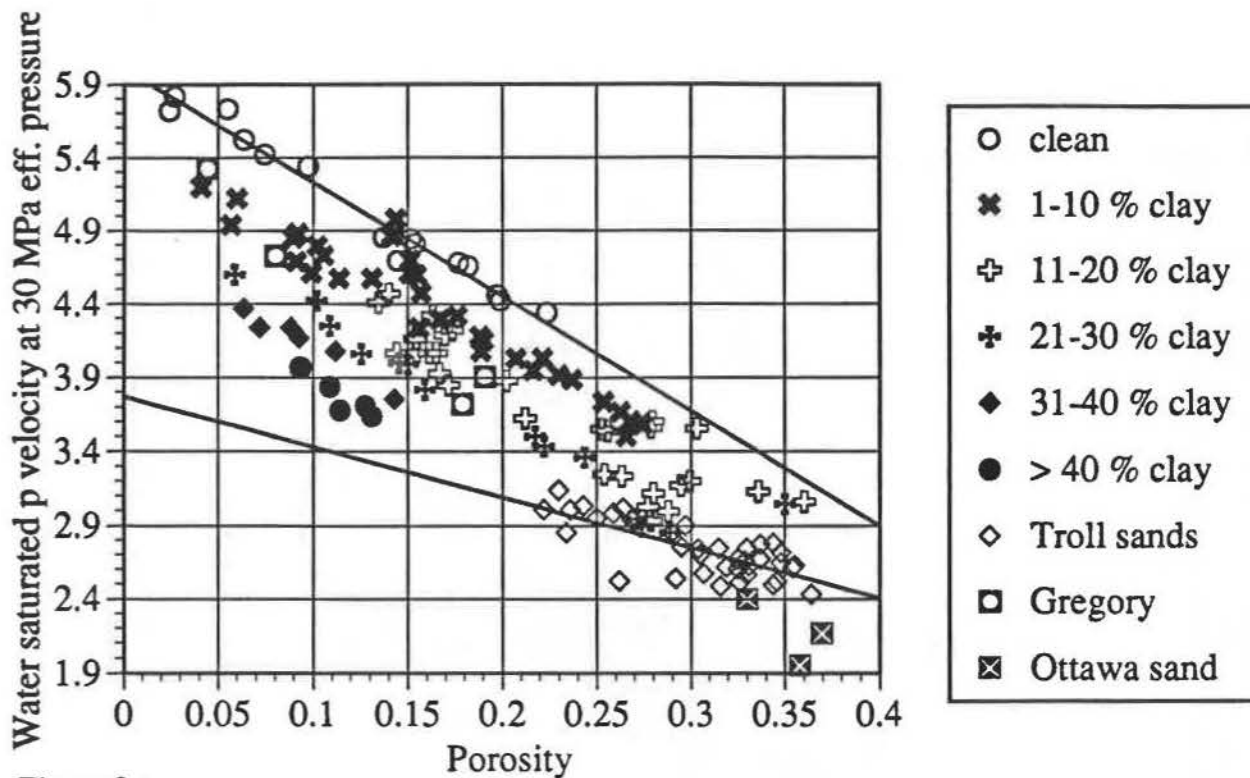


Figure 3 : Comparison between water saturated compressional velocities at 30 MPa effective pressure.

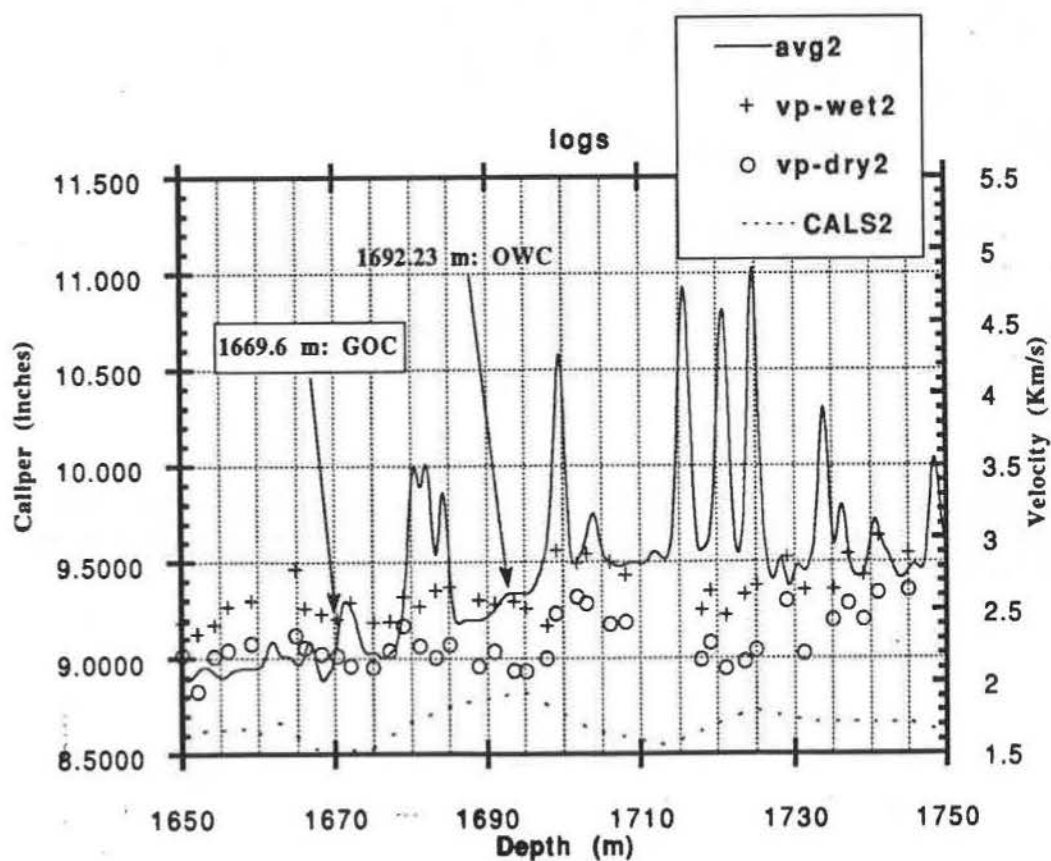


Figure 4: Comparison between log-derived (sonic) compressional velocities, and core measured compressional velocities under reservoir conditions in dry and saturated states. The caliper log is a good indicator of the borehole condition.

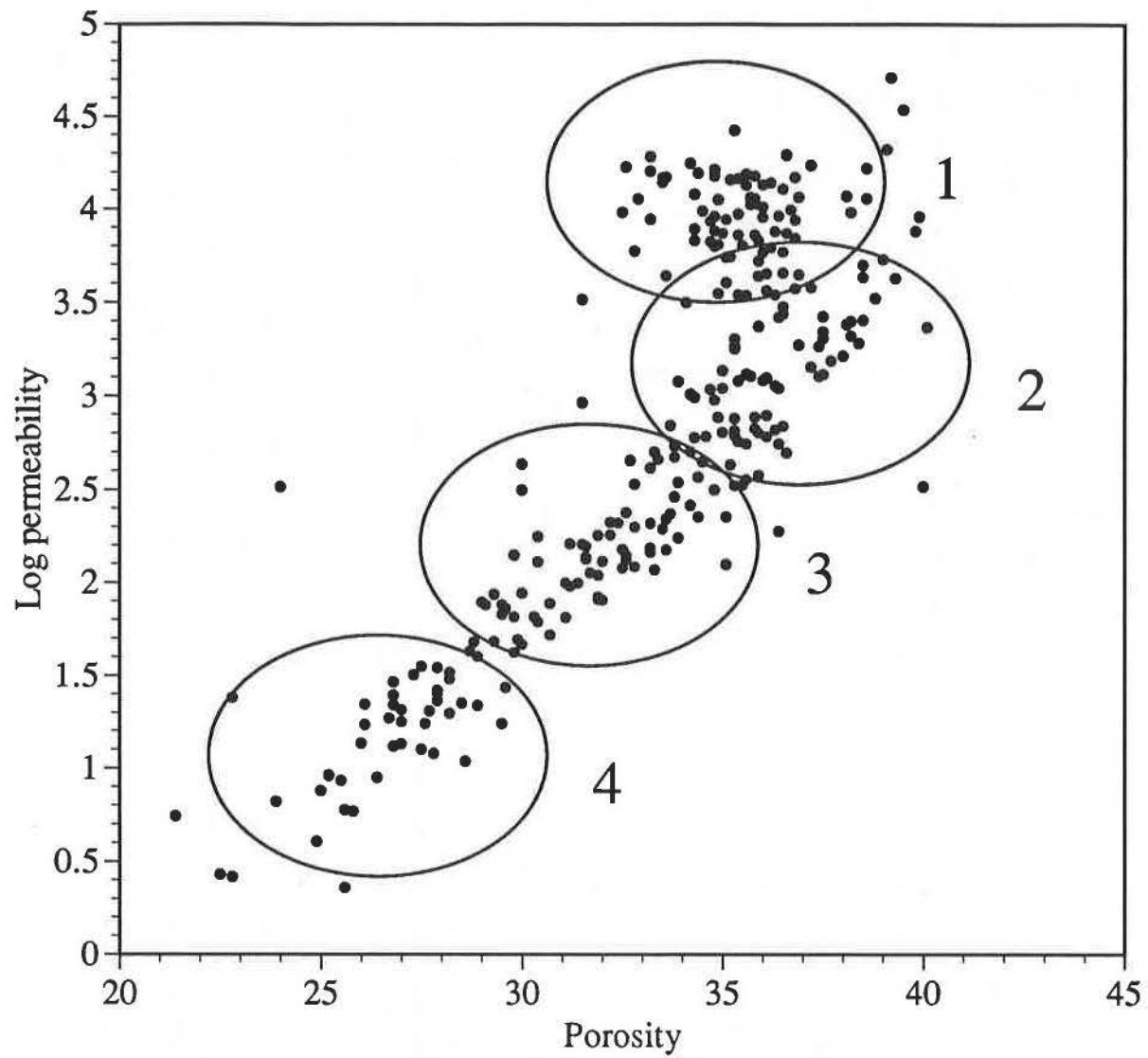


Figure 5 :

Log permeability versus porosity. Four lithologies corresponding to different fluid flow regimes are indicated on the figure. 1 - Medium grained clean sands; 2 - Coarse grained clean sands; 3 - Medium grained micaceous sands; 4 - Fine grained micaceous sands.

# RECONCILIATION OF DIP DATA AND VSP DATA, AND THE ILLUMINATION OF WEST TEXAS REEFS

D. McCall, L. Bennett, J. Caldwell  
Schlumberger Well Services

## Introduction

This paper describes the use of Dip data from the Formation MicroScanner (FMS)\* Logging tool in combination with offset-Vertical Seismic Profile (VSP) data to delineate a small Pennsylvanian Age carbonate reef buildup in West Texas. The study includes log data on 3 wells with VSP data from 2 of the wells. The distance from Well A to Well B is only 320 feet and the distance from Well B to Well C is only 200 feet. In this short distance, the upper reef thickens by 26 feet and the lower reef thickens between 76 and 100 feet.

The combination of FMS Data and offset VSP data allowed the operator to offset a dry hole (Well A) and drill a productive oil well at the reef crest (Well B), 320 feet away. A second reef buildup was identified within the massive reef section. This reef was seen on the offset VSP. This lower reef was tested as gas productive.

The techniques used are very effective for locating the upper reef crest since the upper reef is underneath a shale section resulting in a very strong seismic reflection. Delineation of the

lower reef is much more difficult since it is located within the massive carbonate section where porosity is changing rapidly and little seismic contrast exists. The complexity of the problem is apparent since the VSP and synthetic data do not match except at the upper reef/shale interface.

## Discussion

Well A The location for Well A was selected based on geology and well control. The geologist believed that a reef was near the location of Well A. No surface seismic data was available in the area.

Well A was drilled and the upper reef was Drill Stem Tested and found to be water productive with a trace of hydrocarbons. Based on the DST results, the operator felt that any additional reef buildup would be oil productive.

A FMS Log was run in Well A. The dip data in the shale section directly above the reef indicated that the reef crest was to the West Northwest of Well A (285 degrees azimuth). (Note that the shale - not the erosional reef top - was used to pick the direction to the crest. Also a channel sand cuts the shale about 4 feet above the

---

\*Mark of Schlumberger

reef and the dips in the shale above the channel sand are not representative of the reef location.)

An offset VSP was run in Well A with the source located 1380 feet to the West Northwest (285 degrees azimuth). The VSP data indicated that the crest of the upper reef was located 320 feet West Northwest of Well A. The location for Well B was selected at this point. A second reflector within the reef indicated that a second reef (the lower reef, 200 feet below the upper reef) appeared to be building within the massive reef section. Based on the VSP it was expected that the lower reef in Well B would have at least 50 feet of buildup. The FMS data in Well A showed very little dip in the lower reef zone. This agreed with the VSP data which showed that the buildup began about 100 feet from Well A. Due to the disagreement between the FMS Data (no significant dip) and the VSP Data (50 feet or more buildup expected), a Sonic-Density Synthetic Seismogram was planned for Well B. (Only Density/Neutron/Induction data were available in Well A.)

Well B Well B was drilled based on the FMS and VSP data, 320 feet West Northwest of Well A. Well B encountered 26 additional feet of buildup in the upper reef and was oil productive. The lower reef had 76 feet of additional buildup and was gas productive. A Synthetic Seismogram using Sonic and Density data was used to confirm that the reflections on the VSP were in fact from the upper and lower reefs.

The FMS log in Well B indicated that Well B was drilled at the upper reef crest (2 degree dip was present in the shale just above the reef). The FMS indicated that the lower reef had about 25 degrees dip and was building rapidly to the North Northwest (345 degrees azimuth).

Based on the FMS data, an offset VSP was run in Well B with the source located 1400 feet to the North Northwest (345 degrees azimuth) of Well B.

The VSP in Well B showed a very thick upper reef reflector and it appeared that the lower reef reflector might have merged into the upper reef reflector. The upper reef reflector indicated that the upper reef would thin by 10 to 15 feet, 200 feet North Northwest of Well B.

The VSP data was reprocessed several times and the final interpretation was that the lower reef crest may have merged into the lower reef and in such a case, the crest would be located about 150 feet from Well B. Since Well B was producing, it was decided to pick the location for Well C 200 feet North Northwest of Well B, expecting to be slightly north of the crest. Since the lower reef in Well B was very tight (low porosity) it was hoped that more porosity would be found on the north side of the crest.

Well C Well C was drilled 200 feet North-Northwest of Well B. As predicted, Well C had 14 feet less buildup of the upper reef than Well B.

Contrary to our prediction, the lower reef had 4 feet less buildup of the lower reef but did have

slightly better porosity than Well B. The FMS data in the lower reef indicated about 25 degrees of dip down to the West. Based on the FMS data, it was concluded that Well C had gone completely over the crest of the lower reef and that the crest was approximately midway between the two wells and slightly East of Well C. Based on the dip angles we estimate that the crest of the reef would probably have about 25 feet of additional buildup from Wells B or C or a total buildup of about 100 feet from Well A. Since Well C had less buildup in both reefs than Well B, Well C was plugged and abandoned.

#### Conclusion

The combination of offset VSP data and FMS data will allow operators to accurately locate the crest of carbonate reef structures. In some cases it may also be possible to locate a reef crest within a carbonate structure such as the lower reef in this study. Location of the lower reef is far more difficult as shown by the lack of agreement between the VSP and Synthetic seismogram data. We were unable to fully explain the disagreement between the synthetic seismogram data and the VSP data and the disagreement between the two VSP data sets.

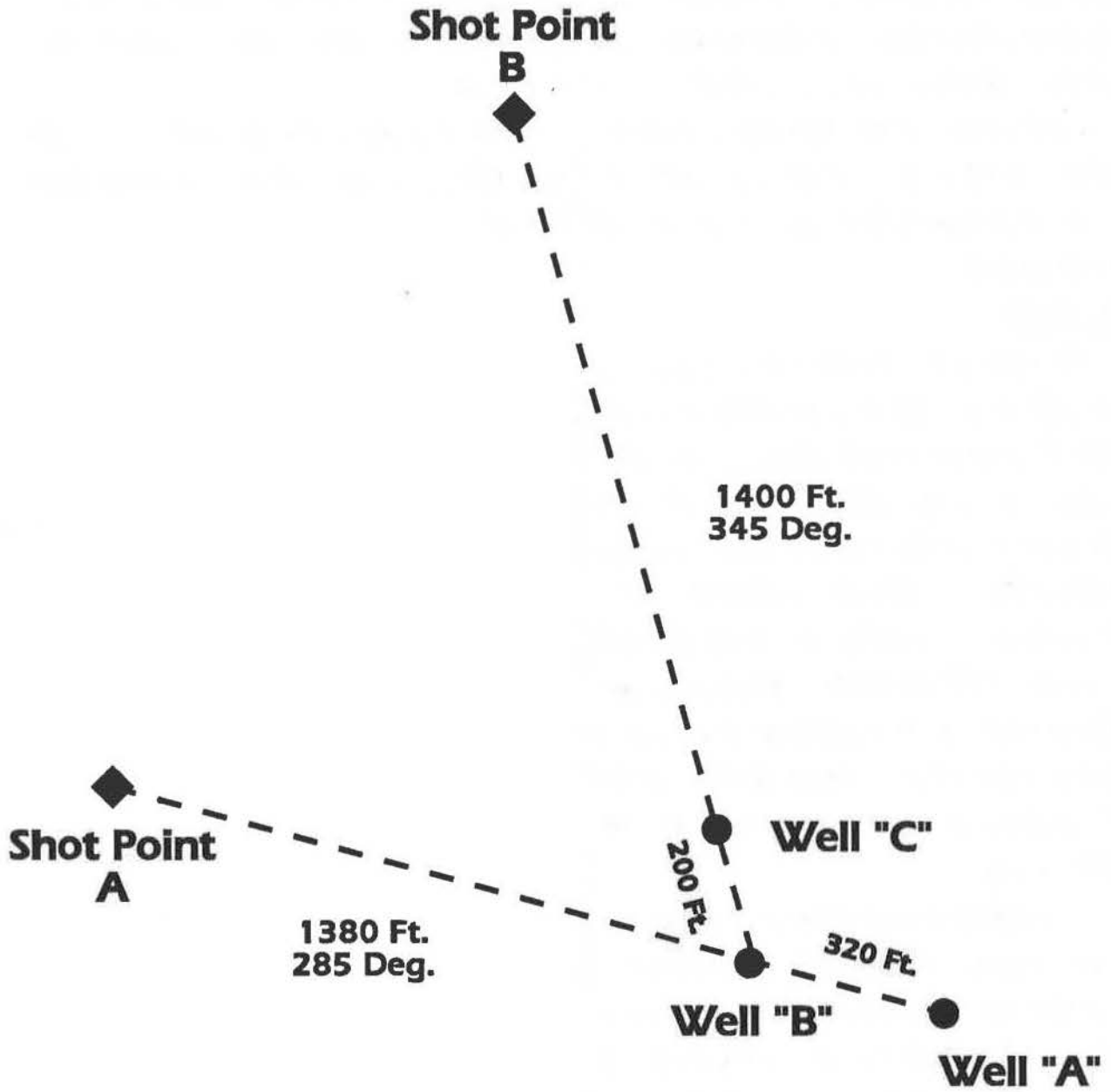
Correlation between wells in carbonate reef structures is often very difficult. Due to an error in correlation, the significant buildup of the lower reef from Well A to Well B was not recognized until the synthetic seismogram and VSP data were combined with the log data.

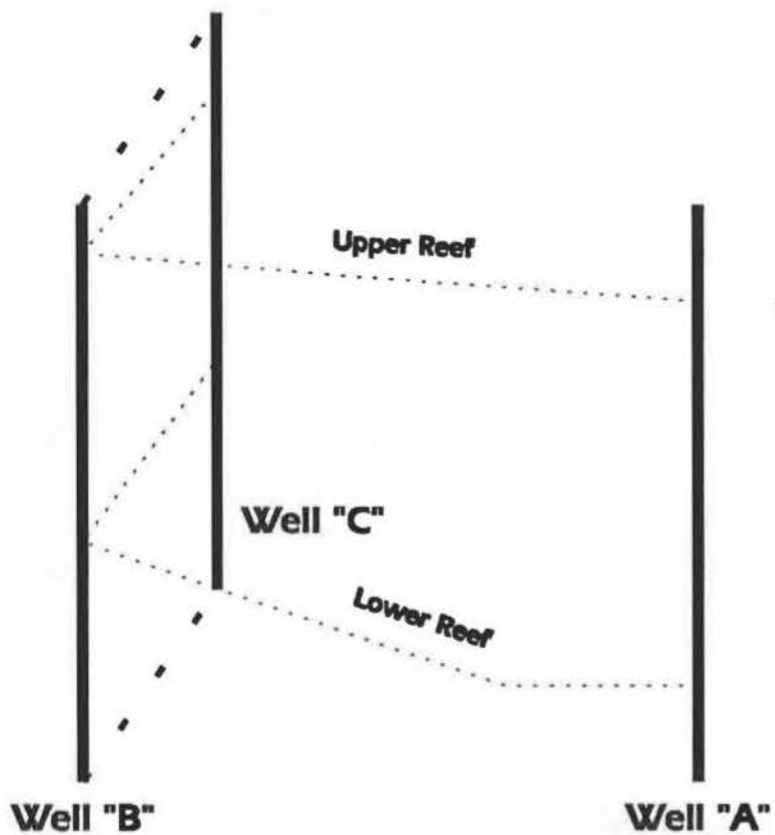
FMS data is very effective for determining the direction to the crest of a reef, even when only a few feet of shale is present on top of the reef. The FMS cannot accurately predict the distance to the crest.

Once the direction to the crest is known from the FMS data, an offset VSP can be acquired (in open hole or cased hole) to determine the distance to the reef crest.

By combining FMS and VSP data we can accurately answer the question: Where's the Reef (Crest)?

# Offset VSP Geometry





### Reef Buildup

	Well "A"	Well "B"	WELL "C"
Upper Reef	0.0 Ft	26 Ft	12 Ft
Lower Reef	0.0 Ft	76 Ft	72 Ft

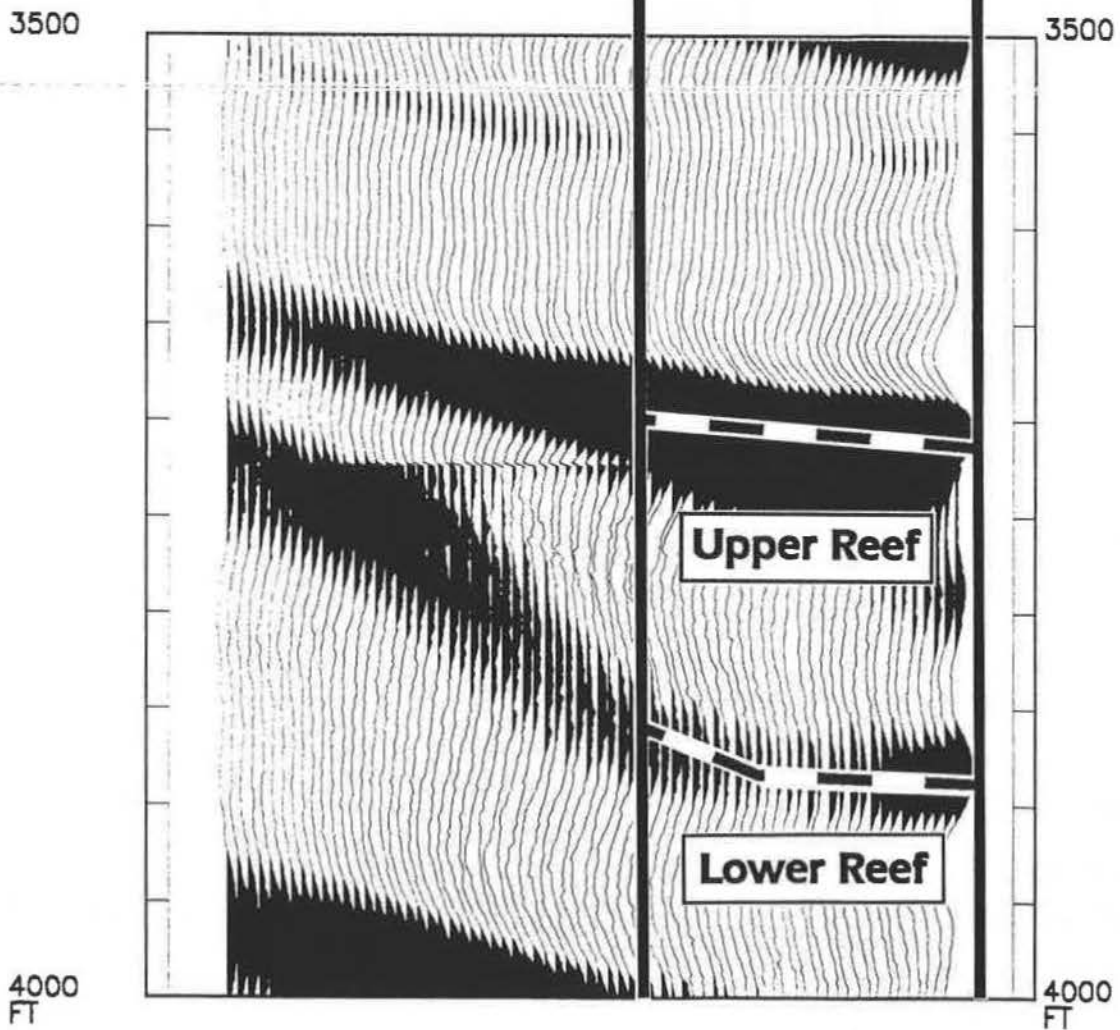
# Offset VSP Well "A"

CDP OFFSET  
FT

- 10.0
- 30.0
- 50.0
- 70.0
- 90.0
- 110.0
- 130.0
- 150.0
- 170.0
- 190.0
- 210.0
- 230.0
- 250.0
- 270.0
- 290.0
- 310.0
- 330.0
- 350.0
- 370.0
- 390.0
- 410.0
- 430.0
- 450.0
- 470.0
- 490.0
- 510.0
- 530.0
- 550.0
- 570.0
- 590.0
- 610.0
- 630.0
- 650.0
- 670.0
- 690.0

Well "B"

Well "A"



**SESSION 4**

**FRONTIER/SUBMATURE EXPLORATION**

Tuesday Afternoon  
Session Co-Chairmen: B. Tatham and D. Nester

## **The effect of small quantities of sand on average interval velocity in overpressured clastic sections**

T. S. Latham  
D. E. Eggers  
ARCO Oil and Gas Company  
Geoscience Exploration Operations  
Plano, Texas

Over large areas of the Gulf of Mexico, one of the major risk factors in hydrocarbon exploration lies in the presence or absence of an amount of sand adequate to form a commercial reservoir. It would be of great value if the presence of even small quantities of sand in an otherwise shale-dominated section could be inferred directly from seismic data. We propose that situations exist in which a small fraction of sand in a stratigraphic column can have an interval velocity signature sufficiently out of proportion to the quantity of sand that the anomaly is identifiable in the relatively low spatial resolution velocity information obtainable from seismic stacking velocities.

### **Relationships between sand percentage, geopressure, and velocity**

The association of abnormal pressure with thick, impermeable shale sections has been recognized for decades. An association of abnormal pressure with low p-wave velocity has also long been recognized. In the absence of structural control of sediment dewatering, we will operate under the premise that dewatering, and consequently abnormal pressure and seismic velocity, are strongly influenced by stratigraphy, and that anomalies in seismic velocity can be interpreted to be stratigraphically controlled.

Sand-rich sections tend to be normally pressured, and velocity tends to increase steadily with depth according to normal compaction trends. Except at very shallow depths, sands in such sections generally have higher velocities than the associated shales, so the average velocity of the section might be expected to increase roughly in proportion to the amount of sand present. Our experience in this situation has been that the variation in velocity with the percentage of sand in the section is generally too small to detect through stacking velocity.

In contrast, within sand-poor sections, which are often abnormally pressured, the low spatial frequency component of interval velocity is strongly influenced by sand percentage. It is of particular interest that the magnitude of the velocity effect in sand-poor sections is not, as might intuitively be expected, a linear function of the sand percentage; much of the velocity effect appears to be due to the first 10-15% net sand in an interval. Two key observations relevant to this nonlinearity have been made in many wells. First, at a given depth in a given well, the velocities of sands and shales tend to be quite similar. Within geopressure, although sands tend to have higher velocities than shales at similar depths, the difference is far too small for a simple linear-mixing model to account for the large variations in average velocity observed between different wells. Second, shale velocities in sand-rich sections often are higher than shale velocities at comparable depths in sand-poor sections. These observations suggest that the addition of a relatively small amount of sand to a shale-

dominated system may enhance the dewatering of the whole system, resulting in a velocity increase out of proportion to the quantity of sand.

We can summarize, then, that abnormal pressure will tend to develop in the absence of sufficient sand to allow dewatering of the section. Such an overpressured section will tend to have a low average p-wave velocity. If even a small quantity of sand is introduced into such a low-velocity, shale-dominated section, dewatering will be locally enhanced, and seismic velocity will locally increase.

### **Seismic Velocity Information**

Seismic data provides only low spatial resolution information. Typically, interval velocity can be accurately determined from stacking velocity only as an average over at least several hundred milliseconds. We would therefore not generally expect to be able to use interval velocity to directly detect sparse sand bodies in a shale-dominated section. However, the velocity anomalies apparently associated with enhanced dewatering through sands persist over a vertical interval substantially greater than the thickness of the sands themselves. We show examples which demonstrate that in this special case, this effect is sufficiently large to produce an anomaly detectable in seismic stacking velocities.

In principle, any seismic velocity estimation technique could be applied to search for the kinds of anomalies described above. For several reasons, we have found horizon stacking velocity analysis to be generally the most useful. It provides a sense of the lateral variation in velocity within specific stratigraphic intervals, and it is robust, inexpensive and fast, making it practical to apply in regional studies of large quantities of seismic data. In areas of structural complexity, prestack time migration velocity analysis can be useful, although stratigraphic interpretation of velocity anomalies in structurally complex areas will of course be ambiguous. If velocity varies over short enough horizontal distances to violate the CDP assumption, prestack depth migration velocity analysis can also be used, with the drawbacks that it is extremely expensive and not as robust as the other approaches.

### **Conclusion**

An absence of sand in a clastic section will tend to inhibit dewatering and compaction, resulting in the development of abnormal pressure and in low p-wave velocity. If a small quantity of sand is present in such a section, dewatering and compaction can locally be enhanced, resulting in a high-velocity anomaly. This velocity effect can extend over a large enough area to be identifiable in seismic stacking or migration imaging velocities. Under these conditions, then, seismic velocities can be used to help identify intervals in which minor sand may be present.

# BRENT CALCITE AND POROSITY PREDICTION USING SEISMIC ELASTIC PERTURBATION MODELING

K. Wrolstad, Unocal

## Abstract

The application of seismic elastic perturbation modeling to conventional surface seismic data from the North Sea resulted in prediction of calcite fraction and porosity in the Brent Formation laterally over a distance of about 1000' on either side of a borehole calibration point. The result implied a geologically reasonable model that low calcite abundance occurred in the Brent at the crest of the field due to the presence of undersaturated meteoric water during the end of Brent faulting and erosion. Downdip Brent sections generally have more calcite due to the influx of oversaturated water from underlying nonmarine Triassic formations. This interpretation is in agreement with the regional trend of calcite distribution in the area based on a grid of well data and a 13 year production history, but was not verified by drilling into the zone of the prediction. Pre-stack amplitude attributes and multi-channel cross correlation were both used in this hybrid approach to pre-stack seismic data inversion.

This modeling project demonstrated the potential for extracting information related to reservoir characteristics using forward elastic synthetic modeling of seismic data in an area with structural complexity and multiple contamination. Because of multiple interference with primary events, elastic perturbation modeling was needed to develop pre-stack signatures for specific lithologic changes. It was noted that changes in porosity produced a different response than changes in calcite cementation as observed in pre- and post-stack seismic attributes.

## INTRODUCTION

An extensive lithologic modeling project was completed in 1987 for six seismic lines with associated vertical wells from the Heather field in the North

Sea as shown in the map in Figure 1. Line 163 and well 2/5-2 (Figure 2) were selected for porosity and calcite cementation prediction because of the particularly good match between elastic synthetic and field data. The Brent sand formation is oil saturated at well 2/5-2 and has about 10% porosity with some calcite cementation.

Glasmann, et al. (1989) describe the geology and the history of diagenesis and fluid migration in the Brent sandstone of the Heather field. The Heather structure is a major fault block, tilted to the northwest and is the result of Mesozoic extensional tectonics. The Brent is a fan delta and wave-dominated deltaic sandstone/shale sequence and is heavily faulted. The field is currently divided into nine contiguous fault blocks that allow pressure communication to a greater or lesser degree. The Heather shale and siltstone provides the seal for the Brent formation. High-energy shoreface and fore-shore depositional environments generally make the best reservoir zones, but local cementation by calcite or quartz, or pore filling by clays often impair reservoir quality (Glasmann, et al., 1989). Thus the detection and mapping of porosity and calcite distributions is crucial to well site locations.

#### METHOD

Elastic lithologic modeling was applied to the problem of lithology and fluid saturation prediction because it has the potential for providing the means for direct detection of these properties. Seismic elastic synthetic shot gathers were generated using volumetrically analyzed well log data to constrain the input models. Petrophysical measurements also provided calibration points for the interpreted well log data. The goal of the synthetic modeling was to calculate traces that "acceptably" match equivalent field data traces. The elastic modeling assumes that the interpreted well log data accurately describes the in-situ rock properties at the well borehole. The conventional well log data contains all the information necessary for the computation of depth interval plane-layer models except for vertical shear wave (SV) velocity. Shear wave velocities are computed by estimating the rigidity using the Gassman-Biot-Geertsma equation:

$$V_p^2 = \frac{1}{\rho} \left[ K_b + \frac{4}{3} \mu_b + \frac{(1 - K_b/K_s)^2}{(1 - \phi - K_b/K_s) \mu_s + \phi \mu_f} \right], \quad V_s^2 = \frac{\mu}{\rho},$$

where,      K = bulk modulus                      b = dry rock  
                $\mu$  = rigidity                              f = pore fluid  
                $\phi$  = porosity                        s = solid material.  
                $\rho$  = density

This simplified form of the Biot equation is at the zero frequency limit and, therefore, is useful at seismic frequencies. The bulk modulus of the dry rock and the shear rigidity are solved given an initial compressional velocity, water saturation, effective porosity an assumed dry rock Poisson's ratio, and densities and bulk moduli of the water, hydrocarbon, and solid constituents of the rock. This procedure has been called the Gregory-Pickett method (Hilterman, 1984, Geertsma, 1961).

The bulk modulus of the solid frame was computed from a Voigt average (isostrain model) of well log estimates of quartz, calcite, and feldspar fractions. In order to compute perturbation models, calcite fraction and/or porosity were modified in the Brent interval and compressional velocities and densities were recomputed at every log sample, becoming "seed" values for new shear velocities. The Vp and density were computed using the time average equation,

$$\frac{1}{V_p} = \phi \left[ \frac{SW}{V_w} + \frac{(1-SW)}{V_{hyd}} \right] + \left[ \frac{f_{clay}}{V_{clay}} + f_{MAT} \left( \frac{f_{calc}}{V_{calc}} + \frac{f_{Kspat}}{V_{Kspat}} + \frac{(1-f_{calc}-f_{Kspat})}{V_{Qtz}} \right) \right]$$

$$\text{and } \rho = \phi \left[ SW \rho_w + (1-SW) \rho_{hyd} \right] + \left[ f_{clay} \rho_{clay} + f_{MAT} \left( f_{calc} \rho_{calc} + f_{Kspat} \rho_{Kspat} + \dots \right. \right. \\ \left. \left. \dots + (1-f_{calc}-f_{Kspat}) \rho_{Qtz} \right) \right]$$

where f = fraction                      k = potassium feldspar  
w = water                                Qtz = quartz  
hyd = hydrocarbon                      SW = fractional water saturation  
calc = calcite                            f<sub>mat</sub> = 1 - φ - f<sub>clay</sub>  
f<sub>calc</sub> + f<sub>Kspat</sub> + f<sub>Qtz</sub> = 1.0

V<sub>Qtz</sub> and ρ<sub>Qtz</sub> are unknowns in these equations, so they were computed as calibration values from log "seed" values of all other parameters. Then new Vp and density values were computed for changed f<sub>calc</sub> and porosity.

Layer interfaces for the models were determined by blocking the log according to the magnitude of acoustic impedance changes as given by the measured bulk density and sonic velocity. Layers from the water bottom to the start of the log data were estimated from sparker and conventional seismic data. Check shots were used to calibrate the time-depth relationships to key formations.

Compressional and shear wave velocities in model layer intervals were averaged according to the method of Backus (1962) to produce a "long-wave equivalent, transversely isotropic medium". Synthetic shot gathers were computed using a ray tracing program that applies Zoeppritz coefficients to reflected and transmitted events at each interface of a plane-layer model. Compressional and shear primaries and multiples were included, and the synthetic spike train was convolved with the measured marine source signature. Receiver array attenuation and geometrical spreading were also included in the synthetics.

The original starting model derived from well 2/5-2 (Model 2) is shown in Figure 3, where the Brent interval is represented by 23 layers. Model 4 represented a wet, low porosity, high calcite fraction Brent interval constructed by layer replacement from another nearby well. Relative velocity changes and layer thicknesses remained the same as Model 2 (Table 1). In this project several perturbation models were computed over ranges of average porosity and calcite fraction for the Brent layers 1A, 1B, and 2A. The lower Brent (layers 2B and 2C) of model 2 were incorporated in higher porosity mod-

els and the lower Brent from model 4 were incorporated in low porosity models. Table 2 gives a complete list of model names and parameters.

## Data Processing

Upon examination of the field data, it became apparent that special attention must be paid in the processing to attenuate strong water bottom multiples interfering with primary reflections in the Brent. Thus, the following processing sequence was used:

1. Pre-stack, source signature deconvolution to produce a zero phase wavelet,
2. Inverse spherical divergence correction,
3. FK multiple attenuation or parabolic filtering (Hampson, 1986),
4. Common offset sum of 5 adjacent common midpoint gathers, and
5. SODAS (Seismic Offset Dependent Amplitude Stack) processing with color attribute plot (Wrolstad, 1988). This method increases signal to noise with a running CMP mix and common offset sum followed by partial stacking and color attribute computation from the comparison of near, mid, and far amplitudes similar to that described by Onstott (1984).

After processing synthetic and field data with a mild FK velocity filter (cut at 85% of primary velocity function), a good match was obtained upon observing stacked trace waveforms and SODAS attributes. Further improvement was expected by substituting parabolic filtering for the FK processing. The results reported in this paper used the latter method.

## RESULTS

Having processed the field and synthetic data through the same above sequence to partial stacks, the SODAS color attributes of perturbation models and field data were compared. Multi-channel cross correlation of the 60 fold synthetic and field data sets were also computed over 100 msec windows encompassing the Brent interval over a CMP range extending 1000' on either side of the 2/5-2 projected borehole location. The cross-semblance relation used was:

$$S = \frac{\sum_j \sum_i x_{ij} y_{(i-l_s)j}}{\sum_j \sum_i x_{ij}^2}$$

where  $x$  is the reference gather,  $y$  is the test or model gather,  $i$  refers to sample, and  $j$  to trace number or offset. An example cross-semblance versus calcite fraction is shown in Figure 4. In this hybrid inversion, "best fit" models were chosen on the basis of peak cross-semblance, SODAS color attributes, and stacked trace waveform. Calcite fraction and porosity changes produced different AVO and stacked trace responses in the synthetics, some locations requiring low calcite and high porosity rather than low calcite and low porosity, for example. This is believed due to interference effects

caused by acoustic impedance differences and pre-stack amplitude differences caused by the fact that porosity and calcite fraction have different effects on the Poisson's ratio or  $V_p/V_s$ .

Of the 19 models considered, 4 were chosen that best represented the field data in a range of 25 CMP's or 625 meters. These models adequately explained the lateral changes in pre- and post-stack amplitude behavior. A trend emerged with calcite decreasing and porosity increasing up dip past the well to a structural high. These results are summarized in Figure 5. This implies a geologically reasonable model that calcite deposition occurred down dip due to the influx of water oversaturated in calcite from underlying Triassic rocks, whereas the up dip Brent formation is a better reservoir due to the local influence of undersaturated meteoric water trapped there during end-of-Brent erosion. It is also possible that there is a small local fault not well resolved seismically that acted as a conduit for some of the fluids involved in the calcite cementation.

## REFERENCES

- Backus, G. E., 1962, Long-wave Elastic Anisotropy Produced by Horizontal Layering, *JGR*, Vol. 67, p. 4427.
- Geertsma, J., 1961, Velocity-log Interpretation: the Effect of Rock Bulk Compressibility, *Soc. of Petrol. Eng. J. (AIME)*, Vol. 1, p. 235.
- Glasmann, J. R., P. D. Lundegard, R. A. Clark, B. K. Penny, and B. K. Collins, 1989, Geochemical Evidence for the History of Diagenesis and Fluid Migration: Brent Sandstone, Heather Field, North Sea, *Clay Minerals*, Vol. 24, PP. 255-284.
- Hampson, D., 1986, Inverse Velocity Stacking for Multiple Elimination, *Journal of the Canadian Society of Exploration Geophysicists*, Vol. 22, PP. 44-55.
- Hilterman, F. J., and M. Graul, 1984, SEG Seismic Lithology Course Notes, Society of Exploration Geophysicists, Tulsa Oklahoma.
- Onstott, G. E., 1984, Processing and Display of Offset Dependent Reflectivity in Reflection Seismograms, Masters Thesis, University of Texas at Austin.
- Wrolstad, K. H., 1988, Resolution of Thin Layers in Elastic Synthetic Seismograms, *SEG Annual Meeting Expanded Abstracts*, Vol. 1, pp. 190-193.

## ACKNOWLEDGEMENTS

The author would like to express his appreciation to Marcia Spriggins for data processing and plotting, to Terry O'Sullivan for log analysis, and to

Beryl McCormack, Richard Baker, Brian Penny, John Ellice-Flint, and Bill Pace for initiating the project, helpful discussions, providing the data, and supporting this work.

TABLE 1

Well 2/5-2 Layer Replacement From 2/5-15 and 2/5-3 in Brent

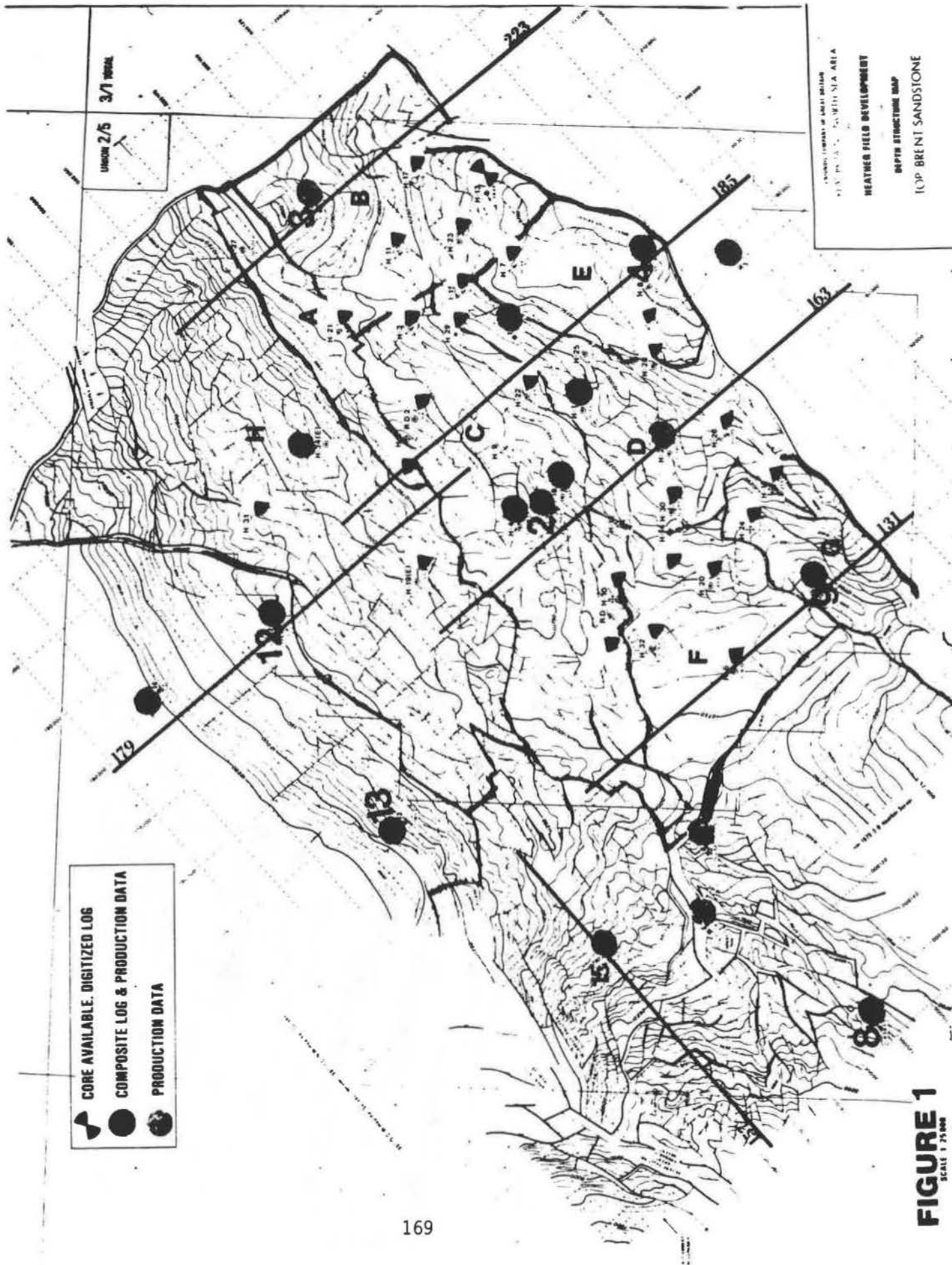
MODEL 2						MODEL 4					
Layer #	Vp	(%) φ	Calcite	Layer #	From Well	Vp	(%) φ	Calcite	Vs	ρ	
67	12013.1	16.4	.03	94	2/5-15	12451.2	13.3	.17	6990.4	2.468	
68	13185.5	12.0	.06	93	2/5-15	15345.4	4.8	.35	7682.3	2.619	
69	12482.2	16.3	0	92	2/5-15	12837.5	4.6	.15	6764.9	2.610	
Layer 1 70	13850.9	10.3	.13	73	2/5-3	15600.7	6.6	.25	9423.9	2.608	
71	Coal										
72	11857.2	10.0	0	76(83)	2/5-3	12190.6	14.1	0	6629.8	2.502	
73	Coal										
74	12649.4	6.0	0	78(84)	2/5-3	13400.3	6.6	.03	7287.3	2.598	
75	12237.8	16.8	.01	88	2/5-3	12740.8	15.6	.03	7634.0	2.417	
Layer 2A 76	18453.5	1.8	.56	not replaced							
77	12471.0	13.5	.04	96	2/5-15	13031.5	10.5	.04	7458.7	2.543	
78	15934.5	5.6	.26	86	2/5-3	16684.8	5.6	.28	10089.5	2.601	
79	13218.1	14.7	.04	87	2/5-3	15088.3	10.3	.28	9194.6	2.498	
80	15662.3	6.5	.28	102	2/5-15	17832.3	7.06	.52	11092.0	2.558	
Layer 2B 81	13035.7	15.0	.05	89	2/5-3	14667.0	8.4	.14	8680.7	2.554	
82	15155.0	9.1	.23	100	2/5-15	16437.8	11.1	.30	10315.9	2.496	
83	13304.5	12.4	.05	107	2/5-15	15711.6	4.7	.33	9077.5	2.608	
84	14413.1	7.3	.18	104	2/5-15	16818.8	.8	.49	9274.3	2.669	
85	13309.1	10.6	.07	96	2/5-3	15661.7	4.2	.26	8922.6	2.620	
Layer 2C 86	17256.1	2.5	.45	109	2/5-15	18266.8	.10	.48	10546.3	2.854	
87	13588.9	6.5	.09	91(99)	2/5-3	16777.4	4.3	.38	10208.3	2.623	
88	16510.4	0.4	.28	108	2/5-15	17515.3	1.15	.52	10188.5	2.681	

TABLE 2

Average Properties in Brent Layers 1A Through 2A

<u>Model #</u>	<u>Porosity</u>	<u>Calcite Fraction</u>	<u>Feldspar Fraction</u>
2B	.098	.09	.09
41	.098	0	.09
42	.098	.20	.09
43	.098	.30	.09
44	.098	.40	.09
45	.098	.50	.09
46	.05	.09	.09 *
47	.15	.09	.09
48	.20	.09	.09
49	.25	.09	.09
410	.30	.09	.09
411	.05	.09	.20 *
412	.05	.09	.09 *
413	.075	.09	.09 *
414	.05	.15	.09 *
415	.05	.25	.09 *
416	.05	.35	.09 *
417	.05	.45	.09 *

\* Lower Brent layers, 2B and 2C, from Model 4.



**3D  
HEATHER LINE 163**

2/5-2 ●

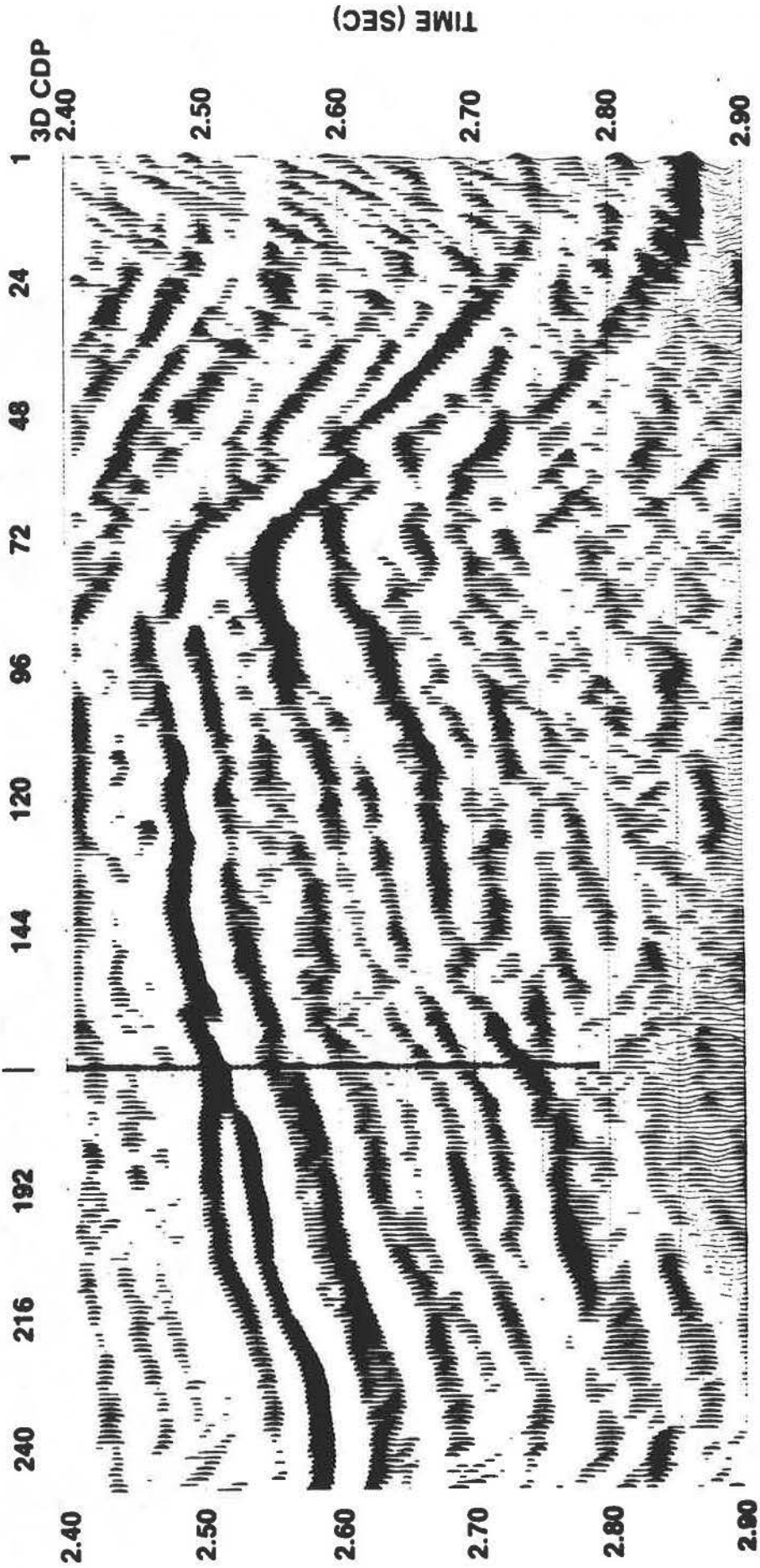


Figure 2

**Figure 3**  
**ELASTIC MODEL FOR WELL 2/5-2**

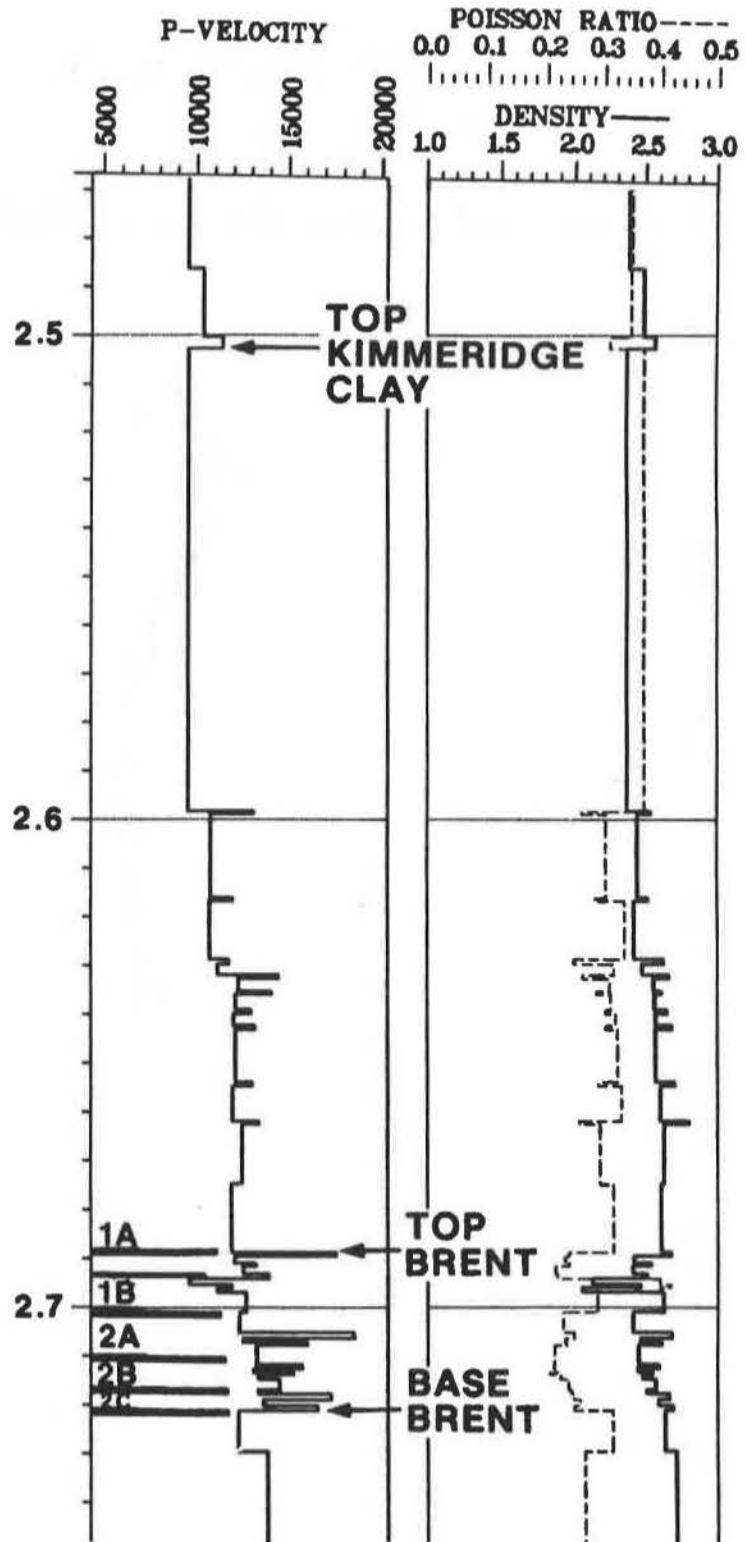


Figure 4  
PRE-STACK ELASTIC PERTURBATION MODELING  
CALCITE FRACTION MEASUREMENTS  
HEATHER WELL 2/5-2  
CDP 135  
Upper Brent Interval (2.69-2.71)

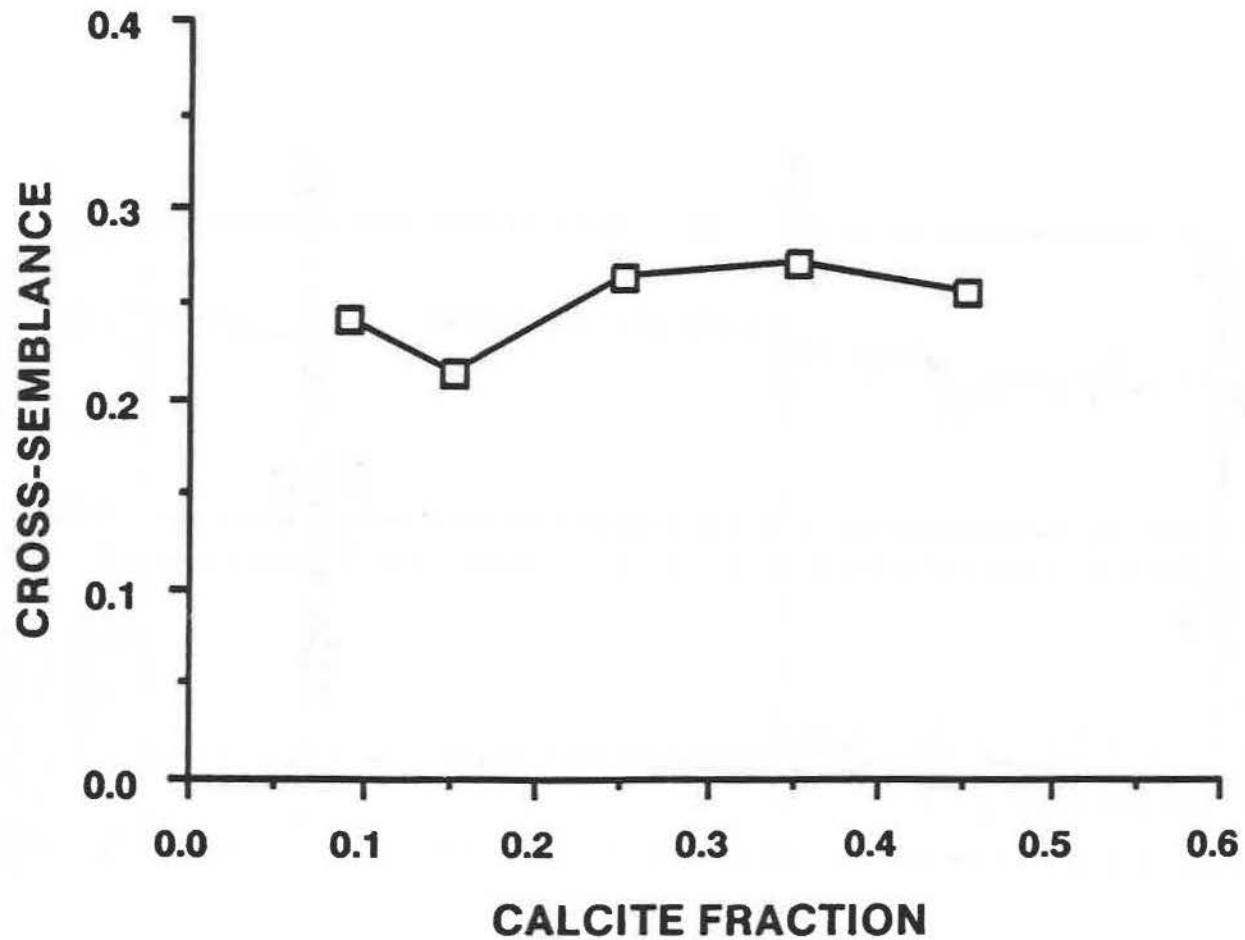
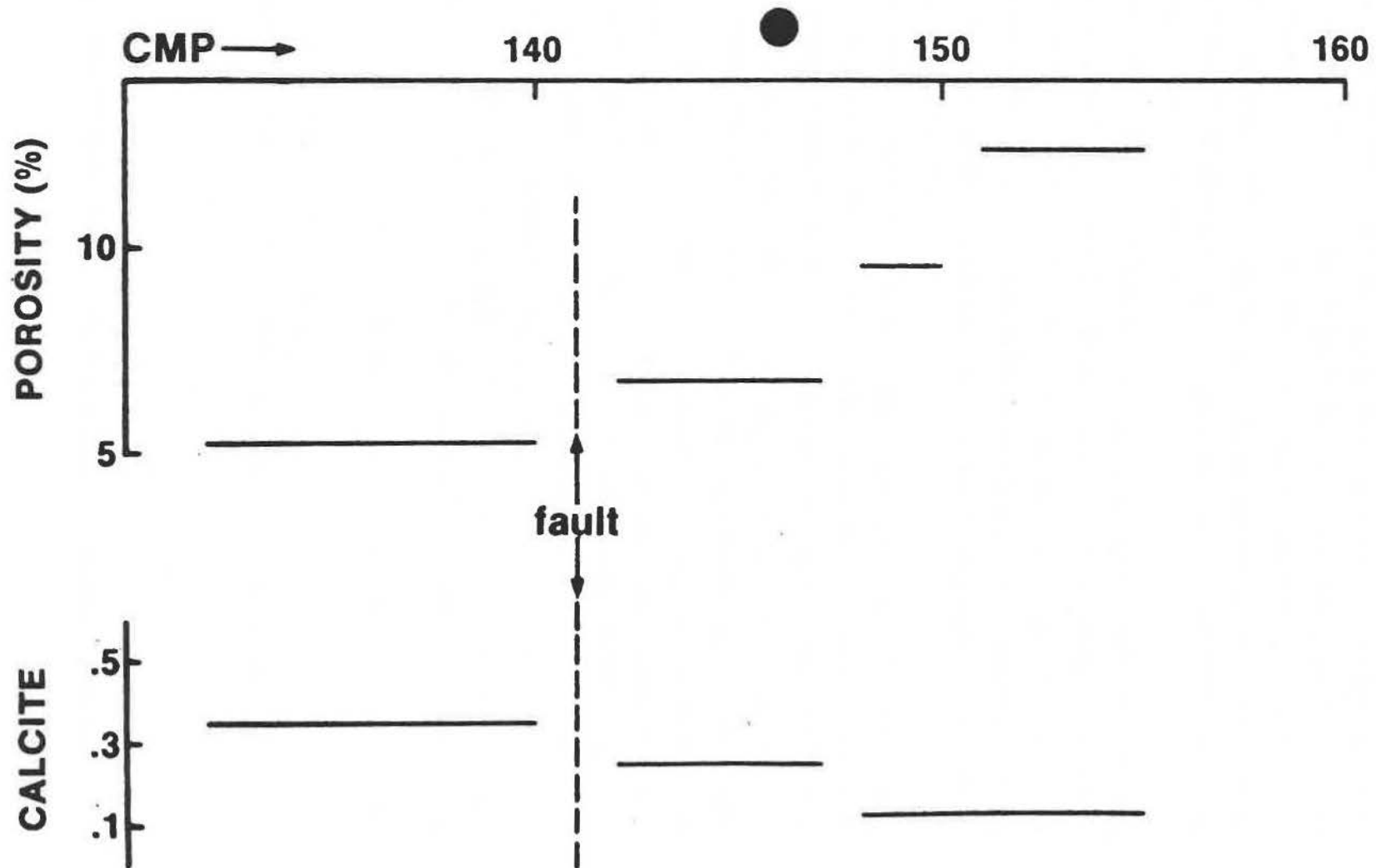


Figure 5  
PRE-STACK ELASTIC PERTURBATION MODELING  
POROSITY AND CALCITE MEASUREMENTS OF  
THE BRENT INTERVAL  
HEATHER LINE 163  
2/5-2



## Chaotic sedimentary sequences inferred from seismic reflectivity well logs

C.J. Karavas<sup>1</sup> and O.G. Jensen<sup>1</sup>

<sup>1</sup> Geophysics Laboratory, Department of Geological Sciences, McGill University, 3450 University Street, Montreal, Quebec, Canada H3A 2A7.

---

Chaotic phenomena in the earth sciences have only recently been recognized. Earthquakes (Huang and Turcotte, 1990; Scholz, 1989), thermal mantle convection (Stewart and Turcotte, 1989) and geomorphological river meandering (Furbish, 1988) are some particular phenomena showing a fundamentally chaotic behaviour. Sedimentary sequence development, a process which reflects the conspiracy of many geological processes, such as sea level fluctuations, tectonism, biological activity, climatic variability, etc., has long been considered in geological modeling (Schwarzacher, 1975, 1985; Velezeboer, 1981; Pan, 1987; Strauss and Sadler, 1989). Quantitative modelling of sedimentary sequence development has been based on Markov chain theory. These models however, do not fully describe complete sedimentary sequence development. Their failure in representing depositional processes derives from the assumption that sequence development is governed by Brownian statistics. This implies that: i) sedimentation is a non-stationary process and ii) present sedimentation depends essentially on the immediately preceding sedimentation state and not on long past influences.

The Markov process description conflicts with our knowledge of basin-fill processes. Deposition of a sedimentary sequence involves many geological processes acting on different temporal scales. The accumulation of a particular lithology in a sedimentary basin depends not only on the existing conditions during deposition, but also on the broad regional conditions that persisted during earlier times. These conditions directly affect the sedimentology and structural style of sedimentary basins (Montgomery, 1983).

Acoustic impedance (the product of density and seismic velocity) is a geophysical measure of formation lithologies. Changes in acoustic impedance correspond to variability in sedimentation as well as to diagenetic processes. Acoustic impedance variations in the geological record exhibit statistical self-similarity - they are fractal (Hosken 1980; Todoeschuck and Jensen, 1988). This means that in a vertical sedimentary sequence *"each small section looks like its neighbours and like scaled down versions of the whole, while retaining its individual identity"*, over a wide range of scales (Walden and Hosken, 1985). That is, they are scale-invariant. Fractal-flicker noise

statistics adequately represent the response of acoustic impedance variations in the sedimentary record. However, there is as yet, no general theory that explains this observation.

Here, we relate the statistical properties of acoustic impedance variations to the development of sedimentary sequences. This will be accomplished by introducing a new mechanism which describes variations in lithology, and thus changes in acoustic impedance. If we were to examine what "rule" governs changes in lithologies and thus in acoustic impedance, we recognize that the "cause" or explanation of this phenomenon is related to the internal organization of the geological processes which interact to produce the particular statistical characteristics of geological well logs. The organization follows a chaotic regime which is suggested by analogies between fundamental properties of chaos and geological process behaviour: "*Chaos describes the origins of variability in our processes. All variability arises from interactions, either in space or in time*" (McGill, 1989). The present problem can only be dealt with on a theoretical basis as no strict mathematical description can yet be obtained. Our analysis is not restricted to a particular site; rather, we will endeavour to describe fundamental characteristics of all sedimentary basins, world-wide.

## FRACTAL-FLICKER NOISE ACOUSTIC IMPEDANCE

In attempting to describe a sedimentary sequence (or an equivalent sedimentation process) as a Brownian process, we assume implicitly that the seismic velocities of the sedimentary layers would wander very far from the initial values (Todoschuck and Jensen, 1988). This challenges a fundamental tenet of geology: the Principle of Uniformitarianism, which implicitly suggests that acoustic impedance changes would be stationary throughout the Earth's history. The inconsistency of Brownian processes with Uniformitarianism suggest that they unsatisfactorily describe sedimentary processes.

Todoschuck and Jensen (1988) show how relative changes in acoustic impedance correspond to seismic reflection coefficients or seismic reflectivity. Such changes in acoustic impedance further correspond to variations in the sedimentation processes and hence relate directly to processes in geology. An examination of the statistics of reflectivity sequences derived from acoustic impedance well logs from a wide distribution of sedimentary basins, have shown that reflection coefficients are not spectrally white but have a fall-off of power at low frequencies (Hosken, 1980; Walden and Hosken, 1985; Todoschuck *et al.*, 1990) typically with a  $f^1$  spectrum (Fig.1). The equivalent acoustic impedance functions show a "Joseph" power spectrum, proportional to  $1/f^\beta$ , where  $f$  is frequency and  $\beta$  is approximately equal to 1 (i.e., a flicker noise process). For stationary geology the power spectral density of the impedance function must have  $\beta$  less than

or equal to unity (Todeschuck and Jensen, 1988). Such a spectrum characterizes a flicker noise process. Seismic reflectivity sequences characterized as  $1/f$  noise are statistical fractal (Mandelbrot, 1983). Spectra of these type belong to a family of spectrally self-scaling noises (Fig.2). With  $\beta$  equal to zero, we have uncorrelated noise "white noise". This offers an unreasonable geological model; for small depth steps, geology is self-correlated. With  $\beta = 2$  we have a Brownian process. Flicker noise is "*intermediate between white and brownian noises and exhibits a balance between randomness and correlation on all time scales*" (Voss, 1983). The fractal-flicker character for the acoustic impedance function, determined by lithological variation, implicitly determines the organizational structure of the sedimentation processes.

## METHODOLOGY

Sedimentary sequences are deposited under a conspiracy of processes which are difficult to separate, and which act on different spatial and temporal scales. In examining geological systems, one cannot focus on each individual process, but rather must examine their behaviour relative to one another. We abandon the classical viewpoint through which the system is analysed in terms of separable components. For a real dynamic and complex geological system this is inappropriate. We attempt to study geological processes holistically, exploring the interactive nature of different processes and their behaviour. The sedimentary system here is considered a multiple input-single output system. For the purpose of this study various geological processes comprise the multiple inputs and the resulting sedimentary sequence, the single output of the "geosystem".

## STABILITY ANALYSIS

The geosystem comprises many processes related in a complex manner. In principle, their interrelationships can be mathematically represented by a sufficient system of nonlinear differential equations. This mathematical-system model would necessarily involve a large number of parameters, inputs and outputs, all of which relate through complex functional interdependencies. While possible, in principle, quantitative solutions are intractable. *Partially specified systems* offer a useful mathematical simplification of the geosystem. Such systems form a class for which "*the types of feedback among variables (positive or negative) are known but the exact functional relationships are not*" (Slingerland, 1981). Qualitative stability analysis - a technique used for determining the response of partially specified systems - will be used here for the description of the sedimentary system (i.e. the geosystem). The results of this analysis will judge the system's response to changes, and determine whether it is stable or unstable.

We do not try to explain the sedimentation character of individual basins; instead, we describe a geosystem which is appropriate to the study of fundamental characteristics of "any" sedimentary basin "anywhere" in the world. Among the numerous variables which model the implicated geological processes, only those that have the largest influence in sedimentary sequence deposition will be considered. Stability is defined as the ability of the geosystem to recover from a disturbance or change of state. A stable system will return to a previous state. An unstable system will tend to evolve to a different state (mode) after a disturbance or perturbation. In the case of the geosystem, each different state represents a different condition of lithological deposition.

### Theory

If we consider a geological system of  $n$  variables,  $\vec{X}$ , which vary over time as functions  $\vec{F}$  of each other, we have:

$$\frac{d\vec{X}}{dt} = \vec{F}(\vec{X}). \quad (0.1)$$

If  $\vec{C}$  is an equilibrium point for the system, a deviation of  $\vec{X}$  from equilibrium is given by  $\vec{x}$ :

$$\vec{x} = \vec{X} - \vec{C}. \quad (0.2)$$

From equation (1) we obtain

$$\frac{d\vec{X}}{dt} = \vec{F}(\vec{x} + \vec{C}). \quad (0.3)$$

A Taylor expansion of the right side of equation (1) gives

$$\frac{d\vec{X}}{dt} = \vec{F}(\vec{C}) + \mathbf{A}\vec{x} + \vec{g}(\vec{x}) \quad (0.4)$$

where  $\vec{g}(\vec{x})$  is a vector of polynomials with terms of two or higher order, each small compared to  $\vec{x}$ . They vanish at  $\vec{x} = 0$ .  $\mathbf{A}$  is an  $n \times n$  interaction matrix whose elements are of the form  $\partial F_i(\vec{C}) / \partial X_j$ .

$$\mathbf{A} = \begin{pmatrix} \frac{\partial F_1(\vec{C})}{\partial X_1} & \cdots & \frac{\partial F_1(\vec{C})}{\partial X_n} \\ \vdots & & \vdots \\ \frac{\partial F_n(\vec{C})}{\partial X_1} & \cdots & \frac{\partial F_n(\vec{C})}{\partial X_n} \end{pmatrix}$$

The matrix entries reflect interactions among the geological processes (geo-variables).

When  $\vec{x}$  is very small,  $\vec{g}$  is also very small with respect to  $\mathbf{A}\vec{x}$ , and  $\vec{F}(\vec{C}) = 0$  (equilibrium). Thus, from equation (3) we obtain the linearized system

$$\frac{d\vec{X}}{dt} = \mathbf{A}\vec{x} \quad (0.5)$$

Solutions of equation (5) have the form

$$\vec{x}(t) = \vec{v}(\vec{C}) \exp(\lambda t), \quad (0.6)$$

where  $\vec{v}$  are eigenvectors of  $\vec{A}$  corresponding to eigenvalues  $\lambda$ .

The system's response to small changes depends on the eigenvalues. The stability of equation (5) is determined by whether or not the real parts of the eigenvalues,  $\lambda$  of  $\mathbf{A}$  are each greater or less than zero. To analyse the behaviour of the system, we investigate the roots (i.e. the eigenvalues) of the characteristic equation of the matrix  $\mathbf{A}$ .

If all eigenvalues are negative, the system is stable. This can be seen from equation (6); if all  $\lambda$  are  $< 0$  then all  $\vec{x}$  approach zero as  $t$  approaches infinity. Then from equation (2), all  $\vec{X}$  re-approach  $\vec{C}$ . Thus, the system re-approaches the stable equilibrium condition  $\vec{C}$ . If any (at least one) eigenvalue of  $\mathbf{A}$  has a positive real part, the system is unstable (Braun, 1983, p.354) and the values of the variables increasingly deviate from their equilibrium values with time.

The signs of the eigenvalues can be determined indirectly without having to solve the characteristic equation. This is accomplished using the Routh-Hurwitz criterion. The signs of  $\lambda$  are determined by the  $a_{ij}$  components of the system matrix. The Routh-Hurwitz criterion states that the roots of a real characteristic equation have negative parts if and only if all the coefficients  $a_{ij}$  of the equation are positive (Slingerland, 1981).

Applying qualitative stability analysis to the geosystem involves determining the cause-effect components ( $a_{ij}$ ) between the geological processes. Each  $a_{ij}$  represents a particular interaction within the geosystem. Note that not all interactions between the geological processes need be considered. The geological processes which play the role of geo-variables were chosen on the basis of their relative importance to sedimentation, and their generality of participation in geological environments.

### The Geoprocess Model

Figure 3 shows the modelled interacting geological processes. These are: sediment supply, tectonic uplift, sea-level fluctuation and glaciation. Sediment supply in sedimentary basins is a continuous process though varying with time. The most important types of sediments

are clastics (mainly sandstone and shale) and carbonates (mainly limestone and dolomite). Evaporites, volcanics and organic-carbon-rich sediments are also significant. Sediment supply varies depending upon the depositional environment (Edwards, 1986). For example, major rivers provide a larger and faster sediment supply than does pelagic settling (Stow, 1985). Stratigraphic analysis of the Western Canadian Basin has shown that during the Jurassic and Cretaceous, sedimentation varied from 3 m to 300 m/1000 years (Stott, 1984). Eustatic sea-level change can be either glacial, tectonic or geoidal. Glacial eustatic changes result from the changing volume of ice caps, and have rates of up to 10 m/1000 years (Pitman, 1978).

( $-a_{23}$ ) in Figure 3, represents the affect of glaciation to sea-level. Glaciation would cause a fall in sea-level. Pitman and Golovchenko (1983) argue that a sea-level rise of about 60m would result, if all present glaciers and ice caps would melt. The negative sign preceding ( $a_{23}$ ) describes this inverse relationship between sea-level and and glaciation.

( $-a_{32}$ ) represents the affect of sea-level change to glaciers, and the negative sign signifies that a sea-level rise would erode glaciers. Ruddiman and Wright (1987) state that rising sea-level increases calving of icebergs.

( $-a_{21}$ ) specifies the affect of tectonism to sea-level change. A tectonic uplift causes a sea-level fall. This inverse relation is indicated by the negative sign in ( $a_{21}$ ). Stott (1984) documents that tectonic uplift in the Cretaceous western interior of North America has caused seaward advance of the shoreline.

( $-a_{42}$ ) represents the affect of sea-level change to sediment supply. Stow (1986) states that during periods of high sea-level, sediment sources such as rivers do not have direct access to the basin slopes of continental margins, hence decreasing sediment supply and thus the negative sign for ( $a_{42}$ ) in Figure 3.

( $a_{43}$ ) signifies the affect of glaciation to sediment supply. About 10 % of the earth's continental surface is now covered by glacial ice. Glaciers act as erosional agents and thus supply glacial sediments ( $a_{43}$ ). Glacial deposits are observed in both marine and terrestrial settings and in a variety of tectonic and climatic situations. Glaciers also cause tectonic loading depressing the crust ( $-a_{13}$ ). The negative sign signifies the inverse relation between glaciation and tectonic uplift. This effect of glaciation is well demonstrated in the classical Scandinavian example, where glacio-isostatic rebound adjustment has been occurring since the end of the last glacial period.

Sediment supply can also initiate tectonic activity. Sediment loading of basins can contribute to lithospheric subsidence (Turcotte *et al.*, 1977; Cloetingh *et al.*, 1984). ( $-a_{14}$ ) represents the relationship between sediment supply and tectonic uplift and the negative sign specifies the inverse affect.

**Table 1**  
**Geosystem interaction matrix**

	tectonic uplift	sea-level	glaciation	sediment supply
tectonic uplift	0	0	$-a_{13}$	$-a_{14}$
sea-level	$-a_{21}$	0	$-a_{23}$	0
glaciation	0	$-a_{32}$	0	0
sediment supply	0	$-a_{42}$	$a_{43}$	0

The modelled interacting geological processes represented in Figure 3, exclude unique situations such as desert environments, and localized settings such as atolls. The above interrelationships can be assembled into a geosystem interaction matrix (Table 1). Each link between the geological processes in Figure 3, corresponds to a matrix element  $a_{ij}$ .

Rewriting Table 1 in the form of a matrix we have:

$$\mathbf{A} = \begin{pmatrix} 0 & 0 & a_{13} & a_{14} \\ -a_{21} & 0 & -a_{23} & 0 \\ 0 & a_{32} & 0 & 0 \\ 0 & -a_{42} & a_{43} & 0 \end{pmatrix},$$

where each  $a_{ij}$  represents a particular interaction within the geosystem.

The characteristic equation of this interaction matrix  $\mathbf{A}$  is:

$$\lambda^4 - (a_{23}a_{32}) \lambda^2 + (a_{13}a_{32}a_{21} + a_{21}a_{14}a_{42}) \lambda + \det \mathbf{A} = 0 \quad (0.7)$$

The system stability is dependent upon the sign of the coefficients of the characteristic equation. The second term of the characteristic equation is negative. Thus, since all the coefficients of the equation are not positive, the Routh-Hurwitz criterion indicates that the roots of the equation do not all have negative real values. So, at least one eigenvalue of  $\mathbf{A}$  must have a positive real part, and thus, the system is unstable.

This qualitative stability analysis has shown that the geosystem is normally unstable. The sedimentation sequence records the evolution of this system during many millions of years. The

system has many quasiequilibrium states which may persist for long periods of time. These periods coincide with the geological conditions during lithological formation. Changes in lithology of the sedimentary record result from unstable evolution of the geosystem.

## DETERMINISTIC CHAOS

The study of non-linear dynamical systems has led to chaos theory. Nonlinear phenomena often exhibit extremely sensitive behaviour. Small changes in initial values can cause large and unpredictable changes as the geosystem evolves. A dynamical system may be described in terms of its: i) state, which is the essential information about the system, and ii) a rule that describes how its state evolves with time. A visualized representation of an evolving dynamical system can be illustrated in phase - or state-space. An orbit (trajectory) through that space specifies the motion of a particular system as time passes. An "attractor" is that state which the system settles towards, or is attracted to.

Traditionally it has been accepted that simple systems with a few degrees of freedom (or equivalently those sufficiently described by few parameters) are associated with "order" and complex systems with "chaos". This association is not totally correct since simple physical models with very few degrees of freedom, can display chaotic behaviour (Huang and Turcotte, 1990), even though they are governed by simple sets of deterministic equations. A chaotic system is deterministic (Ruelle, 1989) and its evolution with time is characterized by extremely sensitive dependence on initial conditions.

The study of equilibrium and stability of nonlinear systems reveal information about their behaviour. The number and stability of equilibrium points of a set of differential equations could change, when the coefficients of the equation change (Middleton, 1990). Those points of change in the behaviour of the system are called *bifurcations*. At a bifurcation point, a system "switches" from one stable operating mode to another. A system that has passed through a bifurcation point and has stabilized by its feedback, will remain in the new state until its next

bifurcation.

### A CHAOTIC SEDIMENTATION SYSTEM

A chaotic geosystem would show sensitivity to initial conditions, abrupt shifts in operating mode, and unpredictability. North and Crowley (1985) show via mathematical modelling of climate (an important process in large-scale sedimentation) that only a small alteration of parameters is required to cause a sudden potential for glaciation over large areas of the Earth's surface. They state that change of atmospheric carbon dioxide over geological time, can induce radical changes in continental ice cover. Also, even small changes in the mean climate result in dramatic changes in the frequency of extreme events as temperature and meteoric precipitation (di Castri and Malcolm, 1988). When some stable climatic variables fall below a critical threshold value, extreme "nonlinear" climatic events may appear (Wigley, 1985). Abrupt climatic change in geological records of the Quaternary are documented (Broecker *et al.*, 1985). These show evidence for rapid climatic "swings" in the interstadial preceding the last glacial maximum. Such climatic behaviour affects sedimentary processes on the Earth. Abrupt shifts in climate have an effect on changing carbonate sedimentation resulting in creation of different lithotypes (Crowley and North, 1988).  $CO_2$  measurements from ice cores show that the Earth has two modes of ocean-atmosphere interaction (Broecker *et al.*, 1985). Oxygen isotope records of ice core data "jump" from one stable mode to another. One interpretation of this phenomenon, proposed by Oeschger *et al.*, (1984), is that variations in the sediment production rate "kick" the ocean-atmosphere system from one quasi-stable mode to another.

Abrupt shifts in climate are evidenced by worldwide sedimentation rates. During Oligocene and Paleocene times, sediment rates were low, while in the Miocene and Eocene rates were high (Davies *et al.*, 1977). Different modes of weathering have been suggested for this discrimination. The sedimentation variation imply climatic variability during those periods. Nicolis, C. and Nicolis, G. (1984) suggest that long term climatic change exhibit the deterministic, unstable dynamics of the chaotic attractor. This change reflected in sedimentation variability in basins

does not exhibit periodicity.

A geological environment which has completely adjusted to environmental conditions is in a state of equilibrium (a stable state). Such stable states could still be punctuated by episodic events which will abruptly shift the environmental equilibria to another stable state. These abrupt changes or punctuated events, are more frequent than we have previously realized (Phillips, 1986). Geologists have referred to such events as "*punctuated aggradational cycles*" (PACs) in explaining episodic stratigraphic accumulations (Goodwin and Anderson, 1985). These episodes or crises, superposed on the normal sedimentation trends, originate within the geosystem itself (Bergé *et al.*, 1986). "*Abrupt changes are inherent in normal geological processes*" (Parker, 1985). Oscillations or disturbances caused by changes in the endogenetic system control the sediment output in time and space (Montgomery, 1983).

We view such behaviour of the sedimentary system indicating chaos. Sedimentation exhibits long periods of relative stability separated by abrupt shifts. During times of dynamic equilibrium, the geosystem is quasi-stable. Quasi-stable geological conditions are responsible for the deposition of a particular lithology. Its chaotic nature causes the sedimentation system to find other operating states. Under these new geological, quasi-stable conditions, a new lithology deposits. Following some unpredictable interval of time, the system evolves through its next bifurcation point, and into a new state. The duration the system spends in each state determines the thickness of the formation lithologies. These successive, abrupt shifts in the operating mode of the sedimentation system, due to basin conditions and conditions of climate cause sensitive sedimentological and structural effects (Montgomery, 1983; Furbish, 1988). Lithological changes and equivalently, their geophysical measures; i.e. acoustic impedance variations represent a chaotic attractor in phase-space. The chaotic attractor represents evolution of the sedimentary system through different lithological states. Thus, the evolution of the strange attractor represents the common underlying mechanism of acoustic impedance variations.

The relationship between  $1/f$  spectra and strange attractor solutions has been addressed for electronic systems. Arguments provided by Shaw (1980) support the idea that strange attractors or ensembles of strange attractors often show the  $1/f$  power spectrum of scaling flicker noise. In addition, he states that any chaotic mechanism which would purport to explain the ubiquitous occurrence of  $1/f$  noise must itself occur ubiquitously. Mandelbrot (1983) notes that "*Many scaling noises have remarkable implications in their fields and their ubiquitous nature is a remarkable generic fact.*" Mandelbrot and Voss (1983) also directly state, that "... $1/f$  noise may be related to turbulence or chaotic behaviour and nonlinearities". Acoustic impedance variations – the geophysical measures of lithological variability – with their well known fractal-flicker noise ( $1/f$ ) character could well result from the chaotic geosystem. Such geological processes, "self-organized critically" are responsible for the statistically self-similar character which is observed in sedimentary basins.

## SUMMARY AND CONCLUSIONS

The sedimentation system has been described as a partially specified system amenable to qualitative stability analysis. The interrelationships among the geological processes have been examined via an interaction matrix. This allows for abrupt shifts from one stable mode reflecting one lithotype to another state, reflecting a new lithology. We argued that changes arising from the internal structure of the geosystem (i.e. within the system) cause the geosystem to evolve among various stable operating states.

As shown by Montgomery (1983), geological process-interaction over long time periods is sensitively dependent on initial sedimentological and structural conditions. Any small deviation of one among the geological processes of the geosystem can have a tremendous effect on the geosystem's output response – its deposition of sediment. Still, the exact lithology cannot be predicted due to the essentially chaotic character of the geosystem. We have thus argued in

support of our claim that a sedimentary sequence is the result of a chaotic geosystem. Sedimentary sequence development does exhibit fundamental characteristics of chaos and the strange attractor solutions of the chaotic geosystem are equivalently manifest as stable lithological formations. The fractal-differential flicker noise ( $f^1$ ) character of seismic reflectivity sequences and equivalently the fractal-flicker noise ( $1/f$ ) character of the acoustic impedance function of depth, are also consistent with a geosystem governed by chaos.

### ACKNOWLEDGMENTS

The authors wish to thank Imperial Oil Limited which supported this research through the award of a University Research Grant to Olivia Jensen. The Natural Sciences and Engineering Research Council of Canada (NSERC) also provided support through an Operating Grant awarded to Olivia Jensen. We thank Dr. J-C. Mareschal for his helpful comments on the initial manuscript. This research was supported by the Canadian Society of Exploration Geophysicists (CSEG) through a Fellowship to C. Karavas.

### REFERENCES

- Bergé, P., Pomeau, Y., Vidal, C., 1986. *Order within Chaos*, John Wiley and Sons Publ. 329 p.
- Braun, M., 1983. *Differential equations and their applications*, N.Y. Springer-Verlag. 341 p.
- Broecker, W.S., Peteet, D.M., and Rind, D., 1985. Does the ocean-atmosphere system have more than one stable mode of operation?, *Nature*, **315**, 21-26.
- Cloetingh, S.A.P.L., Wortel, M.J.R., and Vlaar, N.J., 1984. Passive margin evolution, initiation of subduction and the Wilson cycle, *Tectonophysics*, **109**, 147-163.
- Crowley, T.J., and North, G.R., 1988. Abrupt climate change and extinction events in earth history, *Science*, **240**, 996-1002.

- Davies, T.A., Hay, W.W., Southam, J.R., and Worsley, T.R., 1977. Estimates of Cenozoic oceanic sedimentation rates, *Science*, **197**, 53-55.
- di Castri, F., and Malcolm, H., 1988. Enhancing the credibility of ecology: Interacting along and across hierarchical scales, *GeoJournal*, **17**, 5-35.
- Edwards, M., Glacial environments, in *Sedimentary environments and facies*, Reading, H.G. ed., Blackwell Scien. Publ., 445-470, 1986.
- Furbish, D.J., 1988. *The river meandering process: Evidence for nonlinear chaos*, Geological Society of America. Abstract-1104
- Goodwin, P.W., and Anderson, E.J., 1984. Punctuated aggradational cycles: A general hypothesis of episodic stratigraphic accumulation, *Jour. Geology*, **93**, 515-533.
- Hosken, J.W.J., 1980. *A stochastic model of seismic reflections*, 50th Ann. Mtg. Soc. Explor. Geophys. Abstract G-69.
- Huang, J., and Turcotte, D.L., 1990. Are earthquakes an example of deterministic chaos ?, *Geophys. Res. Lett.*, **17**, 223-230.
- Mandelbrot, B. B., and Voss, R. F., Why is nature fractal and when should noises be scaling?, in *Noise in physical systems and 1/f noise*, Elsevier Science Publishers, Amsterdam, 31-39, 1983.
- Mandelbrot, B.B., 1983. *The Fractal Geometry of Nature*, W.H. Freeman and Co., San Francisco, 468 p.
- McGill, B.K., Return to chaos, in *43rd Annual Quality Congress Transactions vol.43, May 8-10, 1989, Toronto, Ontario*, ASQC Milwaukee, 781-792, 1989.
- Middleton, G.V., 1990. Nonlinear dynamics and chaos: Potential applications in the earth sciences, *Geoscience Canada*, **17**, 3-11.
- Montgomery, K., 1983. Concepts of equilibrium and evolution in geomorphology: the model of branch systems, *Progress in Phys. Geography*, **13**, 47-66.

- Nicolis, C., and Nicolis, G., 1984. Is there a climate attractor, *Nature*, **311**, 529-532.
- North, G.R., and Crowley, T.J., 1985. Application of a seasonal climate model to Cenozoic glaciation, *J. geol. Soc. Lond.*, **142**, 475-482.
- Oeschger, H., Beer, J., Siegenthaler, U., Stauffer, B., Dansgaard, W., Langway, C.C., Late glacial climate history from ice cores, in *Am. Geophys. Un. Monogr. Ser. 29, Climate processes and climate sensitivity, M. Ewing vol. 5*, Hansen, J.E., Takahashi, T., eds., 299-306, 1984.
- Pan, G., 1987. A stochastic approach to optimum decomposition of cyclic patterns in sedimentary processes, *Math. Geol.*, **19**, 503-521.
- Parker, R.B., 1985. Buffers, energy storage, and the mode and tempo of geologic events, *Geology*, **13**, 440-442.
- Phillips, J.D., 1986. Sediment storage, sediment yield, and time scales in landscape denudation studies, *Geographical Analysis*, **18**, 161-167.
- Pitman, W.C., 1978. Relationship between eustacy and stratigraphic sequences of passive margins, *Geol. Soc. Amer. Bull.*, **89**, 1389-1403.
- Pitman, W.C., and Golovchencho, The effect of sea level change on the shelf edge and slope of passive margins, in *The shelfbreak*, Stanley, D.J., and Moore, G.T., ed., Spec. Publ. Soc. econ. Paleont. Miner. **33**, 41-58, 1983.
- Ruddiman, W. F. and Wright, H. E. Jr., Introduction, in *Ruddiman, W. F. and Wright, H. E. Jr., eds., The geology of North America v. K-3, North America and adjacent oceans during the last deglaciation*, 1-12, The Geological Society of America, Boulder Colorado, 1987.
- Ruelle, D., 1989. *Chaotic evolution and strange attractors*, Cambridge University Press, New York, 93 p.
- Scholz, C.H., 1989. Global perspectives of chaos, *Nature*, **338**, 459-460.
- Schwarzacher, W., 1975. *Sedimentation models and quantitative stratigraphy*, Developments in Sedimentology **19**, Amsterdam Elsevier, 382 p.

- Schwarzacher, W., Principles of quantitative lithostratigraphy, in *Quantitative stratigraphy*, 361-386, Gradstein, F.M., Agterberg, F.P., Brower, J.C., and Schwarzacher, W.S., eds., D. Reidel Publ. Co., Dordrecht, 1985.
- Shaw, R.H., 1980. Strange attractors, chaotic behavior, and information flow, *Z. Naturforsch.*, **36a**, 80-112.
- Slingerland, R., 1981. Qualitative stability analysis of geologic systems, with an example from river hydraulic geometry, *Geology*, **9**, 491-493.
- Stewart, C.A., and Turcotte, D.L., 1989. The route to chaos in thermal convection at infinite Prandtl number: Some trajectories and bifurcations, *J. Geophys. Res.*, **94**, 13707-13717.
- Stott, D.F., Cretaceous sequences of the foothills of the Canadian Rocky Mountains, in *The Mesozoic of Middle North America*, Stott, D.F., and Glass, D.J. ed., CSPG Memoir 9, 85-107, 1984.
- Stow, D.A.V., Deep-sea clastics: where are we and where are we going?, in *Sedimentology: recent developments and applied aspects. Geological Society Special Publications 18*, Brenchley, P.J., Williams, B.P.J., eds., Blackwell Scientific Publications, 67-93, 1985.
- Stow, D.A.V., Deep clastic seas, in *Sedimentary environments and facies*, Reading, H.G. ed., Blackwell Scien. Publ., 399-444, 1986.
- Strauss, D., and Sadler, P.M., 1989. Stochastic models for the completeness of stratigraphic sections, *Math. Geol.*, **21**, 37-59.
- Todoeschuck, J.P., and Jensen, O.G., 1988. Joseph Geology and seismic deconvolution, *Geophys.*, **53**, 1410-1414.
- Todoeschuck, J.P., Jensen, O.G., and Labonte, S., 1990. Gaussian scaling noise model of seismic reflection sequences: Evidence from well logs, *Geophys.*, **55**, 480-484.
- Turcotte, D.L., Ahren, J.L., and Bird, J.M., 1977. The state of stress at continental margins, *Tectonophysics*, **42**, 1-28.

- Velzeboer, C.J., 1981. The theoretical seismic reflection response of sedimentary sequences, *Geophysics*, **46**, 843-853.
- Voss, R.F., 1/f Flicker noise: A brief review, in *Proceedings of the 33rd Annual Symposium on Frequency Control*, Atlantic City, 40-46, 1983.
- Walden, A.T., and Hosken, J.W.J., 1985. An investigation of the spectral properties of primary reflection coefficients, *Geophys. Prosp.*, **33**, 400-435.
- Wigley, T.M.L., 1985. Impact of extreme events, *Nature*, **316**, 106-107.

## FIGURE CAPTIONS

Fig.1: Power spectrum of a synthetic reflection sequence which conforms to the empirical models derived by Todoeschuck *et al.*, (1990).

Figure 2: Spectrally self-scaling noises: (a) differential flicker noise (with  $1/f^1$  spectrum as characteristic of seismic reflectivity sequences-such as shown spectrally in Figure 1), (b) White Gaussian noise (a stationary uncorrelated process with a  $1/f^0$  spectrum), (c) flicker noise process (its  $1/f$  spectrum is characteristic of seismic acoustic impedance sequences), and (d) Brownian process or "random walk" (non-stationary process with a  $1/f^2$  spectrum). Flicker noise, for which  $\beta=1$ , lies on the boundary between stationarity and non-stationarity. It possess the greatest value of  $\beta$  and greatest weight of low frequencies, while remaining stationary.

Figure 3: Geoprocess Model. Sea-level change, tectonic uplift, glaciation and sediment supply comprise the variables of the geosystem. Each  $a_{ij}$  represents a particular interaction between the geo-variables (processes). The subscripts define the two processes and the sign signifies their relationship. The first subscript  $i$  denotes the end point of the link and the second,  $j$ , the point of origin. The sign of  $a_{ij}$  depends on whether the relationship is to increase increase effect (solid arrow) or to decrease effect (open arrow).

# Spectrum of $f$ -noise reflectivity sequence

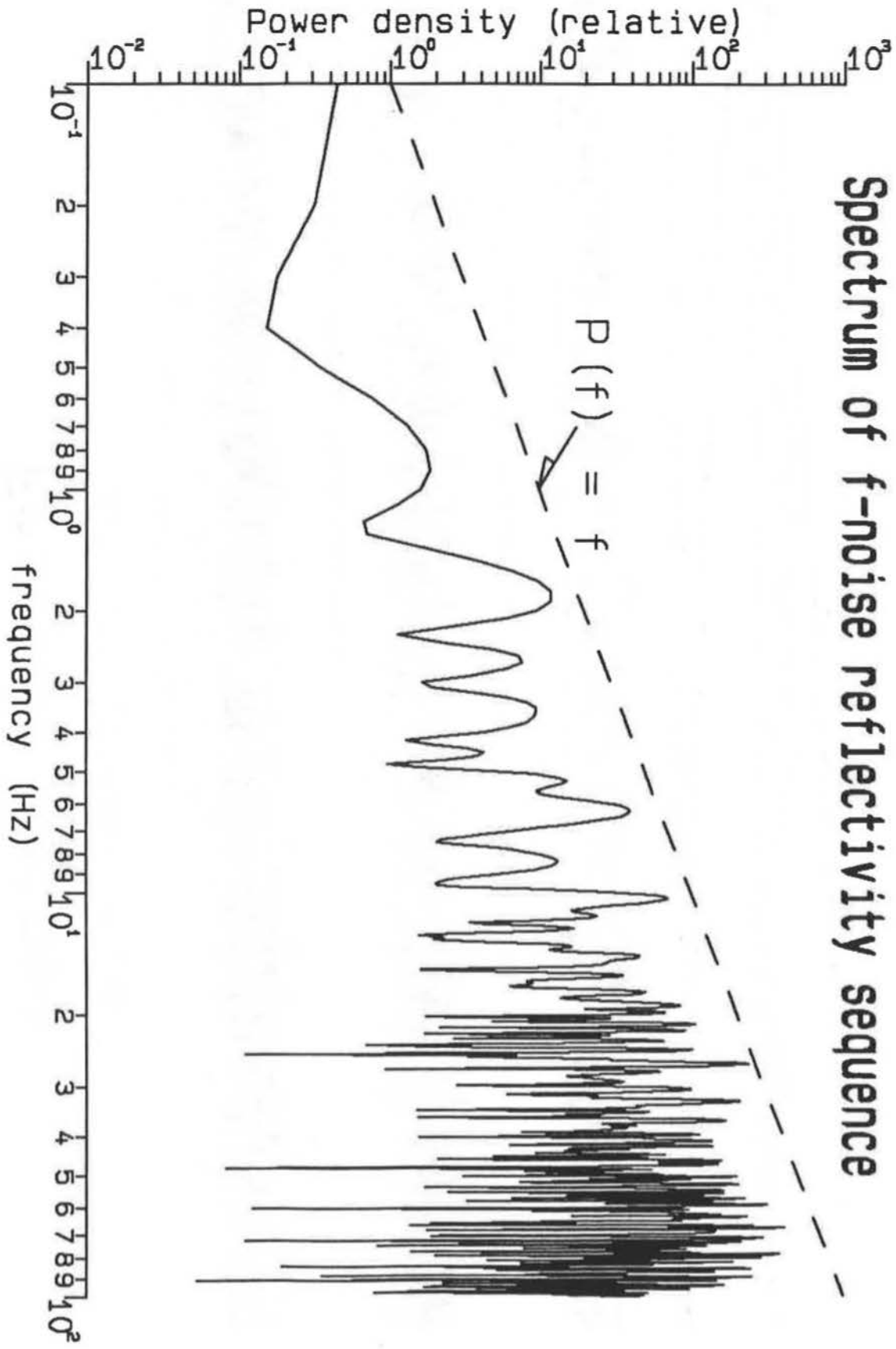
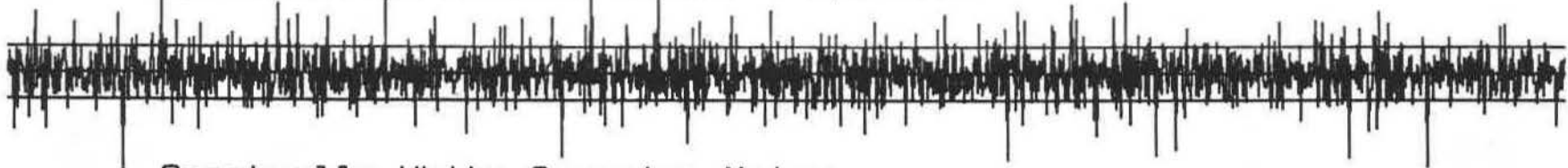


FIGURE 1

# Fractal Noises

1280 variates/sequence

Differential Flicker Noise:  $f$  Spectrum



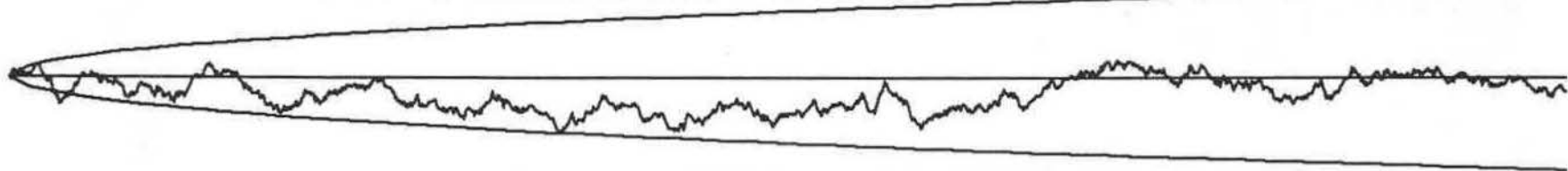
Spectrally White Gaussian Noise



Flicker Noise:  $1/f$  Spectrum



Brown noise (random walk): " $1/f^2$  Spectrum"



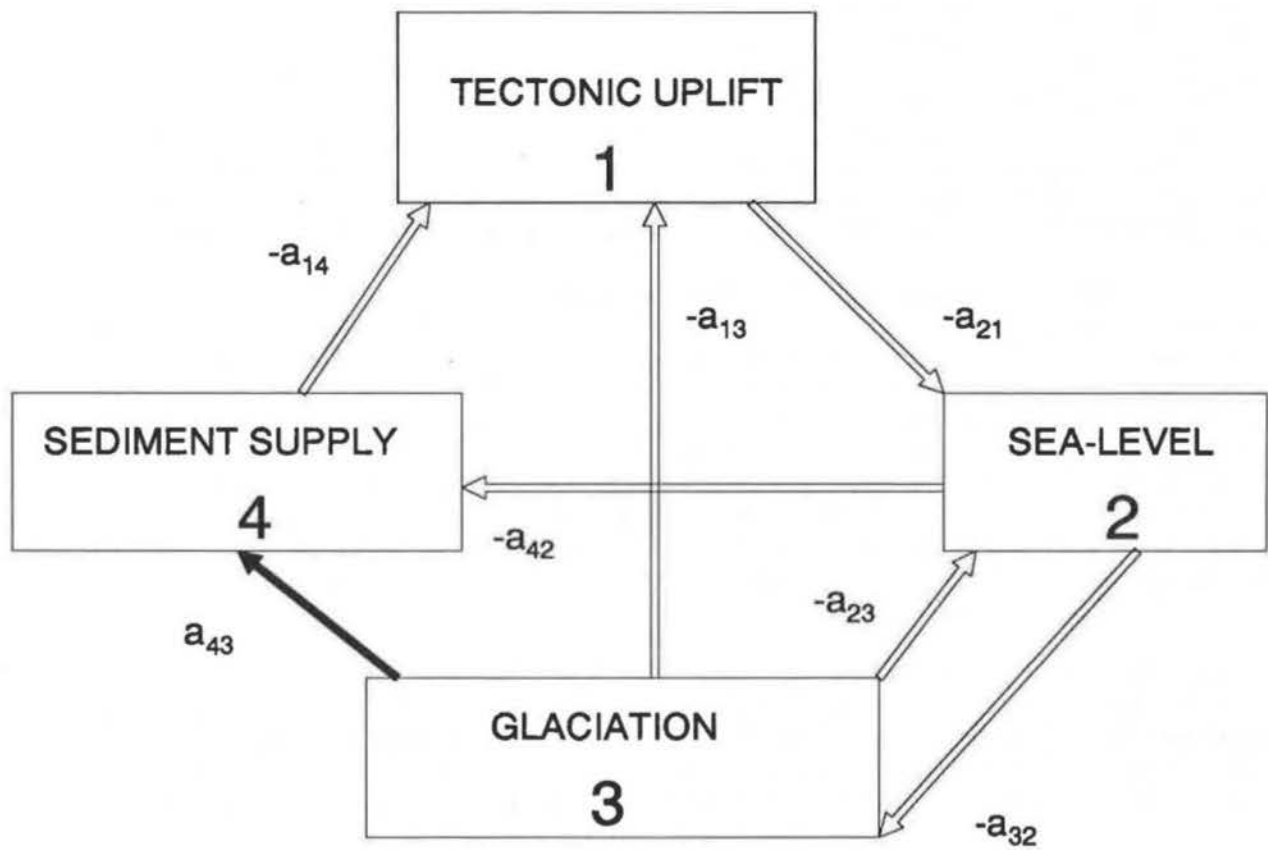


Figure 3

# PREDICTION OF PORE FLUIDS USING POISSON'S RATIOS FROM SEISMIC DATA

D.R. Miles, Terra Linda Canada Ltd.

## Abstract

Poisson's ratio - P wave velocity crossplots graphically show the relationship between the pore fluids and the lithology in a specific zone or layer; Figure 1. Poisson's ratio is calculated from the p and s wave velocities which are obtained from the seismic data, either conventional or three-component. In conventional p wave seismic data, the s wave velocity and Poisson's ratio are estimated from the amplitude changes with offset. In three-component seismic data, both p wave and s wave velocity are calculated directly from the seismic data. Poisson's ratio is then calculated from this data and confirmed by the p wave and s wave amplitude effects with offset.

Basin wide prospecting for reservoirs can be accomplished with three-component seismic data, three-component AVO and s wave isopach to p wave isopach ratio to develop Poisson's ratio contour maps. The p wave reflectors can be tied to s wave reflectors through three-component AVO inversion or full waveform sonic logs; then the top and bottom of a specific formation can be identified. The actual Poisson's ratio can be calculated from the p and s wave time thicknesses at that location and Poisson's ratio anomalies evaluated. Further detail of one-dimensional three-component seismic or three-dimensional three-component seismic can yield an accurate outline of the field, even before drilling.

The true value of this method and the crossplots lies in the fact that all relationships are relative. It does not require absolute measurements of velocity from the seismic data only time thicknesses. The margin for error is greatly reduced because of this and we will therefore make predictions with much greater certainty.

## Introduction

Since the mid 1970's, s wave velocity contrasts, Poisson's ratio contrasts or AVO effects have been shown to predict the presence of hydrocarbons. Only in the last several years, however, has the reason these methods worked been accepted. Poisson's ratio - p wave velocity crossplots have definite trends for hydrocarbons versus water. The crossplotting of several points from a specific layer shows trends which even if the absolute numbers are in error allows for an interpretation of pore fluid. Thus, the interpretation of pore fluids from seismic is the result of the realization that attributes on the seismic data could be indicative of elastic parameters.

## P Wave - Poisson's Ratio Crossplot

Crossplots allow the interpreter to take measurements of different rock parameters and deduce properties which are a portion of both measurements. For example, p wave velocity changes as a function of mostly lithology but also changes due to porosity and pore fluid. Poisson's ratio, on the other hand, changes mostly with pore fluids but also with porosity and lithology. Thus, when they are crossplotted, pore fluid is the major change in the trends with porosity showing the distance along those trends and lithology causing minor changes.

Lithologies with no porosity are single points on the p wave velocity - Poisson's ratio crossplot. A specific lithology can be defined in terms of its percentages of pure minerals (ie. a marble may be 98% limestone, 2% quartz). The p wave velocity is a weighted sum of the velocity of the minerals (Wylie et al, 1958) that is  $0.98 * 6,650 \text{ m/sec} + 0.02 * 7,400 \text{ m/sec} = 6,665 \text{ m/sec}$ . Similarly, Poisson's ratio is also a weighted average of the Poisson's ratios of the minerals making up the formation. For example  $0.98 * 0.32 + 0.02 * 0.29 = 0.31$  in the case above. Thus, each solid lithology or matrix lithology can be defined as a single point on the crossplot.

Similarly, with the addition of a fluid or gas to the formation, one merely adds the weighted average of the fluid  $V_p$  or Poisson's ratio to the matrix. This means that changes in porosity will lie along a line from the lithology end member to water or to hydrocarbons depending on the fluid in the pores, see figure 2. If the water saturation in the pores changes but not porosity nor lithology, then the points will lie on a nearly vertical line between the water saturated and hydrocarbon saturated lithologies. Thus, if one has several p wave velocity, Poisson's ratio pairs from several points in a given formation, then the slope of the trend of these points will tell if changes are in pore fluid porosity or lithology.

## Determination of P Wave Velocity

To determine pore fluid, the first step is to obtain p wave velocities at a given location on a line for AVO inversion or to obtain the information for all the shot points along a seismic line for 3-component seismic analysis. P wave interval velocities are obtained fairly routinely from seismic data (Dix, 1955, Gonzales-Serrano et al, 1984). The methods require identification of the top and bottom reflections from a formation. Next, either Dix's equation, Clarebout and Serano's interval velocity equation or others are used to compute p wave velocity. Similarly, the s wave velocity may be calculated from the s wave section.

Since Poisson's ratio is a  $V_p/V_s$  ratio; the usual way of calculating it is from the p wave interval velocity and the shear wave interval velocity, yet it may also be calculated from the s and p time isopachs. Calculating the shear wave interval velocity is straight forward, however correlating the shear wave information with the p wave information is more difficult. Without the shear information correlated correctly by the p wave information, calculation of Poisson's ratio is impossible. Thus, the most important step in obtaining Poisson's ratio from seismic is tying the p wave information to the s wave information.

In single component AVO inversion, the shear wave velocity is calculated directly from the p wave reflector so there is no s wave data to which to correlate. The amplitude changes with offset are a function of the Poisson's ratio contrast across the boundary. Thus, Poisson's ratio and shear velocity are calculated directly from the p wave reflections. The AVO inversion is affected by source and receiver arrays, amplitude changes above the zone of interest, thickness of the zone of interest, composition changes in the near surface and buried focuses (Gassaway et al, 1983). Though AVO inversion solves the correlation problem, these sources of noise cause errors in the analysis and thus cause errors in the interpretations. In addition, only a very few companies do AVO inversion. Most of what is called AVO inversion only matches the data to a model, without calculating a shear velocity or Poisson's ratio for each layer.

More accurate shear velocities can be obtained from shear wave sections. First, shear wave velocities can be calculated using the same algorithms as for p wave interval velocities. S waves have NMO just like p waves with the same velocities so inversions for interval velocities or calculations of interval velocities will work on shear sections. For p wave velocity inversions, the low frequency component of the velocity is obtained from well logs; but there are very few shear velocity logs, so the low frequency component of the shear must come from AVO information or other sources such as broader spectrum recording. This gives the interpreter an accurate value for the s wave interval velocity but does not tie the p wave data to the s wave data.

#### Determination of Poisson's Ratio

Correlation of p and s wave reflectors can be accomplished with either three-component AVO inversion, or shear wave velocity logs. Shear wave velocity logs can be made into synthetic seismograms, then specific formations can be correlated on the stack. This provides a direct correlation to the formations identified on the p wave section. But the correlations are not always correct, or the synthetics match a couple of ways, or even worse do not match at all; these all introduce uncertainty in the answers. Even for p waves, some correlations take several lines and wells before the interpreter has confidence in the correlation.

Three-component AVO correlates p wave reflectors with the shear wave reflectors with a greater degree of certainty from the information derived in the analysis. The p wave amplitude changes with offset analysis give the shear velocities and Poisson's ratio. Using the p wave velocities, p wave time and calculated shear wave velocities, one can predict a shear wave time and AVO response. Similarly, the shear wave AVO analysis gives the p wave velocity; and from the shear wave time, shear wave velocities and calculated p wave velocities, one can calculate a p wave time, and AVO response. The calculated p and s wave AVO responses can then be compared to the measured responses to check the accuracy. Thus, one has a two way check on the shear velocities and reflectors at a specific location. Other locations can be analysed to make a grid of correlation points or to correlate where needed.

With the p wave reflectors tied to s wave reflectors, one can calculate Poisson's ratio using time isochrons rather than velocities. Tatham, 1976 proposed the s wave time thickness of a layer divided by the p wave time thickness is equal to the  $V_p/V_s$  ratio. From the  $V_p/V_s$  ratio, Poisson's ratio can be calculated directly. This has the advantage of not having to calculate the velocities from the NMO or by other method. In addition, at the well log or AVO inversion, Poisson's ratio can be checked by a third method. The disadvantage is that neither velocity is known, only Poisson's ratio.

After the p and s wave sections are tied, Poisson's ratio maps maybe developed to show areas of low Poisson's ratio. The crossplot will show the type of trend, and whether or not hydrocarbons are likely along the line or if they are off the line and in what areas.

### Conslusions

Thus, by using three-component seismic to record p and s wave data, one can calculate Poisson's ratio and rapidly evaluate a basin for oil and gas occurences. This method will, in the early stages of exploration, show the major accumulations of hydrocarbons but not the thinner plays. When more data is available on the geologic setting, lithologies, and type of play, more detailed mapping of Poisson's ratio will show these subtle plays.

## References

1. Dix, C.H., 1955, "Seismic Velocities From Surface Measurements", *Geophysics*, 20, pp. 68-86.
2. Domenico, S.N., 1976, "Effect of Brine-Gas Mixture on Velocity in and Unconsolidated Sand Reservoir," *Geophysics*, vol. 41, no. 5, pp. 882-894.
3. Gassaway, G.S. and Richgels, H.J. (1983), "SAMPLE: Seismic Amplitude Measurements for Primary Lithology Estimation," SEG National Convention Abstracts, Sept. 1983, Las Vegas, NV., pp. 610-613.
4. Gassaway, G.S. (1984), "Effects of Shallow Reflectors on Amplitude Versus Offset (Seismic Lithology) Analysis," SEG National Convention, Atlanta, GA.
5. Gonzales-Serrano, A. and Clarbout, J.F. (1984), "Wave-Equation Velocity Analysis," *Geophysics*, vol. 49, no. 9, p. 1432-1457.
6. Gregory, A.R., 1976, "Fluid Saturation Effects on Dynamic Elastic Properties of Sedimentary Rocks," *Geophysics*, vol. 41, no. 5, pp. 895-921.
7. Lama, R.D. and Vutukuri, V.S. (1978), *Handbook on Mechanical Properties of Rocks*, three volumes: Trans. Tech. Publications.
8. Tatham, R.H., Stoffa, P.L., 1976, "Vp/Vs - A Potential Hydrocarbon Indicator," *Geophysics*, vol. 41, no. 5, pp. 837-849.
9. Wang, Zhijing, and Nur, Amos (1986), "Effect of Temperature on Wave Velocities in Sand and Sandstones with Heavy Hydrocarbons," SEG Expanded Abstracts, pp. 3-5.
10. Wylie, M.R.J., A.R. Gregory, and G.H.F. Gardner, 1958, "An Experimental Investigation of the Factors Affecting Elastic Wave Velocities in Porous Media", *Geophysics*, vol. 23, pp. 459-493.

Limestone	
Shale & Arkose	
Sandstone	
gas	

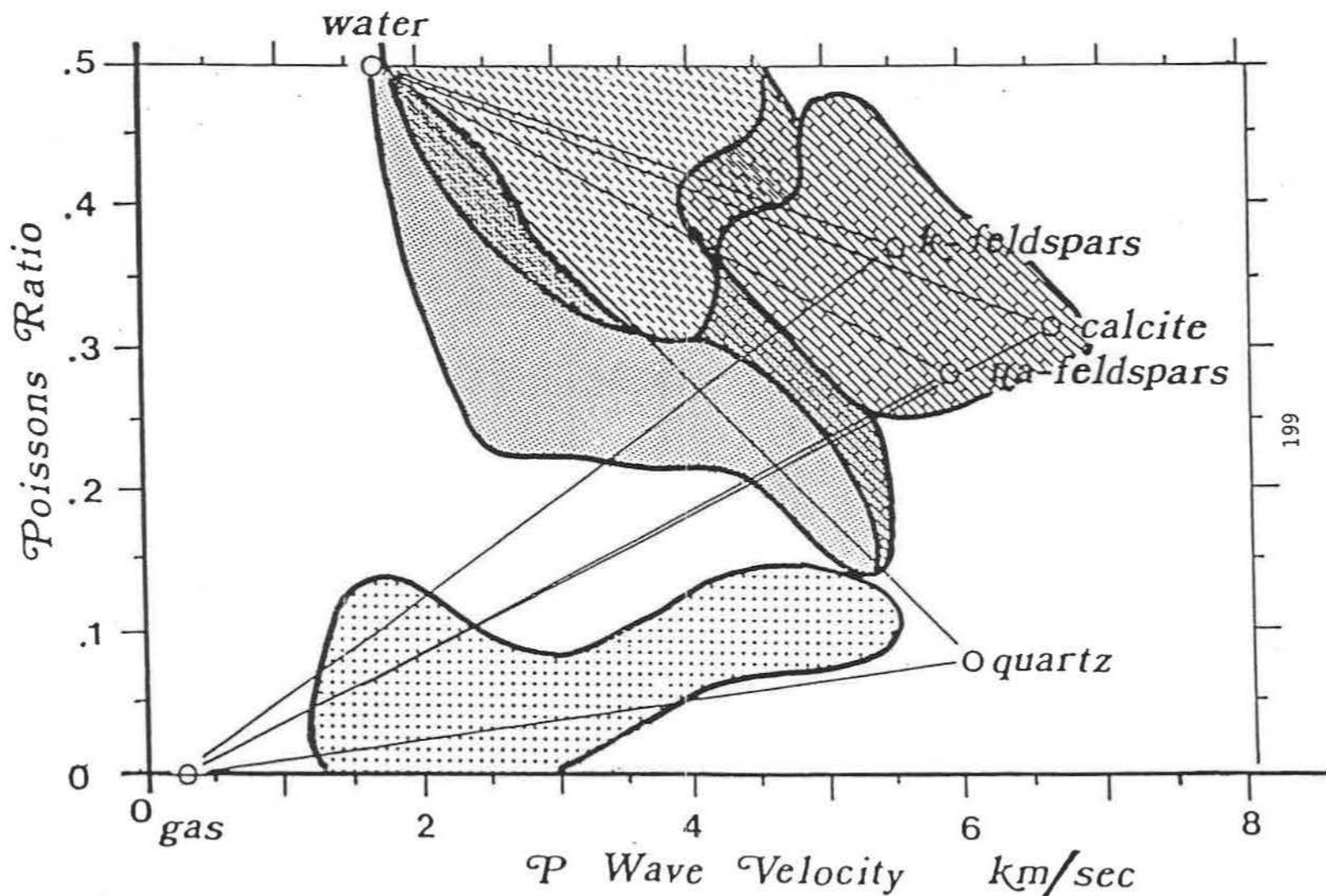
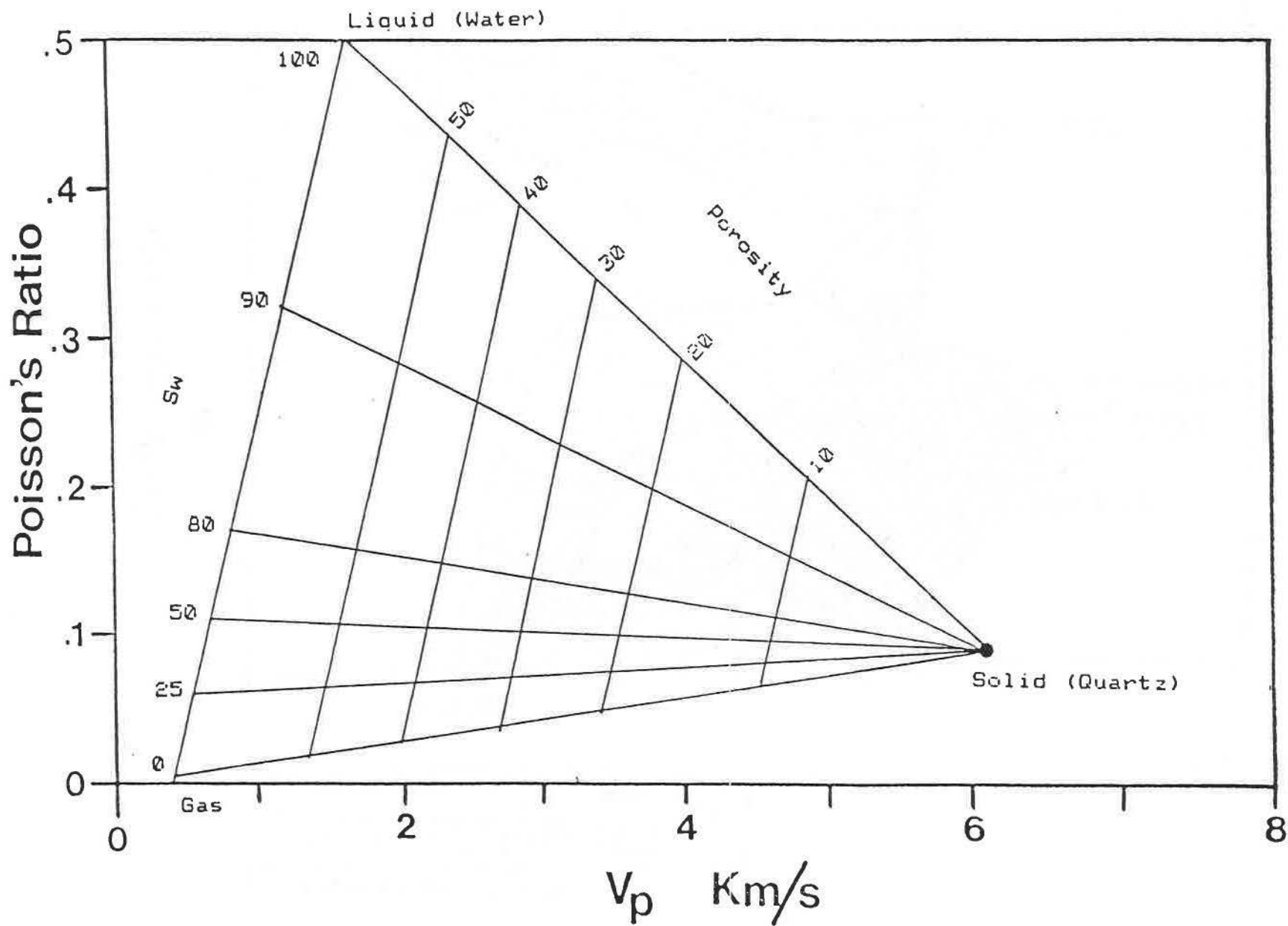


Figure 1: Poisson's Ratio - P wave Velocity Crossplot showing where various lithologies and pore fluids are found.

Figure 2: Poisson's Ratio - P wave Velocity Crossplot showing lines of constant porosity (nearly vertical) and lines of constant water saturation ( $S_w$ ) for a clean quartz sandstone.



## RECONNAISSANCE AVO ON SURFACE SEISMIC DATA

H. AHMED, SIMON-GEOLITHIC, ENGLAND

### INTRODUCTION

Contrasts in the elastic parameters of neighbouring rocks often cause distinguishable amplitude phenomena in surface recorded seismic data. Various techniques have evolved to analyse and highlight such phenomena for their potential use as a Direct-Hydrocarbon Indicator (DHI). For many years, it has been a common practice to use Bright Spots, Flat Spots, and Dim Spots in seismic data interpretation, using complex trace analysis (Taner et al, 1979), as visual signatures for DHI. More recently, techniques have been developed based on the variation of reflection coefficient with angle of incidence; i.e. Amplitude-Versus-Offset (AVO) analysis. For example, Koefoed (1955) found that an increase of Poisson's ratio for the underlying medium of an interface, representing contrasts in the acoustic impedance, causes an increase of the reflection coefficient at higher angles of incidence. Gassaway and Richgels (1983) and Ostrander (1984) effectively used the AVO phenomena to distinguish between gas-generated and non-gas-generated amplitude anomalies in sandstone reservoirs.

The objective of this paper is to verify the AVO analysis technique as a qualitative mean to indicate and possibly delineate hydrocarbon reservoirs on surface seismic data.

### AMPLITUDE VARIATION WITH OFFSET

The seismic reflection amplitude at an interface separating two media has been found to be dependent upon the source-receiver offset and the depth of the reflector (i.e.; angle of incidence), and the contrast in the elastic properties of the two media. The amplitude or reflection coefficient is, furthermore, observed to vary according to the Poisson's ratio of the two media. The relative variation of the reflection coefficient becomes significant at moderate angles (higher than 20 degrees) of incidence, when the two media have a large contrast in Poisson's ratio. Gas bearing sands, for example, normally have low Poisson's ratios and they exhibit, therefore, considerable variation of amplitude with offset (Ostrander, 1984 and Rutherford and Williams, 1989). This effect can hence be used in analyzing bright spots to distinguish gas from non-gas saturated formations.

The dependence of plane wave reflection coefficient on the angle of incidence was first expressed in the Zoeppritz Equations (Zoeppritz, 1919 - see Sheriff, R.E., Encyclopedic Dictionary of Exploration Geophysics, second addition, p.284). The

equations express the partition of the seismic energy when a plane wave impinges on an interface defined by contrast in the elastic properties of the formations directly above and below it, for any angle of incidence. Reflection and transmission coefficients are given in these equations as functions of angles of incidence and refraction and six independent elastic parameters; i.e.  $V_p$ ,  $V_s$  and the formation density, on each side of the interface. Four waves; i.e. reflected and transmitted compressional (P) and shear (S) waves, are generated for non-zero incidence angles.

### **SIMPLIFICATIONS OF THE ZOEPPRITZ EQUATIONS**

An exact solution of the Zoeppritz equations is not readily amenable for inversion because of the many variables involved. Most of these variables are, in practice, unknown and difficult to be guessed for the rock formation under investigation. Therefore, a form of approximation is often employed to make the problem tractable.

Simplified versions of the Zoeppritz equations have already been worked out and suggested in many publications; e.g. Aki and Richards, 1980 and Shuey, 1985 and Pan and Gardner, 1987, which can be readily used for qualitative AVO analysis and possibly AVO inversion. Silva and Ahmed (1989) have used, for example, the approximation provided by Pan and Gardner (1987), after it has been re-written in a standard parabolic form to delineate Gas-oil-Contact in a North Sea reservoir. This was done by fitting a parabola to amplitude values measured across NMO-corrected CMP traces. The estimated coefficients a, b and c of the parabola provided a basis for the classification of AVO phenomena associated with the boundaries of the gas saturated zone in the upper part of the reservoir.

In this paper, the Shuey approximation (given in Fig.1) is considered, in a simplified form as a straight line for relatively small angles of incidence, for further exploitation and application to different hydrocarbon reservoirs.

### **AMPLITUDE-VERSUS-OFFSET MEASUREMENT**

Considerable research has been dedicated to determining lithology and pore fluids from analysis of AVO data using the above mentioned straight line relationship. In order to highlight AVO anomalies in the seismic data, a number of attributes is conventionally generated from a linear regression fit of measured reflected amplitudes across NMO corrected CMP gathers. The intercept ( $R_0$ ) of the regression is approximately the reflection coefficient at normal incidence (i.e. zero offset) which is directly related to the contrast in the P-wave velocities and formation densities at any

reflector; e.g. top or base of a hydrocarbon reservoir. The slope (  $G$  ) of the line is the gradient which represents the degree of variations in the  $V_s/V_p$  ratio (or the Poisson's ratio) and formation density at the relevant interface.

Reconnaissance AVO plots generated from combinations of the  $R_0$  and  $G$  have been developed based on the variation of reflection coefficient with angles. They indicated for different reservoir types (of both the lithology and pore-fluid saturants) significant differences in their attribute responses. AVO attributes are investigated and presented as follows;

- |                         |                                 |
|-------------------------|---------------------------------|
| 1. The Intercept $R_0$  | 2. The Gradient $G$             |
| 3. $R_0 \times G$       | 4. $\text{sign}(R_0) \times G$  |
| 5. $R_0 + (G \times k)$ | ; where $k$ is a scaling factor |

Further reservoir modelling is, therefore, essential to evaluate the significance of the AVO anomaly observed. Seismic modelling is normally carried out to simulate the reservoir situation, using available borehole data and implementing a conventional survey geometry, for further study of expected AVO features on the field data. Computed synthetic seismic traces will be sorted to CMP gathers after application of NMO corrections, reflection amplitudes will be picked for identifiable events and the AVO attributes will then be determined by straight line regression.

Figure 2 shows theoretically computed AVO anomalies for two sandstone reservoirs typically of the North Sea. Figure 3 represents AVO attributes for an Eocene Turbidite gas sand from a North Sea reservoir, and Fig 4 for a gas-bearing Rotliegendes Sandstone reservoir of the Southern North Sea basin. They indicate different signatures related to the difference in the stratigraphy and rock elastic properties of each gas reservoir.

### RECON AVO

Seismic modelling is implemented to determine to what extent a relationship exists between the type of AVO anomaly found and the lithology and type of pore-fill.

The investigation proceeds along two independent routes:-

- 1) Using the borehole sonic and a lithology calculated from conventional logs, an empirical algorithm is used to calculate the shear-wave sonic at the log sampling rate. A synthetic CMP gather is then generated.

- 2) The recorded seismic gathers are processed so as to maintain True Relative Amplitudes, the traces are sorted to CMP gathers and NMO corrections will then be applied using results of seismic velocity analysis.

Both gathers are then considered for estimation of  $R_0$  and  $G$  using a linear regression algorithm, as mentioned above, of amplitude as a function of incident angle (e.g. amplitude  $A$  versus  $\sin^2 i$ ). Angle of incidence ( $i$ ) may be calculated using a ray-tracing algorithm for the depth zone of interest using the actual survey geometry.

To minimise the effect of noise on the seismic data, that can erroneously influence the regression analysis, a robust regression analysis (Walden, 1990) is performed. This is because least-squares estimation of straight lines can give undesirable results in the presence of a few contaminated data points. Application of such a technique enables greater confidence in the derived AVO attributes.

## CONCLUSION

It has been indicated that AVO attributes can greatly add to conventional DHI techniques. The amplitude strength /or the reflection coefficient and variation rate of offset amplitudes have proved valuable signatures for identification of lithology and fluid type in the reservoir. With field-case studies in various geologic provinces, AVO signatures can be established for later correlation with nearby prospects. Seismic modelling is necessary to verify, to calibrate and/or to test the reliability of the observed anomalies in the seismic data. Reconnaissance AVO is achieved by comparison of amplitude variations identified in NMO corrected CMP gathers of seismic field data, after careful processing, with the AVO signature obtained from modelling of well data. Where a lack of borehole control exists, unreliable interpretation of the AVO signature will result.

**REFERENCES:**

- Aki,K. and Richards,P.G.,1980, Quantitative seismology - Theory and methods: W.H. Freeman and Co.
- Gassaway,G.S. and Richgels,H.J.,1983, SAMPLE: Seismic Measurement for Primary Lithology Estimation: Presented at the 53rd Annual Meeting of the SEG, Las Vegas.
- Koefoed,O.,1955,On the effect of Poisson's ratio of rock strata on the reflection coefficients of plane waves:Geophys.Pros., 3,381-387.
- Ostrander,W.J.,1984, Plane-wave reflection coefficients for gas sands at non-normal angles of incidence: Geophysics,49,1637-1648.
- Pan,N.D. and Gardner,G.H.F.,1987, The basic equation of plane elastic wave reflection and scattering applied to AVO analysis: Seismic Acoustic Laboratory University of Houston Annual Progress Review Vol.19,123-139.
- Rutherford,S.R. and Williams,R.H.,1989, Amplitude-Versus-Offset variations in gas sands:Geophysics,54,680-688.
- Shuey,R.T.,1985, A simplification of the Zoeppritz equations: Geophysics,50,609-614.
- Sliva,R. and Ahmed,H.,1989, The application of the AVO technique in Production Geophysics: Presented at the 59th Annual Meeting of the SEG, Dallas,SI 6.5,836-838.
- Taner,M.T., Koehler,F. and Sheriff,R.E.,1979, Complex trace analysis: Geophysics,44,1041-1063.
- Walden,A.T.,1990, Making AVO sections more robust: Presented at the 52nd Meeting of the EAEG, Copenhagen.
- Zoeppritz,K.,1919, Erdbebenwellen VIII B, Uber Reflexion und Durchgang seismischer Wellen durch Unstetigkeitsflachen: Gottinger Nachr.1,66-84.

## A SIMPLIFICATION OF THE ZOEPPRITZ EQUATIONS

[R.T. Shuey, 1985]

$$R(\theta) = R_o + \left[ A_o R_o + \frac{\Delta\sigma}{(1-\sigma)^2} \right] \sin^2\theta$$

Amplitude at Normal Incidence      Amplitude at Intermediate Angles ( $\theta < 30^\circ$ )

$$+ \frac{1}{2} \frac{\Delta V_p}{V_p} \left[ \tan^2\theta - \sin^2\theta \right]$$

Amplitude at Critical Angles ( $\theta > 30^\circ$ )

$$R_o \equiv \frac{1}{2} \left( \frac{\Delta V_p}{V_p} + \frac{\Delta D}{D} \right), \quad A_o = B - 2(1+B) \cdot \frac{1-2\sigma}{1-\sigma},$$

$$A = A_o + \frac{1}{(1-\sigma)^2} \cdot \frac{\Delta\sigma}{R_o}, \quad \text{and} \quad B = \frac{\Delta V_p / V_p}{\Delta V_p / V_p + \Delta D / D}$$

## **A SIMPLIFICATION OF THE ZOEPPRITZ EQUATION**

For  $\theta < 30^\circ$       (Straight-Line Relationship)

$$R(\theta) = R_o + G \sin^2\theta$$

Intercept      Gradient

$$\text{For: } \frac{V_p}{V_s} = 2$$

$$\Delta\sigma = \frac{4}{9} (R_o + G)$$

# EOCENE TURBIDITE GAS SAND (North Sea)

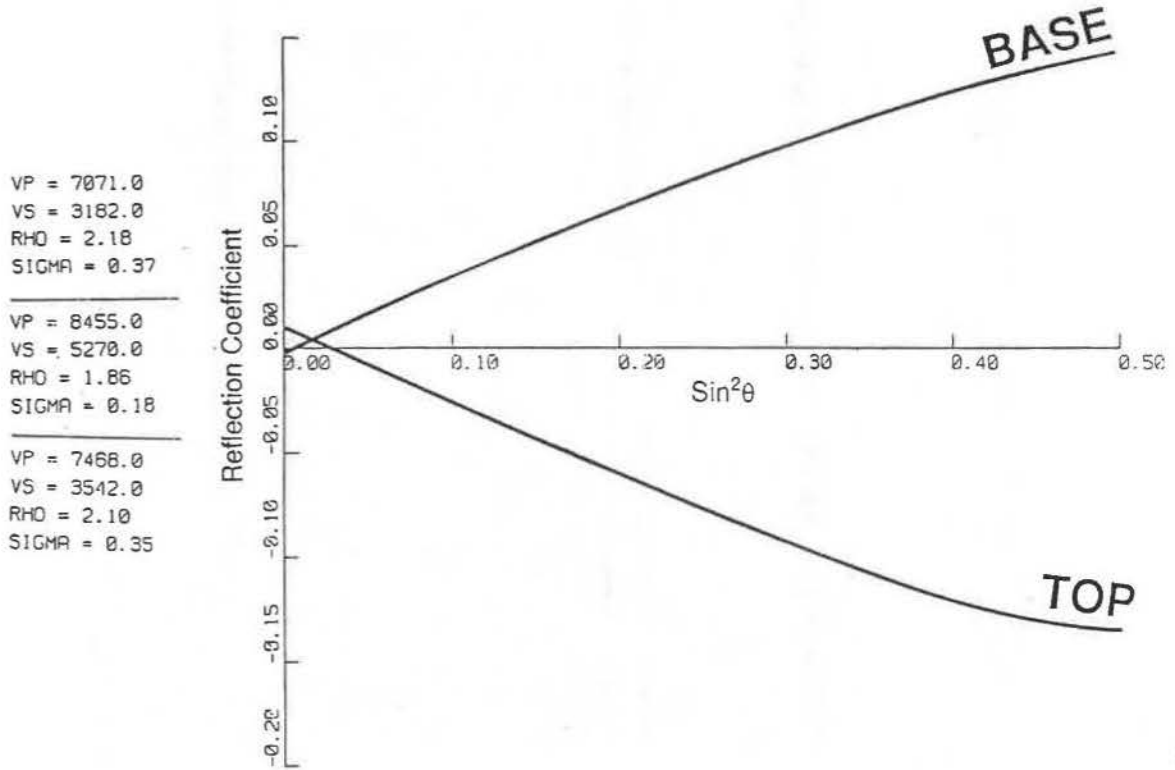


Figure 2a

# ROTLIEGENDES GAS SAND (Southern North Sea Basin)

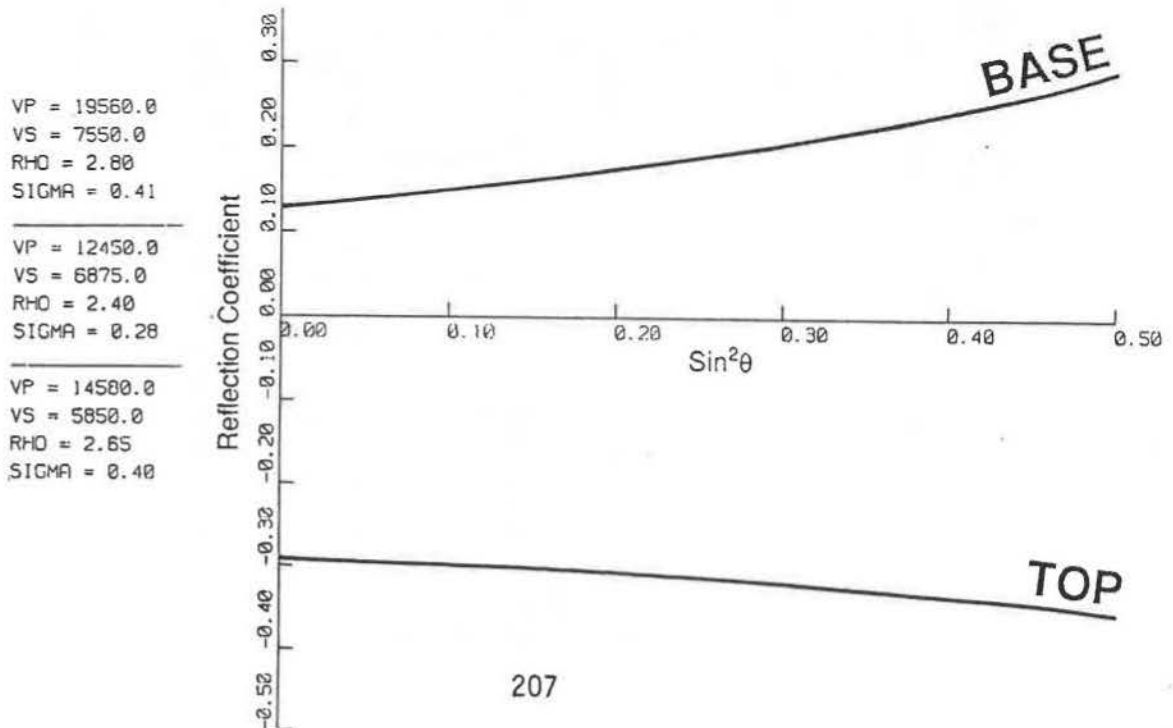


Figure 2b

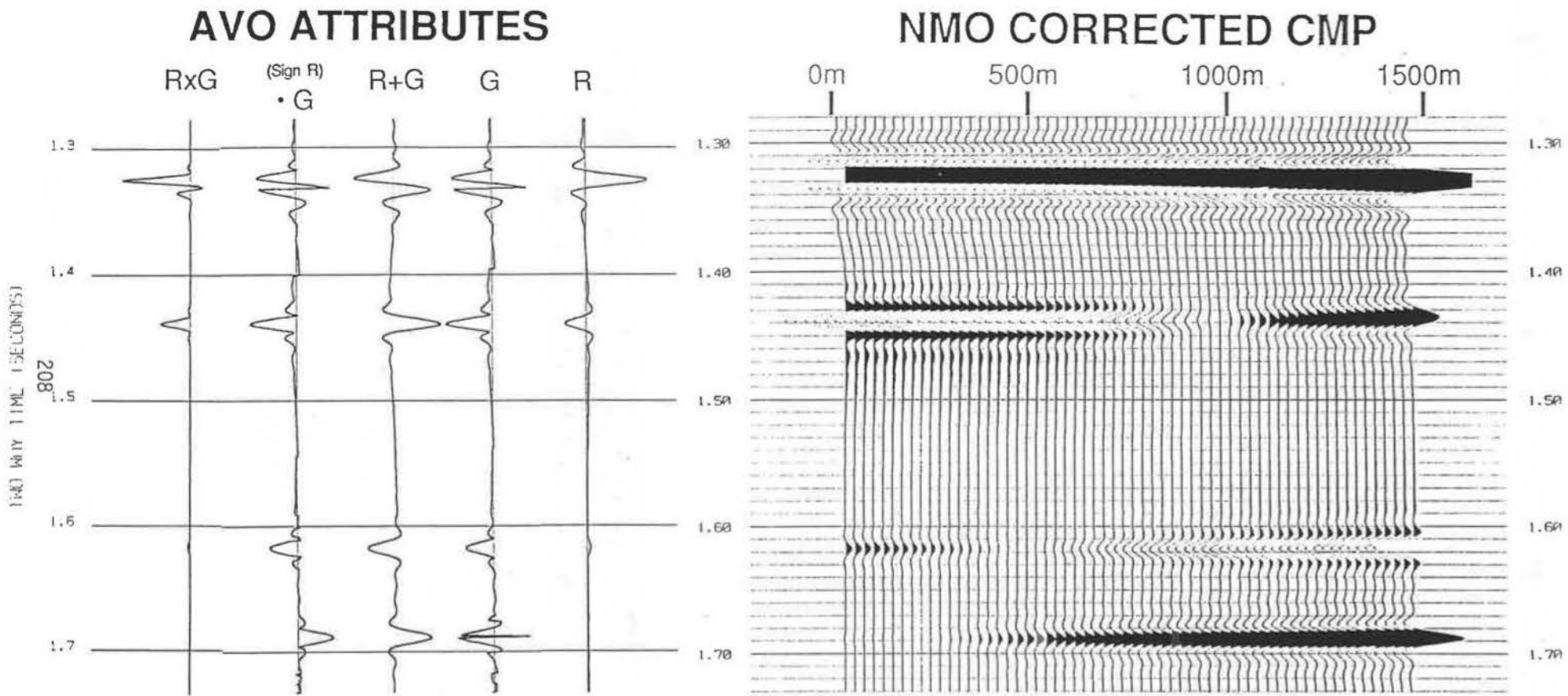


Figure 3. AVO Analysis for the EOCENE GAS-SAND

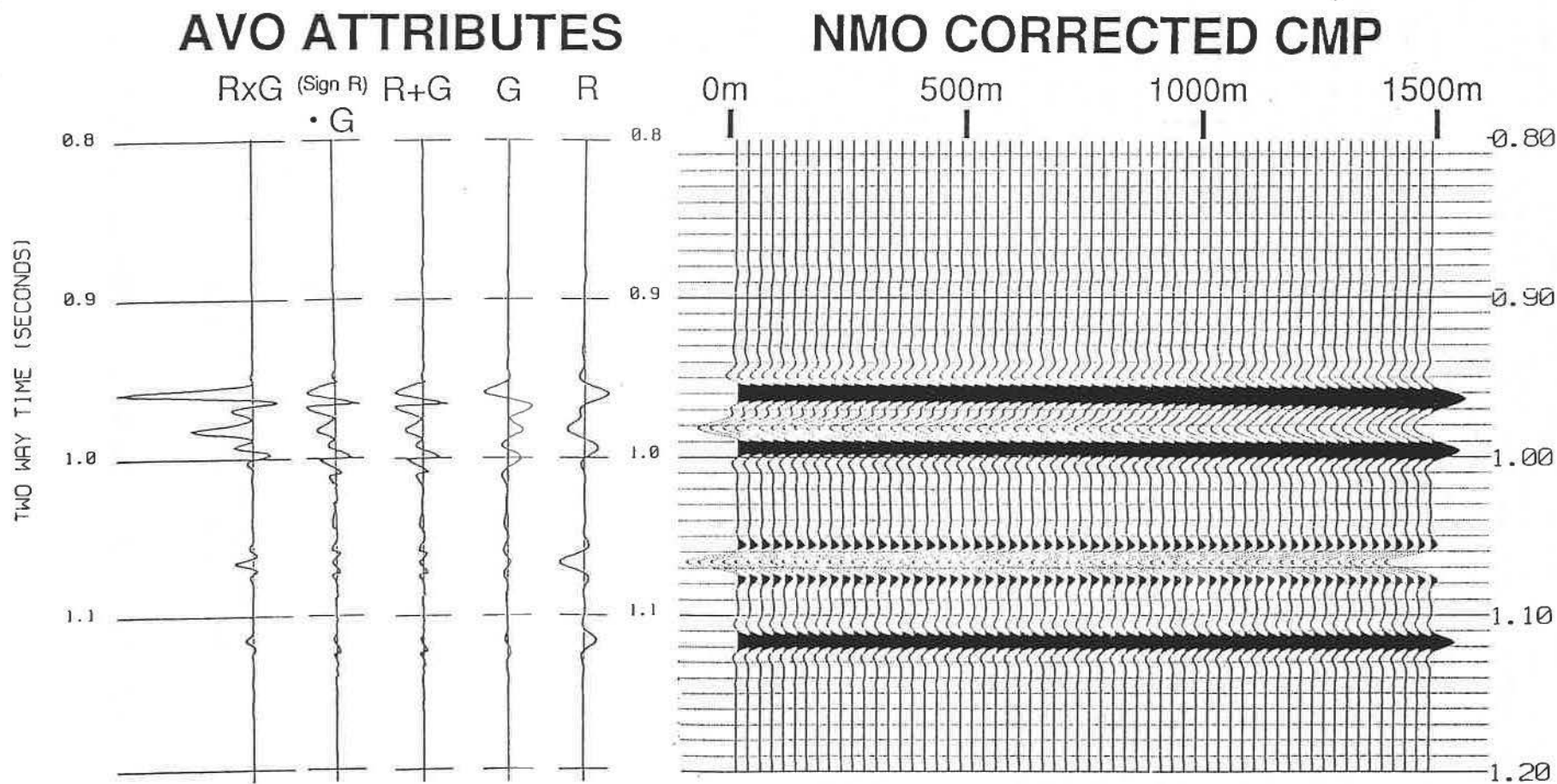


Figure 4. AVO Analysis for the ROTLIEGENDES GAS-SAND

## GEM: A NEW CONCEPT IN QUANTITATIVE CORE CHARACTERIZATION

C.H. Sondergeld and C.S. Rai  
Amoco Production Company

GEM is an acronym for Geophysical Evaluation Modules. The development of this system was spurred by the coincidence of three events: (1) the recognized importance of physical properties measurements; (2) the demand to efficiently characterize a large number of core plugs; and (3) the embarking upon a continuous coring program. The laboratory created is an improvement upon existing stationary facilities in many ways. The shortcomings of existing facility are: (1) the orientation toward research studies; (2) the inefficiency of the methodologies employed; (3) the lack of a coherent information distribution system; and (4) the lack of complete core characterization.

As petrophysicists, geologists or geophysicists we tend to approach a problems from a specific discipline point of view. Specifically, we are concerned with only those physical properties affecting our immediate problem. This creates a demand for core characterization by discipline and there exists no composite characterization for any one core plug. Permeabilities would be measured on one plug, velocities on another, grain densities, porosities and perhaps capillary pressure data are measured on another plug and yet another would be supplied for mineralogy by X-ray or modal analysis, etc. Sample heterogeneity prohibits the correlation of these data sets. When attempted, some correlations would be obvious and others would not. One only need examine the porosity variability in cores taken from a wellbore to be convinced of the futility of correlating these data sets. The general sporadic correlative core studies leave doubt of the efficacy of the efforts. Additionally costs for a complete suite of physical properties were either difficult to justify or limited the number of such data sets acquired. This produces a vicious cycle with few cores. Variability produced by heterogeneity, geology and measurement errors reduce the number of useable data sets and further cast serious questions as to the usefulness of the remaining datasets. This situation is exacerbated by the prohibitive times required for complete characterization and the need to utilize a multiple vendors. This last requirement was naively overcome by simultaneously sending adjacent core plugs. It necessarily

forces serial processing of the core through multiple vendors to achieve the ultimate objective, i.e. complete quantitative core characterization on the same core plug.

Geology presents the most perplexing problem to any empiricist. The two classical approaches to understanding its imprint on a seismic signal are (1) to carry out detailed studies of a well characterized material such as Berea sandstone wherein the environmental variables are controlled to emulate nature and (2) to characterized very precisely many core samples from many geological environments. Both approaches have merit, the latter was never an economical consideration. We have created in GEM a system which maintains the integrity of experimental measurements and yet reduces both cost and time for core characterization by an order of magnitude. Moreover as a consequence of its high degree of automation, compactness and autonomy, the system is also portable. Portability opens new capabilities. The system can be transported to a well site, nearby town or deployed to an international or domestic core facility. This permits the characterization of extremely friable core and opens access to traditionally inaccessible core repositories. Portability makes GEM a natural and integral part of Amoco's slim-hole drilling system. With regards to this project, it is quite evident from past efforts and our own slim-hole efforts that the real incentive to employ this technology must be driven by the quest for knowledge and information. Obtaining the core is only a small part of the problem. The major contribution is realized by the timely and cost effective extraction of information locked in the core. Slim-hole drilling is not synonymous with inexpensive drilling. The economics must be evaluated carefully for each prospect. However, the economic benefits of reducing risk by making sound decisions based upon reliable and quantitative information often offsets pure expenditure considerations.

The capabilities of new communication systems, computers, and GEM produce yet another attractive combination, a real-time interactive exploration system. The data produced in GEM can be sent to a central facility via satellite or phone line and then accessed for input into potential field modelling, seismic migration, modelling, and processing and prospect evaluation. Certainly field based seismic could be coupled with GEM to help refine acquisition parameters, new seismic line directions and seismic acquisition coverage.

GEM as it is currently configured measures the following properties routinely:

- Grain, Dry and Saturated Densities
- Boyle's Law Porosity
- Effective Saturated Porosity
- Magnetic Susceptibility
- Compressive Strength (Static moduli)
- Compressional Velocities as a function of effective pressure
- Polarized Shear Wave Velocities as a function of effective pressure
- Birefringence (difference in velocity between two polarized S waves)
- Qualitative Mineralogy

Quantitative Mineralogy (weight percent) and a few other properties of interest. Velocities are measured for dry and wet states of saturation. The system has a very high sample throughput, approximately 50 samples can be characterized in a 12 hour shift. The system is quite rugged. Our experience has been obtained through continuous use of the system over the last 4 years both in the field, at core facilities and at international locations.

A natural product of GEM is a quantitative data set, all derived from a small controlled volume of sample which has been used to create a premier rock properties database. The existence of such a database permits one to address a multitude of exploration, production, and exploitation problems.

GEM presents new information in a new format. It can therefore be viewed as either a threat or an opportunity. Experience indicates that once supplied with a vast amount of core derived data, a worker will seek to compare the information to log derived data. At the same time, having only log derived data forces one to seek reaffirmation through a coring program. We will show comparisons between core, log and seismic data which should inspire people to ask new questions and to pursue new approaches to exploration problems.

# **GEOSTATISTICAL APPLICATIONS FOR EXPLORATION AND DEVELOPMENT: POROSITY ESTIMATIONS FROM 3-D SEISMIC DATA CONDITIONED TO WELL DATA**

**R. L. Chambers, Amoco Production Company**

## Introduction and Purpose

The low spatial resolution of well data does not provide the necessary details to adequately infer the spatial heterogeneities within reservoirs, therefore, alternative data sources are needed to provide dense interwell information. Seismic data is one of the logical data sources. High quality 3-D seismic data has been widely used to map external reservoir geometry, with seismic stratigraphic techniques often detailing internal geometries of reservoir bodies. Recent advances in true amplitude seismic processing offers a potential source of dense, "soft" data useful for inference of rock properties.

Within recent years, the petroleum industry has been actively evaluating geostatistical methodologies as a supplemental technique to analyze and integrate various types of datasets. In May, 1988, Amoco's Geophysical Research Division initiated a joint project with its Houston Region to evaluate a geostatistical approach to reservoir characterization at the seismic scale. The goal of the project is to use geostatistical methods to predict lithology from seismic data and limited well data.

This poster session illustrates the quantitative integration of 3-D seismic data, calibrated to well data, to map porosity in a multilayered dolomitic-siltstone reservoir at the seismic scale.

A producing west Texas field was selected for the project because an extensive digital well-log database was readily available. From the 1400 wells in the field, 600 were selected to construct stratigraphic and structural cross-sections on a 1320 foot average well spacing. Approximately 70 wells, with core measured porosity and permeability on a one foot interval, were used to calibrate sonic derived porosity at uncored wells. Other criteria for consideration was the structural simplicity of the field, the necessity of a seismically resolvable interval and the field's economic importance to Amoco.

The project was divided into three phases: I) Geostatistical analysis of well data only; II) Seismic acquisition, processing and interpretation; III) Calibration and integration of well data with seismic data to infer interwell porosity variability.

## Geology

The producing formation is a Permian age shallowing upward, prograding carbonate shelf sequence formed under moderately low to moderately high energy conditions. Lithologically, the formation is composed of alternating dolomites and siltstones for a total thickness of about 460 feet, with a net pay of 175 feet. Structurally, the field is described as a north-south trending asymmetrical anticline, dipping gently from west to east into the Midland Basin.

Reservoir engineers divide the reservoir into multiple flow units on the basis of porosity and permeability. The flow units do not always correlate to lithologic tops. One of several siltstone intervals was selected for study because: 1) the layer is relatively thick (40 - 90 feet); and the 2) the reflection coefficients, calculated from log data, are sufficiently large enough to suggest that the interval should be resolved on high quality seismic data.

## Well Data

Petrophysical properties studied in Phase I include: porosity, permeability, interval transit time, and porosity-thickness. The values for each of these parameters represent arithmetic averages calculated across the siltstone interval. Other parameters include true depth to the top of the siltstone interval, total interval thickness and variables related to permeability threshold levels. For Phase I, the siltstone interval represents the actual lithostratigraphic sequence as defined by Houston geologists.

For Phase III, the interval over which rock properties were averaged was modified in an attempt to represent a "seismically" defined interval. The siltstone interval was picked on synthetic seismograms created for each well with the same zero phase wavelet used in the processed seismic data.

## Seismic Data

A high resolution 3-D seismic dataset was acquired over the central portion of the field. Fifty-five of the calibrated wells are included within the survey area, covering approximately 4 square miles. Depth point spacing is 40 feet inline and 80 cross-line with a total of 41134 CDP's.

Seismic acquisition and processing objectives were: 1) to obtain frequencies sufficient to "resolve" the siltstone interval; 2) high lateral resolution; 3) preservation of relative amplitudes; 4) areal coverage large enough to sample the maximum range of variability seen in Phase I results; and 5) inversion of seismic reflection amplitude to acoustic impedance.

Because the phase can have a significant impact on the seismic interpretation, and especially lithology prediction, the seismic data must be dephased prior to inversion to acoustic impedance or interval velocity. A dephasing wavelet was constructed from a well which was logged from the near surface to approximately 1000 feet below the interval of interest.

There is an excellent tie between the zero-phase synthetic seismogram, generated from sonic and density logs, and the dephased seismic data. The top of the siltstone interval is expressed as a well developed trough on the seismic data. Dephasing filters are really only valid near the well from which the filter was designed. However, only one well was logged over an interval of sufficient length to design a proper dephasing filter. A qualitative visual analysis of all the seismic lines suggests that the phase does not vary significantly across the survey area, which is not too surprising, because no CDP is more than 1.5 miles from the well.

The siltstone interval was interpreted on 131 dip lines and 314 cross-lines. The data was datumed on the picked horizon with peak amplitudes and their x-y coordinates dumped to an ASCII flat file. The reflection amplitude sections were also inverted to acoustic impedance sections using 400 time-velocity pairs as the low frequency component of the inversion. The data was datumed with total  $Z_p$ , the low and high frequency components of  $Z_p$  and their x-y pairs dumped to an ASCII flat file.

#### Phase I - Well Study

An initial geostatistical study was completed on 261 wells covering an area 3.4 miles (E-W) by 6.8 miles (N-S), with the wells on a 40 acre spacing. The maps produced by kriging and conditional simulations are consistent with the known geology of the siltstone interval. Porosity and permeability show a 4:1 anisotropy ratio north to south and a correlation range of approximately 16000 feet, N-S, and 4000 feet, E-W. The interval thickness was almost isotropic, with porosity-thickness only slightly anisotropic (2:1, N:E).

Maps of porosity, porosity-thickness, permeability and interval thickness for Phase I results are illustrated in the poster session. The results of this study were used to select a subarea which was representative of the variability seen in the larger area for a 3D seismic acquisition program.

#### Phase III - Data Integration

Because the fundamental goal of this study is to use seismic data to infer interwell rock properties, it is necessary to calibrate the seismic data to the well data. The calibration process requires knowledge of the seismic attributes at the well locations. The usual method of calibration is to establish a correlation between the two attributes,

in this case average porosity and reflection amplitude,  $Z_p$  or the low and high frequency components of  $Z_p$ . The correlation coefficient,  $\rho$ , between reflection amplitude and porosity = -0.54, for  $Z_p$  and porosity,  $\rho = -0.42$ , for the low frequency  $Z_p$  component,  $\rho = 0.66$  and for the high frequency component,  $\rho = -0.54$ . For comparison, the correlation between core porosity and interval transit time for the well data is 0.82, which establishes the upper limit of the correlation we might expect between a seismic attribute and porosity. Therefore, the correlations cited above are 51% to 80% of the maximum likely correlation. The low correlations are not too surprising because these seismic attributes are not only affected by changes in porosity, but also to changes in rock and fluid type, and to some extent temperature and pressure. There is reason to assume, based on laboratory studies, a first order relationship between porosity and the seismic data.

A geostatistical method known as external drift is used to integrate the sparse well data with the densely sampled 3-D seismic data. A generalized covariance model is calculated to capture the spatial information in both datasets, then during the kriging or conditional simulation, maps the seismic data into the units of porosity.

Three examples will illustrate the external drift method. The first example, more typical in the early stages of field development, shows porosity maps inferred from more than 33,000 seismic data, calibrated to only 10 wells. The second case uses 15 wells, and the third example illustrates a data integration with all 55 wells. Illustrations include examples of kriging and conditional simulations of porosity, with and without seismic data integration.

### Conclusions

Despite the low local correlation between porosity and the seismic attributes, the spatial correlation between the data is great enough that seismic information can be used to infer interwell variations in porosity.

Kriging provides smoothed averages of the lateral variations for each porosity. These maps are useful for economic considerations, but are not especially good at assessing uncertainty or risk. In contrast, conditional simulations yield a family of alternative realizations, all consistent with the data and spatial correlation structure, and can be used to assess uncertainty in the porosity estimates.

# PREDICTING LITHOFACIES FROM SEISMIC DATA USING SEQUENCE STRATIGRAPHY PRINCIPLES

D.L. Risch, Geco-Prakla

An integrated seismic and well log sequence stratigraphy analysis was done on an offshore Texas seismic line 52 miles long. Sequence and systems tract boundaries were identified based on the SP and GR log curves, seismic facies analysis, biostratigraphy and oxygen isotope ( $^{18}\text{O}$ ) data. Good correlations exist for most of the integrated data. A portion of the interpreted seismic line and the integrated well data is shown to illustrate the technique. Sand rich areas have been interpreted from the seismic data based on the systems tract model and calibrated with lithology determined at the wells. This sequence stratigraphy technique can be used to refine reservoir models as well as predict sand rich areas in frontier basins within the context of systems tracts.

## INTRODUCTION

The seismic sequence stratigraphy method is being used by the oil industry to improve the geological interpretation of mature areas as well as basin analysis in frontier regions. In a field development case, a detailed chronostratigraphic and lithostratigraphic framework can be constructed using high quality seismic data and biostratigraphy. In frontier exploration, lithofacies predictions can be made from seismic data and sparse well control based on systems tract models.

Brown and Fisher (1976) introduced the concept of systems tracts to seismic stratigraphic analysis and recently many people have expanded and refined this idea (Vail, 1987; Van Wagoner et al., 1987; Sangree et al., 1990). Vail (1987) recognized that a sequence is deposited during one cycle of sea level rise and fall. He subdivided the sequence into 3 lowstand and 2 highstand systems tracts. The relationship of each systems tract and associated stratal patterns is illustrated in Figure 1.

## SYSTEMS TRACTS

The basal systems tract deposited during the lowest sea level is the basin floor fan (BFF). It is generally a well sorted beach or delta front sand carried into the slope and basin by storms or gravity slides. It has a mounded seismic character with downlap onto the underlying sequence boundary.

The overlying slope fan systems tract (SF) is comprised of submarine turbidite fans with good channel and overbank sands. These complexes have chaotic or concave upward, "gull-wing" seismic reflection patterns. Slumping frequently occurring during this time can be readily recognized as chaotic or hummocky seismic data. Shales predominate outside the channel/overbank and fan lobe areas.

The prograding wedge systems tract (PW) derives its name from deltas prograding at the shelf edge. This systems tract generally has ample reservoir sands but updip seals can be a problem. Seismically, this systems tract is typified by moderate to high

amplitude, continuous reflectors that respond to alternating sands and shales of delta deposition.

The transgressive systems tract (TST) is deposited during a rapid rise in sea level, resulting in a fossil-rich, condensed section shale, developed on the slope and in the basin. Planktonic flora proliferate during the warming period associated with the rising sea. The combination of the floral "bloom" and low terrestrial sedimentation results in an increase in the fossil abundance within this shale (Beard et al., 1982; Shaffer, 1987; Louitit et al., 1988). This easily recognized abundance peak in any condensed section shale establishes the basis for the dating of the marine sequences and systems tracts.

During the highstand systems tract (HST) deposition, sea level rises to a standstill and begins to drop with sedimentation again prograding basinward. This systems tract is usually silty and not as productive as the prograding wedge tract.

#### APPLICATION OF THE TECHNIQUE

The sequence stratigraphy technique was applied to an offshore Texas seismic line 52 miles long with 7 wells along the transect. Figure 2 shows a portion of this seismic line with data from one well integrated to establish the chrono- and lithostratigraphy of the Plio-Pleistocene sediments. These sediments were deposited on the slope based on analyzed benthonic foraminifera.

Three chronostratigraphic methods are shown with the SP curve. The primary age dating data are the planktonic nannofossils and foraminifera shown as abundance curves. The peaks deflecting to the right (Figure 2) indicate the location of the condensed section shales of the transgressive and slope fan systems tracts. These condensed section shales have a significant SP response and high gamma ray reading. The oxygen isotope  $^{18}\text{O}$  curve correlates well with the biostratigraphy and in one case at 2.45 Ma, corroborates the seismic evidence for that transgressive boundary in the absence of a fossil abundance peak. A decrease in the  $^{18}\text{O}$  (deflection to the right) is associated with an influx of fresh glacial meltwater and rising sea level. The magnetic reversal scale is included to illustrate its agreement with the dated biostratigraphy and encourage its use in the absence of fossils, such as in non-marine sediments.

The sequence boundary lies just above the transgressive tract and seismically marks a vertical change from layered parallel reflectors below to chaotic and hummocky reflectors above. The SP curve usually shows a sharp sand break just above the transgressive tract in this bathyal setting. This abrupt sand/shale break is due to an influx of shelf sands deposited at the onset of the lowstand system following a drop in sea level. These basal basin floor fans are highlighted on the SP curve and their lateral extent shown on the seismic data just above the sequence boundaries labelled 3.0, 2.4, 1.4, and 0.6 Ma. Seismically, these sands are mounded and

downlap onto the sequence boundary.

The slope fan systems tract is thick in this region of the line and contains discrete sand bodies interpreted from the seismic data and SP curve. Channel sands are associated with concave upward reflectors within a hummocky, discontinuous seismic facies. This systems tract is the easiest to identify because it generally has a hummocky and/or chaotic seismic character. This unique character is interpreted to be stacked and coalescing submarine channels or mass sediment slumping. A fan lobe sand has been interpreted on the seismic data at 1350ms at the well based on the SP curve.

The prograding wedge is thin below 1.0 Ma but thickens in younger sequences as the shelf progrades basinward. The prograding wedge top was omitted for clarity but lies just below the very thin transgressive systems tract. Shales predominate at this deep water location but sands are interpreted updip.

The highstand and transgressive systems tracts are shaly on the slope and provide a seal for underlying lowstand sands. In older sediments, these deposits can be good source rocks.

#### CONCLUSION

Lithofacies predictions have been made on a 52 mile long seismic line of offshore Texas using the principles of sequence stratigraphy and associated systems tract facies models. The sequence and systems tract boundaries were interpreted from SP and GR log curves as well as analyzing seismic reflections and facies. The boundaries were dated along the transect by noting increases in fossil abundances that are found in condensed section shales of the slope fan and transgressive systems tracts. Oxygen isotope,  $^{18}\text{O}$ , data correlated well with the biostratigraphy and was used to confirm the age of a seismically defined sequence at 2.4 Ma. Sand rich areas are interpreted in the context of systems tract facies models and calibrated at the well with the electric and gamma ray logs.

This technique can be used to refine lithofacies models for field development as well as basin analysis in frontier areas. The development of a field producing from a laterally continuous and homogeneous prograding wedge sand will be drastically different than producing a field from discontinuous stacked channel and overbank sands of the slope fan systems tract. In a frontier area with only sparse well control and seismic data, this technique can be used to predict lithofacies and prospective sand rich areas based on the systems tract model.

Beard, J.H., J.B. Sangree, and L.A. Smith, 1982, Quaternary chronology, paleoclimate, depositional sequences, and eustatic cycles, American Association of Petroleum Geologists, V. 66, p. 158-169.

Brown, L.F., Jr., and W.L. Fisher, 1976, Seismic-stratigraphic interpretation of depositional systems: examples from Brazilian rift and pull-apart basins, in: Payton, C.E., ed., Seismic Stratigraphy - Applications to Hydrocarbon Exploration, American Association of Petroleum Geologists Memoir 26, p. 213-248.

Loutit, T.S., J. Hardenbol, P.R. Vail and G.R. Baum, 1988, Condensed sections: The key to age dating and correlation of continental margin sediments, in: Wilgus, C. and others (eds.) Sea Level Changes: An Integrated Approach: Society of Economic Paleontologists and Mineralogists Special Publication No. 42, p. 183-186.

Sangree, J.B., P.R. Vail, and R.M. Mitchum, Jr., 1990, A summary of exploration applications of sequence stratigraphy, in: Armentrout, J.M., ed., Sequence Stratigraphy as an Exploration Tool, Eleventh Annual Research Conference, Gulf Coast Section, Society of Economic Paleontologists and Mineralogists, p. 321-327.

Shaffer, B.L., 1987, The Potential of Calcareous Nannofossils for recognizing Plio-Pleistocene climatic cycles and sequence boundaries on the shelf, in: Barnette and Bulter, eds., GCSSEPM Foundation Eighth Annual Research Conference, Houston, p. 142-145.

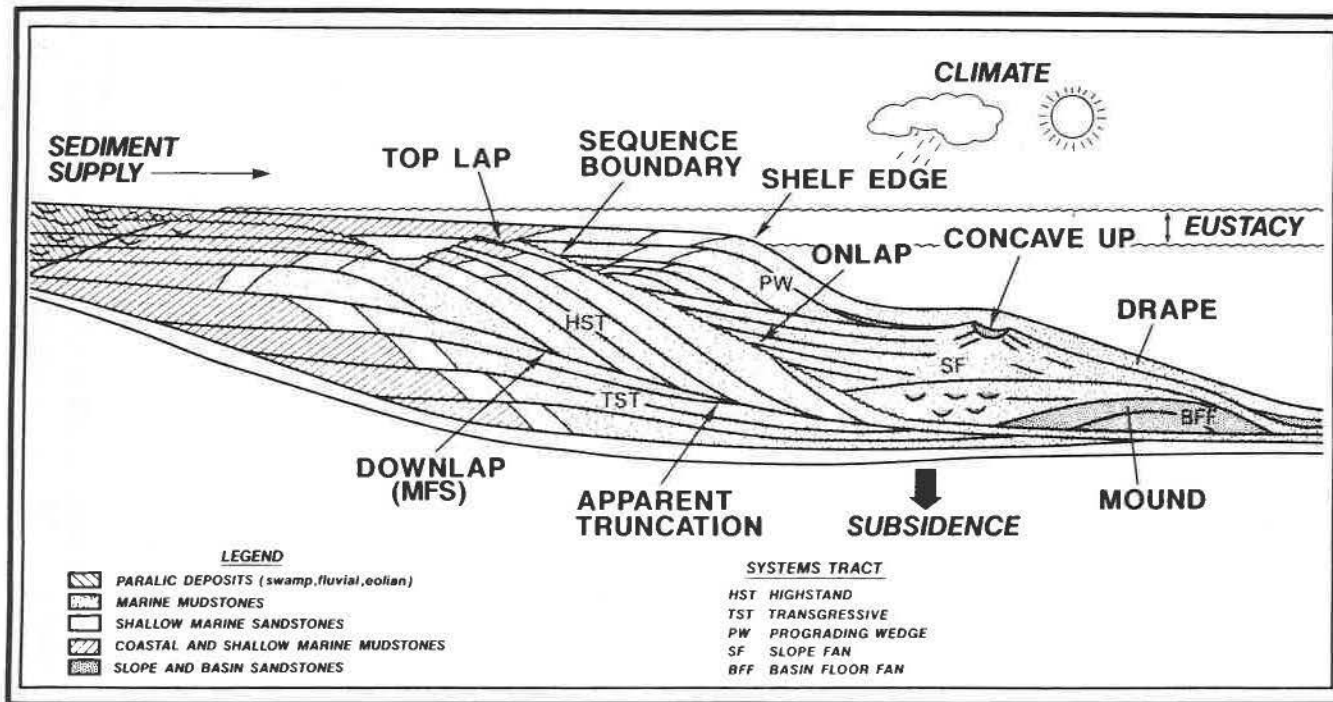
Vail, P.R., 1987, Seismic stratigraphic interpretation procedure, in: Bally, A.W., ed., Atlas of Seismic Stratigraphy: American Association of Petroleum Geologists, Studies in Geology 27, p. 1-10.

Van Wagoner, J.C., R.M. Mitchum, Jr., H.W. Posamentier, and P.R. Vail, 1987, Key definitions of sequence stratigraphy in: Bally, A.W., ed., Atlas of Seismic Stratigraphy, V. 1, American Association of Petroleum Geologists Studies in Geology 27, p. 11-14.

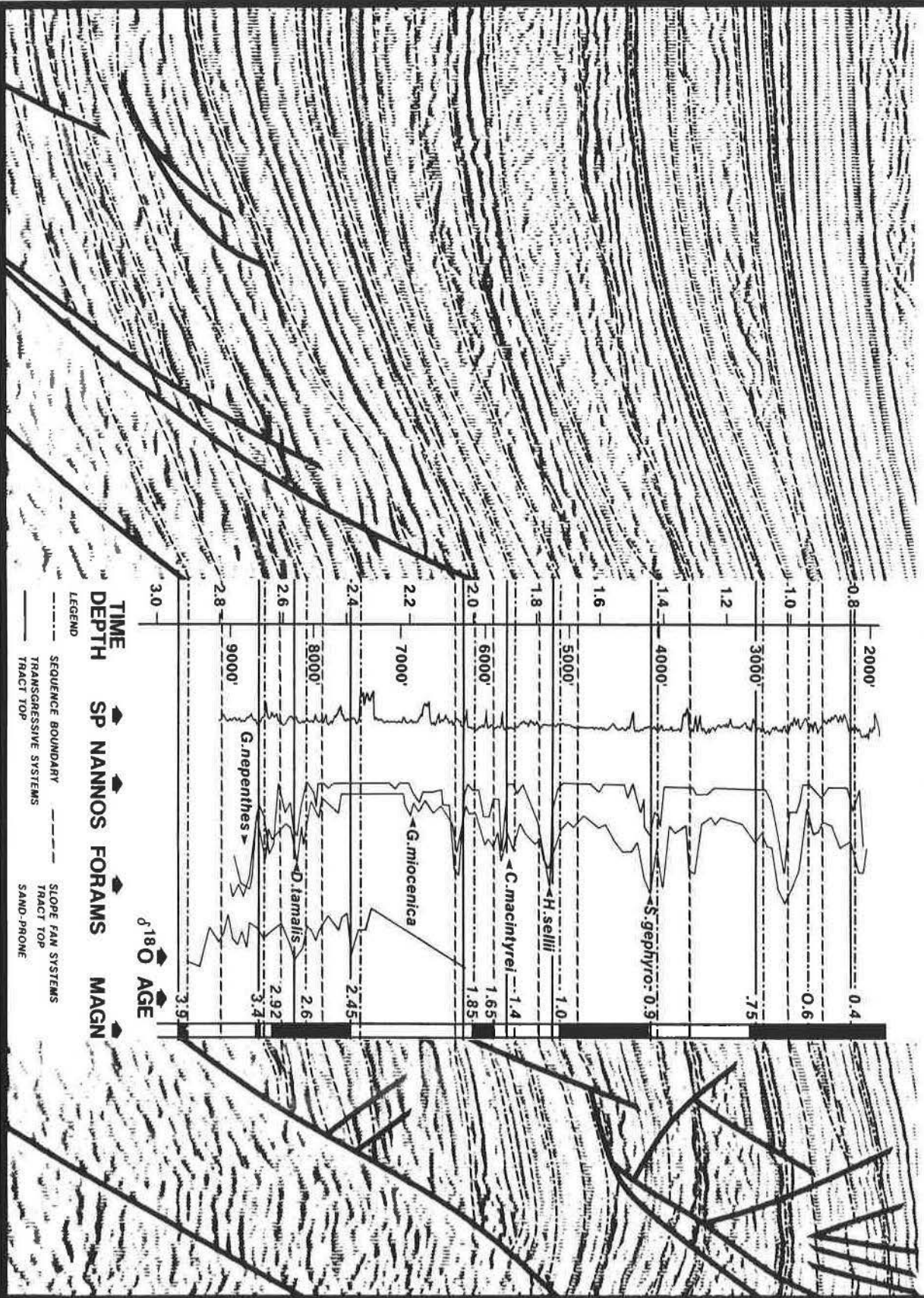
### Figure Captions

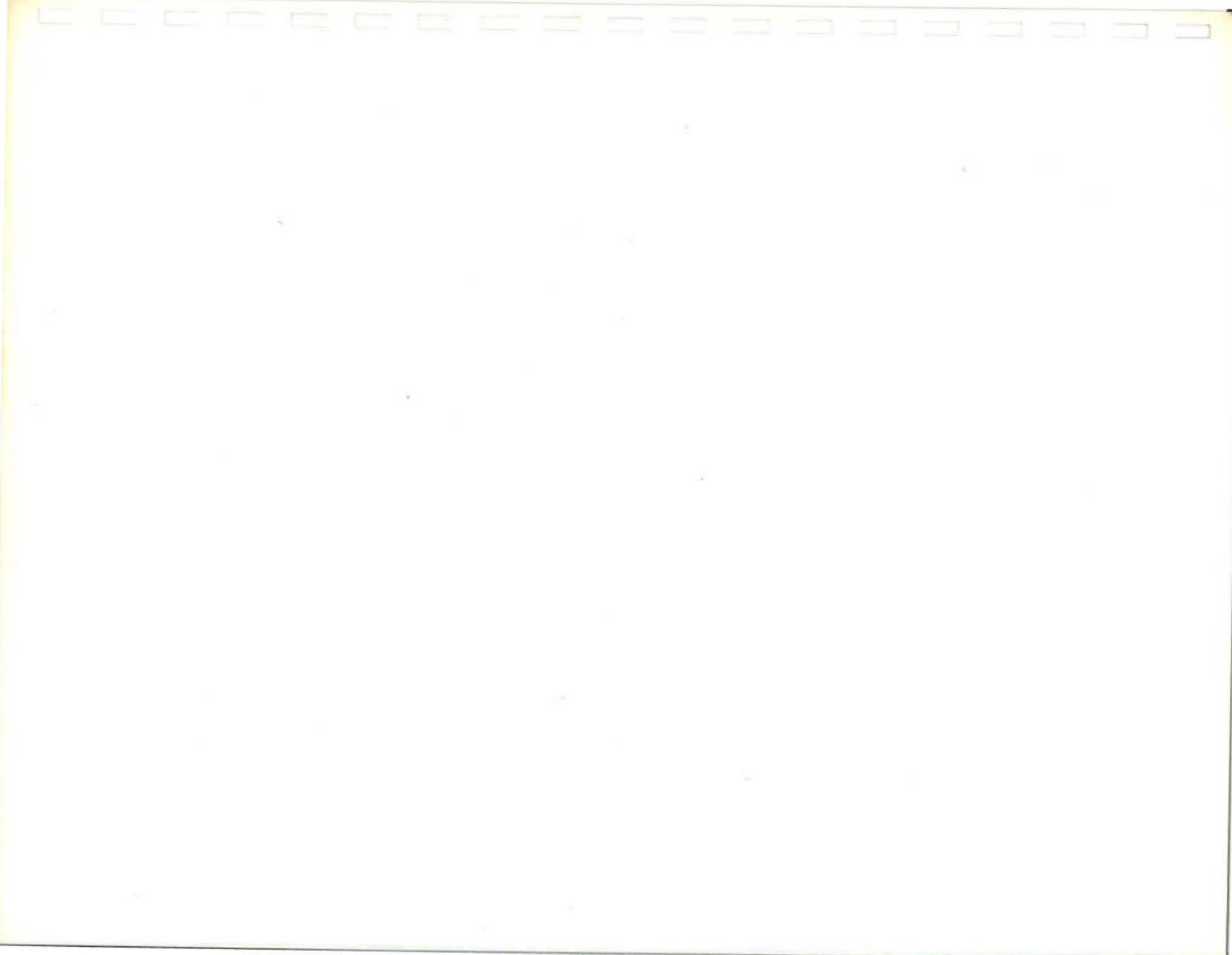
Figure 1. Model of stratal and seismic patterns of systems tracts with lithofacies (modified from Vail, 1987).

Figure 2. A segment of an offshore Texas line illustrating the integration of the SP log curve, bio-, magneto-, and chemostratigraphy with the seismic data. Sand interpretations (gray areas) are based on the systems tract models and calibration with the SP log curve.



# CHRONOSTRATIGRAPHY & LITHOLOGY INTEGRATED WITH SEISMIC DATA





May 7, 1991

Mr. Jack Caldwell  
SEG Summer Research Workshop  
Box 702740  
Tulsa, OK 74170-2740

Dear Jack,

Enclosed is the abstract we discussed for the 8th Annual SEG Summer Research Workshop to be held in St. Louis, Missouri on July 28-August 1, 1991. I still do not have budget allowance from Landmark to attend the workshop and am not sure how to get the poster to St. Louis since it is very large, but will work on both of those if the abstract is of interest.

The paper was put together for the AAPG by V. Kolla, Brad Macurda and myself. It is titled "The Systems Tracts of the Zambezi Delta, Mozambique." I am still working on getting others to submit abstracts to you by Friday as requested.

Sincerely yours,

✓ H. Roice Nelson, Jr.

VITA

Enclosure

cc: V. Kolla  
Brad Macurda  
Bob Peebler

# **The Systems Tracts of the Zambezi Delta, Mozambique**

by

V. Kolla, Elf Aquitaine  
D. Bradford Macurda, Jr., The Energists  
and H. Roice Nelson, Jr., Landmark Graphics Corporation

## **ABSTRACT**

During the Neogene and Quaternary, Mozambique shelf margin, close to the Zambezi river delta, prograded for distances of 75 to over 100 km into the Indian Ocean. A regional seismic grid shows numerous unconformities and correlative conformities in the platform shelf, slope and deeper basinal areas. Based on downward shifts of reflection terminations and onlaps at or below shelf edge offlap break, more than 25 sequences have been identified. Within the gross Neogene package, the basal section is characterized by aggradation, followed by rapid and significant (oblique) progradation, which is then followed by numerous aggradational-progradation and progradation packages in the upper, younger sections. From recognition of aggradation-progradation patterns and from well information, it appears that the first, significant and rapid progradation occurred after Mid-Miocene. The earliest of the Neogene sequences appears thicker towards the south and thinner towards the north. Subsequently, more progradation occurred in the north for sometime, compensating for the earlier lesser progradation in that region. On the whole, the depocenters, mainly shelf edge prograding wedge complexes, deposited during relative lowstands, shifted in position back and forth in the region. The number of sequences, their modes of stacking and thickness distributions, reflect relative sea-level changes, the points of sediment input as the river inputs shifted in position, and the depositional topography.

The Mozambique passive continental margin near the Zambezi Delta, located in the Indian Ocean Basin, is a stable platform as opposed to the unstable continental margins off the Mississippi, McKenzie and Niger deltas and is geographically far from the stable margins which were the basis of the Haq, et. al. cycle-chart (1987). Thus, the Mozambique continental margin provides an independent test case for verification of eustatic cycles and for the evaluation of allogenic (eustatic) vs autogenic (subsidence and delta switching) effects on depositional systems and systems tracts.



**SEG Research Workshop on  
Lithology: Relating Elastic  
Properties to Lithology at  
all Scales**

**July 28-August 1, 1991  
St. Louis, Missouri**

*Workshop Chairman*

Jack Caldwell  
Schlumberger  
4100 Spring Valley Rd.  
Suite 600  
Dallas, Texas 75244  
Telephone: (214) 385-4040  
Telecopy: (214) 385-3429

*Workshop Organizing  
Committee*

C.H. (Arthur) Cheng  
Francis Muir  
Norman Neidell

H. Roice Nelson, Jr.

Sue Raikes  
Yoram Shoham  
Tracy J. Stark  
M. Turhan Taner  
Robert H. Tatham  
Leon Thomsen  
Don Winterstein  
Ed Witterholt

Sponsored by  
the Society  
of Exploration  
Geophysicists  
Research Committee



May 24, 1991

**TO: Organizing Committee Members**

**CONGRATULATIONS!** We have enough papers submitted now to insure a full 4 sessions of posters for the first two days of the meeting. I want to thank all of you for your help in what has been a wee bit of a struggle, due, primarily, I think, to the other closely related meeting going on at Tamarron. Major oil company participation in our meeting is still somewhat disappointing, but we do not need to continue to beat the bushes for any more papers. Please follow up and finalize arrangements for any papers you still have dangling out there.

The next primary task for us as a committee is to reconfirm the assignment of discussion session chairmen, and to start thinking about how to insure good discussion sessions. I will be calling you shortly to get your suggestions, and to reconfirm your roles.

Attached please find the following items:

- (1) the overall Lithology Workshop agenda
- (2) the current (but certainly not final) listing of papers by session and author
- (3) my Welcome Letter, for the information brochure being sent out the last week in May from SEG Headquarters
- (4) the description of the meeting format, also to be contained in the information brochure.

Please note that Chuck Edwards, former Chief Geophysicist for Chevron, will be presenting the keynote address on Sunday evening preceding the meeting. The title of his talk is "Multi-Facets of Lithology for Multi-Disciplined Scientists".

Thank you.

Regards,

*Jack Caldwell*  
Jack Caldwell

JGC:cs0  
Attachments



June 4, 19

**SEG Research Workshop on  
Lithology: Relating Elastic  
Properties to Lithology at  
all Scales**

July 28-August 1, 1991  
St. Louis, Missouri

H. Roice Nelson, Jr.  
Landmark Graphics Corp.  
333 Cypress Run  
Houston, TX 77094

*Workshop Chairman*

Jack Caldwell  
Schlumberger  
4100 Spring Valley Rd.  
Suite 600  
Dallas, Texas 75244  
Telephone: (214) 385-4040  
Telecopy: (214) 385-3429

*Workshop Organizing  
Committee*

C.H. (Arthur) Cheng  
Francis Muir  
Norman Neidell  
H. Roice Nelson, Jr.  
Sue Raikes  
Yoram Shoham  
Tracy J. Stark  
M. Turhan Tamer  
Robert H. Tatham  
Leon Thomsen  
Don Winterstein  
Ed Witterholt

Sponsored by  
the Society  
of Exploration  
Geophysicists  
Research Committee



Dear Roice:

Your paper entitled **The Systems Tracts of the Zambezi Delta, Mozambique** has been chosen for presentation at the SEG Research Workshop on Lithology: Relating Elastic Properties to Lithology at all Scales to be held at the Adams Mark St. Louis Hotel in St. Louis, Missouri, July 28 - August 1, 1991.

Your poster presentation is scheduled in the Tuesday afternoon, July 30, Frontier/Submature Exploration Session. The poster presentation portion of that session will be held from 1:00 p.m. to 5:00 p.m..

Presentation Area Set Up

Your booth will be a cubicle formed with two 4' x 4' side walls and a 4' x 8' back wall of white Seletex (fiber board). You will be able to display material on all three walls of your area. Push pins will be provided by SEG to aid in the display of your materials. Tape and/or Velcro will damage the boards; therefore, their use is prohibited.

Poster paper set up is scheduled from 2:00 p.m. until 6:00 p.m. on Sunday, July 28. Your display set up should be completed no later than 6:00 p.m. on Sunday, just prior to the Welcoming Reception which will be held in the Promenad Ballroom, and it should stay in place throughout the Workshop.

### Expanded Abstract

According to the instructions in the Call for Abstracts, the initial abstract required was 400 to 500 words in length. An expanded abstract (1,000 to 2,000 words) of papers to be presented are also required and should be sent to the following address **no later than July 10:**

Mr. Jack Caldwell  
c/o SEG  
PO Box 702740  
Tulsa, OK 74170

(Street Address: 8801 S. Yale, Tulsa, OK 74137)

The expanded abstracts will be photographed as received and published for distribution at the Workshop.

To refresh your memory on the presentation of poster papers, we have enclosed a copy of the SEG's POSTER PRESENTATION MANUAL. It will assist you in planning, designing, displaying and presenting your poster paper.

**IMPORTANT:** YOU ARE ASKED TO BE IN YOUR BOOTH AREA DURING AN ASSIGNED HALF OF YOUR HALF-DAY SESSION OR AS ASSIGNED BY YOUR SESSION CHAIRMAN.

### Housing, Registration, and Special Airfares

An Advance Registration packet of information on the Workshop will be sent to you later this week along with a layout of the poster presentation area showing the location of your paper. As a speaker, you will be given priority in the reservation of rooms at the Adams Mark St. Louis Hotel. Please return the Housing Reservation form to the address on the form as quickly as possible.

The Advance Registration form should be returned to SEG. Your registration materials will be waiting for you at a special Advance Registration Desk in the foyer area outside the Promenade Ballroom on Sunday, July 28, from 2:00 p.m. until 6:00 p.m. provided you return the Advance Registration form to SEG.

### Lapel Ribbon

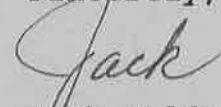
Enclosed is a lapel ribbon designating you as a **SPEAKER**. Please bring this with you to the Workshop and attach it to your badge that you receive when you register.

Publication Rights

Papers are presented at SEG Research Workshops with the understanding that the Society's journals, GEOPHYSICS and THE LEADING EDGE, hold first claim on their publication.

If you have any questions concerning the above information, please contact Beverly Gray at (918) 493-3516. We look forward to seeing all of you in St. Louis.

Sincerely,



Jack Caldwell  
Workshop Chairman